Unterschrift BetreuerIn

DISSERTATION

Elemental analysis of bone tissue by laboratory- and synchrotron-based µXRF, including approaches to combining µXRF with other imaging techniques

ausgeführt zum Zwecke der Erlangung des akademischen Grades einer

Doktorin der Naturwissenschaften

unter der Leitung von

Ao.Univ.Prof. Dipl.-Ing. Dr.techn. Christina Streli

E141 – Atominstitut

eingereicht an der Technischen Universität Wien

Fakultät für Physik

von

Anna Turyanskaya

[redacted]

Wien, am

A. Turyanskaya

Contents

Acknowledgements

First and foremost, I would like to express my deepest appreciation to the supervisor of my PhD thesis Dr. Christina Streli, for introducing me to the completely new and enigmatic world of X-ray physics, patient guidance on this path and lots of encouragement. Thank you for taking a chance on me!

The journey would not be possible without my closest colleague Mirjam Rauwolf, with whom I shared all my work travels, majority of the experiments, and many other activities. At least half the success is due to our teamwork!

Peter Wobrauschek, Peter Kregsamer, Dieter Ingerle, Josef Prost, Jan Welch and all the former and current members of X-ray physics group at Atominstitut, many thanks to you! I could not wish for better colleagues!

I would like to thank the cooperation partners from the "Bone team" – Andreas Roschger, Jochen Hofstätter, Paul Roschger – for providing the much needed samples, help in directing the focus of research and drafting the publications. I would also like to mention the colleagues from Ludwig Boltzmann Institute of Osteology for their help in sample preparation and supporting measurements.

Many thanks to Rolf Simon (ANKA), Ivo Zizak (BESSY-II), Kawal Sawhney (Diamond Light Source), Manfred Burghammer (ESRF) for their support during beamtimes.

Being a part of MEIBio doctoral school, I wish to thank Dr. Martina Marchetti-Deschmann and all the faculty members and fellow students. Special thanks go to Anastasiya Svirkova, Stefan Smetaczek and Dr. Andreas Limbeck with whom we established a productive 'multimodal' collaboration.

Many thanks to my family and friends for all the encouragement and support (in many cases long-distance). I would like to express my deepest gratitude to my partner Thomas for advice, support and understanding in highs and lows, and to the little NN for the final motivational kick.

To all those, who guided, accompanied, and supported me on the way of my PhD project – thank you!

The research leading to these results has received funding from the Austrian Science Fund (FWF, project number: P27715), some parts of this project were funded by the PhD program "MEIBio (Molecular and Elemental Imaging in Biosciences)" provided by TU Wien.

Kurzfassung

Im Rahmen dieser Doktorarbeit, wurden physikalische Analysemethoden verwendet, um die chemische Zusammensetzung biologischer Proben zu untersuchen. Der Fokus war 1) die derzeit verfügbaren analytischen Methoden und Techniken weiterzuentwickeln, und 2) Problematiken mit biomedizinischer Relevanz zu lösen.

Die ersten Ziele wurden durch das Doktoratskolleg „Molecular and Elemental Imaging in Biosciences“ (MEIBio) initiiert und realisiert. Eine erfolgreiche Kombination der bereits existierenden analytischen Methoden für die folgenden Paare erreicht: Labor µXRF – MALDI-MSI und Labor µXRF – LA-ICP-MS.

- Die Kombination der Methoden Labor µXRF – MALDI-MSI wurde an Schnitten von Hühner-Phalangen durchgeführt. Diese Testproben ermöglichten die Messung verschiedener Gewebetypen und histologischer Strukturen. Da die technischen Aspekte der Messmethodenkombination von Interesse waren, wurde ein Fokus auf die Probenpräparation, die Wahl des Einbettmaterials und auf die Reihenfolge der Messungen gelegt. Mehrere Kombinationen wurden getestet, um sowohl elementare als auch molekulare Information der Schnitte zu bekommen. Die damit erstellten Bilder konnten übereinandergelegt und korreliert werden.
- Die Kombination von Labor µXRF – LA-ICP-MS konnte ebenfalls erfolgreich durchgeführt werden. Von beiden Methoden erhält man Informationen über die elementare Zusammensetzung, die räumliche Auflösung ist vergleichbar. Daher ist diese Kombination eine vielversprechende Variante, um die Grenzen der einzelnen Methoden zu überwinden sowie zum Vergleich der Ergebnisse. Dünne Schnitte vom menschlichen Oberschenkelkopf wurden zuerst mit µXRF und danach mit LA-ICP-MS gemessen. Das wichtigste Ergebnis dieser Kombination sind die qualitativen und quantitativen zweidimensionalen Bilder, die durch diese Methoden erstellt wurden.
- Die dritte geplante Kombination war Synchrotron-basierter µXRF und ToF-SIMS. Die hervorragende sub-µm räumliche Auflösung von ToF-SIMS im sub-µm Bereich kann nur mit Synchrotron-basierter µXRF-Analyse kombiniert und verglichen werden. Versuche zeigten: das Experiment muss sehr genau geplant werden, mit einem Fokus auf Probenvorbereitung und Auswahl von Messbereichen, passend für beide Methoden.

Der zweite Teil der Arbeit umfasst mehrere Projekte mit dem Ziel, die qualitative (und, wenn möglich, quantitative) Zusammensetzung von Haupt-, Neben- und Spurenelementen in Knochengewebe zu untersuchen.

- Die Untersuchung von Rattenknochen mit bio-resorbierbaren Mg-basierten Implantaten in verschiedenen Stadien der Resorption wurde mit Labor µXRF durchgeführt. Während Mg mit konstanter Geschwindigkeit in Knochengewebe/Organismus inkorporiert wird, ohne Anhäufungen und Agglomerationen; wurde gezeigt, dass Y tiefer in den Knochen gelangt.
- Ein Set menschlicher Proben wurde mit Synchrotron-basierter µXRF-Analyse untersucht, um einen Zusammenhang zwischen Osteoporose Mn Gehalt zu finden. Es scheint, dass menschliche Knochenproben (Transiliac-Knochenbiopsien) von männlichen Patienten mit idiopathischer Osteoporose insgesamt weniger Mn enthalten als gesunde Kontrollproben.
- Ein weiteres Projekt war auf die Untersuchung von Gd-Anhäufungen im menschlichen Knochengewebe fokussiert. Eine mögliche Quelle von Gd im menschlichen Organismus könnte die Verabreichung von Gd-haltigen Kontrastmittel für Magnetresonanztomographien sein. Proben mit bekanntem und vermutetem Kontakt zu Gadolinium-basierten Kontrastmitteln wurden am Synchrotron untersucht. Detaillierte Bilder der elementaren

Zusammensetzung wurden erstellt und für eine der Proben wurde die Gd-Konzentration abgeschätzt.

Abstract

In the frame of this thesis, physical methods of analysis were used to investigate the chemical composition of biological samples, with a view to 1) further advance currently available analytical methods and techniques, and 2) solve questions of bio-/medical relevance.

The first set of aims was initiated by and realized within the TU Wien doctoral program "Molecular and Elemental Imaging in Biosciences" (MEIBio). Successful combination of the existing analytical methods was achieved for the following pairs of techniques: laboratory µXRF – MALDI-MSI and laboratory µXRF – LA-ICP-MS.

- The combination of modalities laboratory µXRF – MALDI-MSI was performed on chicken phalangeal cuts. This choice of a test sample allowed measurements of various types of tissues and histological structures. Since the technical aspects of the combination were primarily within the focus of the project, specific attention was paid to the sample preparation, choice of the supporting materials and to the order in which the techniques can be used. Several pipelines were tested out, providing us with both elemental and molecular information for the very same slices, so that the obtained maps could be finally superimposed producing correlated images.
- The pair laboratory µXRF – LA-ICP-MS has also been fruitful. Both modalities yield elemental information, and the lateral (spatial) resolution of the techniques is in the same range. Therefore, such a combination is a promising tool in overcoming the limitations of a single technique and for cross-validation of the results. Thin sections of a rather complex sample, human femoral head cuts, were scanned first with µXRF and then with LA-ICP-MS. The main achievement of this coupling is the qualitative and quantitative information (images) provided by both methods.
- The third conceived pairing was planned for the synchrotron-based µXRF and ToF-SIMS. Having an outstanding sub-µm lateral resolution, ToF-SIMS can only be compared and combined with synchrotron-based µXRF analysis. The lesson learnt from the attempted testing: a careful design of such an experiment is needed, with the emphasis on sample preparation and area selection fitting for both techniques.

The second part of work comprises several projects which were mainly devoted to the investigations of the sample composition – qualitative (and, if possible, also quantitative) analysis of major, minor, and trace elements in bone tissue.

- The investigation of rat bone samples carrying biodegradable Mg-based implants at different degradation timepoints was performed using the laboratory µXRF. Whereas Mg seemed to be incorporated into the bone tissue/organism at a steady pace without leaving visible clusters or aggregations; the tendency for Y was found to migrate deeper into the bone.
- A set of human samples was studied using synchrotron-based µXRF in order to test out the link between osteoporosis and Mn content. It appears that human bone samples (transiliac bone biopsy samples) from male patients with idiopathic osteoporosis tend to contain less Mn globally in bone tissue as compared to healthy controls.
- Another project was devoted to the investigation of Gd accumulation in human bone tissue. One of the potential sources of Gd in the human organism can be administration of gadolinium-based contrast agents for magnetic resonance imaging procedure. The measurements of samples with known and suspected administration of gadolinium-based contrast agents were conducted at the synchrotron, yielding detailed elemental maps, furthermore, for one of the samples Gd concentration could have been estimated.

Only the work directly related to this thesis is listed here. For a complete list of publications and conference contributions produced over the duration of my doctoral work, please refer to the end of the thesis.

Parts of this work have been published in the following peer-reviewed articles:

1. Turyanskaya A, Rauwolf M, Grünewald T, Meischel M, Stanzl-Tschegg S, Löffler J, et al. µXRF Elemental Mapping of Bioresorbable Magnesium-Based Implants in Bone. Materials (Basel) [Internet]. 2016 Sep 30;9(10):811.
2. Svirkova A, Turyanskaya A, Perneczky L, Streli C, Marchetti-Deschmann M. Multimodal imaging of undecalcified tissue sections by MALDI MS and µXRF. Analyst [Internet]. 2018; 143(11): 2587–95.
3. Turyanskaya A, Rauwolf M, Pichler V, Simon R, Burghammer M, Fox OJL, et al. Detection and imaging of gadolinium accumulation in human bone tissue by micro- and submicro-XRF. Sci Rep [Internet]. 2020 Dec 14; 10(1):6301.
4. Turyanskaya A, Smetaczek S, Pichler V, Rauwolf M, Perneczky L, Roschger A, et al. Correlation of µXRF and LA-ICP-MS in the analysis of a human bone-cartilage sample. J Anal At Spectrom. 2021;36(7):1512–23

Conference contributions related to parts of this work have been presented:

Talks:

1. A. Turyanskaya, M. Rauwolf, A. Roschger, B. Pemmer, J. Prost, R. Simon, P. Roschger, J. G. Hofstaetter, T. Landete-Castillejos and C. Streli. Synchrotron µXRF analysis of Manganese distribution in antler and human bone. International Conference on Progress in Bone and Mineral Research 2015 and the Annual Autumn Conference of the Austrian Society for Bone and Mineral Research, Vienna, Austria; 3-5 December 2015

2. A. Svirkova, A. Turyanskaya, C. Streli, M. Marchetti-Deschmann. Sample preparation of sections with undecalcified bone for multimodal MALDI-MS and µ-XRF imaging. 12th ASAC-JunganalytikerInnen-Forum, Graz, Austria; 10-11 June 2016

3. A. Turyanskaya, M. Rauwolf, A. Roschger, J. Prost, P. Hischenhuber, T. Landete-Castillejos, R. Simon, P. Wobrauschek, P. Roschger, J.G. Hofstaetter, C. Streli. Manganese distribution in antler and human bone by SR-µXRF analysis. European Conference on X-ray Spectrometry, Gothenburg, Sweden; 19-24 June 2016

4. A. Turyanskaya, M. Rauwolf, P. Wobrauschek, C. Streli. Elemental bioimaging in bone by micro-X-ray-fluorescence spectroscopy (µXRF). 16th International Symposium on Trace Elements in Man and Animals (TEMA-16), International Society for Trace Element Research in Humans (ISTERH 2017), St. Petersburg, Russia; 26-29 June 2017

5. A. Turyanskaya, M. Rauwolf, L. Perneczky, A. Svirkova, M. Bonta, A. Limbeck, M. Marchetti-Deschmann, A. Roschger, P. Roschger, P. Wobrauschek, C. Streli. Multimodal Imaging of Biological Samples: Correlation of µXRF with MALDI-MSI and with LA-ICP-MS. Annual Denver X-ray Conference 2017, Big Sky, USA; 31 July – 4 August 2017

6. A. Svirkova, A. Turyanskaya, C. Streli, M. Marchetti-Deschmann. Molecular and Elemental Imaging for comprehensive information - the combination of MALDI MSI and µXRF.

Austrian Cluster for Tissue Regeneration - Annual Meeting 2018, Vienna, Austria; 12-13 March 2018

7. M. Marchetti-Deschmann, M. Holzlechner, A. Svirkova, M. Bonta, A. Turyanskaya, J. Lohninger, C. Streli, A. Limbeck. Molecular and Elemental Imaging by Mass Spectrometry and micro X-Ray Fluorescence. 36th Informal Meeting on Mass Spectrometry, Köszeg, Hungary (**invited**); 06-09 May 2018; abstract in: "36th Informal Meeting on Mass Spectrometry Book", (2018), ISBN: 978-963-7067-37-2

8. M. Marchetti-Deschmann, M. Holzlechner, A. Svirkova, M. Bonta, A. Turyanskaya, J. Lohninger, C. Streli, A. Limbeck. Molecular Mass Imaging Combined with Elemental Information - From Multiple Modes to Multiple Sensors. Talk: 66th ASMS Conference on Mass Spectrometry and Allied Topics, San Diego, CA, USA; 03-07 June 2018; abstract in: "ASMS Annual Proceedings", (2018)

9. A. Turyanskaya, M. Rauwolf, L. Perneczky, A. Svirkova, S. Smetaczek, A. Limbeck, M. Marchetti-Deschmann, A. Roschger, P. Roschger, P. Wobrauschek, C. Streli. Multimodal imaging of biological samples: correlation of µXRF with MALDI-MSI and with LA-ICP-MS. EXRS/European Conference on X-Ray Spectrometry, Ljubljana, Slovenia; 24-29 June 2018

10. C. Streli, M. Rauwolf, A. Turyanskaya, D. Ingerle, P. Wobrauschek. Elemental imaging of trace elements in bone samples. Keynote Lecture: XVI Conferencia Latinoamericana de analisis por tecnicas de rayos X, Pucon, Chile (**invited**); 04-07 November 2018

11. C. Streli, M. Rauwolf, A. Turyanskaya, D. Ingerle, P. Wobrauschek. Elemental Imaging of Trace Elements in Bone Samples. Annual Denver X-ray Conference 2019, Lombard, IL, USA (**invited**); 5-9 August 2019

12. A. Turyanskaya, M. Rauwolf, V. Pichler, R. Simon, O. J. L. Fox, K. J. S. Sawhney, M. Burghammer, J. G. Hofstaetter, A. Roschger, P. Roschger, P. Wobrauschek, C. Streli. Gadolinium mapping in bone by XRF spectroscopy.17th International Congress on Photobiology. 18th Congress of the European Society for Photobiology (2019 ESP-IUPB World Congress), Barcelona, Spain (**invited**); 25-30 August 2019

13. M. Marchetti-Deschmann, M. Holzlechner, A. Svirkova, M. Bonta, A. Turyanskaya, M. Großgarten, A. Balbekova, K. Wieland, B. Lendl, A. Limbeck: Correlative Multimodal Imaging in Mass Spectrometry. 30th MassSpec-Forum Vienna, Vienna, Austria; 19-20 February 2019; in: "Book of Abstracts", (2019), 24

14. A. Turyanskaya, M. Rauwolf, V. Pichler, M. Burghammer, J. G. Hofstaetter, A. Roschger, P. Roschger, P. Wobrauschek, C. Streli, K. Sawhney. Gadolinium mapping in bone by micro-/submicro-XRF. EXRS 2022/European Conference on X-Ray Spectrometry, Bruges, Belgium, 26 June-1 July 2022

Posters:

1. A. Turyanskaya, M. Rauwolf, A. Roschger, B. Pemmer, J. Prost, R. Simon, P. Roschger, J.G. Hofstaetter, T. Landete-Castillejos, K. Klaushofer, P. Wobrauschek and C. Streli: Spatially resolved manganese distribution in antler and human bone. 64th Annual Denver X-Ray Conference, Westminster, USA; 3-7 August 2015

2. A. Turyanskaya, T.A. Gruenewald, M. Meischel, M. Rauwolf, J. Prost, H. Lichtenegger, S.E. Stanzl-Tschegg, A.M. Weinberg, P. Wobrauschek and C. Streli: Magnesium diffusion

from implant into bone tissue observed by µXRF imaging. 64th Annual Denver X-Ray Conference, Westminster, USA; 3-7 August 2015

3. A. Svirkova, A. Turyanskaya, G. Allmaier, C. Streli and M. Marchetti-Deschmann: Sectioning of undecalcified bone tissue for multimodal MALDI-MS and µ-XRF imaging. Ourcon III, Pisa, Italy; 27-29 October 2015

4. A. Svirkova, A. Turyanskaya, T. Bretschneider, C. Streli, M. Marchetti-Deschmann. Sample preparation of tissue containing undecalcified bone for multimodal MALDI-MS and µ-XRF imaging. 27th MassSpec Forum Vienna, Vienna; 23-24 February 2016

5. A. Turyanskaya, M. Rauwolf, A. Roschger, J. Prost, B. Pemmer, R. Simon, P. Roschger, J.G. Hofstaetter, T. Landete-Castillejos, P. Wobrauschek, C. Streli. Manganese distribution in bone tissue by SR-µXRF. 43rd Annual European Calcified Tissue Society Congress, Rome, Italy; 14–17 May 2016

6. A. Turyanskaya, T.A. Gruenewald, M. Rauwolf, M. Meischel, J. Prost, L. Perneczky, H. Lichtenegger, S.E. Stanzl-Tschegg, A. Weinberg, P. Wobrauschek, C. Streli. Magnesium-based biodegradable orthopedic implants by µXRF. European Conference on X-ray Spectrometry, Gothenburg, Sweden; 19-24 June 2016

7. A. Turyanskaya, M. Rauwolf, A. Roschger, J. Prost, P. Hischenhuber, R. Simon, P. Roschger, J.G. Hofstaetter, K. Klaushofer, P. Wobrauschek, C. Streli. Manganese distribution in healthy and osteoporotic human bone. 65th Annual Denver X-Ray Conference, Rosemont, USA; 1-5 August 2016

8. A. Turyanskaya, T.A. Gruenewald, M. Meischel, M. Rauwolf, J. Prost, L. Perneczky, H. Lichtenegger, S.E. Stanzl-Tschegg, A.M. Weinberg, P. Wobrauschek, C. Streli. Elemental imaging on biodegradable orthopedic implants by µXRF. 65th Annual Denver X-Ray Conference, Rosemont, USA; 1-5 August 2016

9. A. Turyanskaya, M. Rauwolf, L. Perneczky, T.A. Gruenewald, M. Meischel, H. Lichtenegger, S.E. Stanzl-Tschegg, A.M. Weinberg, P. Wobrauschek and C. Streli. Exploitation of µXRF spectrometer for Bio-Imaging. X-Ray Microscopy Conference (XRM2016), Oxford, UK; 15-19 August 2016

10. A. Svirkova, A. Turyanskaya, C. Streli, M. Marchetti-Deschmann. Method development for sample preparation of sections with undecalcified bone for multimodal MALDI MS and µ-XRF imaging. Ourcon IV, Ustron, Poland; 17-21 October 2016

11. A. Turyanskaya, M. Rauwolf, L. Perneczky, T. Gruenewald, M. Meischel, H. Lichtenegger, S.E. Stanzl-Tschegg, A. Weinberg, P. Wobrauschek, C. Streli. µXRF spectrometer at Atominstitut for bio-imaging applications. 26th Seminar Activation Analysis and Gamma Spectroscopy (SAAGAS 26), Vienna, Austria; 20-22 February 2017

12. A. Turyanskaya, M. Rauwolf, T. Bretschneider, P. Wobrauschek, C. Streli, A. Roschger, J. Hofstätter, P. Roschger, I. Zizak. Investigation of the Local Manganese Distribution in Bone in Female and Male Osteoporosis Compared to Healthy Controls. Annual Denver X-ray Conference 2017, Big Sky, USA; 31 July – 04 August 2017

13. A. Turyanskaya, M. Rauwolf, O. Fox, I. Pape, K. Sawhney, T. Grünewald, M. Burghammer, J. Hofstätter, A. Roschger, P. Roschger, P. Wobrauschek, C. Streli. Detection of Gadolinium accumulation in bone by XRF. EXRS 2018/European Conference on X-Ray Spectrometry, Ljubljana, Slovenia; 24-29 June 2018

14. A. Turyanskaya, M. Rauwolf, V. Pichler, P. Wobrauschek, C. Streli, T. Grünewald, M. Burghammer, O. Fox, I. Pape, K. Sawhney, J. Hofstätter, A. Roschger, P. Roschger. Detection on of Gadolinium Accumulation in Bone by XRF. Denver X-ray conference (2018), Westminster, USA; 06-10 August 2018

15. A. Svirkova, A. Turyanskaya, L. Perneczky, C. Streli, M. Marchetti-Deschmann. Multimodal imaging of undecalcified tissue sections by MALDI MS and µXRF. XXII International Mass Spectrometry Conference, Florence, Italy; 26-31 August 2018; abstract in: "Conference Program of the XXII International Mass Spectrometry Conference", (2018), ISBN: 9788890738852; 913 - 914

16. A. Turyanskaya, A. Svirkova, L. Perneczky, C. Streli, M. Marchetti-Deschmann: Correlative multimodal imaging of chicken phalanx sections by µXRF and MALDI MSI. CMI Imaging in the Life Sciences Meeting 2018, Vienna, Austria; 20-21 September 2018

17. A. Turyanskaya, M. Rauwolf, V. Pichler, T. Grünewald, M. Burghammer, O. Fox, I. Pape, K. Sawhney, J. Hofstätter, A. Roschger, P. Roschger, P. Wobrauschek, C. Streli. Imaging of Gadolinium accumulation in bone by XRF. CMI Imaging in the Life Science Meeting 2018, Vienna, Austria; 20-21 September 2018

18. A. Turyanskaya, M. Rauwolf, V. Pichler, R. Simon, M. Burghammer, O. Fox, K. Sawhney, J. Hofstaetter, A. Roschger, P. Roschger, P. Wobrauschek, C. Streli. Imaging of Gadolinium accumulation in bone by XRF. Biennial Meeting ViCEM – Vienna Center for Engineering in Medicine, Vienna, Austria, 14-15 November 2019

19. A. Turyanskaya, S. Smetaczek, V. Pichler, M. Rauwolf, A. Roschger, P. Roschger, A. Limbeck, C. Streli. Correlation of µXRF and LA-ICP-MS in analysis of human bone-cartilage sample. Conference on Multimodality Imaging in Life Sciences 2019, COMULIS & BioImaging Austria – CMI, Vienna, Austria, 21-22 November 2019

20. A. Turyanskaya, M. Rauwolf, V. Pichler, M. Burghammer, O. Fox, K. Sawhney, J. Hofstätter, A. Roschger, P. Roschger, P. Wobrauschek, C. Streli. Imaging of Gadolinium accumulation in human bone by XRF. Online Conference: 2020 Virtual SSRL/LCLS Users' Meeting, Stanford, USA; 28 September – 10 October 2020

21. A. Turyanskaya, St. Smetaczek, V. Pichler, M. Rauwolf, L. Perneczky, A. Roschger, P. Roschger, A. Limbeck, C. Streli. Correlation of µXRF and LA-ICP-MS in analysis of human bone-cartilage sample. 31st MassSpec Forum Vienna (2020), Vienna, Austria; 25-26 February 2020

1. Motivation

The ability to get a clearer view of objects, to peer through and see the details, which are otherwise-invisible to the naked eye, must have been fascinating humans for thousands of years. There are such archaeological finds as magnifying lenses dating back at least as early as 1200 B.C. The first microscopes, which had been developed in 17th century, were wielded specifically to examine the biological objects. Novel, revolutionary methods of analysis allow us to continue this pursuit – not only can we now eyeball the tissues and cells on a microscale, but we can also study their elemental and molecular structure and 'record', i.e. image it.

Although the living biological tissues are built primarily out of complex organic molecules, it is nevertheless fascinating to look into the underlying, more basic 'building blocks' – namely, the elements. Human body consists of four abundant elements (oxygen, carbon, hydrogen, and nitrogen), but it is not uncommon that macro- (e.g. calcium, phosphorous, magnesium, sodium, potassium, iron) and micro-/trace- (e.g. manganese, copper, chromium, iodine, zinc, cobalt) elements are being affected and decisively define the state of health or disease. Within the array of elemental analysis methods, only few allow non-destructive investigations. One of such methods is micro-beam X-ray fluorescence (µXRF) spectrometry, which is capable of elemental imaging on the micrometre and sub-micrometre level – and which was employed within this work. The characteristics of the technique make it specifically qualified for the examinations of biological tissues, and also render it into a favourable candidate for coupling with other elemental and molecular methods of analysis.

The PhD program "Molecular and Elemental Imaging in Biosciences" (abbreviated as MEIBio) aimed to advance the imaging techniques available at TU Wien and to develop the multimodal (i.e. when two or more imaging techniques/modalities are combined) imaging approaches for instrument combinations. Some of the goals which have been identified in the MEIBio framework are:

- to overcome the limitations of a single imaging technique;
- to understand better the requirements – especially with regard to sample preparation – of a multimodal approach;
- to test out various multimodal imaging pipelines;
- and finally, to obtain the superimposed spectral, elemental and molecular information (images) of the biological objects.

As mentioned above, the method of choice for this doctoral thesis is µXRF analysis. And within the frame of the MEIBio project, following method combinations were realized/tested out: (1) laboratory µXRF – MALDI-MSI; (2) laboratory µXRF – LA-ICP-MS; (3) synchrotron-based µXRF – ToF-SIMS.

Furthermore, few additional projects (funded by Austrian Science Fund/FWF, project P 27715 "3D und 2D Spurenelementverteilungen in krankhaften menschlichen Knochen und in histologischen Übergangszonen – ein Ansatz zur Darstellung der Elementverteilungen mit Micro- und Nanometerauflösung mittels Synchrotron XRF") were undertaken – using both laboratory µXRF and synchrotron radiation induced X-ray fluorescence analysis – in order to investigate the elemental composition of bone tissue. The topics range from investigation of innovative biomedical materials (studying the degradation of Mg bioresorbable implants in bone tissue) to potentially population-relevant health issues – e.g. role of specific trace elements (manganese) in osteoporosis, and possible accumulation of unwanted/hazardous substances (gadolinium) in osseous tissue. Where it is possible and fitting the questions (and associated problems) of sample preparation and quantification are addressed.

Overall, this work strives to demonstrate the versatility of the μXRF spectrometry and promote further employment of the method in biological and medical applications, both individually and also coupled with other modalities.

2. X-ray fluorescence analysis

X-ray Fluorescence (XRF) spectrometry is an analytical technique ideally suited for elemental analysis. From here on we will discuss the variant of XRF called micro-beam X-ray fluorescence spectrometry (µXRF). µXRF is one of the most popular elemental imaging methods for the analysis of biological samples (1), but generally can be applied in a wide variety of sample matrices. The ultimate advantage of µXRF compared to other elemental imaging techniques is its non-destructive nature (2).

In a nutshell, the technique is based on the excitation of the sample by X-rays, which results in the emission of characteristic radiation by each particular element, provided that the excitation energy is above the absorption edge of the element of interest. The fluorescence radiation emitted is then registered by an energy dispersive detector – thus, the information about multiple elements present in the sample may be obtained simultaneously (Fig. 1). The resultant characteristic spectrum can be deconvoluted, using a specific software, by factoring in spectral overlaps and artefacts, as well as background to extract information about a specific element. Usually, the sample is raster-scanned, yielding elemental maps. The spatial resolution of such a scan/map depends on the size of the X-ray beam. In the case of µXRF, the beam is focused to a few tens of micrometres in size, thus yielding a resolution in range of µm.

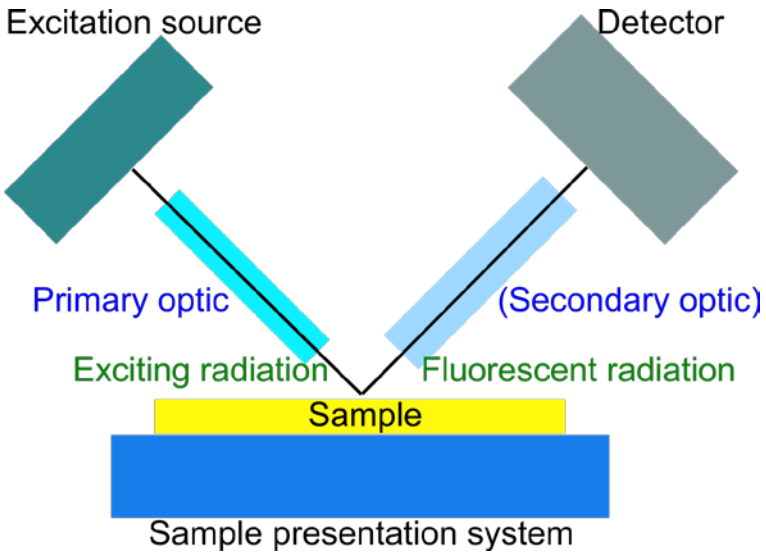

Figure 1. Basic scheme and the main components of an X-ray spectrometer (optionally with a secondary optic, which is required for confocal XRF)

µXRF can be loosely subdivided into laboratory µXRF, where the most common source of X-rays would be an X-ray tube, and synchrotron-based µXRF (SR-µXRF), performed at large-scale synchrotron radiation facilities.

Within this chapter we will discuss the technique, instrumentation, and components of spectrometers (with the focus on the ones used in the actual experiments), as well as approaches to µXRF data analysis. But before we launch into the specifics of the method, it is necessary to discuss the basic principles of X-ray fluorescence analysis.

2.1 Interaction of photons with matter

The properties of X-rays (Fig. 2) – wavelengths in the range of the atomic distances (corresponding to the energies in the kilo-electronvolt range (0.01–100 keV)) and the high penetration into matter open various possibilities for the examination of materials.

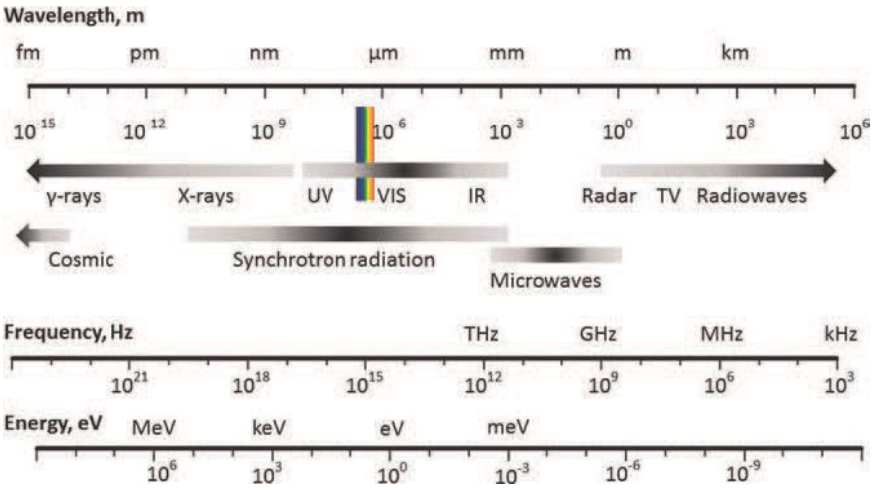

Figure 2. Spectrum of electromagnetic radiation (3)

There are different ways X-rays interact with the material, e.g. absorption, scattering or diffraction, refraction, and emission (schematically shown in Fig. 3). Those phenomena can be used "individually" as a basis for material probing (e.g. X-ray absorption spectroscopy, X-ray scattering techniques); in any case, they will inevitably contribute to any analysis performed using X-rays. Hence, a short description for the most important types of interactions is provided below.

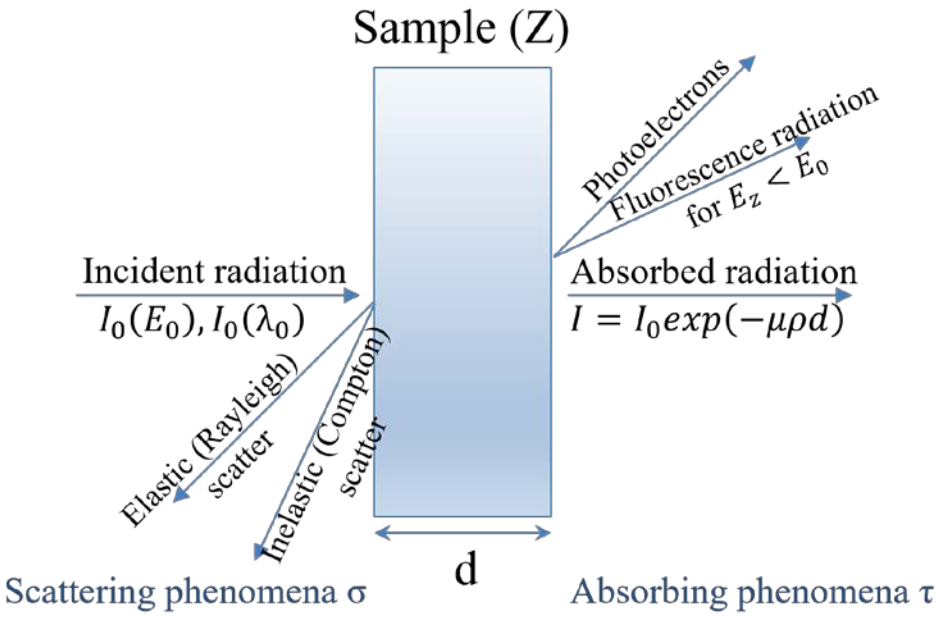

Figure 3. Interaction of photons with matter

2.1.1. Absorption

The incident beam of X-ray photons will interact with the material of atomic number Z and will be attenuated (4). This interaction is described by the mass attenuation coefficient μ, which includes

contributions from absorption and scattering – described by τ and σ, respectively. The contribution of scattering σ to attenuation is relatively small, therefore

$$\mu = \tau + \sigma \text{ can be simplified as } \mu \approx \tau$$

Within the absorption process the number of photons (the intensity of the beam) is reduced, but their energy is generally unchanged. According to the law of Lambert-Beer, absorption depends on the mass attenuation coefficient μ, the density of the material ρ and the thickness of the material d:

$$I = I_0 exp(-\mu \cdot \rho \cdot d)$$

where

- I_0 primary intensity
- μ mass attenuation coefficient as function of energy
- ρ density of the absorbing material
- d thickness of the absorbing layer

The mass attenuation coefficient (Fig.) depends on the radiation energy i.e. $\mu = \mu(E)$. For a complex multicomponent matrix, mass attenuation coefficient can be calculated from the mass attenuation coefficients of the n constituting elements:

$$\mu_{compound} = \sum_{i=1}^{n} w_i \mu_i$$

where

- w_i mass fraction of element i
- μ_i mass absorption coefficient of element i

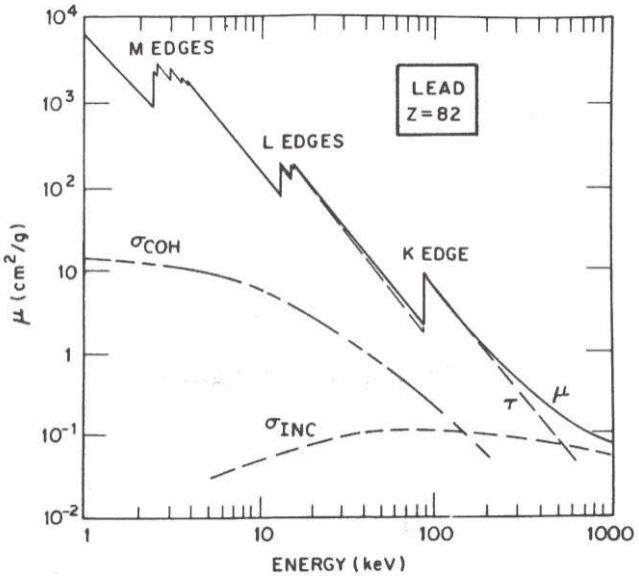

Figure 4. Mass attenuation coefficient and its components for lead as a function of incident photon energy (reprinted by courtesy of EG&G ORTEC) (5)

Imaging methods based on the absorption of the X-rays are widely used and very well known in medical applications. Upon illumination, X-rays penetrate human body, but will be absorbed to a different degree by various tissues (cf. bones and soft tissues) and organs. Furthermore, to increase the contrast, the materials with different absorption properties can be introduced into human body (via blood circulatory system or digestive system) – these are typically contrast agents containing heavy elements.

The array of spectroscopic techniques based on the absorption phenomenon deserves a special mentioning. X-ray absorption spectroscopy (XAS) allows elucidation of the binding modes (type and number of ligands, distances, and geometry) and oxidation states of metals and other trace elements in crystalline as well as non-crystalline samples. An absorption spectrum is divided in two areas, bringing forth corresponding methods of analysis: X-ray absorption near edge structure (XANES) part, from 50 eV before the absorption edge to 50 eV after the edge, and the extended X-ray absorption fine structure (EXAFS) part, from 50 to up to 1000 eV after the edge. The typical areas of application for XAS techniques include materials science, chemical and biochemical research.

2.1.2 Emission

The next type of interaction, sequential to the absorption, is emission (4,6). In the photoelectric absorption process, an incident photon is completely absorbed by the atom and, consequently, a photoelectron is ejected. Due to the high energy of the incident X-ray, the ejected electron can originate from the inner shells of an atom. Part of the photon's energy is used to overcome the binding energy of the electron and the rest is transferred in the form of kinetic energy. After the interaction, the now-ionized atom is in a highly excited state, with a vacancy in one of the inner shells. Returning to a more stable configuration can then happen via two competing processes – either by emission of an Auger electron, or by emission of a photon (Fig. 5). The energy of the emitted photon will be characteristic of the atom involved; thus, another term is often used for this photon – characteristic radiation. The process of the characteristic X-ray photon emission is called X-ray fluorescence.

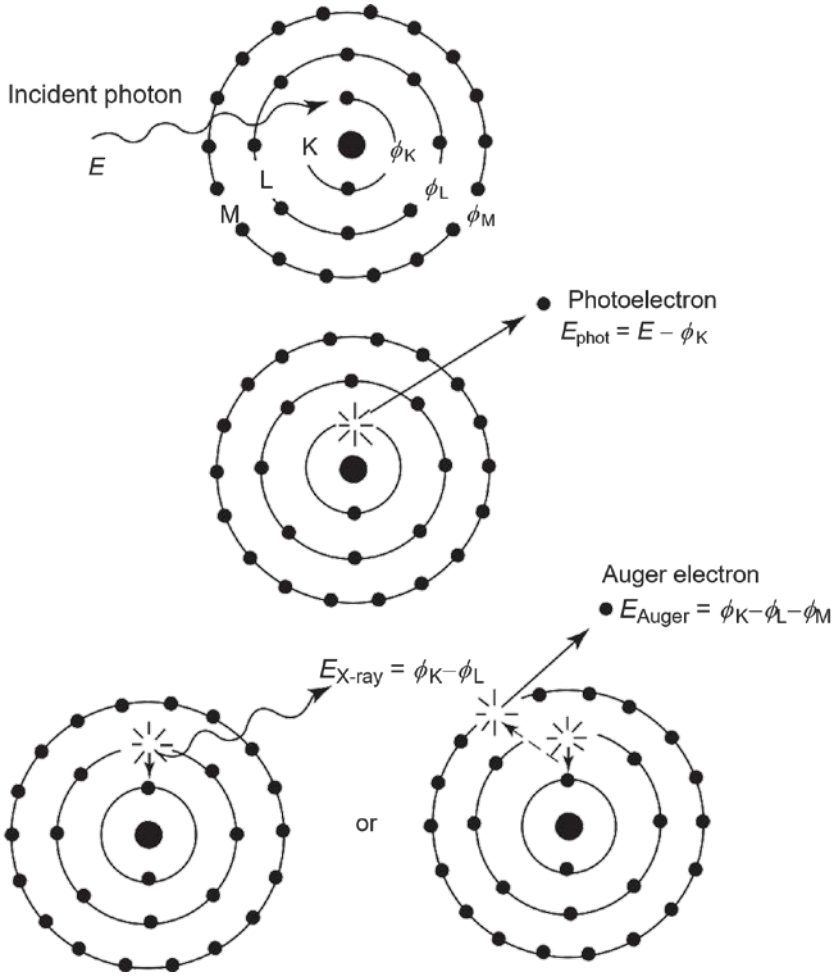

Figure 5. Emission of characteristic X-rays or Auger electron

The probability of transition p of an outer shell electron to the vacancy created by the emission of the photoelectron is different for various transitions. The energy difference

$$E_{diff} = E_{vacancy} - E_{outer}$$

between the binding energy of the two electron shells involved in the transition can be emitted directly by an X-ray, and corresponds to the energy of characteristic radiation.

The relation between the energy of characteristic radiation E and the atomic number Z of the emitting atom is described by Moseley's law:

$$E = C_1 \cdot (Z - C_2)^2$$

with C_1, C_2 constants which depend on the electron shells involved in the process.

As already mentioned above, the other, competing, process is the Auger effect. In this case the energy E_{diff} is transferred within the atom to an outer electron which leaves the atom with the energy:

$$E_{Auger} = E_{diff} - E_{binding}$$

Both processes have Z-dependent probabilities: the Auger yield is higher for light elements and the fluorescence probability is higher for heavy elements. And since only one of the energy emission processes takes place at a given interaction event, the probability for their sum is unity:

$$p_{Auger} + p_{X-ray} = 1$$

The probability for an X-ray emission is commonly referred to as fluorescence yield ω (Fig. 6).

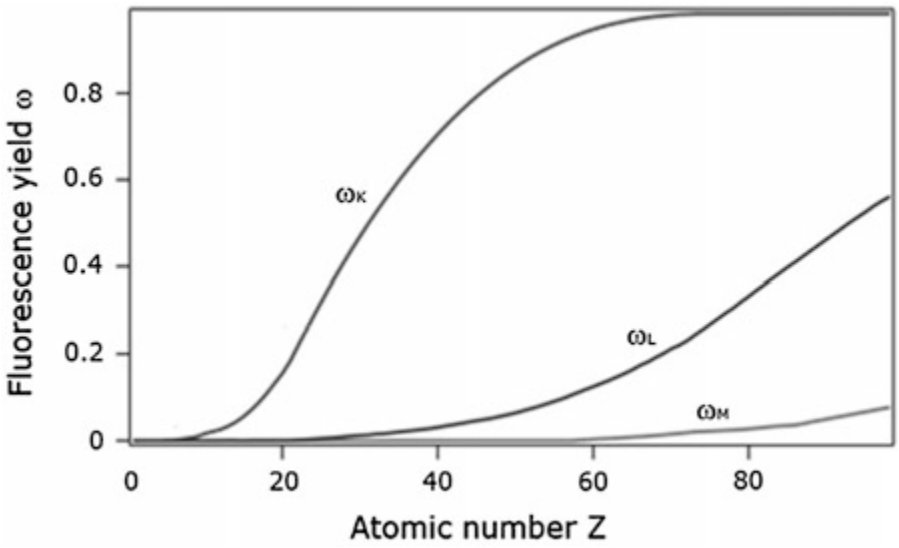

Figure 6. Fluorescence yield as a function of atomic number (4)

Returning to the subject of an electron transition: while each unique atom has a number of available electrons that can take part in the process, it has to be noted that only certain transitions are allowed. A set of transition (or selection) rules, defines the possible de-excitation routes. Figure 7 graphically describes the most important transitions for the K, L, M and N shells.

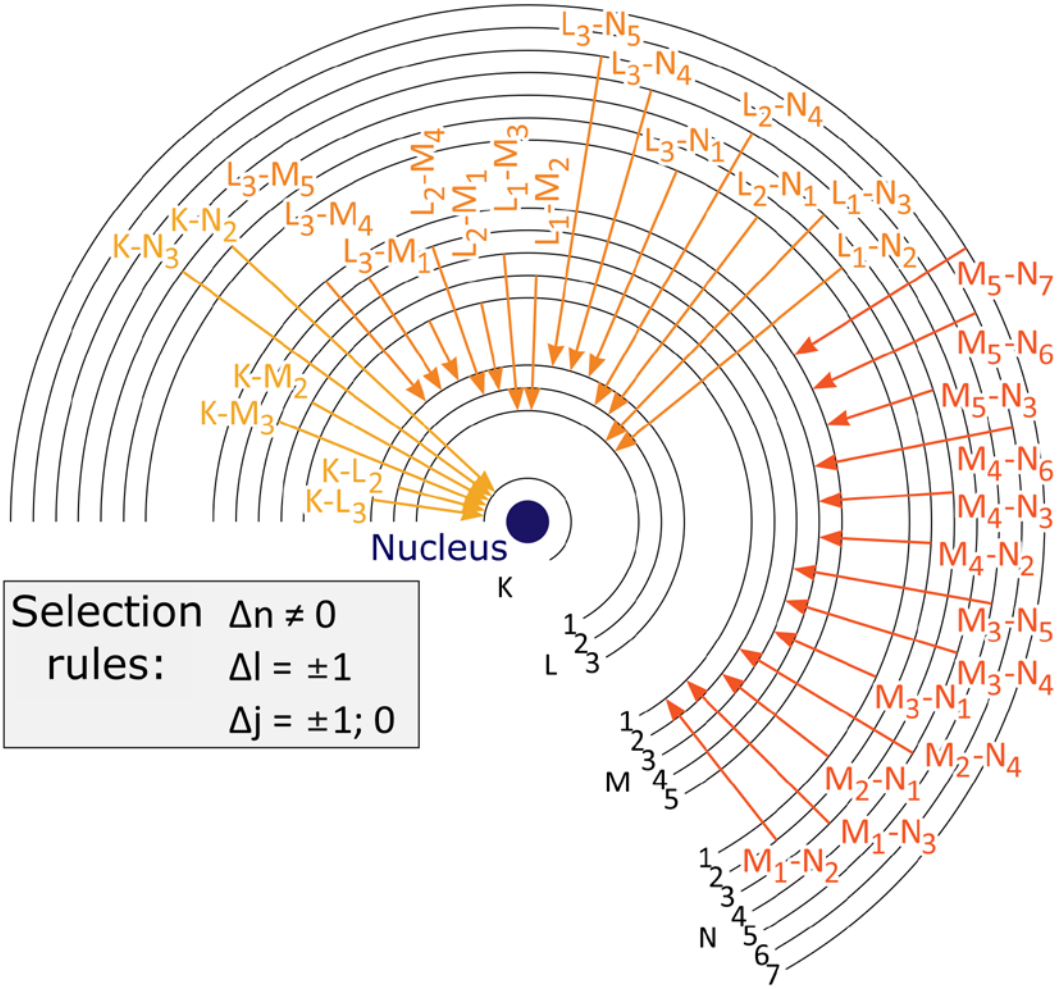

Figure 7. Electron transitions that are possible in an atom of heavy element (7)

Two approaches to nomenclating the transitions are usually used: a classical Siegbahn notation and a later introduced IUPAC (International Union of Pure and Applied Chemistry) notation.

Siegbahn notation is based upon the relative intensity of lines. The three principal series within this notation – the K, L, or M, originate when the inner vacancy being filled is in the K, L, or M shell. A Greek letter, will indicate the intensity of a line: i.e. most intense peak is called α, the next less intense peaks in descending order are called β, γ, η, and l. Finally, Arabic numeral subscript denotes the sublines.

In **IUPAC notation**, which is solely based on the shell/subshell designation, first the shell with the vacancy is given, then, separated by a hyphen, a subshell contributing an electron.

The Table 1 compares the two nomenclature systems:

Table 1. Principal X-ray lines (IUPAC and Siegbahn notations) and their approximate relative intensities relative to the major line in each subshell (6)

Series	IUPAC name	Siegbahn name	Relative intensity
K-lines	$K\text{-}L_3$	$K_{\alpha 1}$	100
	$K\text{-}L_2$	$K_{\alpha 2}$	~50
	$K\text{-}M_3$	$K_{\beta 1}$	~17
	$K\text{-}M_2$	$K_{\beta 3}$	~8

L_3-lines	L_3-M_5 L_3-M_4 L_3-$N_{5,4}$ L_3-M_1 M_3-N_1	$L_{\alpha 1}$ $L_{\alpha 2}$ $L_{\beta 2,15}$ L_l $L_{\beta 6}$	100 ~10 ~25 ~5 ~1
L_2-lines	L_2-M_4 L_2-N_4 L_2-M_1 L_2-O_1	$L_{\beta 1}$ $L_{\gamma 1}$ L_η $L_{\gamma 6}$	100 ~20 ~3 ~3
L_1-lines	L_1-M_3 L_1-M_2 L_1-N_3 L_1-N_2	$L_{\beta 3}$ $L_{\beta 4}$ $L_{\gamma 3}$ $L_{\gamma 2}$	100 ~70 ~30 ~30
M-lines	M_5-N_7 M_5-N_6 M_5-N_6	$M_{\alpha 1}$ $M_{\alpha 2}$ M_β	— — —

Since the energy states of atomic electrons are quantized and *characteristic* of a specific chemical element, all the emitted X-ray photons will display discrete sharp lines (or peaks) *characteristic* of that element (3). The unique fingerprint of an element in form of an X-ray spectrum is, therefore, referred to as a *characteristic spectrum*. Consequently, determination of an elemental composition can be performed by analysing a spectrum via intensity maxima of the characteristic peaks – and thus, identifying the specific elemental constituents of a sample.

2.1.3 Fluorescence

As indicated in the previous section, the emission of the characteristic X-rays is the central process in the X-ray fluorescence analysis, and it will be, therefore, the focus of this work. The qualitative part of the analysis is rather straightforward, although relies on the scrupulous spectrum evaluation (see chapter 2.6). Since the intensity of the characteristic lines is related to the concentration of an element in a specimen, the quantitative X-ray fluorescence analysis is also possible. However, the relationship between the intensity and concentration of an element is generally not linear, and Figure 8 and equation (reproduced from (7)) below provide more insight into this issue. Each part of the beam/X-ray path on the figure is color-coded in accordance with the certain part of the equation:

- the red part between source and sample represents the intensity of the X-ray source with its solid angle;
- the intensity loss within the sample on the path to the analysed volume is taken into account by the blue part according to Lambert-Beer law;
- the green part between x and x + dx describes the volume/element being excited and which, consequently, emits fluorescence radiation;
- the intensity loss on the path from the excited volume to the surface of the sample is shown in magenta;
- the last two factors in the equation – in cyan – represent the absorption between sample and air and the detector efficiency for the characteristic energy photons.

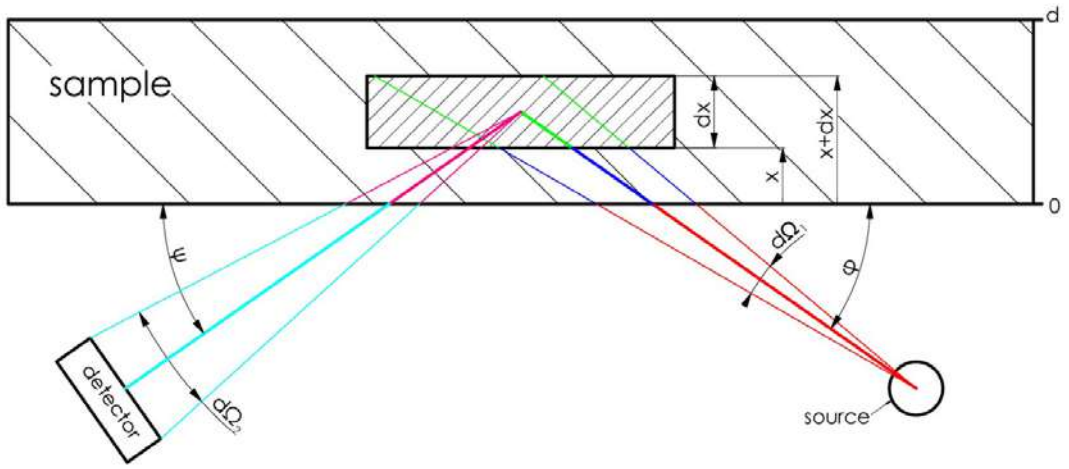

Figure 8. Graphical representation of the geometry involved in the calculation using fundamental parameters (7)

As the result, the following expression for the energy-dependent intensity of a specific line $I(E_{i,j,k})$ as a function of the matrix composition can be obtained:

$$I(E_{i,j,k}) = \int_{E_{abs}}^{E_{max}} dE \int_{0}^{d} dx \int_{\Omega_1} \frac{1}{4\pi r_1^2} \cdot d\Omega_1 \int_{\Omega_2} \frac{1}{4\pi r_2^2} \cdot d\Omega_2 \cdot I_0(E) \cdot exp\left(-\left[\left(\frac{\mu}{\rho}\right)_E \cdot \frac{x}{\sin(\phi)} \cdot \rho_s\right]\right) \cdot$$

$$c_i \cdot \frac{\rho_s}{\sin(\phi)} \cdot \left(\frac{\tau_k}{\rho}\right)_{i,E} \cdot \omega_{i,j} \cdot p_{i,j,k} \cdot V_i(E) \cdot exp\left(-\left[\left(\frac{\mu}{\rho}\right)_{E_{i,j,k}} \cdot \frac{x}{\sin(\psi)} \cdot \rho_s\right]\right) \cdot f(E_{i,j,k}) \cdot \epsilon(E_{i,j,k})$$

with:

i . . . . . element i
j . . . . . final shell
k . . . . . initial shell
r_1 . . . . . distance between sample and source
r_2 . . . . . distance between sample and detector
$I(E_{i,j,k})$ . . . . . intensity of a specific line
E_{max} . . . . . maximum excitation energy
E_{abs} . . . . . energy of the absorption edge of element i and shell k
d . . . . . thickness of the sample perpendicular to sample surface
Ω_1 . . . . . solid angle of the source
Ω_2 . . . . . solid angle of the detector
$I_0(E)$ . . . . . intensity of the source in dependence of the energy
$\left(\frac{\mu}{\rho}\right)_E$ . . . . . mass attenuation coefficient in dependence of the energy
ϕ . . . . . angle of the incident radiation
ρ_s . . . . . density of the sample
c_i . . . . . concentration of the element i
$\left(\frac{\tau_k}{\rho}\right)_{i,E}$ . . . . . photoelectric mass absorption coefficient of element i and shell k
$\omega_{i,j}$ . . . . . fluorescence yield of the shell j
$p_{i,j,k}$ . . . . . emission probability for the initial shell k
$V_i(E)$ . . . . . factor that takes secondary excitation into account
$\left(\frac{\mu}{\rho}\right)_{E_{i,j,k}}$ . . . . . mass attenuation coefficient of the energy Ei,j,k
ψ . . . . . take-off angle of the fluorescence radiation

$f(E_{i,j,k})$ . . . . . absorption of the fluorescence radiation between sample and detector
$\epsilon(E_{i,j,k})$ . . . . . sensitivity of the detector

2.1.4 Scattering

The last interaction type which will be addressed within this chapter is scatter. Within this process, the primary photons do not ionize and excite an atom, but instead are scattered on electrons and deflected from their original track.

Elastic (also Rayleigh, coherent) scattering occurs when an X-ray photon collides with a strongly bound inner electron, which can lead to a change of direction of the photon, but is not accompanied by photon's energy loss.

Inelastic (also Compton, incoherent) scattering is a collision of a photon with a loosely bound electron accompanied by a change of photon's direction and a loss of energy of the photon (Fig. 9). A strict relationship exists between energy loss and angle of deflection (3).

Both processes will be reflected in an X-ray spectrum as two clearly distinguishable peaks – one with the intensity maximum corresponding to the excitation energy (i.e. elastic/Rayleigh scatter), and the other, broader peak with the energy lower – since the energy loss occurred – than the excitation energy (inelastic/Compton scatter, respectively). The energy of a scattered Compton photon E_f can be derived via the expression:

$$E_f = \frac{E_i}{1 + (E_i/m_0c^2)(1 - \cos\theta)}$$

using the scattering angle θ and the initial photon energy E_i.

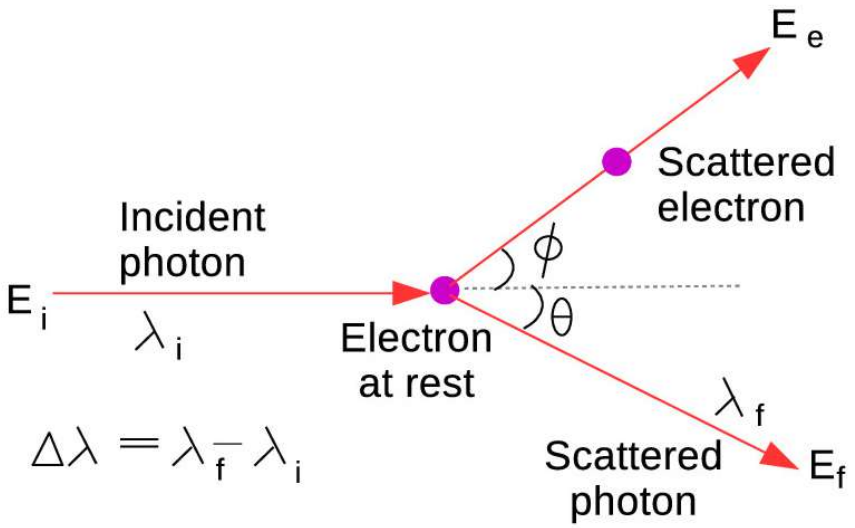

Figure 9. Schematic of Compton scattering process (8)

To conclude this section, it has to be pointed out that the three competing processes – photoelectric effect, Compton scattering, and pair production are interconnected (see Fig. 10). The latter is observed in the energy region above the usual X-ray fluorescence spectroscopy range, therefore, is not considered in this work. Compton scattering processes are overwhelmingly dominant for energies around 1 MeV (which is still much higher than the energies used X-ray fluorescence spectroscopy), but also will be affecting measurements of low-Z targets throughout the range of energies.

Nonetheless, the photoelectric effect predominates for range below 100 keV and is the most important in X-ray spectroscopy.

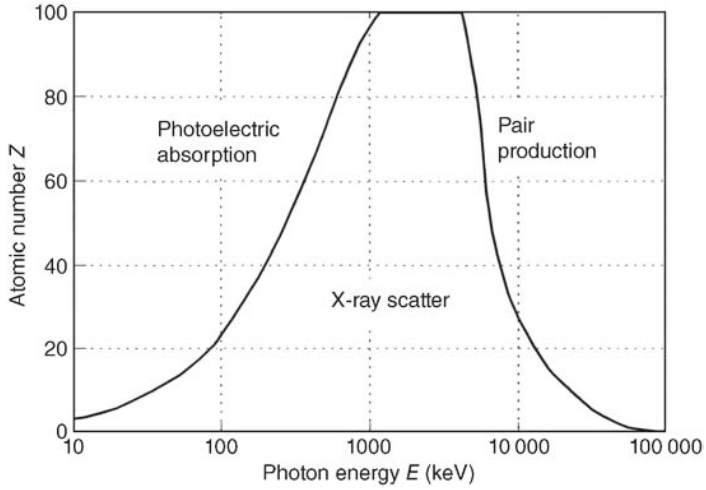

Figure 10. Predominant effects for the attenuation of X-rays as a function of energy and atomic number of the medium (3)

2.2 X-ray sources

Two most common X-ray sources were already mentioned above: X-ray tubes and synchrotron radiation; further, radioactive isotopes and free-electron lasers (FEL) can be noted.

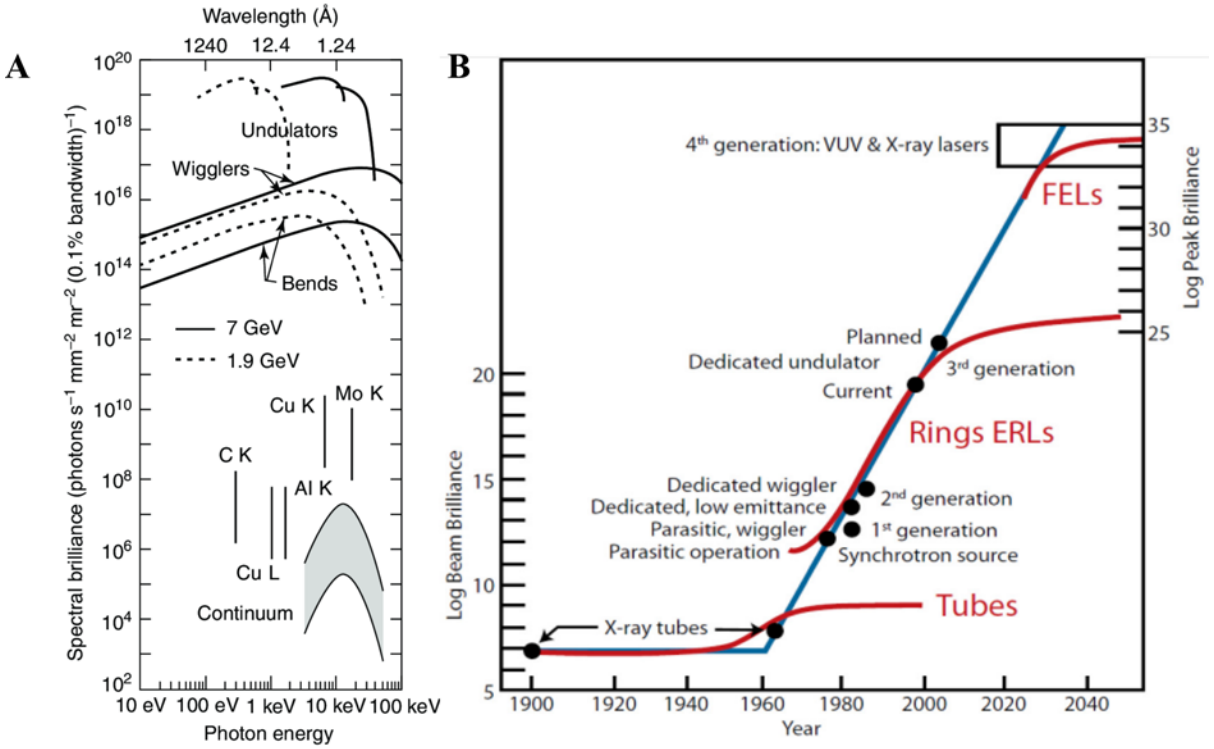

Figure 11. (A) Spectral brilliance for several synchrotron radiation sources and conventional sources (modified from (9)). (B) X-ray brilliance with orders of magnitude increase with time. Tubes represent X-tubes generally used in laboratory, Rings: storage rings of synchrotron facilities, ERLs: energy recovery LINACS, FELs: free electron lasers; VUV-lasers: vacuum ultraviolet lasers (courtesy of M. Rivers) (10)

Figure 11A shows a comparison of several conventional sources (X-ray tubes with different anode materials) and synchrotron radiation sources in terms of brilliance; while Figure 11B represents a historical overview of the sources. The next sections are devoted to X-ray tubes and synchrotron facilities as these sources were used in the scope of this work.

2.2.1. X-ray tube

X-ray tubes are the most common excitation sources. A typical X-ray tube consists of a vacuum-sealed casing (Fig. 12). A tungsten filament serves as a cathode, and a pure-metal target, e.g. Cr, Cu, Mo, Rh, as an anode. The heated filament emits electrons, which are accelerated by an applied high voltage in the direction of the anode. The high-energy bombardment of the target produces heat above all (therefore, the cooling of the anode is essential), while the electrons are absorbed, retarded, or scattered (3). The efficiency of an X-ray tube is low: only about 1% of the electric power is converted into X-rays, while the rest is dissipated as heat (6). The produced X-rays are then delivered through a thin Be exit window.

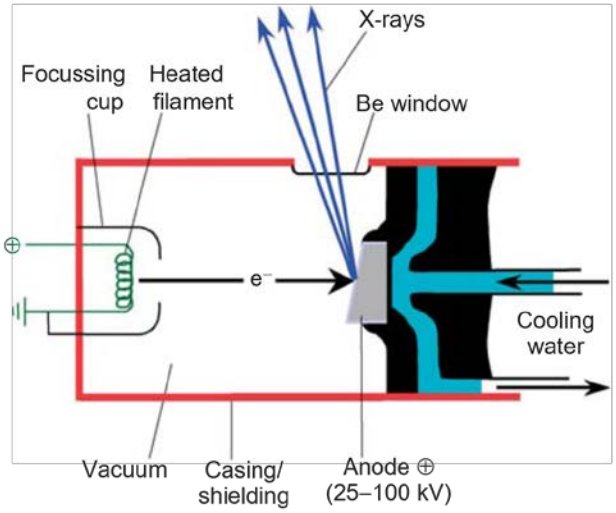

Figure 12. Cross section of a sealed X-ray tube (6)

The emission spectrum (Fig. 13) of an X-ray tube consists of two principal components: a *bremsstrahlung continuum* (which is the product of deceleration of high-energy electrons in a strong Coulomb field of nuclei) upon which the *characteristic lines* of the anode target material are superimposed (6).

Excitation efficiency of an X-ray tube can be tuned by changing the operating parameters – voltage (see Fig. 13) and current (has a linear influence on the tube intensity), but only within a limited range.

Modern modifications of X-ray tubes go in the direction of miniaturization and increasing ease of use (e.g. air-cooled systems), as well as alternative solutions for the anode: mixed-anode materials, rotating anodes, liquid-metal-jet.

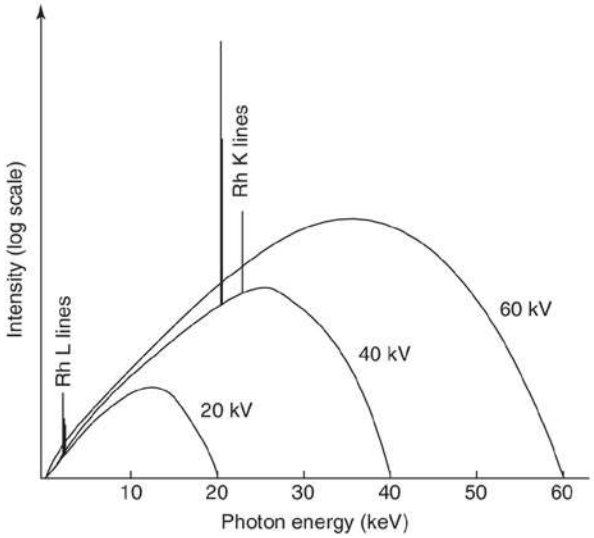

Figure 13. Polychromatic spectra emitted by a Rh anode X-ray tube operated at 20, 40 and 60 kV (6)

2.2.2 Synchrotron radiation

Synchrotron source is an appealing alternative to the X-ray-tube-based systems. Synchrotron radiation (SR) is produced by high-energy (GeV) relativistic particles (electrons – for XRF experiments), confined to and circulating within a storage ring (Fig. 14).

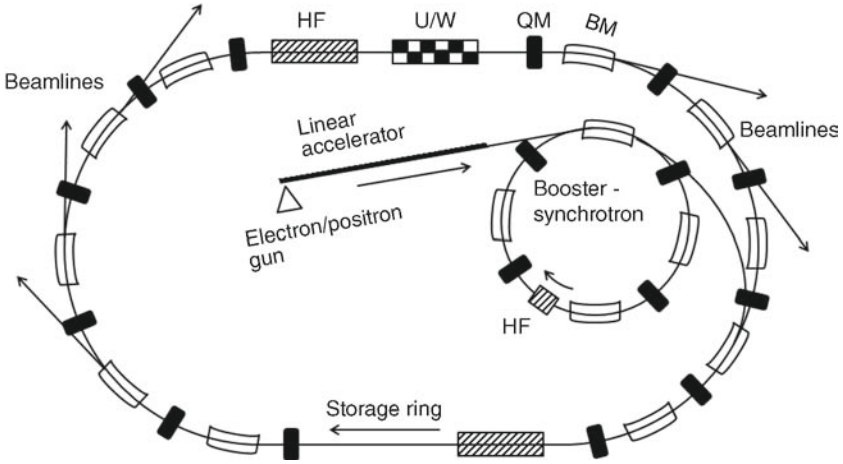

Figure 14. Schematic representation of a synchrotron radiation facility (BM – bending magnet, HF – high frequency cavity, QM – quadrupole magnet, U/W – undulator or wiggler) (3)

Under the continuous acceleration and being deflected within strong magnetic field, the electrons emit radiation in a small cone tangentially to the path of the particles. Compared to the conventional X-ray tubes, SR sources are several (six to twelve) orders of magnitude brighter, the emitted radiation has a natural collimation in the vertical plane, and is linearly polarized in the plane of the orbit. The spectral distribution is continuous or shows sharp maxima at a limited number of energies – so-called harmonics. By monochromatization of the continuum or by selection of one of the harmonics, it is possible to fine-tune the excitation conditions and selectively excite the element(s) of interest (6).

As pointed above, the radiation originates from a minute source point and is released in a very narrow angular range, thus, it can easily be focused into micro- and/or nanobeam. Further advantage of the SR is a low spectral background – due to the high degree of polarization, and, therefore, reduced

scattering. High intensity of the synchrotron beam in combination with low spectral background, in their turn, allow achieving excellent detection limits – down to the parts per billion level.

Few parameters and definitions ought to be introduced when discussing SR, and which are especially helpful in characterizing and comparing various synchrotron sources (see also section 2.2, Fig. 11):

- *Intensity I(E)* is the accumulated count of X-ray photons per unit time (second):
$$I(E) = \frac{photons}{s}$$
- *Spectral flux Φ(E)* is defined as a number of photons per second per unit of bandwidth (relative bandwidth – 0.1% ΔE/E):
$$\Phi(E) = \frac{I(E)}{0.1\%\ energy\ bandwidth} = \frac{photons}{s \cdot 0.1\% \frac{\Delta E}{E}}$$
- *Brightness Φ(E, ψ, θ)* additionally considers beam divergence (in both angular directions: ψ – angle of emission perpendicular to the plane and θ – angle of emission in the plane of the electron orbit):
$$\Phi(E, \psi, \theta) = \frac{\Phi(E)}{beam\ divergence} = \frac{photons}{s \cdot 0.1\% \frac{\Delta E}{E} \cdot mrad^2}$$
- *Brilliance Φ(E, ψ, θ, x, z)* is the most commonly used parameter (and, confusingly, is referred to as brightness in English-speaking countries) – also factors in the source size in horizontal *x* and vertical *z* planes:
$$\Phi(E, \psi, \theta, x, z) = \frac{\Phi(E, \psi, \theta)}{source\ size} = \frac{photons}{s \cdot 0.1\% \frac{\Delta E}{E} \cdot mrad^2 \cdot mm^2}$$

It is clear that the brilliance of a synchrotron will depend on the technical equipment and the hardware used at the facility. The most crucial components (at least in the 3rd- and 4th-generation synchrotrons) are:

- Bending magnets
- Wigglers
- Undulators

Bending magnets, as is enclosed in the term, deflect the beam and define the geometry of the accelerator. They produce the simplest form of synchrotron radiation.

On the straight sections of the path the additional alternating magnetic structures are positioned (Fig. 14). These are conventionally referred to as insertion devices, and their role is to increase the total emitted photon flux. The following insertion devices are common: wavelength shifter, multipole wiggler, and undulator. Here we will only discuss wiggler and undulator, since they are the most frequently used insertion devices at the synchrotrons visited by our team.

A *wiggler* consists of a series of equal dipole magnets with alternating magnetic field direction; the end poles must be configured to make the total device neutral to the geometry of the electron beam path (Fig. 15, left).

An *undulator* is constructed similarly to wiggler magnets, as can be seen from Figure 15 (right), but is operated at a much reduced magnetic field strength. The difference between wigglers and undulators lies in the amount of angular deflection produced by the magnetic poles.

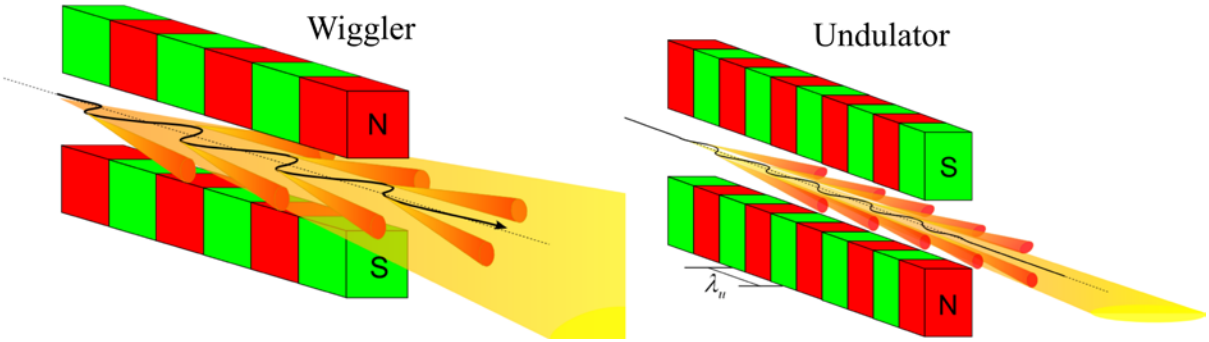

Figure 15. Schematic comparison of a wiggler and an undulator (adapted from (11))

The spectral distribution of all three devices – bending magnet, wiggler and undulator – is compared in Fig. 16. Unlike the smooth, continuous spectrum produced by bending magnets and wigglers, interference effects in undulator radiation result in peaks at one or a few wavelengths/energies. At these tunable wavelengths/energies undulator radiation has high spatial and spectral brilliance (12).

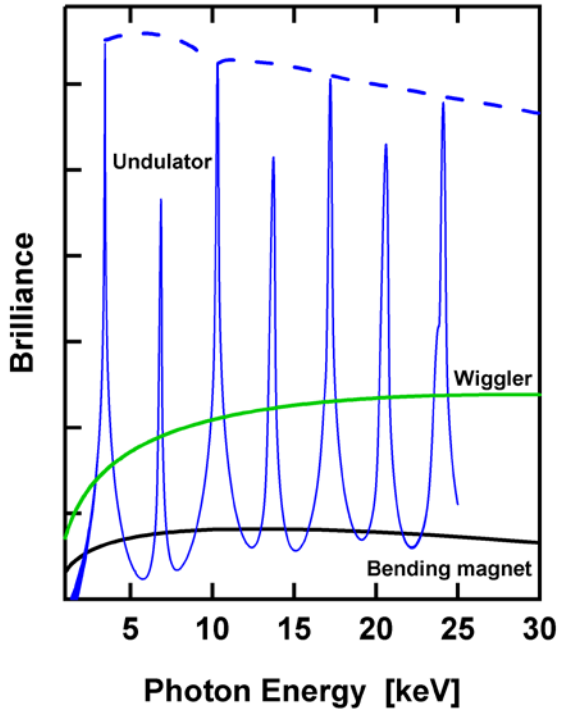

Figure 16. Spectral distribution produced by a bending magnet, a wiggler and an undulator (11)

2.3 Energy dispersive X-ray detectors

The next crucial part of an XRF measuring system is a detector. Historical development of the detection systems started with photographic plates and gas-filled ionization chambers. Nowadays, the most common type of the detectors are solid-state semiconductor detectors, namely Ge- and Si- based. Since in our experiments we only dealt with the latter type, a short overview is given below for a lithium-drifted silicon detector (Si(Li) detector) and a silicon drift detector (SDD).

2.3.1 Si(Li) detector

A Si(Li) detector is based on a small cylindrical section of a single crystal of *p*-type silicon (about 1 cm in diameter and ca. 3 mm thick) of *p*-type silicon. Lithium ions are 'drifted' into the silicon crystal to neutralize the crystal defects in a particular zone, the so-called intrinsic zone. Under applied reverse-bias voltage, the device acts as a PIN-diode. An incoming X-ray photon enters through a thin beryllium window and causes a production of a number of electron-hole pairs (see Fig. 17). The electrons drift to the rear contact, and the total charge collected at the rear contact will be directly proportional to the energy of the detected photon.

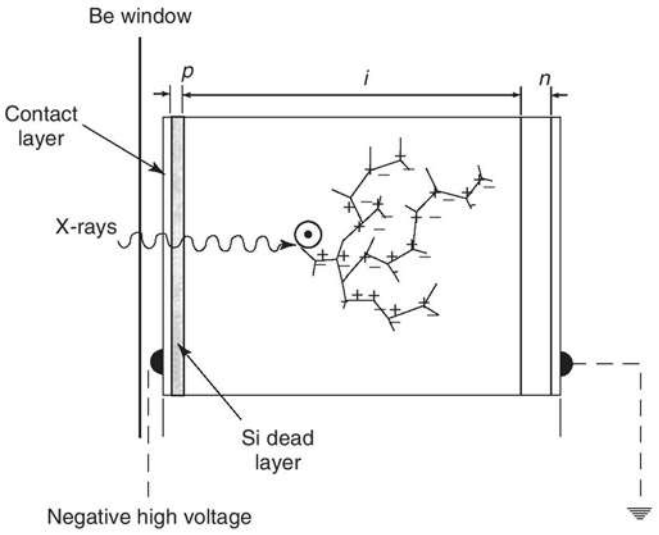

Figure 17. Working principle of a Si(Li) detector (6)

The Si(Li) detectors have relatively good energy resolution, around 150 eV at 5.9 keV (more specifically, full width at half maximum (FWHM) of the Mn-Kα-peak, which is positioned at 5.9 keV; this energy is habitually used when describing energy resolution). However, one of the main limitations of Si(Li) detectors is the need for liquid nitrogen (LN_2) cooling. The LN_2-dewars are rather large, require certain competence to be handled, and, naturally, have to be (re-)filled in the due time. Si(Li) detectors are used at synchrotron facilities, but also at stationary laboratory setups.

2.3.2 SDD

A less demanding in use alternative to Si(Li) detector is silicon drift detector (SDD). SDDs are essentially Si discs with a thickness of only about 500 µm, whereas the active area size can range from 5 mm^2 up to 150 mm^2. As can be seen from Figure 18 X-rays enter through a thin p+-doped cathode at the front area. On the opposite side the concentric drift electrodes are located. Under applied bias the produced electrons will be directed towards and collected at the small central anode. The energy resolution of SDDs can be as low as 125 eV at 5.9 keV. Besides their compact size, the main advantage of SDDs in comparison to Si(Li) detectors is the thermoelectric cooling (by means of a Peltier element) instead of LN_2-cooling. This allows not only the extensive usage within laboratory and synchrotron setups, but also integrating SDDs into mobile/transportable and hand-held XRF devices. However, the X-ray detection efficiency of the SDDs is limited by the total thickness of the wafer. While the efficiency of SDDs at 10keV is about 90%-100% (13,14), it drops down quickly for higher energies. The Figure 19 provides a comparison between three semiconductor detector types (please mind that the Ge-detectors were not used in this work) – and demonstrates that Si(Li) detectors can be used for higher energy X-rays compared to SDDs.

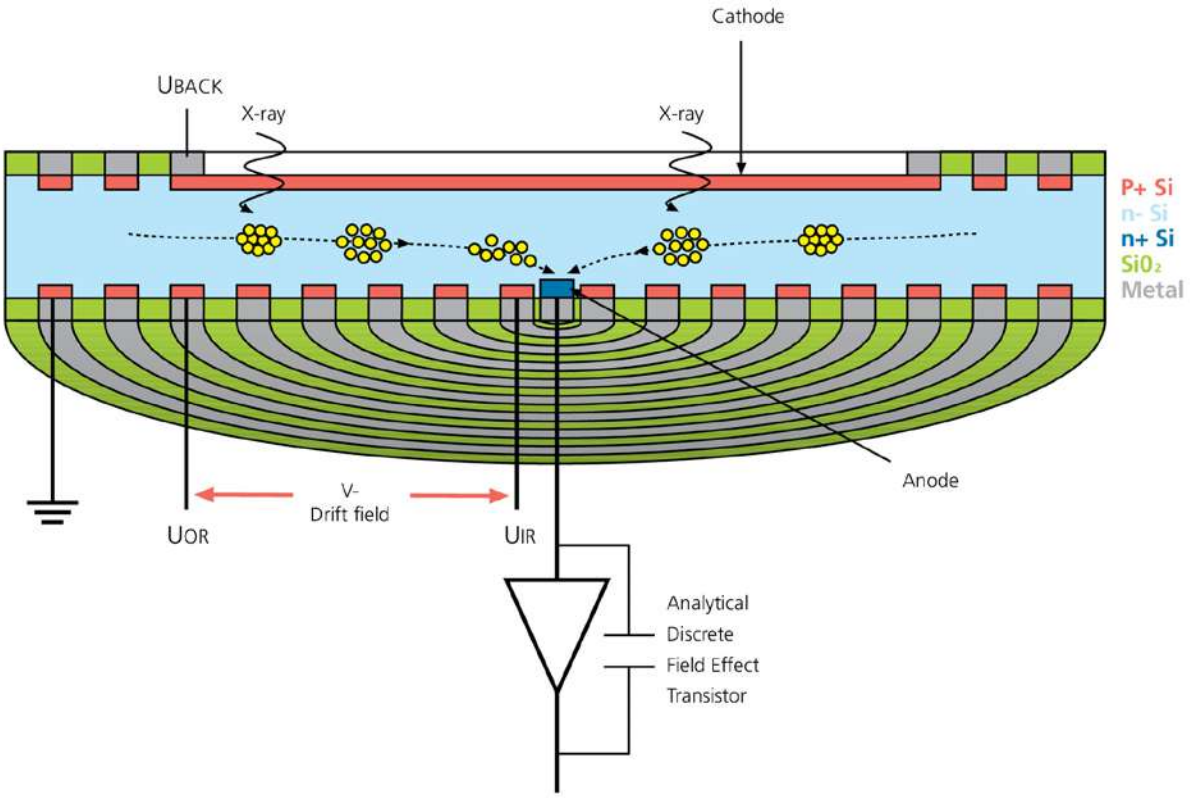

Figure 18. Schematic cross section and working principle of a silicon drift detector (15)

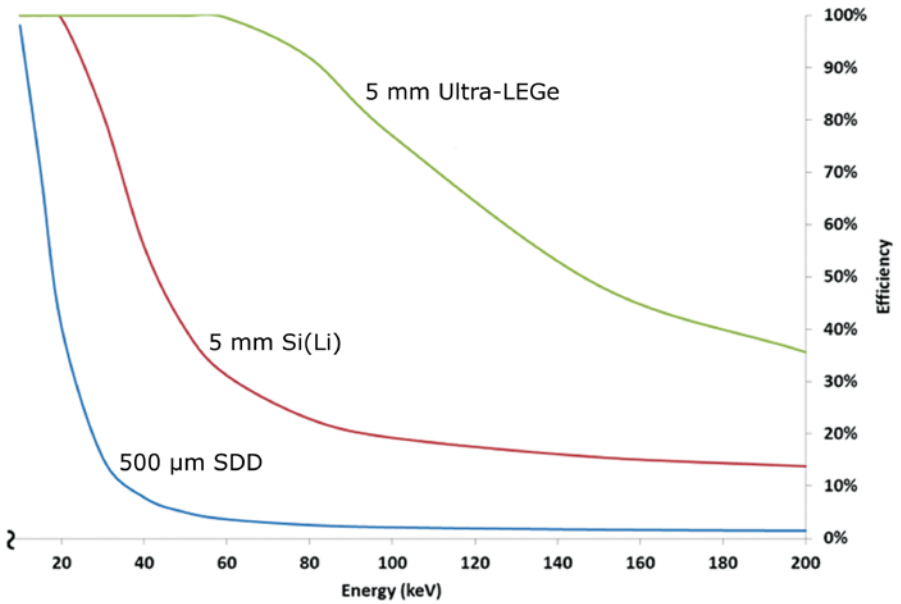

Figure 19. Comparison of detector efficiency for Si-based and Ge-based products by Mirion Technologies (Canberra), Inc. (14)

2.4 X-ray optics

The X-ray optics is a broad term under which the instruments used to focus, monochromatize or reflect X-rays are gathered. The three types of optical elements described below are polycapillary lenses, Kirkpatrick-Baez mirrors, and multilayer monochromators – those are the instruments which were mostly used within the scope of this thesis.

2.4.1 Polycapillary lenses

Polycapillary lenses consist of up to 100 000 small hallow glass tubes (with the individual capillary diameter down to 1.5 µm) which are bundled in a glass sleeve in a honeycomb arrangement. An X-ray beam will be repeatedly totally reflected off the smooth inner walls of the bent capillaries. Depending on the overall arrangement of the lens, the beam can be collimated or focused. The Figure 20 shows the existing types of lenses – a full polycapillary (Fig. 20, top) and half lenses (Fig. 20, middle and bottom).

A full lens captures the radiation from the source, directs and concentrates the beam onto a small focal spot. In dependence of the direction, half lenses are used to either focus a beam to a single spot or to define and limit the area seen by a detector. The spot size, intensity distribution and transmission function are the important parameters when describing a polycapillary lens. Using a polycapillary lens a focus of 10-100 µm diameter can be achieved. This type of optics can be used in the laboratory, as well as synchrotron setups.

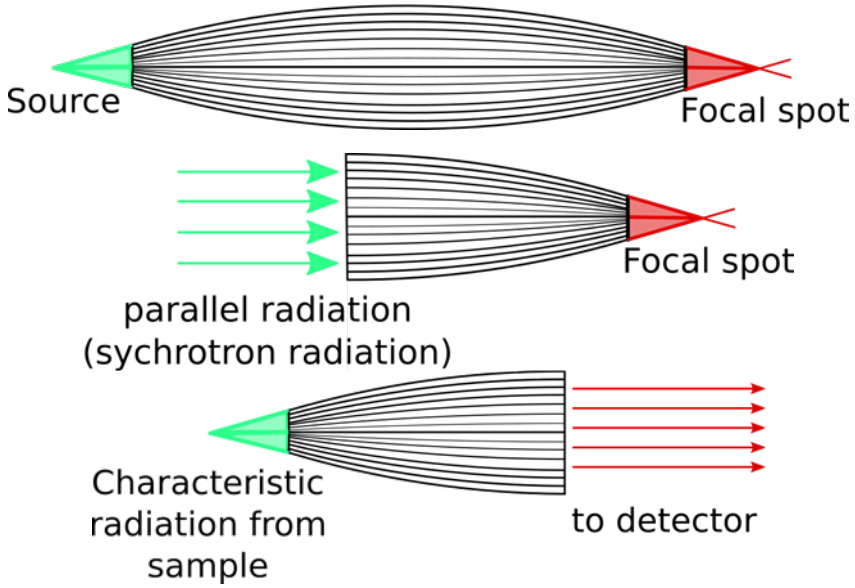

Figure 20. Polycapillary lenses (16)

2.4.2 Kirkpatrick-Baez mirrors

Kirkpatrick-Baez (KB) mirror system is another type of focusing optics. KB system consists of a pair of elliptically bent mirrors – one is focusing the X-rays horizontally and the other one vertically (Fig. 21). The alignment of the two mirrors is quite delicate and is realized by sophisticated and highly precise mechanics; the process has to be assisted by computer. The KB systems are quite expensive, but due to their excellent focusing capabilities (impressive focusing of sub-10 nm has been achieved using figured/multilayer KB mirrors (17)) are installed in many synchrotron beamlines.

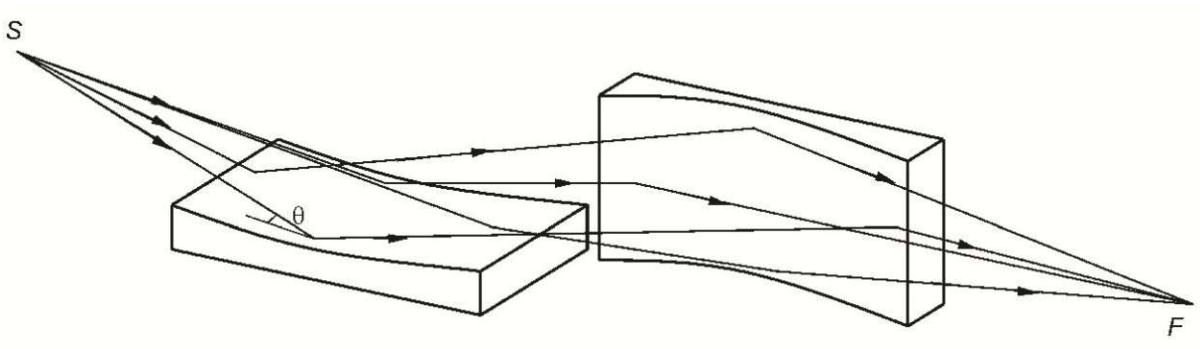

Figure 21. Schematic sketch of a Kirkpatrick-Baez mirror system (18)

2.4.3 Multilayer monochromator

As the name implies, multilayer monochromators serve a different (from the focusing optics described above) function. They allow selecting a certain range of an X-ray spectrum, i.e. monochromatization. The system consists of alternating layers of heavy (reflector) and light (spacer) elements of the constant thickness d (the period of a multilayer).

The beams of X-rays are hitting the monochromator under an incident angle of θ, will be reflected within the multilayer structure and will interfere with each other (Fig. 22). X-rays of certain wavelengths λ, which are satisfying Bragg's law will be reinforced in intensity by constructive interference; the rest will be annihilated by destructive interference.

$$n\lambda = 2d \sin\theta, \;\; where\ n\ is\ an\ integer\ (n = 1, 2, 3, \dots)$$

The energy range of multilayer monochromators used at the synchrotrons can vary from ~50 eV to 100 keV. Different material systems are available, depending on the desired application and customers' request. The energy resolution ΔE/E (energy bandwidth, where ΔE denotes the energy width of transmitted radiation band and E the energy of the photons to be transmitted) achieved is typically a few percent.

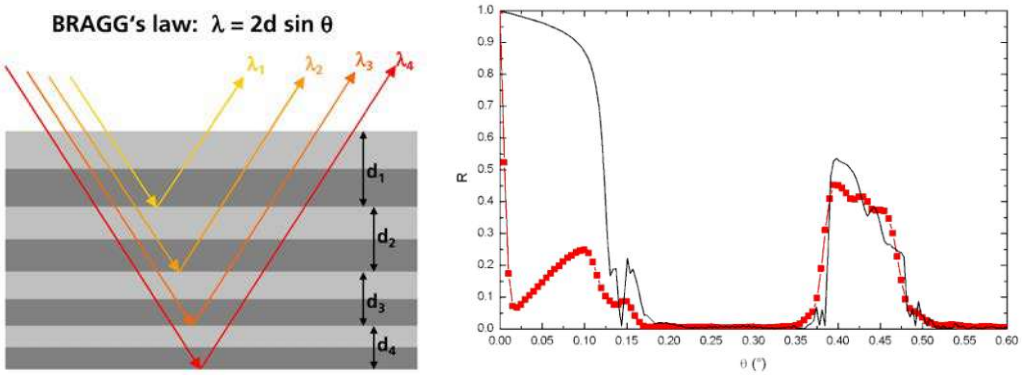

Figure 22. Working principle of a depth-graded multilayer (left). Reflectivity vs. grazing angle for a 22% bandwidth multilayer mirror at 22.2 keV (red: measurement, black: simulation) (right) (19)

2.5 Wrap-up on laboratory system and visited synchrotrons

This chapter will give a short overview of the setups, both laboratory and synchrotron, which were employed within the scope of this thesis.

2.5.1 Laboratory μXRF system at Atominstitut

The μXRF setup at Atominstitut, TU Wien was designed in-house. It is suited for the detection of a wide range of elements. The detailed description of the system can be found in previous publications of the group (20,21). The setup is equipped with Rh-anode low power tube (20 W). The chamber can be evacuated, facilitating measurement of low-Z elements. At the time of our experiments, a 30 mm^2 Si(Li) detector with an ultrathin polymer window (UTW) was used. The UTW allows more efficient measurement of the low energy fluorescence radiation.

The following tube settings were usually employed: voltage 50.0 kV and the current 0.4 mA. A polycapillary optic (full lens) was used to focus the primary beam on the sample surface; the beam size determined for Cu-Kα was 50 μm × 50 μm. The setup was predominantly used in non-confocal arrangement (Fig. 23), however for several experiments, a second optic, polycapillary half-lens, had been installed.

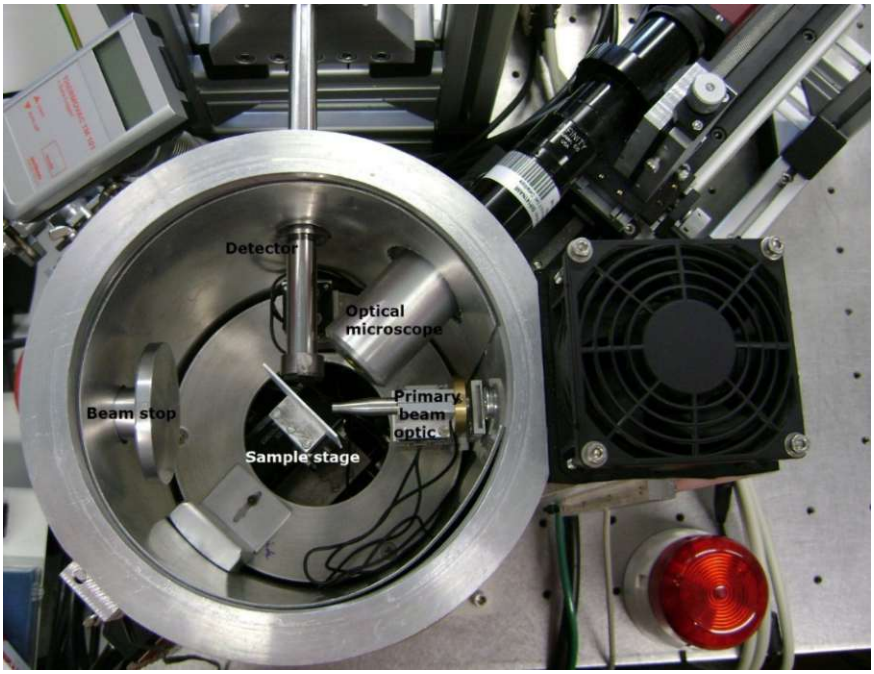

Figure 23. Laboratory μXRF setup at Atominstitut

2.5.2 ANKA

ANKA (Angströmquelle Karlsruhe) synchrotron facility of Karlsruher Institut für Technologie (KIT) is located in Karlsruhe, Germany. The 2.5 GeV second generation storage ring has a circumference of 110.4 m. The storage ring is injected with electrons twice a day; the starting ring current is usually about 150 mA and decreases over time.

Our experiments (see chapter 5) were performed at the confocal setup of the FLUO beamline (the general layout can be seen in Fig. 24). The setup is equipped with a W/Si double multilayer monochromator, a 50 mm^2 silicon drift detector (Vortex) and, in the confocal arrangement, two polycapillary half lenses (Fig. 25).

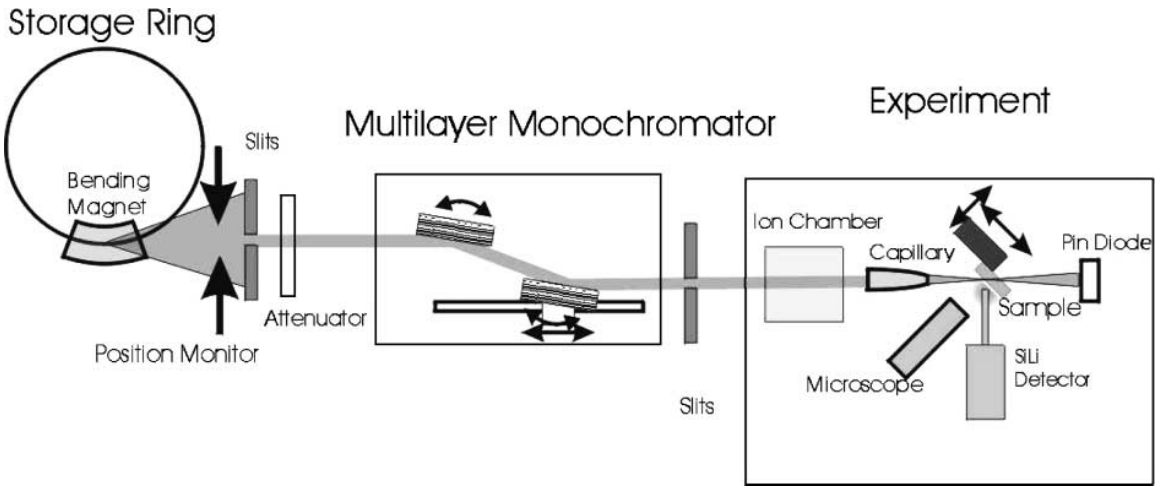

Figure 24. Schematic layout of the fluorescence beam line, not drawn to scale (22)

In order to achieve the optimal excitation of Mn, the excitation energy was set for 9.2 keV. The actual detection volume had to be determined for each experimental session, this was done using Ti-Kα line (4.5 keV). The step size was selected according to the detection volume, and was 25 µm × 15 (17) µm.

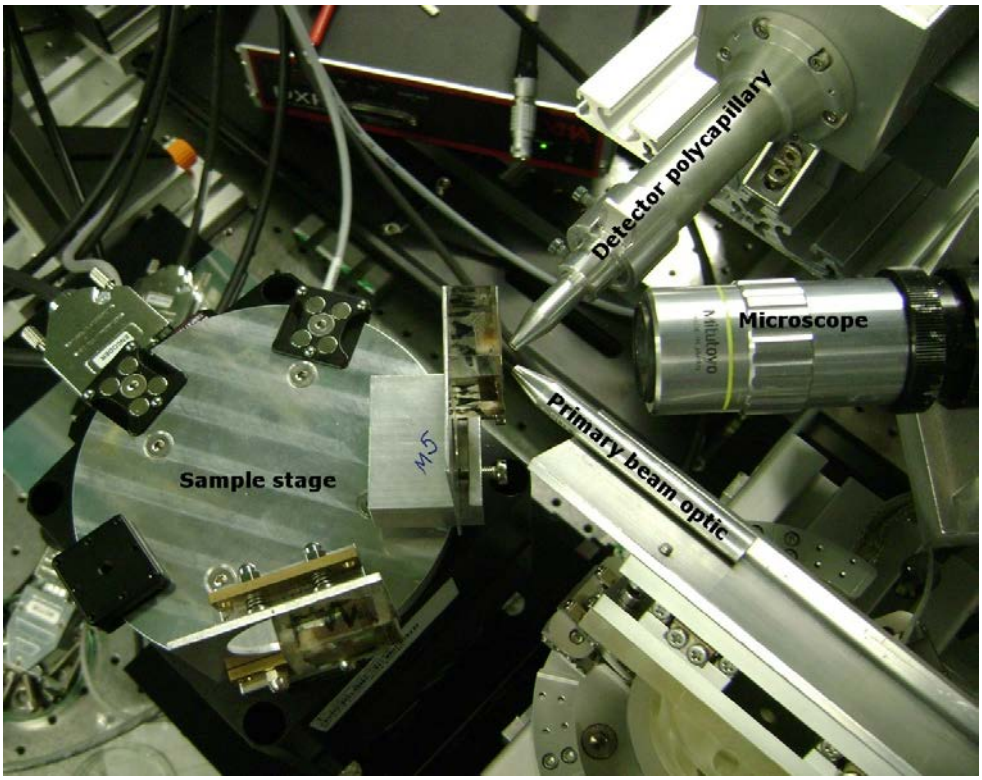

Figure 25. Confocal µXRF setup at FLUO beamline, ANKA

2.5.3 BESSY-II

BESSY-II (Helmholtz-Zentrum Berlin für Materialien und Energie (HZB)) is a third-generation synchrotron radiation source, located in Berlin, Germany. The ring (electron energy: 1.7 GeV) is regularly topped up with new electron bunches, the nominal beam current is 300 mA.

The mySpot beamline (see the layout on Fig. 26) endstation can be converted into a confocal setup (Fig. 27), and was used for the measurements of the additional bone samples from Mn dataset (see chapter 5). The setup is equipped with a MoB_4C multilayer (2 nm period) monochromator and a 7-element Si(Li) detector (Gresham) with an active area of 30 mm^2. The excitation energy was set to 9.2 keV (to match the conditions of ANKA experiment). In the confocal arrangement, two polycapillary half lenses are installed, the angle between them is 90°. However, the second optic (between the sample and detector) is not in the same plane as the first, but offset by an angle of 20° (to see more scattering from the sample for more effective measurement of the low Z elements). The step size was selected according to the defined detection volume, and was 30 (35) µm × 20 (30) µm.

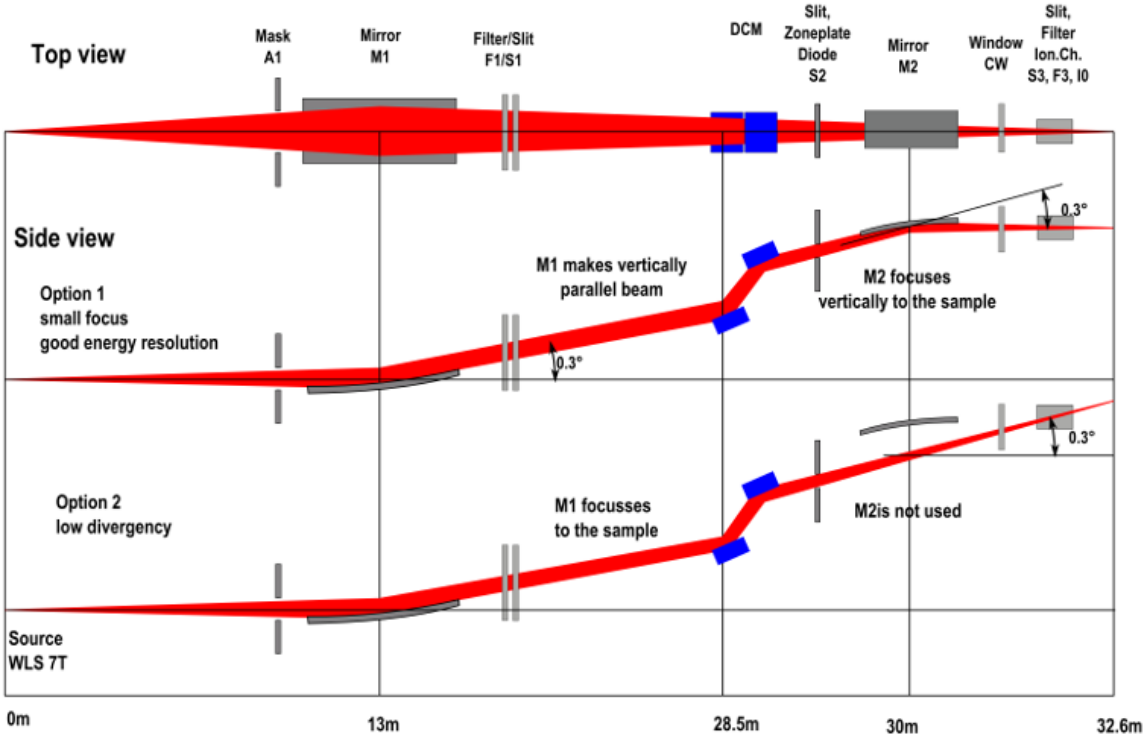

Figure 26. Schematic view of the beamline with two different configurations: option 1 is optimized for narrow energy band width as required for spectroscopy and option 2 is optimized for low divergency as required for scattering experiments (23)

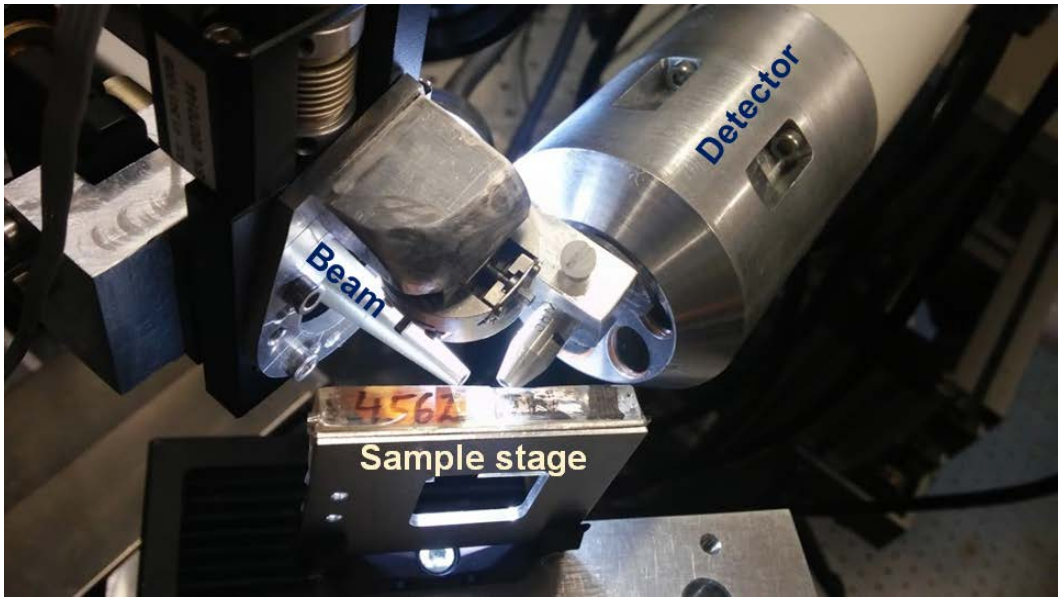

Figure 27. Confocal µXRF setup at µSpot beamline, BESSY-II

2.5.4 ESRF

European Synchrotron Radiation Facility (ESRF) is located in Grenoble, France. It has been the very first synchrotron of the third generation type and the most powerful source (6 GeV) to be built in Europe (also at the time of our experiment in 2017). On August 2020, the ESRF-Extremely Brilliant Source (ESRF-EBS) re-opened as the world's first fourth-generation high-energy synchrotron.

Measurements (see chapter 6) were performed at the ID13 microfocus beamline (24). The beam size of impressive 50 nm was defined using Siemens star standard. The excitation energy was set to 12.7 keV (corresponds to highest flux available at the beamline). The beamline was equipped with multilayer Laue lens optics, Vortex-EM silicon drift detector (Hitachi, USA), positioned on the rear side, "behind" the sample (i.e. the angle between source and detector is more than 90°) (see Fig. 28). The step size was 500 nm.

Figure 28. View of the setup with a mounted sample

2.5.5 Diamond Light Source

Diamond Light Source (DLS) is a third-generation synchrotron radiation source, located in Harwell Science & Innovation Campus, Didcot, Oxfordshire, UK. The ring (electron energy: 3 GeV) is operated in top-up mode, the nominal ring current is maintained at 300 mA.

The experiments were performed at B16 Test beamline (see the layout on Fig. 29). This is a flexible and versatile beamline, and setup can be adjusted for conducting sub-µm XRF imaging. In the used arrangement the setup (Fig. 30) was equipped with a RuB_4C multilayer monochromator, 150 µm pinhole and a single-element 90 Ex Vortex detector (50 mm^2), positioned at 90° to the beam. The excitation energy was set to 12.7 keV (to match the conditions of ESRF experiment). The beam size was determined as about 500 nm × 610 nm (V × H) – taking into account the overlap in 45° geometry – using a 50 µm-diameter Au wire knife edge. The step size was set to 500 nm.

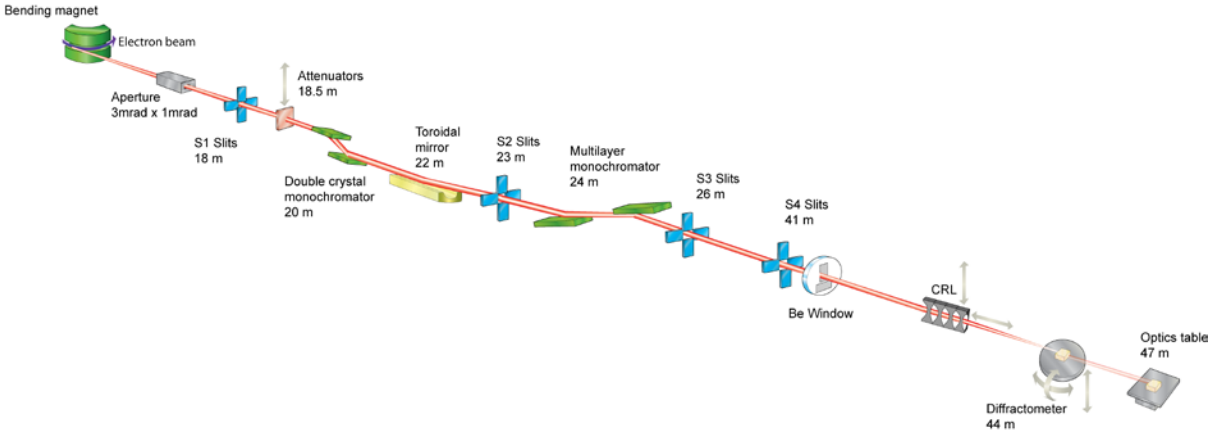

Figure 29. B16 beamline schematic view (25)

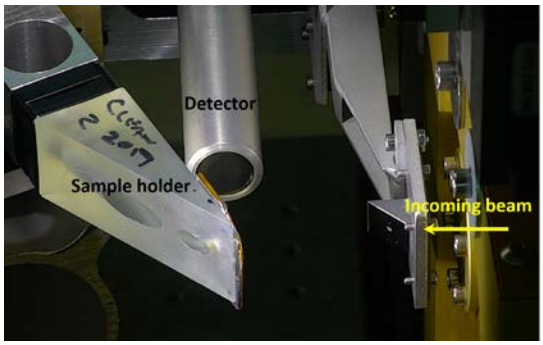

Figure 30. Setup with the sample mounted on the support

The setup with 12.7 keV monochromatic excitation was extensively characterized using standard reference material, NIST SRM 1412 (Multicomponent Glass) (Figures 31-32) and NIST Standard Reference Material 2783 (Air Particulate on Filter Media) (Fig. 33) – which also allowed us the quantitative estimation of Gd content in bone tissue (see chapter 6); the detailed description can be found in (26).

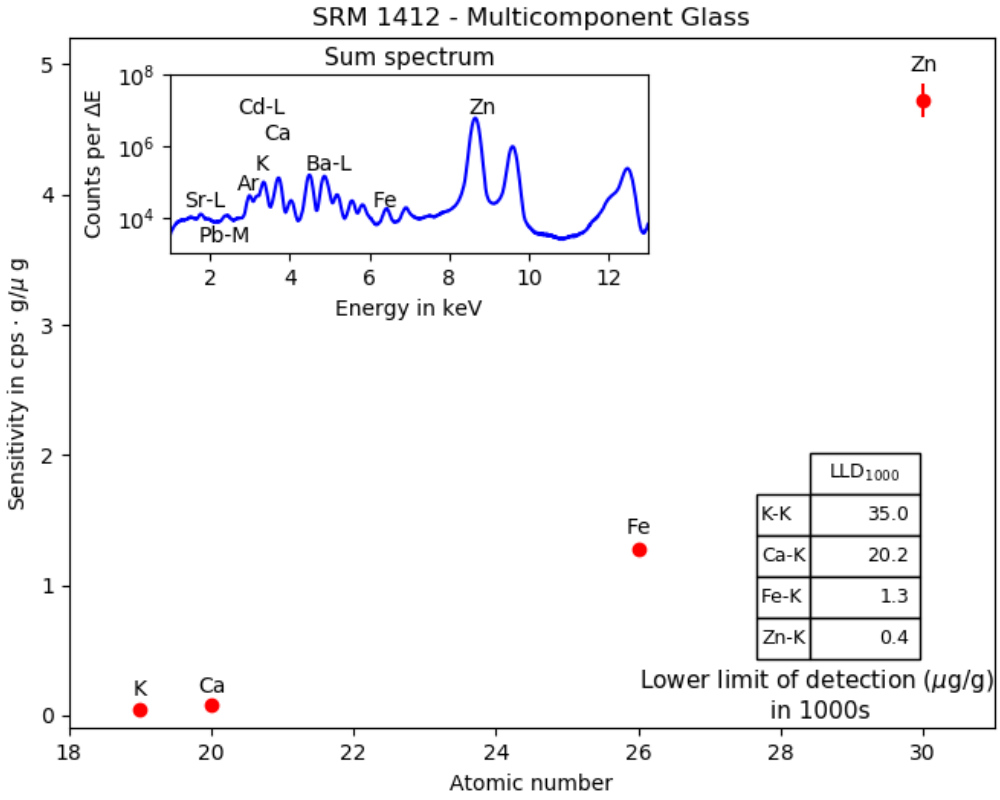

Figure 31. Sensitivities for the K-lines, lower limits of detection (inset table) and sum spectrum (inset) of 36 (6 × 6) pixels - NIST Standard Reference Material 1412 (Multicomponent Glass) with 12.7 keV monochromatic excitation (courtesy of M. Rauwolf)

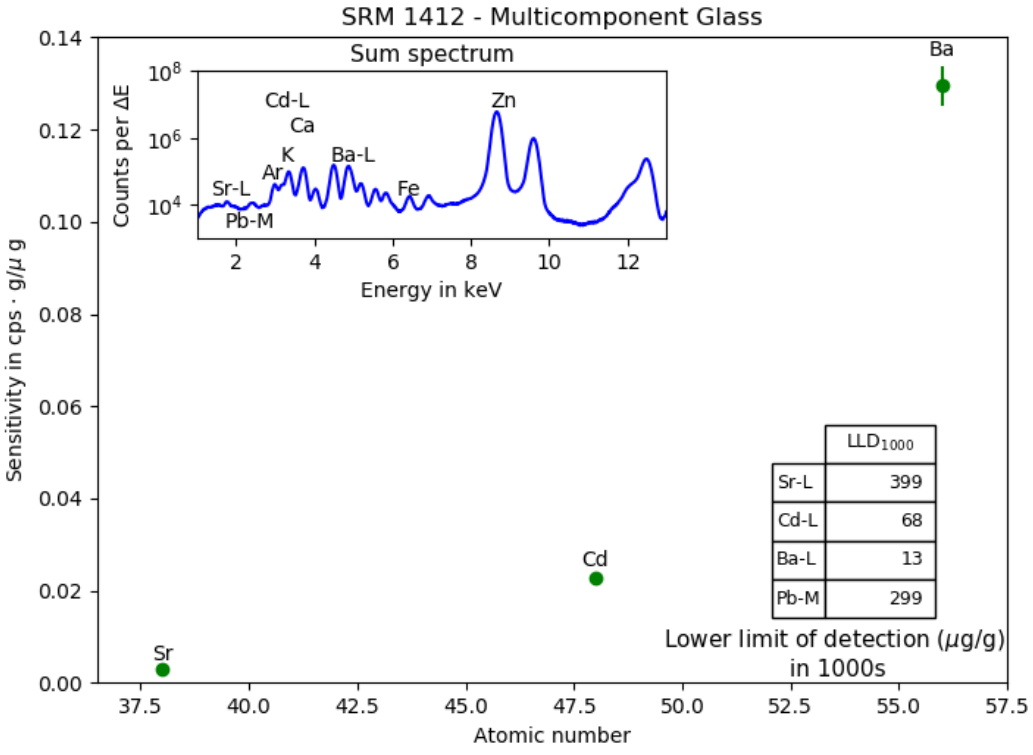

Figure 32. Sensitivities for the L-lines, lower limit of detections (inset table) and sum spectrum (inset) of 36 (6 × 6) pixels measured on the NIST SRM 1412 (Multicomponent Glass) with 12.7 keV monochromatic excitation (courtesy of M. Rauwolf)

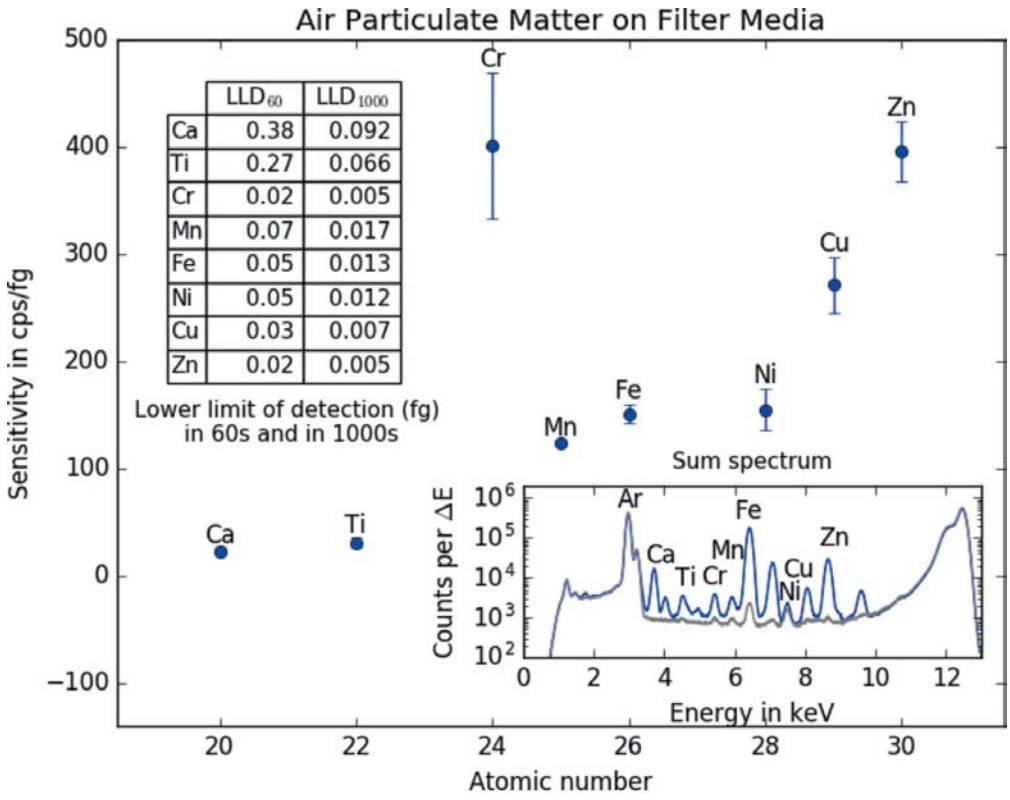

	LLD_{60}	LLD_{1000}
Ca	0.38	0.092
Ti	0.27	0.066
Cr	0.02	0.005
Mn	0.07	0.017
Fe	0.05	0.013
Ni	0.05	0.012
Cu	0.03	0.007
Zn	0.02	0.005

Figure 33. Sensitivities, lower limits of detection (inset table) and sum spectra (inset; in blue for the loaded, grey for the blank filter) of 41 pixels measured on the NIST Standard Reference Material 2783 (Air Particulate on Filter Media) with 12.7 keV monochromatic excitation (26)

2.6 Data analysis and sources of possible errors

The basis of an XRF dataset is a spectrum, a graphical representation of X-ray intensity lines (in 'counts') as a function of energy. The first step in extracting the qualitative information is spectrum evaluation, which primarily includes identification of characteristic X-ray lines, but also discernment of artefacts and assessment of the spectral background.

2.6.1 Spectral artefacts

There are two main types of additional "artificial" lines which can be observed within the spectrum, both of which have their origin due to the detector system:

Sum peaks (also pile-up peaks) arise when the detector does not recognize two signals arriving close together as separate events, but instead sees them as one occurrence. These artefacts are caused by the intense 'parent' lines, and will be positioned within the higher-energy part of the spectrum, corresponding to the sum of the two initial lines.

Escape peaks, by contrast, will be observed at lower energies than the parent peak. Incoming X-ray photons can excite the detector material (in our case Si). As a result, a photon corresponding to 1.74 keV (Si-Kα) will be produced. If this happen near the edge regions of the detector, such photons can 'escape', giving the rise to the signal, which is 1.74 keV smaller than the energy of the original X-ray photon.

2.6.2 Spectrum deconvolution (fitting)

The information a researcher is ultimately seeking for is net counts of an element of interest. Spectrum deconvolution (fitting) is the process of extracting this information, while separating the background, resolving overlapping peaks and considering any spectral artefacts. Here the XRF spectrum fitting software takes the stage, especially when dealing with the dataset consisting of a number of spectra (which is the case in imaging experiments).

The most often used software packages are QXAS-AXIL (IAEA Laboratories Seibersdorf, Seibersdorf, Austria) (27) and PyMCA (28) – both of them were employed for the data analysis within this thesis. Each of those packages has advantages and limitations; the accounts on comparison as well as attempts to combine the functionality of both into a new solution are described in the literature (29,30).

The (batch-)fitting should begin with the creation of a reliable fitting model. It is generally a good practise to start the analysis with the evaluation of the sum spectrum, as it provides an overview of the elements contained in a sample. After adding the elements discovered in the sum spectrum, the background model should be tested and adapted accordingly (this is best done using several different single spectra). If during the initial analysis or the first round of batch-fitting any overlooked elements (or artificial peaks, problems with the background, etc.) are discovered, the model has to be adjusted and the dataset refitted.

2.6.3 Information depth

Another parameter, which can lead to erroneous results, and therefore, needs to be taken into account during the analysis, is the information depth d_{inf}. It is the distance within a sample from which secondary radiation emerges and reaches the detector, more specifically the depth from which 1/e (about 37%) of the fluorescence radiation can escape from the sample. The information depth is always smaller than the penetration depth, and will be influenced by sample/matrix parameters, the energy of the corresponding element of interest and the excitation conditions.

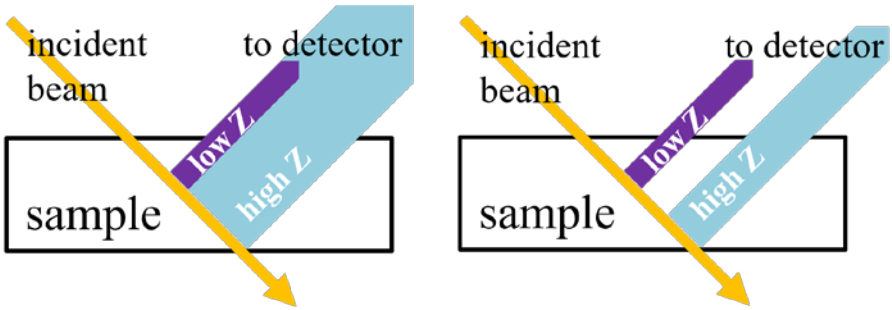

Figure 34. Information depth in a homogeneous (left) and heterogeneous (right) sample for light (low Z) and heavy elements (high Z) (reproduced from (16))

The fluorescence radiation from light elements originates from the surface layer of the sample while radiation from heavier elements can escape from much deeper layers (see Fig. 34). To further illustrate how the information depth differs for low-Z and high-Z elements and the influence of matrix composition: the values we have obtained in cortical bone were 9 µm for P, 39 µm for Ca and 98 µm for Zn, while in the cartilage tissue it was estimated as 16 µm for P, 111 µm for Ca and 872 µm for Zn (31).

Reducing the influence of this parameter on the measurement result can be achieved either by a particular sample preparation methodology, or by using a specialized measurement setup. In the first case, thin slices have to be prepared – couple of µm thick. Alternatively, thick samples can be

measured using a confocal setup, when the area from which the signal is coming is limited by X-ray optic, a polycapillary lens, placed between sample and detector (see examples of such setups at synchrotrons in the sections 2.5.2-2.5.3).

3. Combination of µXRF with other imaging techniques

However powerful a technique, there always will be a limit. A multimodal (i.e. when two or more imaging techniques/modalities are combined) approach can be a solution in expanding the boundaries. For example, pairing of 'rival' elemental analysis techniques could not only serve for cross-validation of the results, but also deliver additional information, as the methods differ in spatial and depth resolution, sensitivity, elemental range, imaging possibility or instrumental effort, etc. (see the comparison of selected methods in Fig. 35).

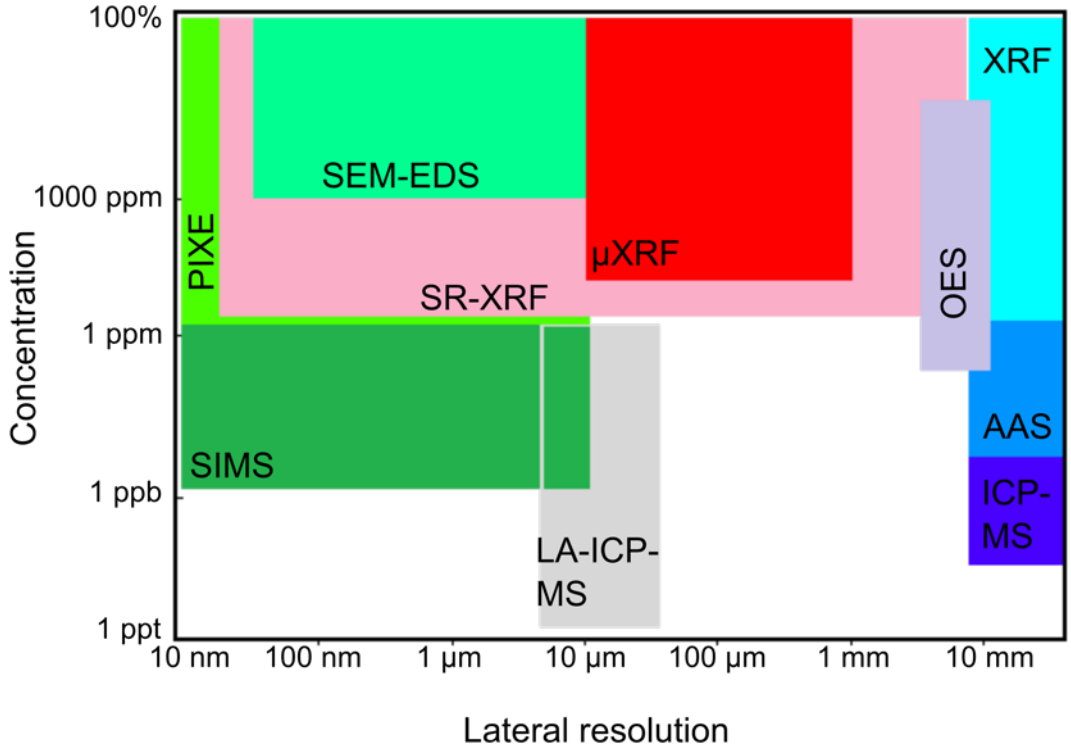

Figure 35. Elemental analytical methods and their spatial resolution and weight fraction range (reproduced from (4))

Evidently, complex research questions could be solved when elemental information is reinforced by molecular, and vice versa: starting from basic information on structure and physiology of cells, tissues, and organisms; to the specific phenomena – e.g. oxidative stress, ligand-associated diseases, (heavy) metals accumulations and so on.

There are a number of researchers working on (among other topics) combined/correlated imaging approaches, for example, groups of Laszlo Vincze (Ghent University, Belgium) and of Uwe Karst (University of Münster, Germany).

Furthermore, the research infrastructure Euro-BioImaging (32) (the Official Imaging Node/Hub in Austria is Austrian Bioimaging/CMI (33)) supports and promotes the correlation and combination of complementary imaging modalities, e.g. through COMULIS COST Action "Correlative Imaging Series".

The PhD program "Molecular and Elemental Imaging in Biosciences" (abbreviated as MEIBio) had been launched at TU Wien with the intention to work on methodological improvements and instrumental innovations for multimodal imaging. This interdepartmental initiative brought together experts in the field of optical, elemental and molecular imaging techniques with the added benefit of expertise in data combination.

Although µXRF has a great advantage of non-destructive analysis, careful consideration has to be given to sample preparation when combining it with other techniques. Therefore, before subjecting a sample to any imaging procedures, it would be recommended to consider – and test out – the size (especially thickness) of a sample, the embedding/cutting/grinding materials and techniques, any coating/labelling media (if required by the complementary method), supporting and mounting materials, etc. The next set of questions which can arise is timing and the sequence of operations. Quantitative information is often desirable in addition to qualitative images; hence it is also advisable to discuss a prospective quantification strategy beforehand.

In a close collaboration with MEIBio colleagues, the following method combinations were realized or tested out and will be further presented in this chapter: laboratory µXRF – MALDI-MSI (section 3.1); laboratory µXRF – LA-ICP-MS (section 3.2); synchrotron-based µXRF – ToF-SIMS (section 3.3).

3.1 µXRF + MALDI-MSI: Chicken phalanx cuts

The project was performed in collaboration with Institute of Chemical Technology and Analytics (CTA) TU Wien within MEIBio doctoral program. MALDI-MSI measurements were performed by Anastasiya Svirkova. Parts of this chapter were previously published in Analyst (34).

The method of matrix-assisted laser desorption/ionisation mass spectrometry (MALDI) allows detection of large, non-volatile and labile biomolecules, such as proteins/peptides, lipids, carbohydrates, nucleic acids, polymers etc. The areas of application include study of drug metabolite pharmacokinetics; identification of disease biomarkers; detection and quantitation of biomolecules; protein, peptide and amino acid analysis (including intact mass, sequencing and post-translational modifications); identification of microorganisms such as bacteria and fungi; analysis of large organic compounds; characterisation of synthetic polymers.

The MALDI workflow includes the following steps: application of a specifically selected MALDI matrix (usually a small laser-light-absorbing organic molecule) onto specimen, irradiation with a laser (upon which – with the aid of matrix – the desorption/ionisation process occurs), and the ions are subsequently analysed in a mass spectrometer. A specific mass-to-charge (m/z) value is thus the sought-after output.

It is possible to perform MALDI imaging in a raster-scanning mode – it is then referred to as MALDI mass spectrometry imaging (MALDI-MSI). A typical MALDI-MSI workflow can be seen in Figure 36.

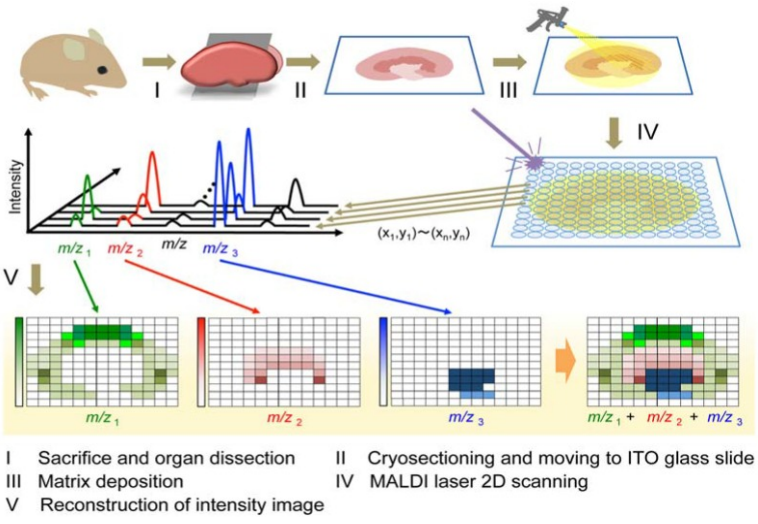

Figure 36. MALDI-MSI experimental workflow (35)

In MALDI-MSI two types of resolution are discerned: mass resolution and spatial resolution. The spatial resolution of MALDI images depends on the laser diameter and the stage step-size, but also such parameters as analyte delocalization and degradation, choice of matrix (crystal size), detector sensitivity are the resolution-affecting factors (36,37). The lateral resolution in the range of 10 µm and higher (close to 1 µm) has been reported in the literature (36–38).

MALDI has following advantages:

- allows detection of broad spectrum of analytes (lipids, proteins, peptides, drugs, and other chemical compounds)
- allows measurements of large amounts of different analytes simultaneously
- it is a label-free technique
- provides semi-quantitative information (via peak intensity)
- since laser shoots only in the matrix layer, the underlying tissue will be almost intact, therefore subsequent analysis/further tissue examination is possible
- it is rather fast (from minutes to a few hours according to image size and resolution)

There is a demand in the fields of medicine and biology for conjoined molecular-elemental information, and the combination of MALDI imaging with µXRF had been previously proposed in the literature (39,40). Combination of MALDI and µXRF imaging, i.e. molecular and elemental information within one sample can open up a new dimension in life sciences research, especially considering that both techniques incur little or no damage to the sample and can theoretically be applied in any order. However, special attention should be given to the sample preparation strategy, as an "ideal" sample must fulfil the requirements of both imaging methods. The combination was realized for the first time in our joined project "Multimodal imaging of undecalcified tissue sections by MALDI-MSI and µXRF" within the scope of the doctoral program MEIBio.

Experimental

Prior to the final imaging experiments, testing of the materials, tissue sections and preliminary imaging was performed using both techniques (e.g. different supporting materials, and specifically for µXRF samples with and without matrix applied). The Figure 37 demonstrates an example of a µXRF pre-testing.

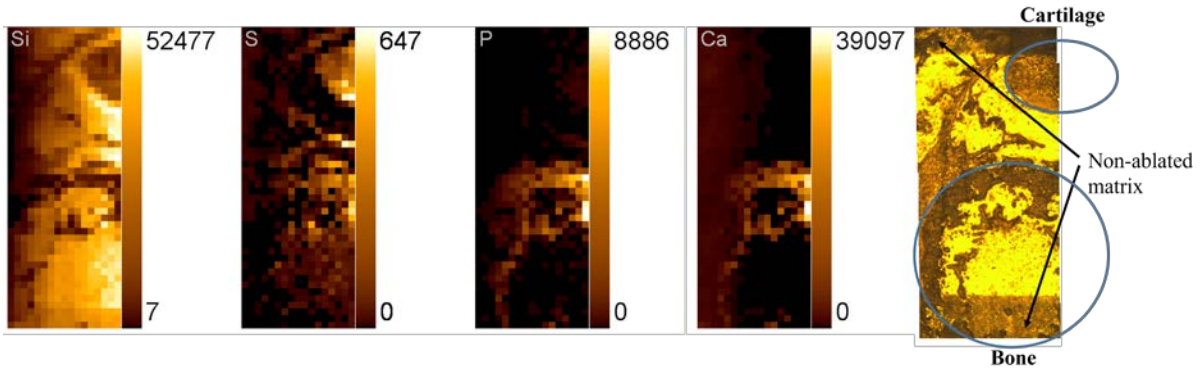

Figure 37. Elemental maps and stacked microscopy image of the scanned area. Matrix was applied and sample was subjected to the MALDI-MSI measurements prior to µXRF. The sample (16 µm cut) was prepared on sticky Kapton and attached to a glass slide – and measured directly, without removing the slide, using confocal setup

The sample preparation was performed by A. Svirkova and described in detail in above-mentioned paper (34). For this proof-of-principle project we chose easily available complex biological material, which included both hard and soft tissues. Frozen chicken digits (purchased from local market) were

embedded in a hydrogel containing sodium carboxymethyl cellulose (NaCMC) 5% and gelatine 20% (w/v); frozen (−57 °C) and subsequently cryosectioned using a non-disposable tungsten carbide knife at −16°C on a CryoStar NX50 (Thermo Scientific). To ascertain sample integrity while sectioning, sample surface was covered with an adhesive tape to stabilize the section and prevent distortion of tissue morphology – the resulting slice was then attached to the tape. Two types of tape were tested – double-sided tape (3M, St Paul, USA) and polyimide one-sided DuPont™ Kapton® tape. Finally, the sections of the phalanx were assembled on a support. MALDI-MSI requires an electrically conductive surface, while in XRF a support "invisible" to X-rays is desirable. We tested the sample assembling either on glass and scotch tape (Fig. 38, #1 and 3), or on glass and Kapton® tape (Fig. 38, #2 and 4). In the latter case, for µXRF measurements glass was further removed, and only the section on Kapton® tape was scanned. In both cases directly before MALDI-MSI measurements dithranol matrix was deposited by sublimation (omitted on Fig. 38, #1 and 2).

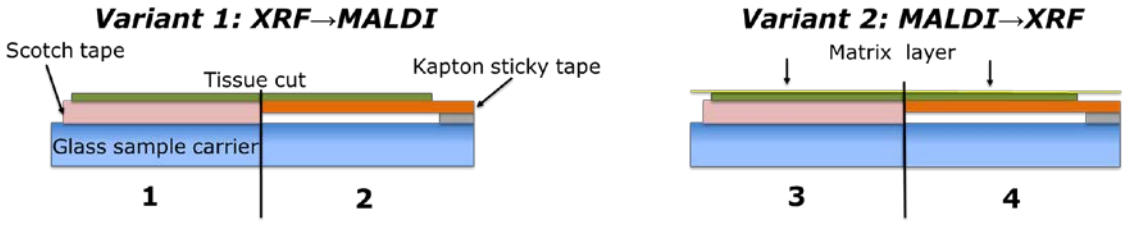

Figure 38. Sample preparation: sequence of measurements and types of sample assembling for final imaging experiments

MALDI-MSI results were obtained using a Synapt G2 HDMS™ system (Waters, Manchester, UK).

For µXRF imaging the laboratory µXRF setup at the Atominstitut was employed. The tube voltage and current were set to 50 kV and 0.4 mA, respectively. The final imaging µXRF experiments were conducted using non-confocal setup under the following measurement conditions (the same for all the scans): step size 150 µm, measurement time 90 s, in vacuum. The complete workflow is demonstrated graphically in Figure 39.

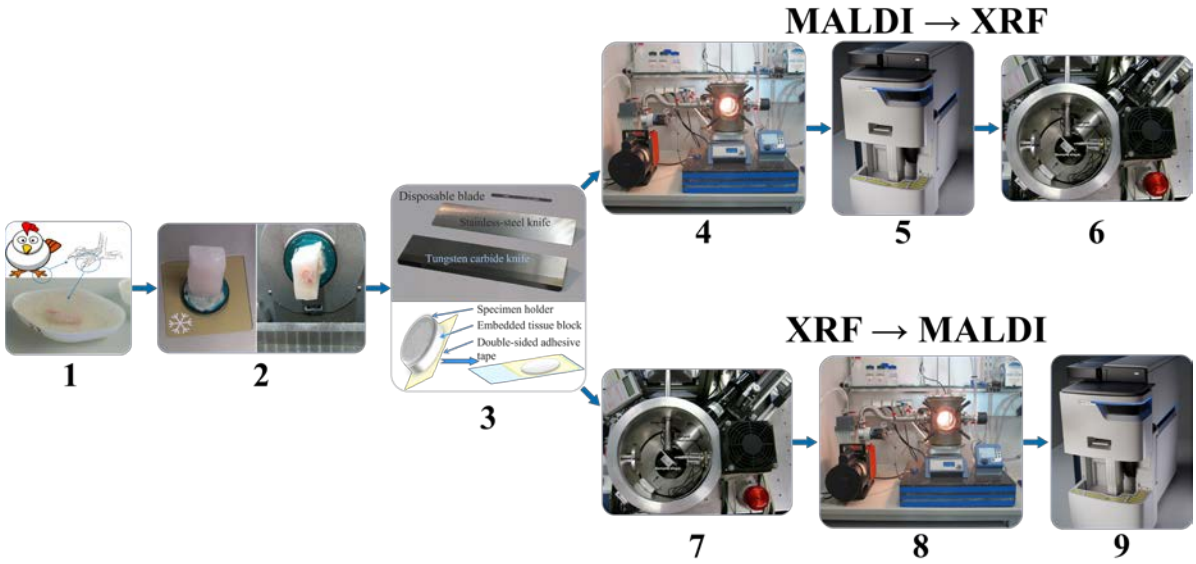

Figure 39. The project workflow: embedding of frozen toes in weighing boats (1); trimming and mounting on the specimen chuck (2); sectioning using a microtome (3); application of dithranol matrix in a home-built sublimation apparatus (4/8); MALDI-MSI (5/9); µXRF (6/7) (modified from poster presentation (41)*, courtesy of A. Svirkova)*

Deconvolution of the XRF spectra was performed using the QXAS-AXIL software package (27), ROI imaging was done using the software LP-map (42). The elemental maps were created with X-Ray Lab software (43) as text files, and plotted with ImageJ (version 1.50b) (44). Origin (version OriginPro 2015, OriginLab Corporation, Northampton, MA, USA) and PyMCA (28) were used for plotting fluorescence sum spectra.

Results and discussion

Interference from supporting materials studied by µXRF

The sample preparation, especially the choice of the supporting/embedding material, can play a pivotal role in the experiment. In principle, µXRF does not require any specific sample treatment, but in the case of non-self-supporting thin sections, the cuts should be flattened and mounted onto a substrate. Ideally, the material should be as thin as possible, as XRF suffers from scattering of the exciting radiation by the sample as well as by the sample carrier. Scattering is the main reason for the spectral background.

The characteristic lines of the element of interest are superimposed on the background, and the detection limits are strongly influenced by both the spectral background and the intensity of the spectral lines. It is important to consider the chemical constituents of the supporting material, as these will be excited along with the sample.

Polyimide Kapton® films (8 µm thick) are relatively "transparent" to X-rays and are quite commonly used (45). Kapton® tape can be used as long as the constituents of the supporting material do not interfere with the elements of interest (46,47). An alternative for biological samples is the even thinner silicon nitride membrane windows (with a thickness of some 100 nm), usually used for small objects (cells, microorganisms), and samples which can easily adhere to the surface (soft tissues). Alternatively, the samples can be mounted directly on a glass microscope slide (45).

The measurements of backing materials were conducted prior to the actual sample measurements; the respective fluorescence spectra are shown in Figure 40. A larger spectral background is observed in the case of the double-sided tape and glass (Fig. 40A). Here, the peaks of sulphur (S), calcium (Ca), iron (Fe) and strontium (Sr) could be confirmed to be originating from the supporting materials. Sulphur, iron and strontium were further excluded from the analysis for this type of backing material. As the content of calcium in the sample tissues, namely, bone, by far exceeds its amount in the backing material, it was subsequently used for mapping.

In contrast, 3M tape made with DuPont™ Kapton® is free from impurities and the spectral background here is lower, which can be seen in Figure 40B. Of particular importance is the knowledge about MALDI matrix interference with µXRF measurements. As can be seen in Figure 40, no difference is observed for experiments with and without the MALDI matrix. Therefore, we can conclude that the MALDI matrix does not influence µXRF measurements.

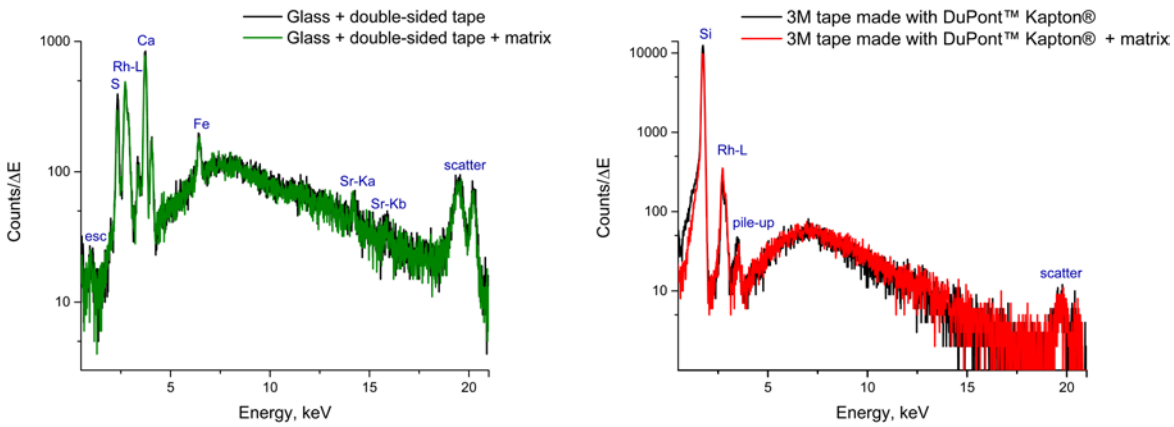

Figure 40. XRF single spectra: double-sided tape and glass without (black) and with a MALDI matrix (green) (left), 3M tape made with DuPont™ Kapton® without (black) and with the MALDI matrix (red) (right). Acquisition time – 90 s, in vacuum

Finally, the µXRF measurements of phalanx tissues samples were performed, and Fig. 4 demonstrates the sum of the fluorescence spectra over all measurement points, specifically for each type of backing material used. The spectra presented were obtained for the samples measured by µXRF first (i.e. samples were not covered with the MALDI matrix) and do not differ considerably from those measured after MALDI-MSI. In the case of a tissue sample mounted on the double-sided tape and glass (Fig. 41, top left), several overlapping peaks are found between 1.5 and 3.2 keV (Fig. 41, top right), which are caused by scattering from the glass-tape support, as well as the sample-itself. This energy range was used as the ROI for all µXRF imaging experiments (i.e. all counts in the ROI were summed up without fitting), as the deconvolution by AXIL was associated with a large error. This uncertainty was caused principally by the overlap of the Rh-L elastic scattering peak with other peaks in this energy region (Si-Kα, P-Kα, S-Kα, and Cl-Kα and the elastic scatter peak of the exciting Rh-L radiation). Calcium (Ca) and phosphorus (P) in the bone tissue could be measured. As for the sample on Kapton® polyimide tape (Fig. 41, bottom), a distinct sulphur (S) signal from soft tissues could be obtained in addition to those from Ca and P. We could also use the silicon peak, which originates from the glue on the Kapton® tape, to gain structural (absorption) information about the sample.

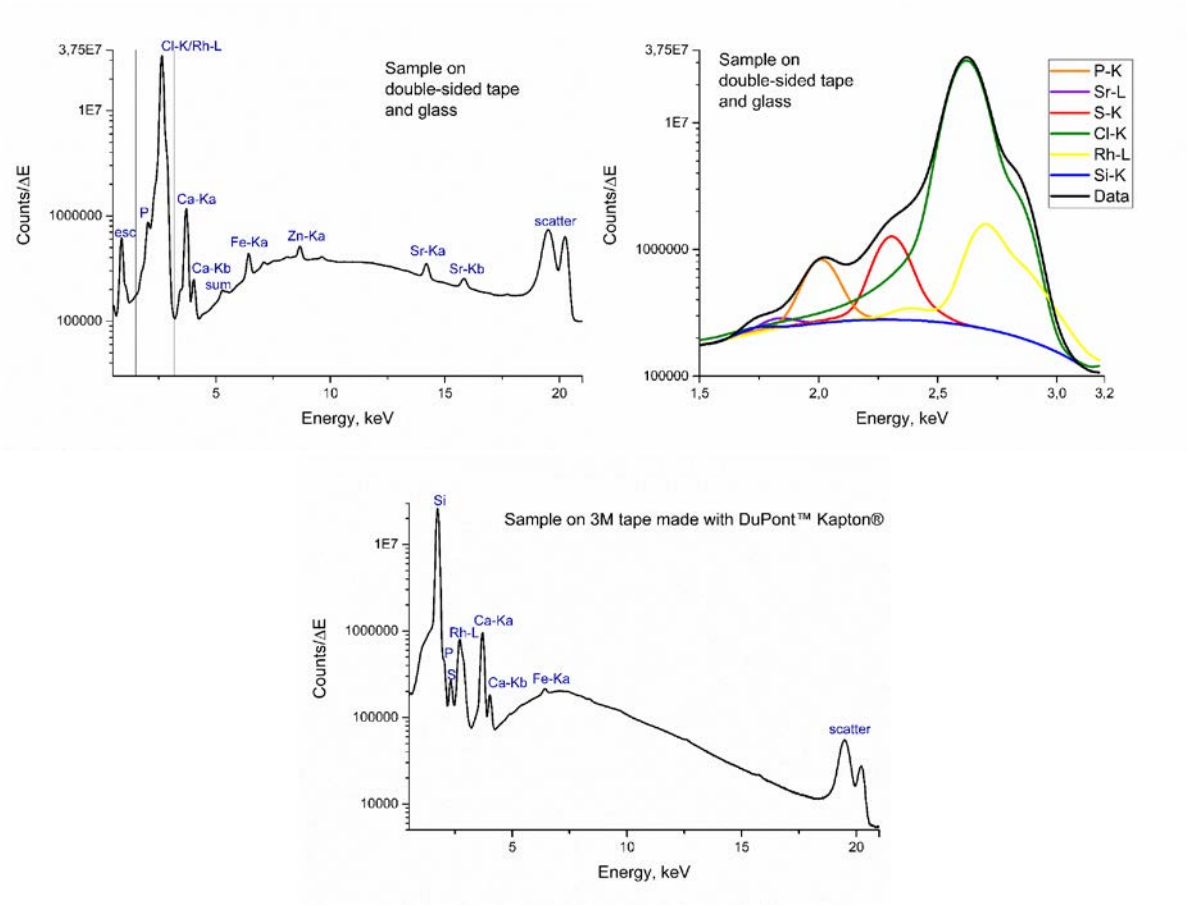

Figure 41. XRF sum spectra: sample prepared on the double-sided tape and glass (top left), with the marked energy region of interest (ROI); zoom into the marked ROI showing details for biologically relevant elements (top right); sample prepared on 3M tape made with DuPont™ Kapton® (bottom)

Imaging by µXRF and MALDI-MSI

Based on the spectral information, the following images could be obtained: Ca, P, and ROI data for the samples on glass + double-sided tape; and Ca, P, S and Si (showing the outline of the sample) for the cuts prepared on Kapton®. No considerable differences could be seen in both pairs, whether µXRF or MALDI-MSI was applied first.

Fig. 5 shows that based on the XRF spectral information, distribution maps of Ca, P, and ROI data (according to Fig. 41) could be obtained for samples fixed to a glass slide with the double-sided tape. For samples mounted on the Kapton® tape, Ca, P, S and Si maps (latter clearly showing the outline of the sample) could be acquired. Please note the differences in sulphur maps in Figure 42 (2 and 4), which are due to the extremely high-intensity hotspot on sulphur map within array 4. If not for the hotspot, the sulphur distributions and intensities are comparable (for a rescaled map with the hotspot removed, please refer to Fig. 43).

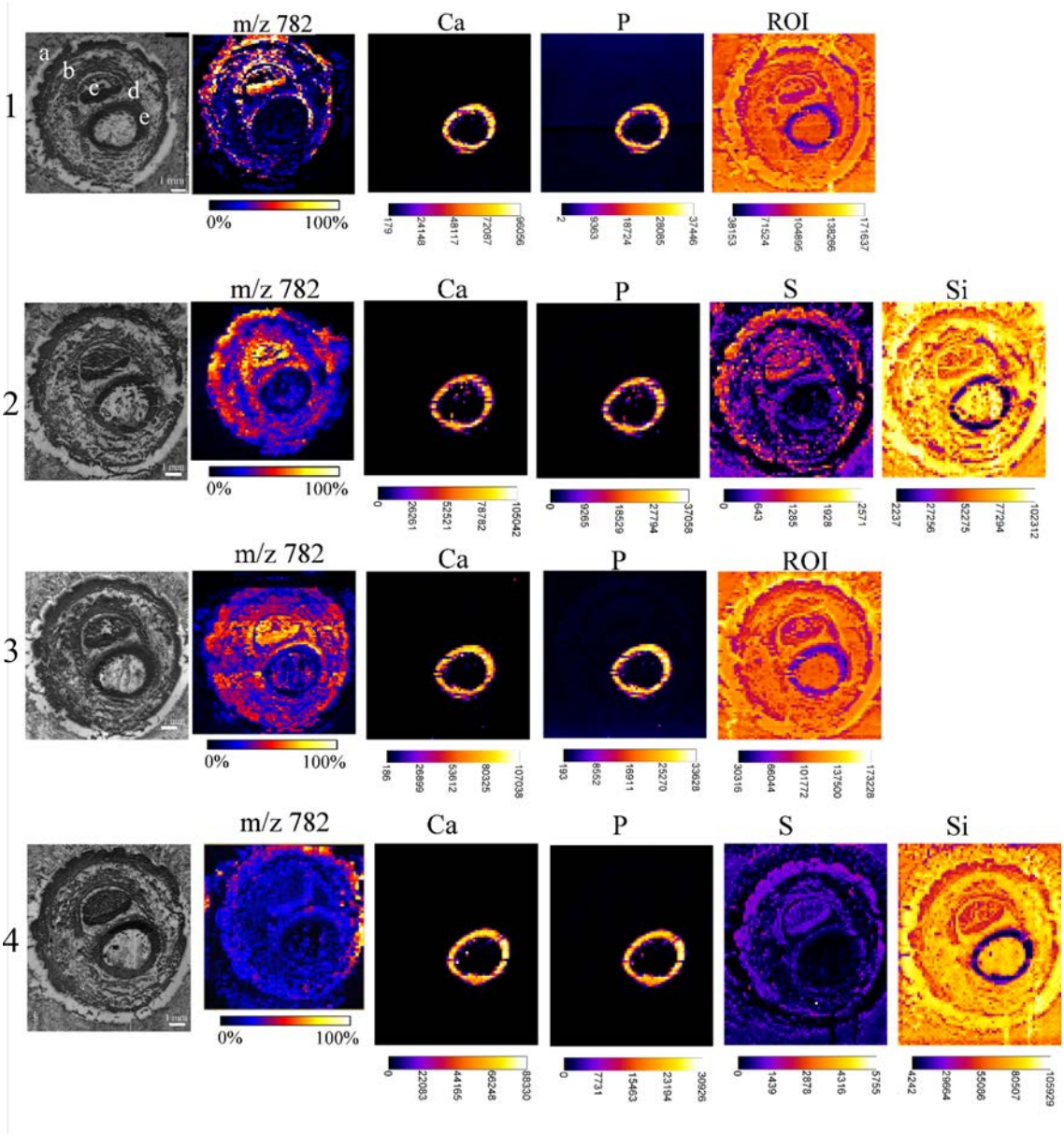

Figure 42. Molecular and elemental maps, see explanations in the text. All MALDI images were normalized to total ion current (TIC) for each ion across the section and an intensity scale bar is placed under the images. Units for XRF elemental maps are counts (the palette modified from (34)*)*

In Figure 42 each array starts with a microscopic image of the tissue sections mounted with different supporting tape, which were measured by MALDI-MSI and µXRF, before covering the tissue with dithranol as the MALDI matrix, if µXRF measurements were performed first, or with a dithranol layer, if MALDI-MSI was performed first. The arrays are given in the same order as a workflow sequence in Figure 38:

1. Double-sided tape, measured first by µXRF, then by MALDI-MSI (marked on the microscopic image – a: skin, b: muscle, c: nail, d: cartilage, e: bone);
2. Kapton® tape, measured first by µXRF, then by MALDI-MSI;
3. Double-sided tape, measured first by MALDI-MSI, then by µXRF;
4. Kapton® tape, measured first by MALDI-MSI, then by µXRF.

Lipid distributions detected by MALDI-MSI are exemplified by the distribution of m/z 782, elemental distributions measured by µXRF from the same sample preparation are exemplified by calcium (Ca),

phosphorus (P) and sulphur (S), extracted from energy ROI as shown in Figure 41 (top right), and silicon (Si).

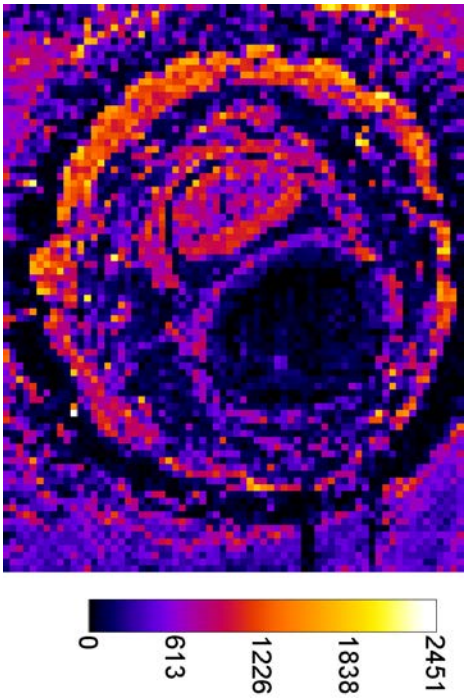

Figure 43. Rescaled µXRF image of sulphur distribution in a tissue section (corresponds to the sulphur map in Fig. XX, array 4). The image had to be rescaled due to a "hot spot". The hotspot was set to zero and the whole elemental map was rescaled according to a new maximum

As a final step of the analysis, the combination of the imaging information by overlaying µXRF and MALDI-MSI maps was attempted and combined into a single image for double-sided and Kapton® tape (Fig. 44).

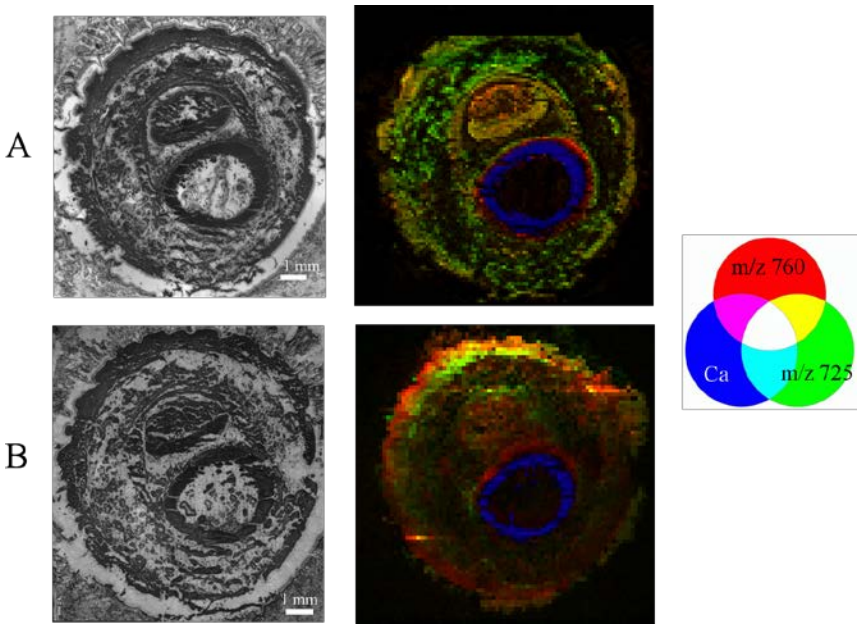

Figure 44. Optical microscopy of sample sections (left) and the superimposed µXRF and MALDI images (right) conducted on double-sided tape (A) and Kapton® polyimide tape (B). Calcium is shown in blue and lipids in green (m/z 725) and red (m/z 760) (34)

Conclusions and outlook

1. To the best of our knowledge, this is the first combination of MALDI-MSI and µXRF. By combining these methods, we acquired both elemental and molecular information.
2. In most cases, when multimodal approach is employed, the measurements are performed on the consecutive cuts. In the current study the measurements by both methods – MALDI-MSI and µXRF were done on the very same samples.
3. Both methods have similar lateral resolution – therefore facilitating the correlation of the images.
4. For both methods thin sections (tens of µm) can be used.
5. As it was anticipated in the reviews on combination of imaging methods (e.g. (40)), the sample preparation might be the stumbling block in the multimodal approach. We tested two types of sample support, and we can conclude, that:

   A) Samples prepared on glass carrier with double-sided tape – which is one of the methods of choice in MALDI-MSI – and naturally, this yielded good results for MALDI imaging. As for µXRF, the thick support made of a low-Z element brought in an issue of high scatter and elevated background, as well as contribution of trace elements contained in the support. However, we could demonstrate, that for elucidation of some questions of biological relevance, i.e. imaging of bone tissue in our case, the µXRF measurements directly on the glass carrier can be performed with very satisfactory results.

   B) Samples prepared on Kapton tape – which is common for µXRF, but have not been used for MALDI-MSI so far, allow imaging of soft tissue (S) by µXRF in addition to bone. The spatial resolution of MALDI images was limited by 150 µm in this case, yet overall, we can conclude that this approach to sample preparation is quite perspective and can further be employed.
6. The design of the experiment set out two workflows:
   - µXRF first, followed by MALDI-MSI
   - MALDI-MSI first, followed by µXRF

Based on our results, we can conclude that,

A) The application of MALDI matrix does not hinder µXRF measurements. Organic MALDI matrix seems not to alter the elemental distribution in the samples, and does not affect the measurements.

B) Predictably, measurements by µXRF performed in the first turn, did not negatively affect MALDI-MSI (as the method itself does not involve any damage to the sample).
Nevertheless, in order to avoid the deterioration of the biomolecules, which normally happens with time, it can be recommended to conduct MALDI-MSI first.

In prospect, confocal µXRF setup can be used for the measurements, which allows to restrict the element information to a well-defined voxel, excluding the sample carrier – this will help limiting the unwanted contributions from the support, and avoiding the obstruction of the elements of interest by scatter.
Also, synchrotron radiation-induced µXRF (SR-µXRF) can shorten the measuring time dramatically, as well as improve limits of detection for trace elements.

3.2 µXRF + LA-ICP-MS: Human femoral head cuts

The project was performed in collaboration with Institute of Chemical Technology and Analytics (CTA) TU Wien within MEIBio doctoral program. LA-ICP-MS measurements were performed by Stefan Smetaczek (15 and 41 µm) and Maximilian Bonta (9 µm). The results are included in a manuscript entitled "Correlation of µXRF and LA-ICP-MS in the analysis of a human bone-cartilage sample", which was published in the "Analyst"(31).

Furthermore, the project benefited greatly from the investigations performed by XRP group students: Angelica De Leon and Lukas Fenninger (project works), Alexander Kleeweiss (48)*, Vanessa Pichler* (49)*. The supporting SEM-EDX measurements of the instruments and materials used in preparations of the cuts were kindly undertaken by Dr. Stéphane Blouin (LBIO).*

Laser ablation inductively coupled plasma mass spectrometry (LA-ICP-MS) is a commonly used method of elemental analysis of solid samples. It is a powerful analytical technique which allows to provide accurate quantitative information on major, minor, trace, and ultratrace elements for industrial, geological, environmental and biological applications (50).

The basic principle of LA-ICP-MS can be described as follows: the sample surface is irradiated by a high-power focused laser shot, which results in ablation of minute amount of sample material. The obtained aerosol is transferred into inductively coupled plasma by a carrier gas, where atomization and ionization of ablated material takes place. Lastly, the ions are analysed via mass spectrometer (e.g. quadrupole).

A scheme of LA-ICP-MS setup is provided in Figure 45:

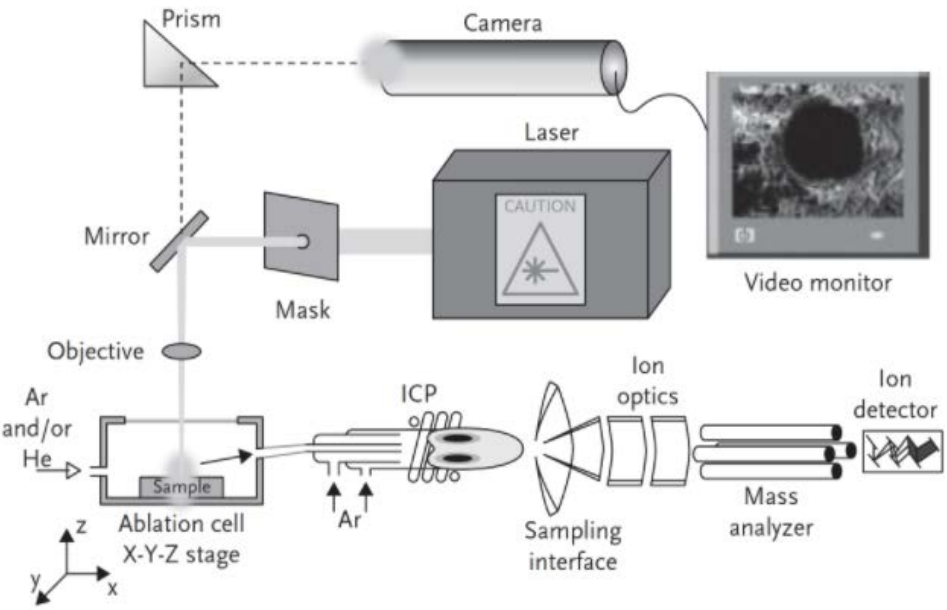

Figure 45. Schematic representation of LA-ICP-MS setup (51)

LA-ICP-MS is most frequently used for 2-dimensional elemental mapping. The spatial resolution of the technique is mostly defined by the laser beam diameter, and can vary from ca. 1 µm to 100 µm (depending on the instrumentation). The resolution range of LA-ICP-MS is comparable to what laboratory µXRF spectrometers can offer (ca. 50 µm @ Cu-Ka for ATI µXRF laboratory setup; and down to 10 µm in commercially available systems (52)) – which is a favourable aspect in combination of these techniques. LA-ICP-MS requires minimal or no sample preparation, furthermore, it is indifferent to the conductive properties of the analysed material (possible to investigate both conductive and non-conductive samples). The latter feature of LA-ICP-MS is especially beneficial in

the analysis of biological samples and once again lessens the need in specialised sample treatment (in comparison to SIMS, see further section 3.3).

Arguably, the most appealing characteristic of LA-ICP-MS analysis is a relatively easy quantification procedure. However, quantification comes at a price – namely, the need for matrix-matched standards. This necessity can be explained by the fact, that the ablation, aerosol transport, and analyte ionization process are material-dependent. The possible alternatives to matrix-matched standards and an overall excellent compilation of quantification strategies in imaging of biological samples with LA-ICP-MS was presented in PhD dissertation of MEIBio colleague, Maximilian Bonta (53).

Reports on comparative and/or complimentary use of µXRF and LA-ICP-MS can be found in literature (54–57). Usually a specific type of tissue is analysed in such a "tandem" and the quantification is performed by LA-ICP-MS only (e.g. (55,57)). We have taken the method correlation one step further by performing the analysis of complex sample with different types of tissues – human femoral head sample (includes bone and cartilage), and in addition to the LA-ICP-MS quantitative data, we also obtained µXRF quantified maps of selected elements.

Experimental

While bone consists mostly of mineralized material and its elemental composition is in focus of investigation (both in health and disease), hyaline cartilage is primarily composed of organic molecules – such as glycosaminoglycans, proteoglycans, collagen; and its elemental content is not well studied. In our proof-of-principle experiment we aimed to characterize the elemental composition of both bone and cartilage tissues. A femoral head biopsy from a female patient (93 years old) was used for experiments. The patient provided consent to sample collection and analysis under an ethics committee approval.

The undecalcified biopsy was fixed in 70% ethanol, dehydrated through a graded ethanol series, and embedded in PMMA. Thin sections were prepared out of a single PMMA block using different approaches. While 9 and 15 µm slices were cut using a microtome (LEICA SM2500; Leica Microsystems GmbH, Wetzlar, Germany); 41 µm was obtained by grinding with sandpaper (first abrasive grit size of 1200 up to the desired thickness, then abrasive grit size 2400 for 1 minute) and polishing using polycrystalline diamond spray (3 µm and 1 µm).

The samples were prepared in such a way as to include both bone and articular cartilage tissues. The Figure 46 shows the morphology of the sample. Three slices of thickness 9, 15 and 41 µm were used for the imaging experiments.

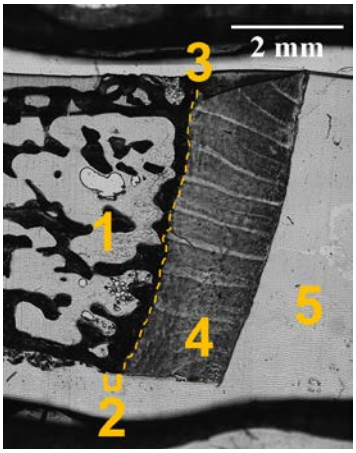

Figure 46. Micrograph of an exemplary sample: 1 – trabecular bone (black); 2 – subchondral cortical bone and mineralized cartilage (black); 3 – tidemark (dashed line); 4 – hyaline cartilage; 5 – PMMA outside of the sample

For µXRF measurements, the samples were sandwiched between acrylic glass frames and attached to a sample holder, which facilitated direct measurement on the sections and eliminated unwanted fluorescent/scattering contributions of backing materials, while ensuring that the sample is flattened during the measurement. After the non-destructive µXRF measurements, an intact sample was transferred to LA-ICP-MS instrument.

The µXRF measurements were performed at the Atominstitut laboratory setup, the tube voltage and current were set to 50 kV and 0.4 mA, respectively. The measurement conditions were: step size 50 µm, acquisition time 60 s per spot (real time), in vacuum. Deconvolution of the spectra was performed by QXAS-AXIL (27). The elemental maps were created as text files using the software LP-map (42) and processed (negative values zeroed for correct representation) and plotted with ImageJ (44). The XRF data were deadtime corrected. The XRF maps were quantified using the sensitivity values obtained via the measurements of IAEA animal bone (H5) certified reference material, the details can be found in the Master's thesis of V. Pichler (49). The sensitivity values (Fig. 47) of the elements for which data was not available – sulphur and potassium, were derived by interpolation. The thickness of the cuts was not considered in quantification.

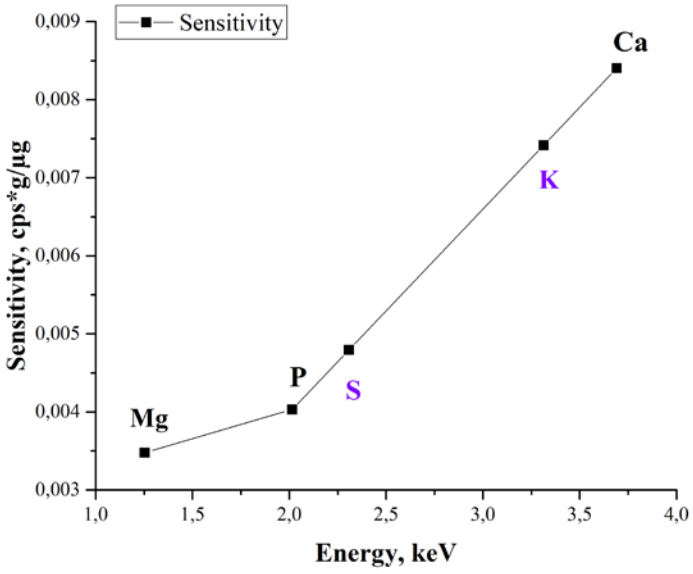

Figure 47. Sensitivities measured on the H5 Bone standard reference material and further used in quantification of XRF elemental maps

The detailed information on the setup, experimental parameters, and details of the analytical procedure as well as data handling for LA-ICP-MS for samples 15 µm and 41 µm are provided in the original manuscript (31). The details of the LA-ICP-MS test measurements on 9 µm slice are not known.

Results and discussion

9 µm slice – test measurements

µXRF imaging was performed first and we specifically selected the measurement area which included bone, articular cartilage tissue and the metabolically active area of tidemark – the interface between calcified and non-calcified cartilage. The corresponding sum spectrum is shown (Fig. 48).

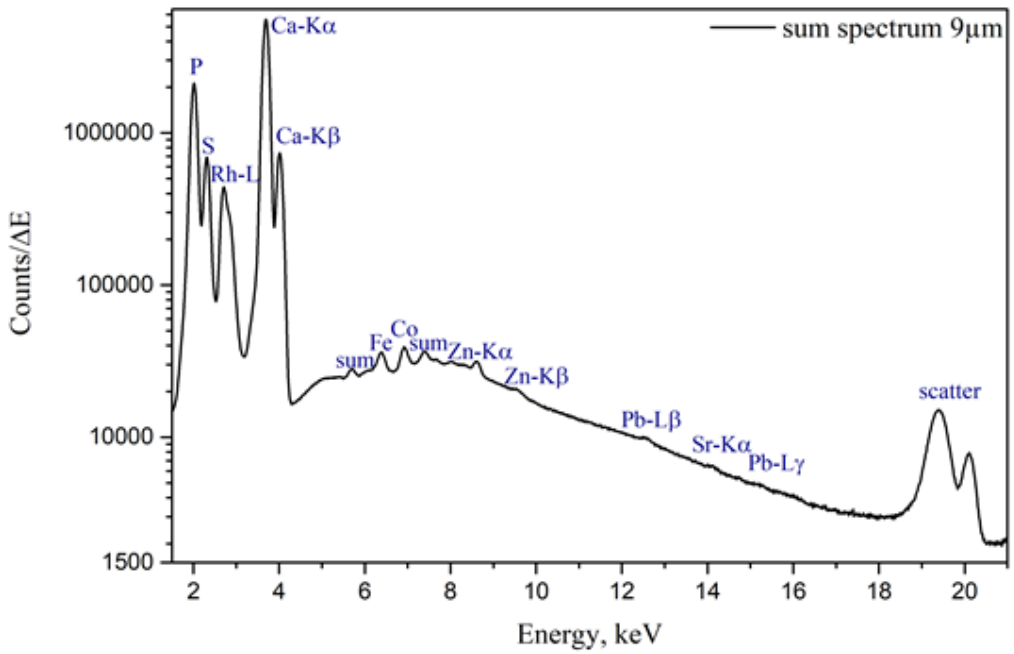

Figure 48. µXRF sum spectrum of 9µm cut of human femoral head sample

In the sum spectrum high content of Ca and P corresponds to the bone and calcified cartilage area, and high S peak can be attributed to the hyaline cartilage. Zn, Pb and Sr are expected to be found in the sample (Zn in both cartilage and bone, accumulation of Zn and Pb in tidemark, Sr – in bone). Since the Pb and Sr peaks were hardly discernible, we excluded these metals from further analysis. Fe, although normally present in tissues (e.g. from blood), can also be introduced in the sample by the cutting equipment, therefore, Fe and Co were considered contaminations (see the section "Supporting SEM-EDX measurements of the instruments and materials used in sample preparation" within this chapter). The µXRF elemental maps for the four elements of interest are shown below (Fig. 49).

The test imaging experiment with LA-ICP-MS was performed with 40 µm lateral resolution – and without quantification. The measurement demonstrated that the following isotopes could be measured: ^{23}Na, ^{24}Mg, ^{31}P, ^{34}S, ^{39}K, ^{42}Ca, ^{50}Cr, ^{55}Mn, ^{56}Fe, ^{59}Co, ^{64}Zn. Below the results for Ca and Zn in comparison with µXRF maps are shown (Fig. 50).

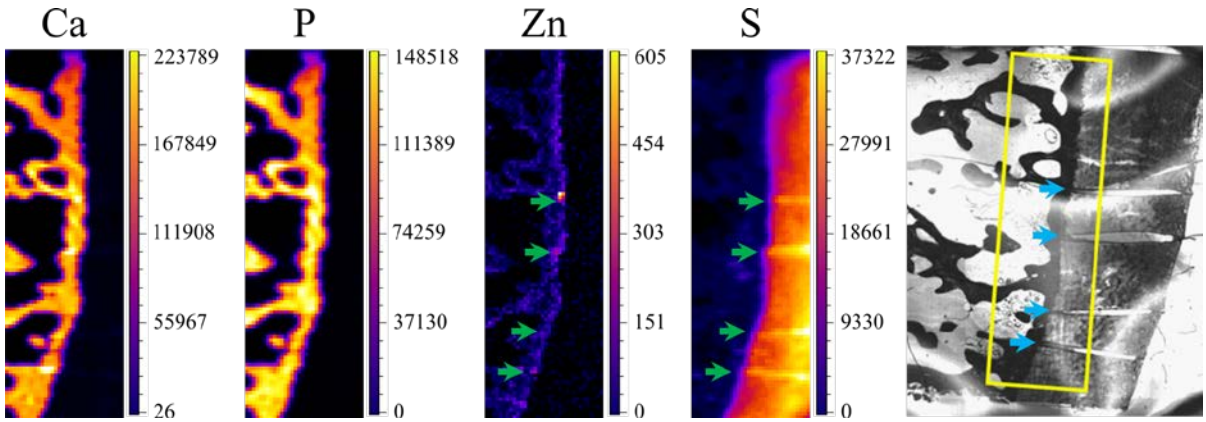

Figure 49. µXRF maps of Ca, P, Zn and S in 9µm slice of human femoral head sample (in µg/g). P, Zn and S negative values were set to zero. Arrows are pointing at the position of the folds – the folds can be seen in the micrograph (marked with blue arrows) and in S map (green arrows). The arrows from S map were directly transferred to the Zn map

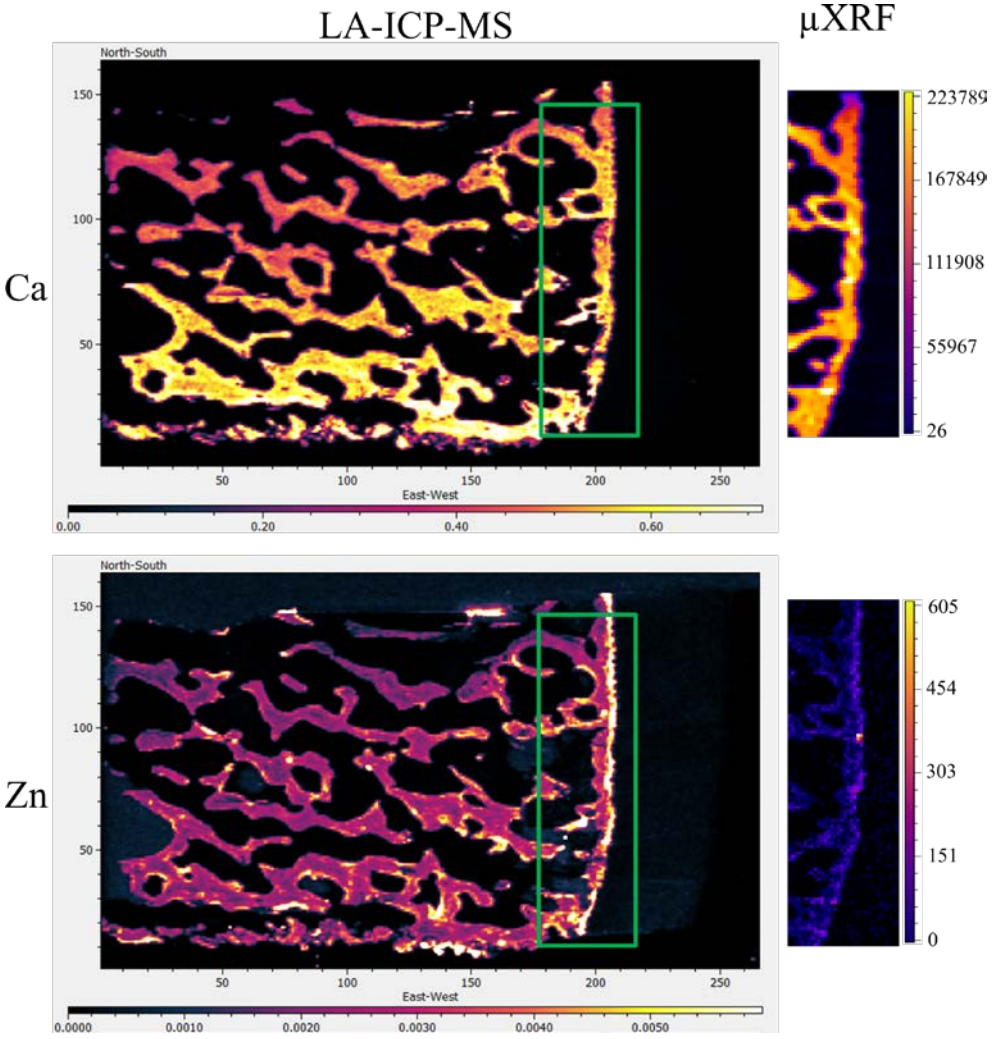

Figure 50. 9µm slice – comparison of test LA-ICP-MS maps and µXRF results for Ca and Zn. Units for LA-ICP-MS – a.u.; for µXRF- µg/g

15 and 41 µm samples – approach to quantitative imaging

The overall composition of the samples 15 and 41 is similar to sample 9 µm. Sum spectra for 9 and 15 µm slices look alike, but in the sum spectrum of 41 µm cut, additionally Ti, Cr and K peaks can be observed (Fig. 51). This can be explained by the different preparation method (grinding and polishing applied).

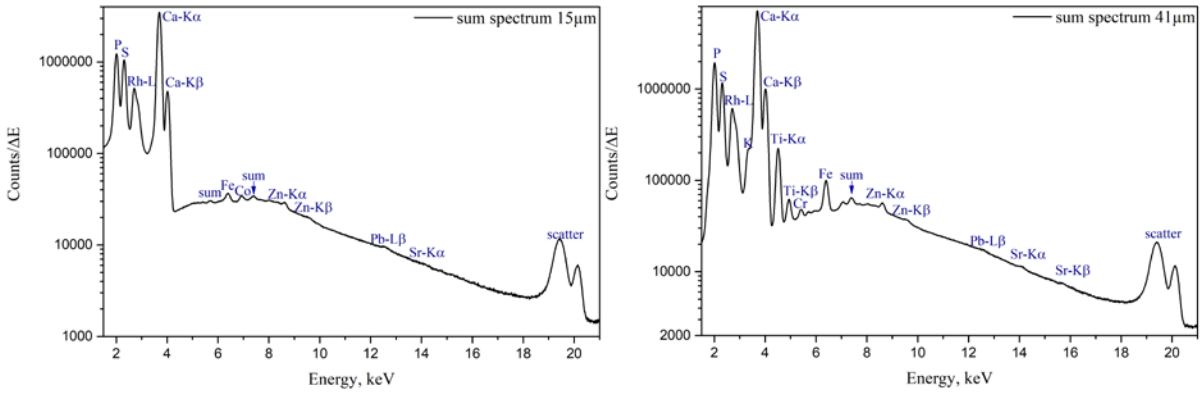

Figure 51. µXRF sum spectra of human femoral head samples, left – 15 µm cut, right – 41 µm cut

In the LA-ICP-MS experiments on 15 µm and 41 µm cuts, mapping was performed with a smaller beam diameter (higher resolution) – 25 µm, area was limited to the region of interest around tidemark. Major elements (Ca, Mg, Na, K, P, S) as well as minor/trace elements (Co, Cr, Fe, Mn, Zn) expected to be found in a sample were included in the LA-ICP-MS analysis. Although C is measurable with ICP-MS, it was excluded from the analysis since the C-rich embedding medium would falsify the analysis. For each analyte, one isotope was chosen using absence of potential (isobaric and polyatomic) interferences as well as natural abundance as selection criteria. List of potential polyatomic interferences is presented below (Table 2):

Table 2. Potential polyatomic interferences ICP-MS analysis

Isotope	**Interference**
^{24}Mg	$^{12}C_2^+$
^{31}P	$^{14}N^{16}O^1H^+$, $^{15}N^{15}N^1H^+$, $^{15}N^{16}O^+$, $^{14}N^{17}O^+$, $^{13}C^{18}O^+$, $^{12}C^{18}O^1H^+$
^{34}S	$^{15}N^{18}O^1H^+$, $^{16}O^{18}O^+$, $^{17}O_2^+$, $^{16}O^{17}O^1H^+$
^{39}K	$^{38}Ar^1H^+$
^{42}Ca	$^{40}Ar^1H_2^+$
^{50}Cr	$^{34}S^{16}O^+$, $^{36}Ar^{14}N^+$, $^{36}S^{14}N^+$, $^{32}S^{18}O^+$, $^{33}S^{17}O^+$
^{55}Mn	$^{40}Ar^{14}N^1H^+$, $^{39}K^{16}O^+$, $^{40}Ar^{15}N^+$, $^{38}Ar^{17}O^+$, $^{36}Ar^{18}O^1H^+$, $^{38}Ar^{16}O^1H^+$, $^{23}Na^{32}S^+$
^{56}Fe	$^{40}Ar^{16}O^+$, $^{40}Ca^{16}O^+$, $^{40}Ar^{15}N^1H^+$, $^{38}Ar^{18}O^+$, $^{38}Ar^{17}O^1H^+$
^{59}Co	$^{43}Ca^{16}O^+$, $^{42}Ca^{16}O^1H^+$, $^{36}Ar^{23}Na^+$, $^{40}Ar^{18}O^1H^+$
^{64}Zn	$^{32}S^{16}O_2^+$, $^{31}P^{16}O_2{}^1H^+$, $^{48}Ca^{16}O^+$, $^{32}S_2^+$, $^{31}P^{16}O^{17}O^+$, $^{36}Ar^{14}N_2^+$

We assume that the information depth of the LA-ICP-MS measurements is about 5 µm, it is similar for both slices independently of their thickness, and only varies among different histological areas, i.e. bone and hyaline cartilage.

^{50}Cr and ^{55}Mn did not provide sufficient signal-to-noise ratios for the generation of elemental maps and were therefore excluded from further analysis. ^{56}Fe and ^{59}Co show significant signal intensities in some sample areas, however, since they most likely originate from contaminations due to sample preparation they were excluded from further analysis as well. The elemental maps of the remaining analytes were quantified via external calibration using the measured IAEA animal bone (H5) certified

reference material as well as the self-made porcine cartilage standard. To keep matrix effects as small as possible, those analytes predominately in the calcified area (^{42}Ca, ^{24}Mg, ^{23}Na, ^{31}P, ^{64}Zn) were quantified using the bone standard, while the cartilage standard was used for those analytes predominately in the hyaline cartilage area (^{34}S, ^{39}K). This means that the analysis is not perfectly matrix-matched for the tissue in which the analyte shows lower concentration (e.g. Ca in hyaline cartilage tissue). However, since the presence of most elements is rather limited to one kind of tissue (e.g. Ca in bone), the resulting error is hardly visible in the elemental maps and therefore negligible. Image quantification was performed without internal standard correction since no element suitable as internal standard (i.e. constant concentration in whole sample) was available.

Results for 15 and 41 µm cuts are shown in Figures 52 and 53.

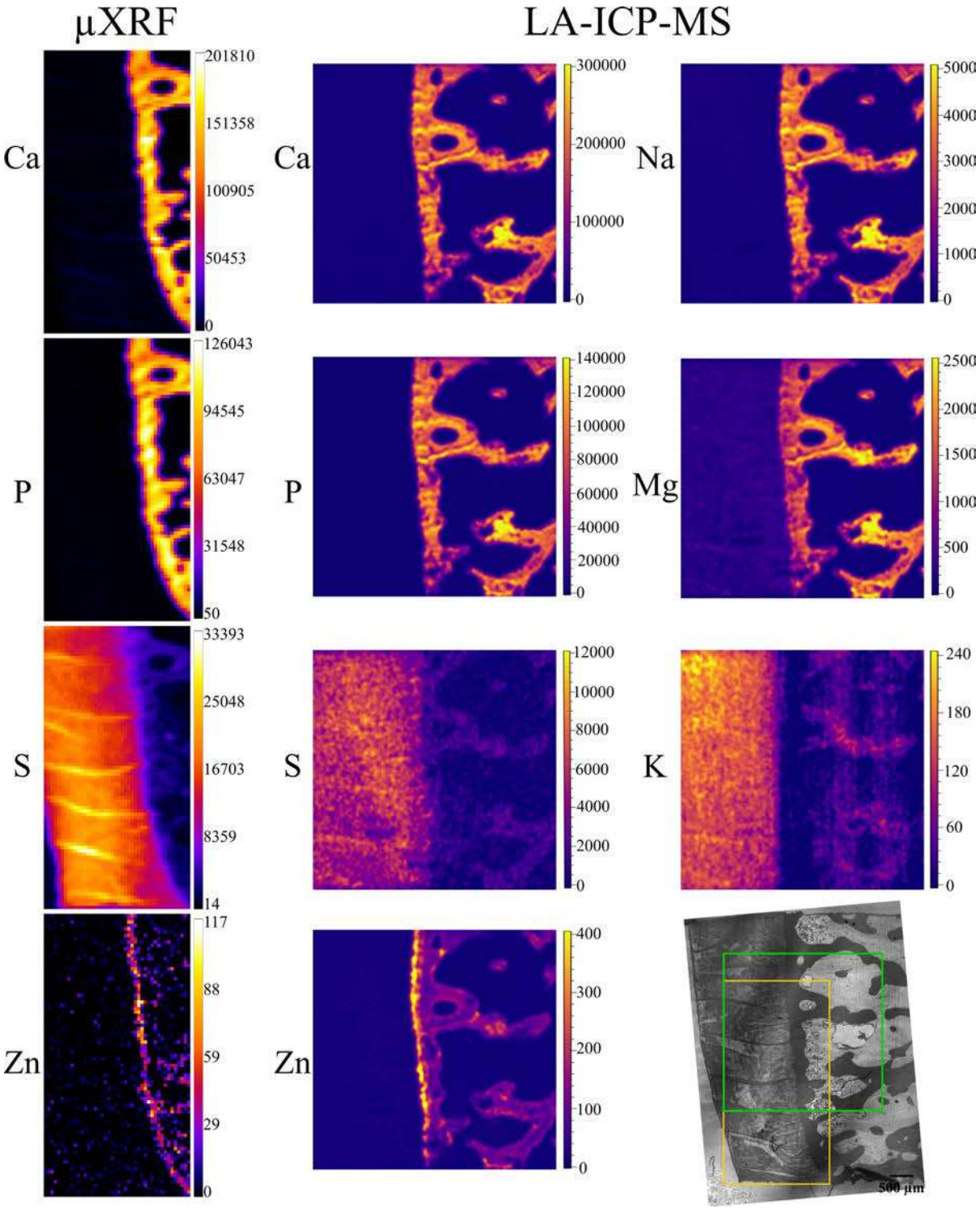

Figure 52. 15 µm slice: elemental maps obtained by µXRF and LA-ICP-MS. The micrograph in the low right corner with the scanned regions (µXRF – yellow, LA-ICP-MS – green rectangle). The units for both µXRF and LA-ICP-MS maps are µg/g

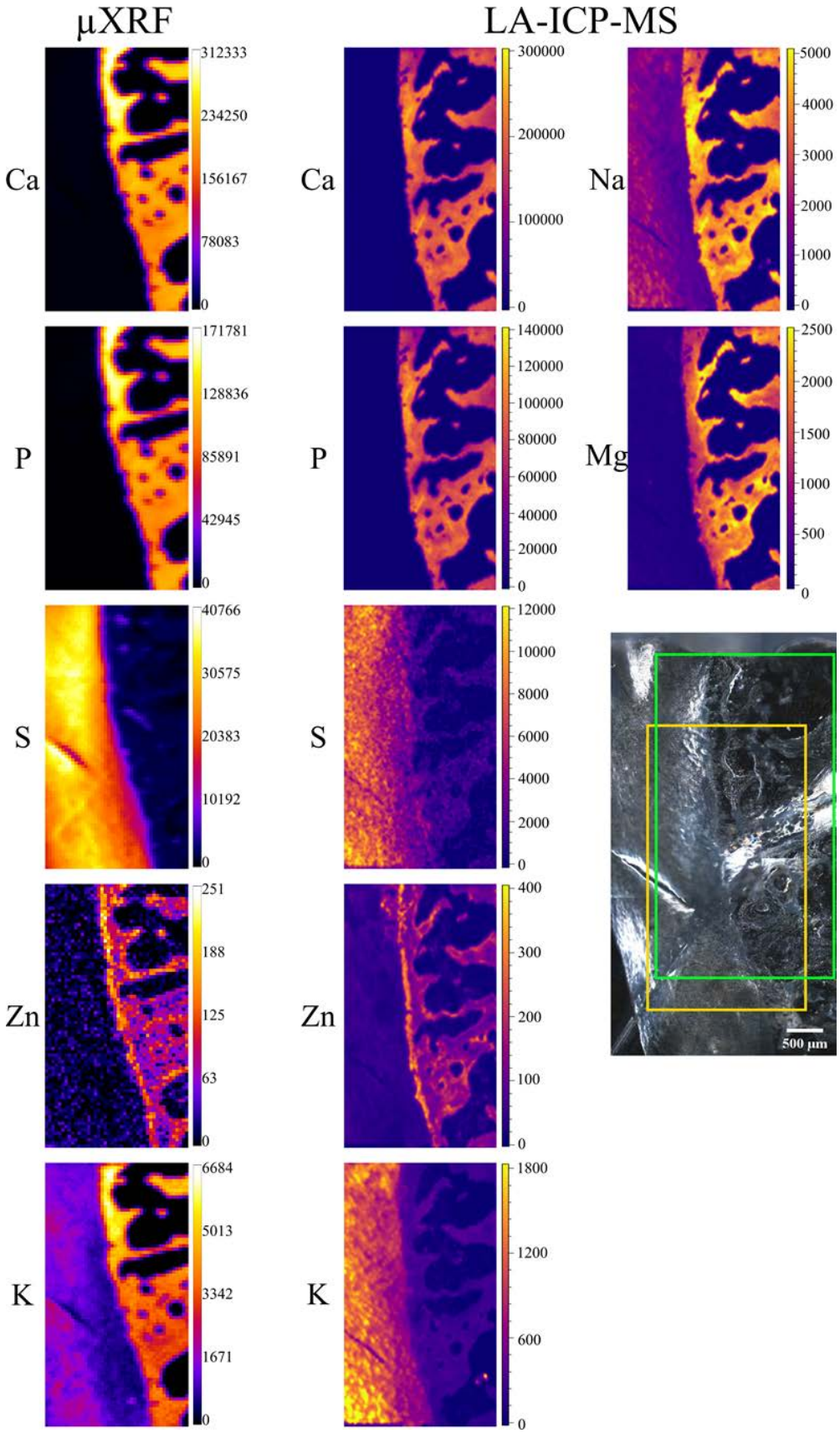

Figure 53. 41 µm slice: elemental maps obtained by µXRF and LA-ICP-MS. The micrograph in the low right corner with the scanned regions (µXRF – yellow, LA-ICP-MS – green rectangle). The units for both µXRF and LA-ICP-MS maps are µg/g

15 and 41 µm samples – histological separation by µXRF

In the µXRF maps we could observe a rather distinct separation of the three histological zones – bone, tidemark, and cartilage, owing to the element-markers, Ca, Zn and S, accordingly (see Fig. 54). Therefore, we performed an additional analysis: by creating the "masks" of these elements in the imaging software and applying them onto quantified elemental maps, we could obtain the concentrations of elements in different histological zones.

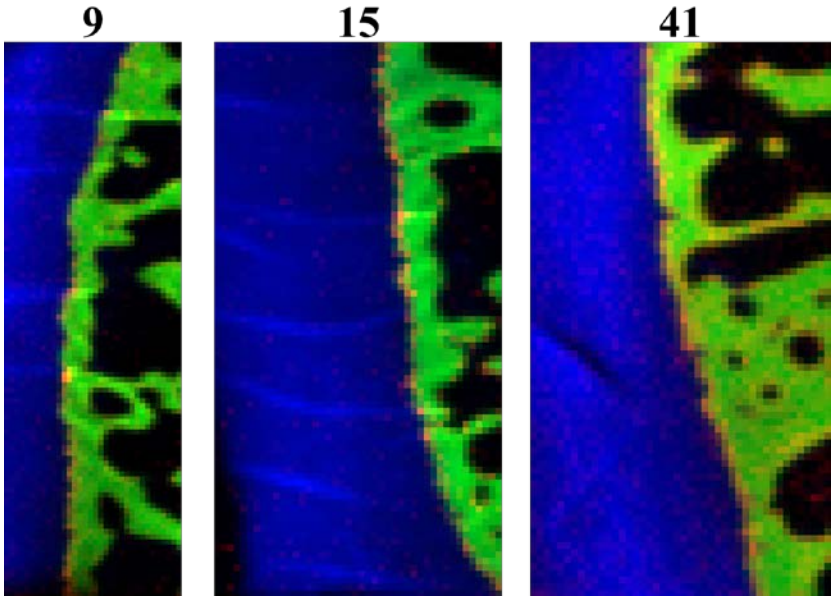

Figure 54. 9, 15 and 41 µm slices: 'composite' maps. Ca – in green ('bone'); Zn – in red ('tidemark'); S – in blue ('cartilage')

The analysis was performed in ImageJ using the original µXRF scans for samples 15 and 41µm. The mask for the calcification area was created on Ca map, tidemark mask – on Zn map, and cartilage mask on S map – see Figure 55. The selection was done subjectively, as to include most of the area of interest, while minimizing the overlap with the adjacent tissue. The calcification zone includes bone and mineralized cartilage.

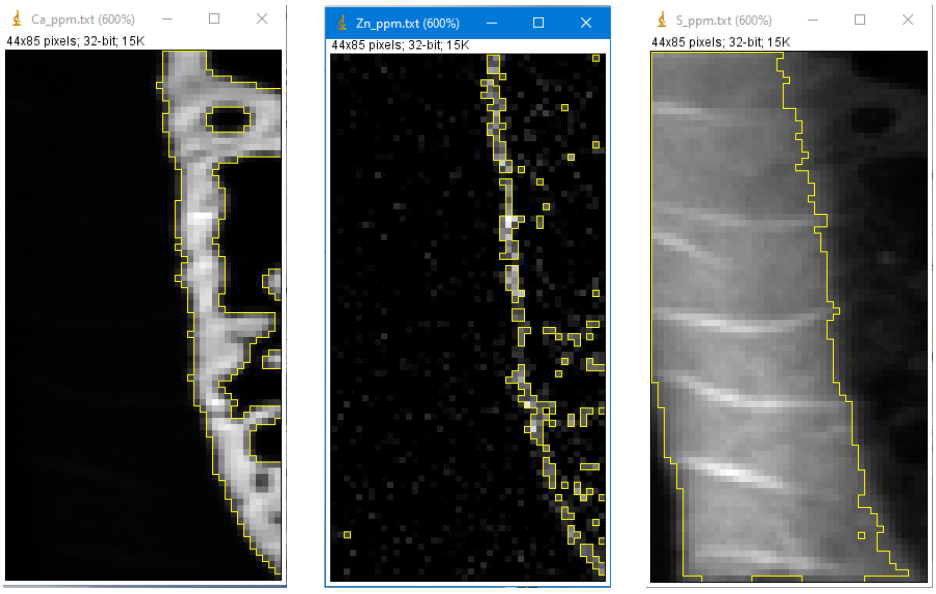

Figure 55. 15µm slice: left – µXRF Ca map with the "calcification zone" mask applied on it; middle – µXRF Zn map with the "tidemark" mask; right – µXRF S map with the "cartilage" mask

The masks (yellow line) were applied to the elemental maps of interest. The mean value, standard deviation for the area within the mask as well as minimum and maximum values for the 15 µm sample are given in Table 3.

Table 3. 15µm slice – comparison of elemental concentrations (µg/g) obtained by µXRF in calcification area, tidemark, and cartilage areas (as shown in Fig. 55)

15 µm	**Calcification area** – 20% Ca signal (XRF), 747 pixels	
	$\bar{x} \pm s$, *in µg/g*	*Range, in µg/g*
Ca	122655.5 ± 36378.9	40366.2 – 201810.4
P	80263.2 ± 22738.3	14149 – 126043.2
Zn	16 ± 21	0 – 117.3
	Tidemark – 5% Zn signal (XRF), 181 pixels	
	$\bar{x} \pm s$, *in µg/g*	*Range, in µg/g*
Zn	48.3 ± 17.3	29.2 – 117.3
Ca	103549 ± 40001	79.9 – 201591.4
P	65510 ± 23769	274.2 – 110238.7
	Cartilage (hyaline) – 62% S signal (XRF), 2331 pixels	
	$\bar{x} \pm s$, *in µg/g*	*Range, in µg/g*
S	17518.5 ± 3663.6	10879.7 – 33392.7
Ca	2540.6 ± 4051.3	725.9 – 102477
P	1174 ± 2358.6	240.9 – 39284.6
Zn	1.3 ± 4.4	0 – 106.5

Similar procedure was performed for µXRF elemental maps of 41 µm slice (Fig. 56). As the tidemark zone is less pronounced, we could not separate this histological area based on Zn; a mask "Zn zone" includes pixels with high Zn values in mineralized cartilage (including the tidemark) and in bone. The results are presented in Table 4.

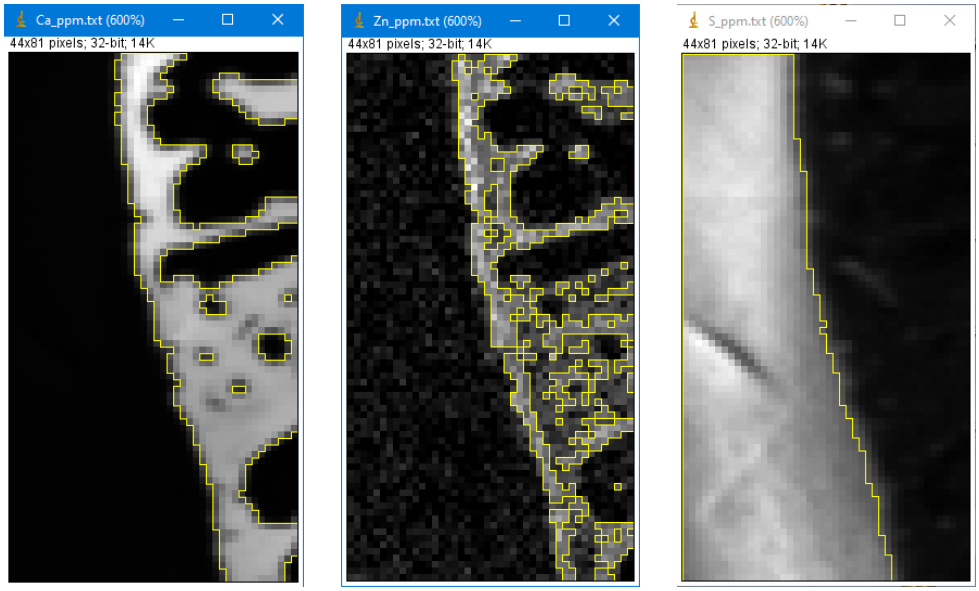

Figure 56. 41µm slice: left – µXRF Ca map with the "calcification zone" mask applied on it; middle – µXRF Zn map with the "Zn zone" mask; right – µXRF S map with the "cartilage" mask

Table 4. 41µm slice – comparison of elemental concentrations (µg/g) obtained by µXRF in calcification area, Zn zone and cartilage areas (as shown in Fig. 56)

41 µm	**Calcification area** – 29% Ca signal (XRF), 1044 pixels	
	$\bar{x} \pm s$, *in µg/g*	*Range, in µg/g*
Ca	189091.4 ± 50386.5	74829.4 – 312333.3
P	100227.8 ± 27150.7	31444.7 – 171781.4
Zn	93.2 ± 38.4	2.9 –250.6
	Zn zone – 16% Zn signal (XRF), 574 pixels	
	$\bar{x} \pm s$, *in µg/g*	*Range, in µg/g*
Zn	120.1 ± 28.9	85.6 – 250.6
Ca	192916 ± 52340.8	3554.7 – 312333.3
P	100955 ± 28672.6	1285.4 – 171781.4
	Cartilage (hyaline) – 52% S signal (XRF), 1839 pixels	
	$\bar{x} \pm s$, *in µg/g*	*Range, in µg/g*
S	27351.8 ± 5879.6	13590 – 40766.2
Ca	4680.8 ± 11184.7	1101.8 – 146076.3
P	2007 ± 6653.8	0 – 82902
Zn	14.2 ± 16	0 – 151.1
K	1330.7 ± 460.1	400.3 – 3872.4

15 and 41 µm samples – correlation of the µXRF and LA-ICP-MS images

The quantitative maps acquired by both methods (in spite the differences in employed quantification approaches) demonstrated the concentrations in the same order of magnitude. In order to directly compare the elemental concentrations obtained by µXRF and LA-ICP-MS, we limited the elemental maps to the very same area (the exact area is demonstrated in the original article (31) and lies within the overlap of the green and yellow rectangles shown in Figures 52 and 53), and then subdivided the maps in two subsections – mineralized tissue (selection criteria: Ca value in µXRF map > 100 mg/g) and hyaline cartilage (selection criteria: S value in µXRF map > 10 mg/g). The averaged values and standard deviation for the elements within these subsections are presented in Table 5 (15 µm slice) and Table 6 (41 µm slice).

Table 5. 15µm slice – comparison of elemental concentrations in mineralized and cartilage (hyaline) areas by average values and associated standard deviations ($\bar{x} \pm s$)

15 µm	**Mineralized tissue** (Ca (XRF) > 100 mg/g)	
	LA-ICP-MS	µXRF
	$\bar{x} \pm s$	$\bar{x} \pm s$
Ca	171 ± 77 mg/g	137 ± 19 mg/g
K	< LOD	–
Mg	1.3 ± 0.6 mg/g	–
Na	3 ± 1.4 mg/g	–
P	77 ± 36 mg/g	90 ± 13 mg/g
S	< LOQ	–
Zn	139 ± 115 µg/g	12 ± 17 µg/g
15 µm	**Cartilage (hyaline)** (S (XRF) > 10 mg/g)	
	LA-ICP-MS	µXRF
	$\bar{x} \pm s$	$\bar{x} \pm s$
Ca	3.5 ± 1.6 mg/g	2.6 ± 5.6 mg/g
K	< LOQ	–
Mg	194 ± 76 µg/g	–
Na	100 ± 42 µg/g	–
P	< LOD	1.4 ± 3.5 mg/g
S	6 ± 1.9 mg/g	17 ± 3.5 mg/g
Zn	7 ± 4 µg/g	1 ± 4 µg/g

Table 6. 41µm slice – comparison of elemental concentrations in mineralized and cartilage (hyaline) areas by average values and associated standard deviations ($\bar{x} \pm s$)

41 µm	**Mineralized tissue** (Ca (XRF) > 100 mg/g)	
	LA-ICP-MS	µXRF
	$\bar{x} \pm s$	$\bar{x} \pm s$
Ca	162 ± 68 mg/g	193 ± 45 mg/g
K	< LOQ	–
Mg	1.5 ± 0.6 mg/g	–
Na	3.5 ± 1.3 mg/g	–
P	72 ± 31 mg/g	102 ± 25 mg/g
S	< LOQ	–
Zn	145 ± 68 µg/g	94 ± 32 µg/g
41 µm	**Cartilage (hyaline)** (S (XRF) > 10 mg/g)	
	LA-ICP-MS	µXRF
	$\bar{x} \pm s$	$\bar{x} \pm s$
Ca	7 ± 30 mg/g	8 ± 23 mg/g

K	1 ± 0.4 mg/g	1.3 ± 0.5 mg/g
Mg	174 ± 193 µg/g	–
Na	1.5 ± 0.7 mg/g	–
P	2.3 ± 14 mg/g	3.9 ± 12.5 mg/g
S	5.9 ± 2.2 mg/g	27 ± 6.7 mg/g
Zn	42 ± 34 µg/g	17 ± 22 µg/g

Generally for µXRF, it should be noted that the excited/detected sample mass in 15 µm is lower than in 41 µm, which leads to different concentration values. As LA-ICP-MS is not affected by sample thickness, similar values are observed for 15µm and 41 µm slices, except for K – which is notably higher in the 41 µm slice. Specifically for K, it should be emphasized, that this element could be detected by µXRF only in the 41 µm slice in cartilage – here we assume the influence of larger sampling volume in thicker sample. The µXRF mean cartilage value for potassium corresponds to the potassium content reported by LA-ICP-MS.

Since S maps are more detailed in µXRF measurements, we conclude that LA-ICP-MS is less sensitive to S, most likely due to the high S-background. In case of Zn, LA-ICP-MS provided more detailed distribution maps for both samples – more features can be seen in slice 15 µm in comparison to µXRF; in slice 41 µm the histological structures are clearer, due to higher depth resolution of LA-ICP-MS.

To further evaluate the agreement between the images obtained by µXRF and LA-ICP-MS, we calculated the correlation between the corresponding elemental maps. We used the Pearson correlation coefficient for the evaluation. It assumes values in the range from −1 to +1, where 1 indicates strongest possible agreement, 0 strongest possible disagreement, and −1 perfect negative correlation. Table 7 displays the result – Pearson correlation coefficients calculated for each analyte obtained by µXRF and LA-ICP-MS. Overall, lower coefficients were obtained for 15 µm compared to 41 µm sample. In case of Ca and P, the methods show excellent agreement with high correlation coefficients for both samples. Also for S and Zn strong correlations can be observed, especially in 41 µm slice. The only analyte showing poor correlation is K. The reason for that is imperfect µXRF spectra fitting, leading to false-positive K distribution in calcified zone (see above), ultimately resulting in mismatched elemental map and, consequently, poor correlation. With the exception of K, the correlation analysis confirms that the µXRF and LA-ICP-MS images are in good agreement.

Table 7. Pearson correlation coefficients for analytes mapped with both techniques

Element	**µXRF vs. LA-ICP-MS**	
	15 µm	***41 µm***
Ca	0.860	0.891
P	0.866	0.896
S	0.698	0.840
Zn	0.427	0.740
K*	–	−0.076

* *since K was not detected by µXRF in 15 µm slice, no value is given for this sample.*

Supporting SEM-EDX measurements of the instruments and materials used in sample preparation

The SEM-EDX measurements of the instruments and materials which were used in sample preparation of the thin cuts described in this section were kindly performed by Dr. Stéphane Blouin (Ludwig Boltzmann institute of Osteology).

Three kinds of samples were investigated: hard tissue microtome knife, polishing ring and grinding paper.

Figures 57-64 show the overview of the hard tissue microtome knife as well as sites on which the analysis was undertaken. EDX settings (Zeiss Supra 40 field emission SEM with X-Max detector and INCA software) were as follows:

- voltage of 10 kV
- specimen current of 1.38 nA
- aperture size of 60 µm
- acquisition time of 240 s
- 0–10 keV spectrum range with 2000 channels
- process time of 4.

The detection limit of the instrument is about 0.05 %.

The results for all the analysed sites of the hard tissue microtome knife are summarized in Table 8:

Table 8. Hard tissue microtome knife, EDX analysis results (atomic %)

Site / Element	C	O	P	Co	W
Site A	37.28	8.62	–	–	54.1
Site B	19.69	42.99	1.47	15.04	20.81
Site C	26.9	30.47	–	10.19	32.43
Non polished part	17.38	47.61	1.31	17.93	15.77

High concentrations of Co and W can be observed in sites B, C, and non-polished part of the blade. The only site where no Co was detected, is site A. This might be due to carbon-coating, or a layer of tungsten carbide, as higher content of both elements was detected in site A compared to other sites.

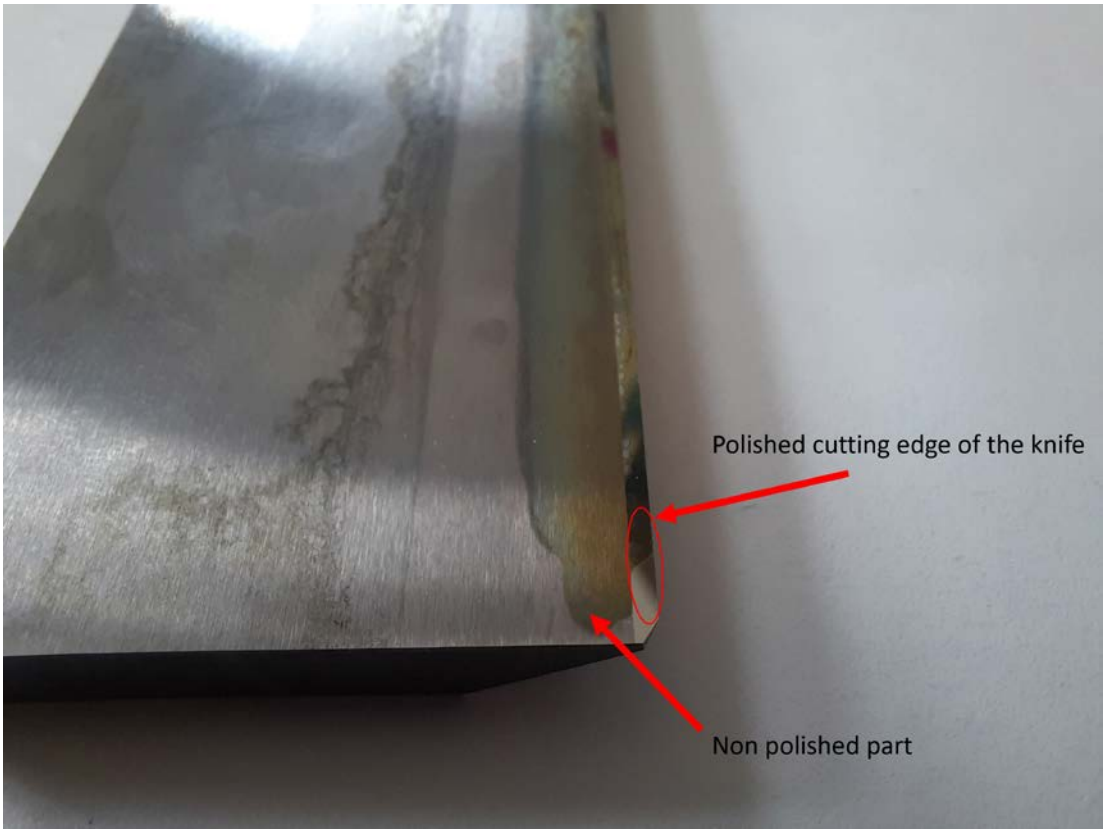

Figure 57. Hard tissue microtome knife, sites where the analysis was performed are indicated (courtesy of S. Blouin)

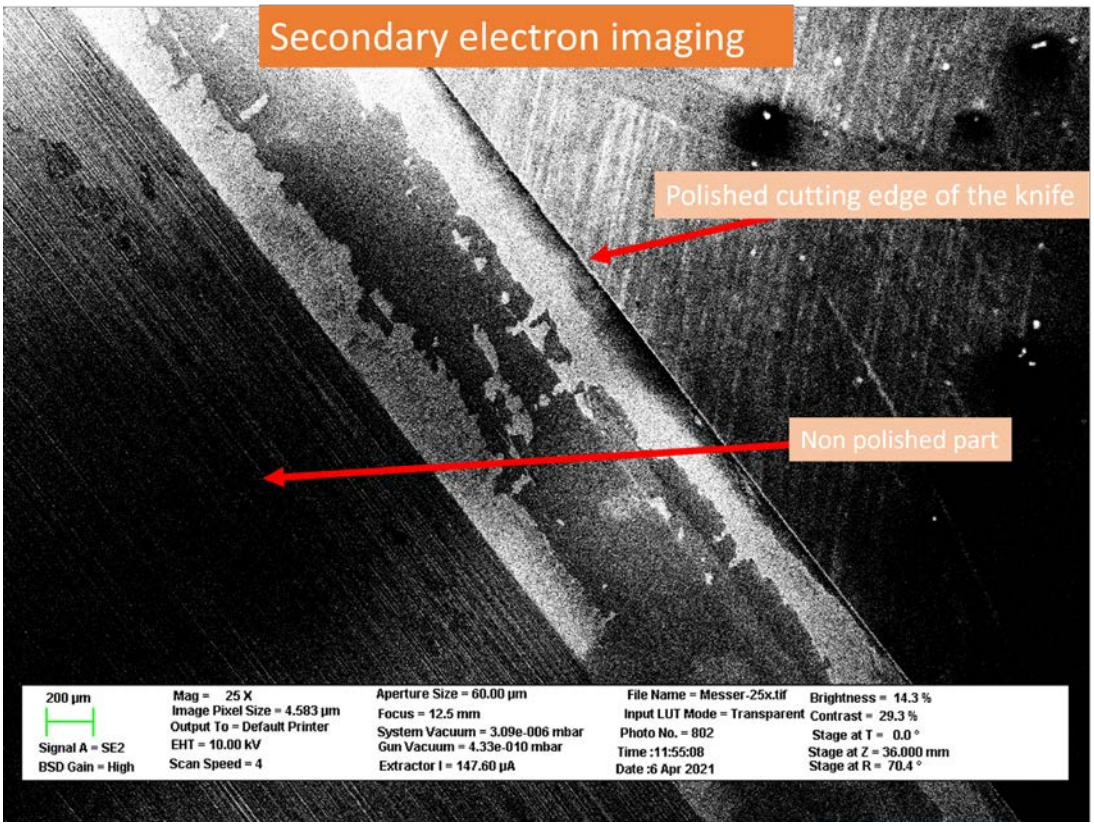

Figure 58. SEM image of the hard tissue microtome knife, including the analysed areas (courtesy of S. Blouin)

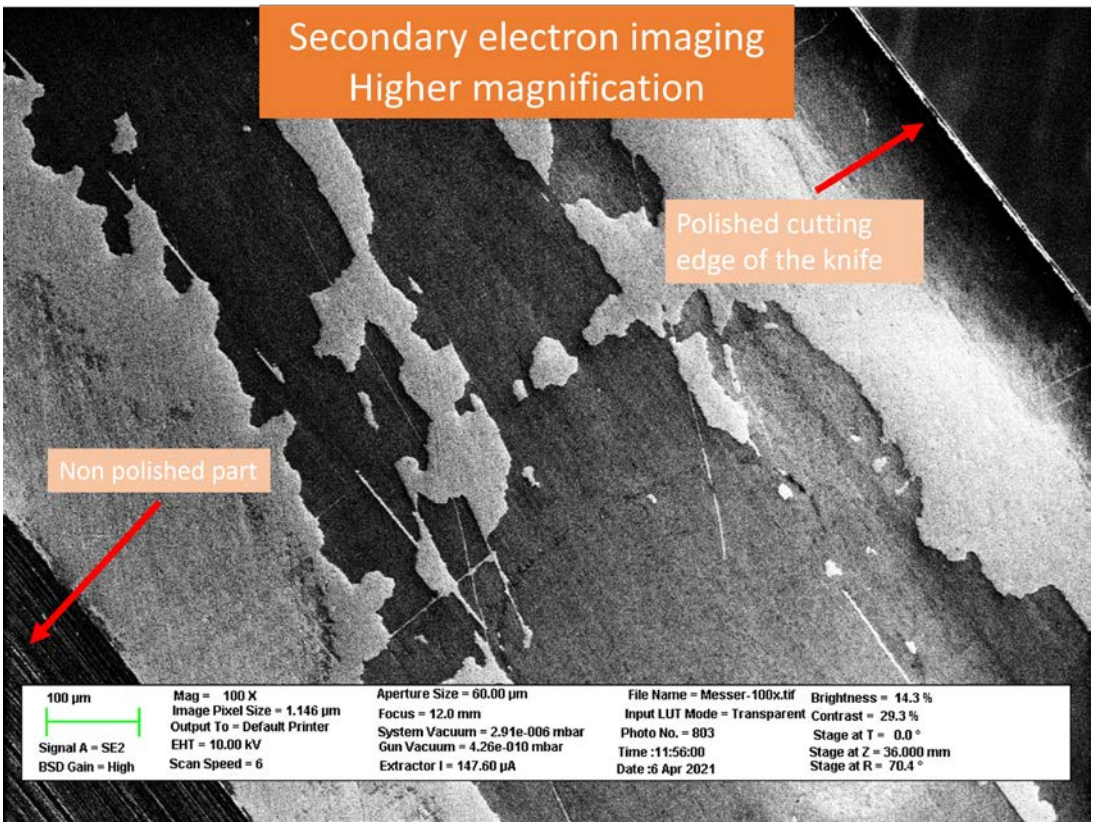

Figure 59. SEM image of the hard tissue microtome knife, areas where the analysis was performed are indicated – higher magnification (courtesy of S. Blouin)

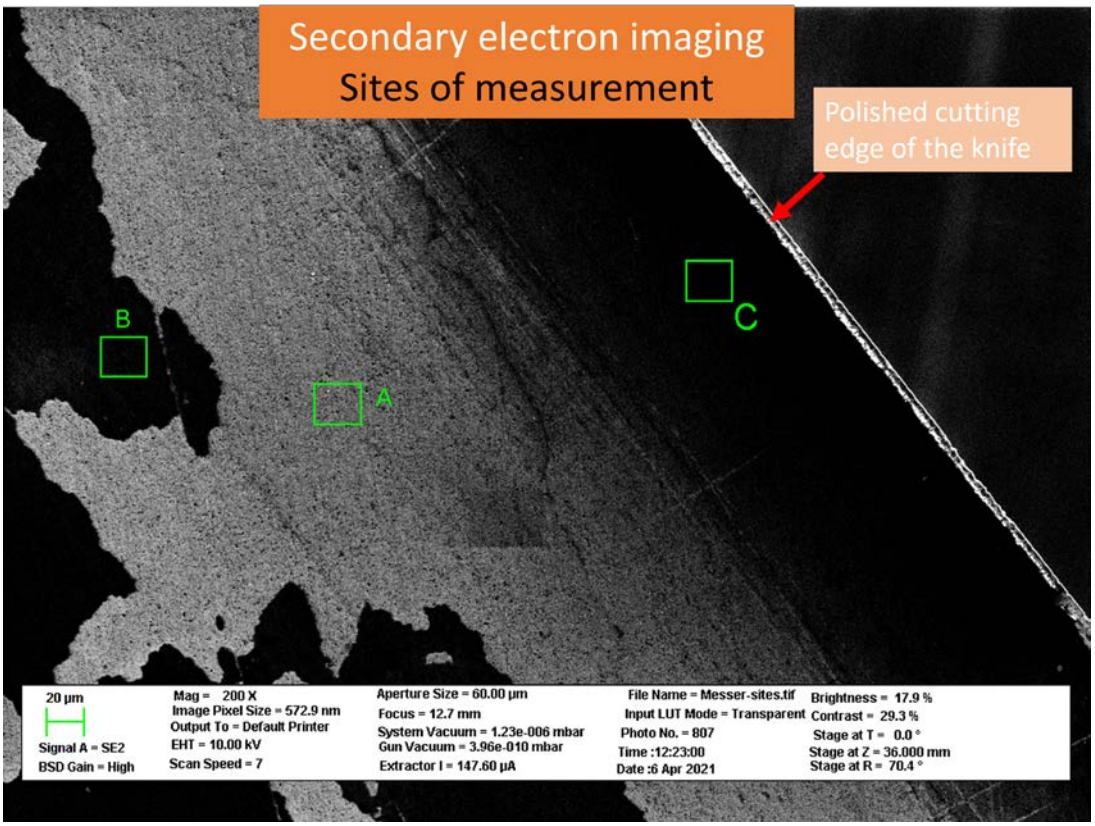

Figure 60. SEM image of the hard tissue microtome knife, polished edge with three analysed sites A, B and C marked (courtesy of S. Blouin)

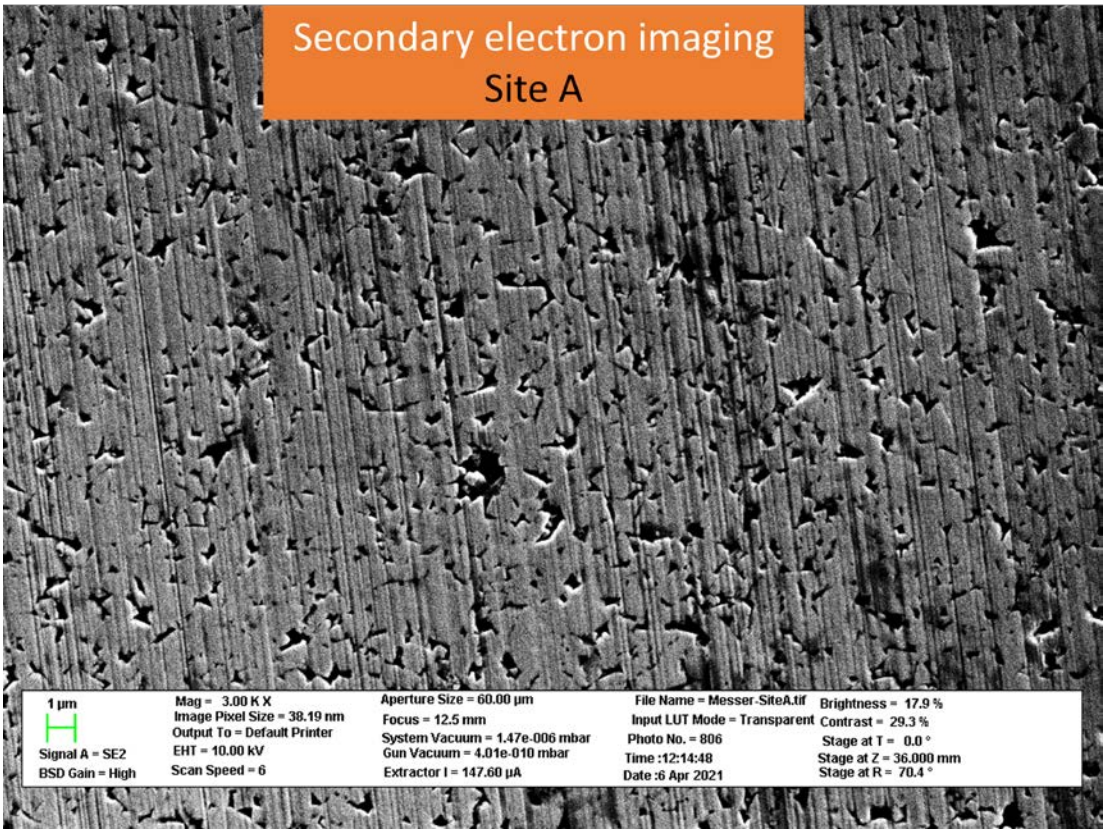

Figure 61. SEM image of the hard tissue microtome knife, site A (courtesy of S. Blouin)

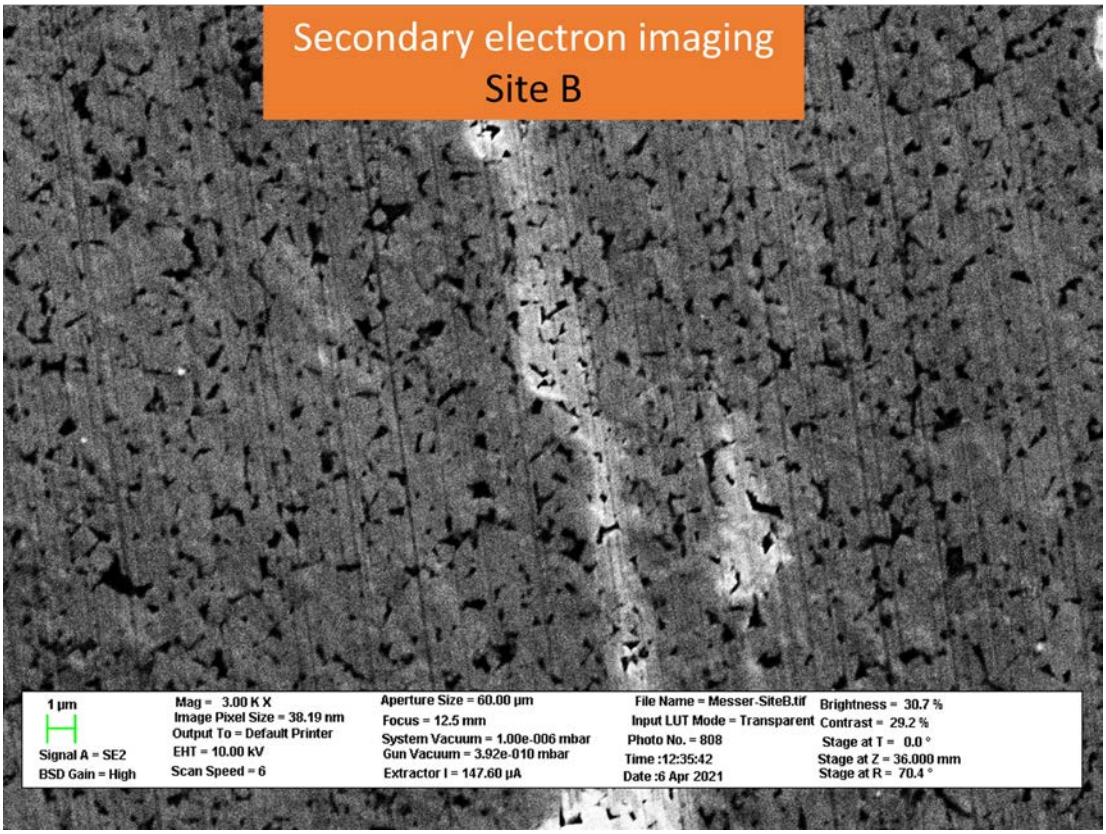

Figure 62. SEM image of the hard tissue microtome knife, site B (courtesy of S. Blouin)

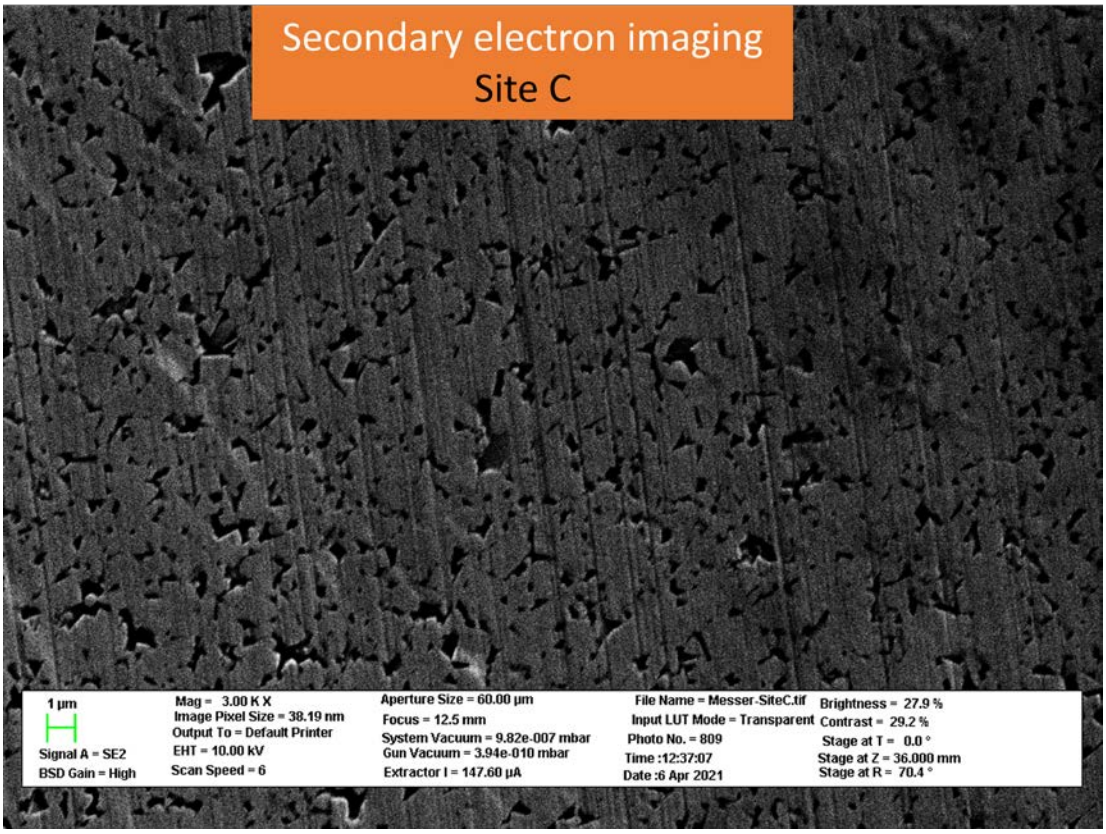

Figure 63. SEM image of the hard tissue microtome knife, site C (courtesy of S. Blouin)

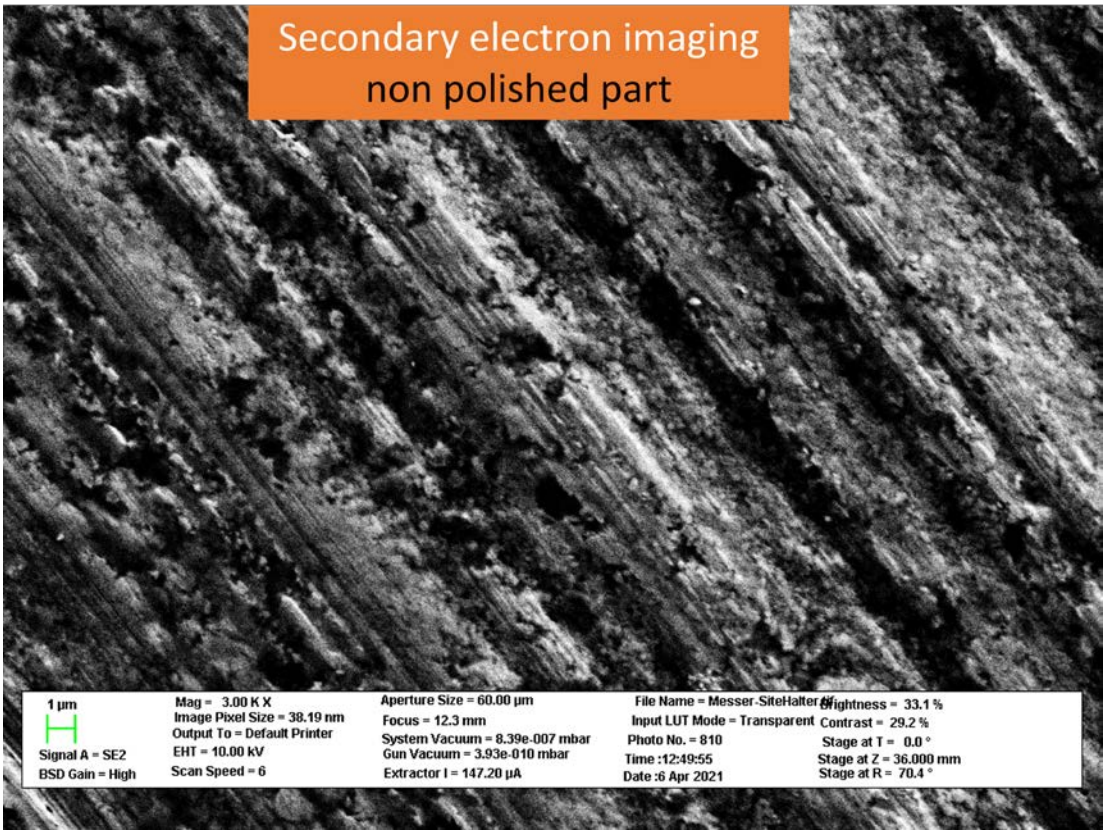

Figure 64. SEM image of the hard tissue microtome knife, non-polished part (courtesy of S. Blouin)

The results of polishing ring measurements together with some measurement parameters are presented in Table 9.

Table 9. Polishing ring, EDX analysis results (atomic %)

Site / Element	C	O	Si	Cr	Mn	Fe	Time, s	Voltage, kV	Process time
1	5.83		0.88	14.78		78.51	60	10	5
2	5.96		0.87	15.89	–1.3	78.58	60	10	5
3	8.43		1.03	13.41	0.77	76.37	60	20	4
4	8.44		1.11	12.55	0.9	77	60	20	4
5	8.6	2.67	1.14	12.24	0.76	74.6	60	20	6
6	5.4		0.85	13.71		80.04	240	10	6

Finally, the analysis of grinding paper was performed. The sample consists of silicon carbide and was additionally carbon-coated for the analysis. Following results were obtained (in atom %): O 18.35%, Si 12.06% and C 69.59%. No metal traces were detected.

Unfortunately, within our project we are unable to identify the nature of Co in the sample and prove or disprove whether the blade of the microtome knife could be the source of this element. However, such an investigation could be very valuable for any future measurements and must be highly encouraged.

Conclusions and outlook

In this proof-of-concept project we investigated a complex biological sample – cuts of human femoral head – with two imaging techniques, LA-ICP-MS and µXRF. The measurements were successfully performed on the very same tissue cuts, first by µXRF and followed by LA-ICP-MS, also allowing comparison of the techniques and correlation of the results.

Distribution information in form of elemental maps was provided for following elements: Ca, P, S, Zn, K (with µXRF only in one sample). LA-ICP-MS also supplemented elemental maps of "light metals" – Na and Mg.

We tested quantitative approaches which allowed – for the first time – characterization of various tissues within femoral head, i.e. hard calcified tissues (bone, mineralized cartilage) and soft tissue (hyaline cartilage). The quantification was provided by both imaging techniques, and the obtained values are in the same order of magnitude. For Ca, P and especially Zn more detailed maps were obtained with LA-ICP-MS (due to higher depth and lateral resolution). S distribution was more detailed with µXRF (polyatomic interferences and a relatively high S-background interfere with LA-ICP-MS measurements). We further analysed the elemental distributions mapped by both µXRF and LA-ICP-MS, and the obtained correlation coefficients indicate mostly good agreement between the methods.

Generally, thin cuts can be recommended for such investigations. In our project, the PMMA-embedded thin slices could be directly measured with both techniques. While LA-ICP-MS results are not affected by the sample thickness, it is important to remember that information depths in µXRF is element-dependent, and this can be illustrated by µXRF Zn maps for 15 and 41 µm slices.

In future experiments, the use of more powerful X-ray sources, such as liquid metal jet tube or synchrotron, could improve detection of Zn, and help obtaining elemental maps of other trace elements. This refers, e.g. to Sr and Pb, which within our experiments could be seen in the XRF sum spectra, but could not be mapped. Further, confocal XRF setups can be employed to address the information depth issue. Finally, synchrotron experiments with focused down to sub-µm X-ray beams could be performed, which will allow high-resolution XRF imaging.

The development of the wider array of commercially available certified matrix-matching standards is invaluable for elemental imaging. Alternatively, finding a way for utilizing internal standardization to compensate differences in material ablation and instrumental drifts could potentially further improve the accuracy of the LA-ICP-MS analysis and would be similarly helpful for µXRF.

The potential influence of the preparation on a sample (e.g. introduction of unwanted elements, which are otherwise not present in the sample; washing out/smearing of the elements or, vice versa, creation of artificial ‘hotspots’ and accumulations) as well as the lack thereof, deserves a separate carefully planned and thorough analysis and must be encouraged and supported by scientific community, and, importantly, published (ideally in open access).

3.3 µXRF + ToF-SIMS: Test on human bone sample

The project was performed in collaboration with Institute of Chemical Technology and Analytics (CTA) TU Wien. ToF-SIMS measurements were performed by Florian Brenner.

Another mass spectrometry method for elemental analysis of solid samples is Secondary Ion Mass Spectrometry (SIMS). Time-of-flight variant of SIMS technique (ToF-SIMS) is a surface-sensitive analytical method, in which an energetic primary ion beam is used to bombard a sample surface. This leads to formation of various sputtered particles, including secondary ions (negatively and positively charged) – those are extracted and analysed in time-of-flight mass spectrometer.

Semiconductor industry and material science are the most common areas in which ToF-SIMS is widely used. Although ToF-SIMS might not be as popular as LA-ICP-MS and XRF in biomedical imaging, it has a unique potential in this application. The method allows detection and imaging of elemental distribution as well as of organic compounds. Within the laboratory-based elemental imaging techniques, ToF-SIMS boasts unbeatable lateral resolution – beyond 100 nm (the best lateral resolution of impressive ~20 nm was obtained using Bi_3^{2+} clusters (58)) and depth resolution in the nanometre range.

The quantification in SIMS, however, is not straightforward – mostly due to matrix effects, and similar to LA-ICP-MS matrix-matched standards are required.

When it comes to sample preparation, a few aspects requested by SIMS are rather common for µXRF/SR-XRF as well. The size of the sample should be amenable to that of an instrument chamber/sample holder – for SIMS an optimal sample is of size and geometry as of a small coin (59). In µXRF and especially in SR-µ/subµ-XRF, the sample size requirements are less strict, nonetheless, it is convenient to work with small samples when areas from tens/hundreds of µm to few mm are scanned. Further, sample surface should be flat and smooth – here again, SIMS and µXRF (especially in confocal arrangement) are in agreement. Clean surface, e.g. absence of contaminations is desirable for both techniques, and although SIMS is much more sensitive to surface contaminations (e.g. salts, oxides, organic residues will affect SIMS analysis, but not XRF), those can be removed by sputter cleaning.

There are further requirements to the sample which should be considered in sample preparation for SIMS, but not XRF:

- compatibility with high/ultra-high vacuum, i.e. 10^{-8}-10^{-9} mbar
- conductive surface

The examples on combination of µXRF and ToF-SIMS within one sample can be found in the literature (60). Laboratory µXRF can be used for non-destructive elemental screening and imaging in low resolution to identify regions of interest, which can be subsequently imaged in high-resolution with ToF-SIMS – such combination was realized for detection of CeO_2 nanoparticles in lung tissue (61). ToF-SIMS and µXRF can be used to obtain information on “molecular context” and elemental distribution, respectively – as it was done in the project on identification of ritual blood in African artifacts (62).

In our measurements, we have tested whether SR-µXRF and ToF-SIMS can be applied to the same human bone sample.

Experimental

The sample used for the experiments was an iliac crest biopsy from a healthy male patient. The sample was prepared as thick PMMA block, the information on sample preparation and qBEI procedure can be found elsewhere (63,64).

The confocal µXRF measurements were performed at ANKA synchrotron (FLUO beamline).

ToF-SIMS imaging analysis was performed using a ToF.SIMS5 (IONTOF GmbH, Münster, Germany) equipped with a 25 keV bismuth liquid metal ion gun (LMIG). The instrument was operated in High Current Bunched (HCBU) mode with lower spatial resolution and higher mass resolution (around 8000-10000 at FWHM); Bi^{3+} cluster primary ions (target current = 0.5 - 0.6 pA, pulsed) were used. Before the analysis, sample was covered with a thin Au-Pd layer to minimize charging artifacts. The field of view was 300 × 300 µm² (resolution: 512 × 512 pixels), further details on experimental setup can be found in dissertation of MEIBio colleague F. Brenner (65).

Results and discussion

The corresponding bone sample was studied within "Mn in osteoporosis" project (see chapter 5) and the SR-µXRF maps are shown in Fig. 65.

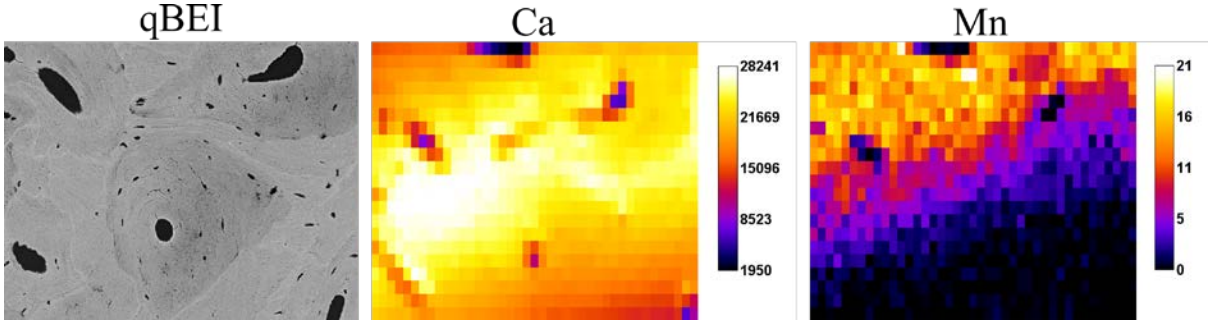

Figure 65. SR-µXRF Ca and Mn elemental maps and the qBEI of the corresponding area. Elemental maps are in cps and normalized to 100 mA ring current. The area of 41 × 21 pixels corresponds to 600 × 500 µm

ToF-SIMS measurements were performed after the synchrotron experiments – and on the different area than the one mapped by SR-µXRF. The ToF-SIMS images are shown in Figure 66. Since the resolution of ToF-SIMS exceeds the resolution of the employed SR-µXRF setup, we expected to obtain more detailed maps. The most interesting ToF-SIMS results we received for Ca^+, PO^+ and Mg^+ – which can be naturally found in bone tissue. Speckles on Si^+ and Al^+ maps point at contamination; and since the block was carbon-coated for qBEI analysis (qBEI was performed prior to SR-µXRF measurements) C^+ distribution most likely originates from this coating. Upon rechecking, it was found that $FeSO^+$ map has to be reinterpreted as SrO^+ (the ions have similar mass). Since Sr is an intrinsic component of bone with Ca-like chemical properties, it is more likely to be found in mineralized tissue. Further, Ba^+ interferes with some fragments containing Ca – and this map might have been misassigned as well.

In this respect, pre-analysis with µXRF or SR-XRF allowing collecting information on elemental composition of the sample and thus helping in interpretation of ToF-SIMS results, is beneficial. This approach, however, was not fully realized in our test measurements, since in SR-µXRF analysis we focused on specific elements (Ca and Mn).

However, the main problem during the ToF-SIMS measurements were the charging effects. This issue can be resolved by optimizing sample preparation – using thin sections instead of thick PMMA blocks. Indeed, according to the literature reports, successful bone measurements with ToF-SIMS can be performed on thin bone cuts – e.g. 30 µm (66) and 4µm (67).

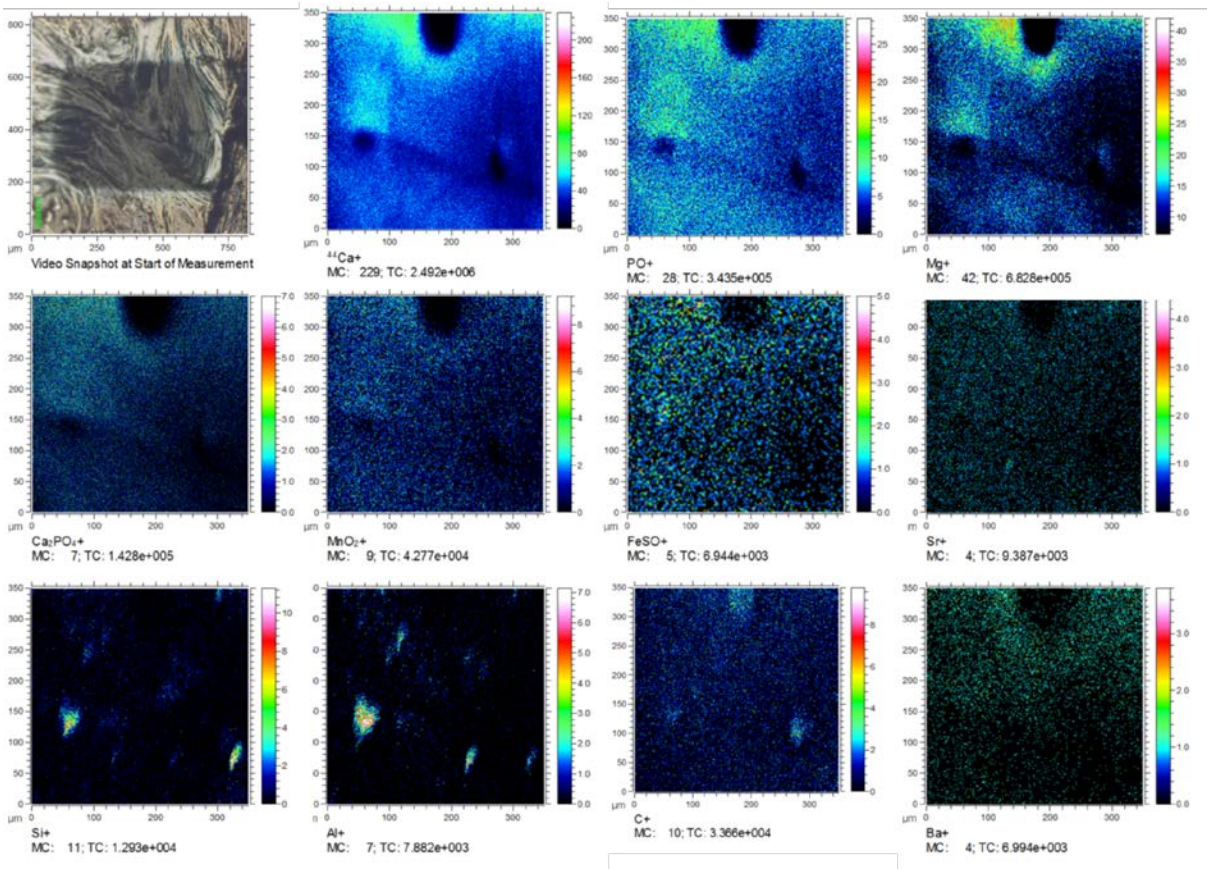

Figure 66. ToF-SIMS measurement area 512 × 512 pixels on 300 × 300 µm² region of interest (400 scans). Intensity units – in counts; MC = maximal counts for a pixel (corresponds to a brightest spot in the image), TC = total counts of a certain secondary ion, summed up. For potentially misinterpreted $FeSO^+$ and Ba^+ maps please refer to the explanation in the text

Conclusions and outlook

1. Applicability of SR-µXRF and ToF-SIMS for the elemental imaging on thick PMMA-embedded bone block was tested;
2. Combination of µXRF (as pre-analysis) and ToF-SIMS within one sample can supply researcher with all-round information on elemental composition, or even molecular information (if the sample preparation strategy allows preserving organic matter);
3. Further, pre-analysis by µXRF can help identifying and obtaining rough scans (in lower resolution) of regions of interest – which are to be then imaged in high resolution with ToF-SIMS;
4. Since in our experiments covering the sample with Au-Pd layer did not help avoiding problems with charge compensation, thin cuts (below 100 µm) would be recommended for future measurements instead of PMMA blocks;
5. Generally – as in all combined imaging experiments – sample preparation strategy has to be carefully considered and well-thought-out;
6. High-resolution imaging can be considered for specific research objectives (e.g. resolving thin structures in bone tissue). Recent developments in SR-µXRF and nanoSIMS made possible breath-taking imaging experiments on subcellular level (60).

4. Mg bioresorbable implants

Parts of this chapter were previously published in Materials (68).

Bioresorbable materials offer a complete rethink of the implant concept and hold great promise in orthopaedic surgery. The rationale for using bioresorbable materials stems from their ability to serve as a load-bearing support for the healing bone, enabling newly-formed healthy tissue to steadily replace the implant and, if possible, even promote tissue formation. Thus, follow-up surgery in order to remove the implant after the tissue has healed is avoided, as well as the risk of problems posed by permanent implants, such as long-term endothelial dysfunction, physical irritation, or chronic inflammatory local reactions (69).

Before the material can be introduced into practice or tested in humans, thorough studies of the processes of implant degradation and the mechanisms of migration/incorporation of the implant constituents into bone tissue must be performed in animal models – in our study rat model was used.

The study was undertaken at Atominstitut in collaboration with Institute of Physics and Materials Science, BOKU; Laboratory of Metal Physics and Technology, ETH Zurich; and Department of Orthopaedics and Orthopaedic Surgery, Medical University Graz. We investigated by means of μXRF analysis the distribution of the elemental constituents of Mg-based implants at various stages of the degradation process in surrounding bone tissue, with a focus on magnesium (Mg), as the main component of the alloy, and yttrium (Y), due to its potential adverse health effects. The measurements were performed on the implant-bearing thin sections of rat bone in a time series of implant degradation between one and 18 months.

Experimental

Implant material

The implant material used for this study was a crystalline magnesium rare-earth-containing WZ21 alloy (detailed description of the alloy can be found elsewhere (70)) with a composition of 2 wt % Y, 1 wt % Zn, 0.25 wt % Ca, 0.15 wt % Mn, and 96.4 wt % Mg. The grain size was determined to be 7 μm. Further information can be found in the literature (71,72). The implant material was manufactured to pins of 1.6 mm in diameter and 7 mm in length.

Rat bone samples

The samples for this investigation (one per dwelling time) were obtained from male Sprague Dawley rat femurs that had been implanted with WZ21 pins at the age of five weeks and were monitored by micro-computed tomography and histological investigations during the course of healing (70). The interfacial mechanical properties of this kind of alloys, as well as details regarding the design of the experiment, can be found in (72,73). The experiments were authorized by the Austrian Ministry of Research and Science (Vienna, Austria) under accreditation number BMWF-66.010/0087-II/3b/2011. In this study, six samples with implant dwelling times of 1, 3, 6, 9, 12, and 18 months were used as longitudinal sections embedded in PMMA resin (Technovit 7100, Heraeus Kulzer, Werheim, Germany). The sections were ground to a thickness of approx. 200 μm using a Struers Planopol-3 (Struers, Ballerup, Denmark) polishing machine with #200 sanding paper. After extensive rinsing with distilled water, the samples were dried and stored under vacuum.

Microscopic images were obtained using a Wild M8 (Wild Heerbrugg, Heerbrugg, Switzerland) stereo microscope with a “PixeLink PL-B686CF” (Ottawa, ON, Canada) camera system to obtain images with 6× and 25× magnification.

Laboratory μXRF analysis at Atominstitut

The μXRF setup at Atominstitut (ATI) was designed in-house and is suited for the detection of a wide range of elements, which was essential for this experiment, as both elements of low atomic number (Mg) and medium atomic number (Y) elements were of interest. The detailed description of the setup can be found in previous publications of the group (20,21). Excellent excitation conditions for the measurements of light and heavy elements are provided by a Rh-anode low power tube (20 W). The Rh tube emits Rh-K line (20.3 keV) radiation which excites Y, but it also emits Rh-L line (2.7 keV) radiation, which excites Mg (Kα = 1.25 keV) excellently. As the setup is in vacuum, the low-energy radiation is not absorbed by air. The following tube settings were employed in the experiment: the voltage was 50.0 kV, and the current was 0.4 mA. The system features a 30 mm^2 Si(Li) detector with an ultrathin polymer window (UTW), and is LN_2-cooled. The UTW allows the efficient measurement of the low energy fluorescence radiation from Mg. Excitation and detection conditions, together with the operation under vacuum, facilitates analysis of low atomic number elements, e.g., magnesium. A polycapillary optic (full lens) was used to focus the primary beam on the sample surface; the beam size determined for Cu-Kα was 50 μm × 50 μm.

The measurement conditions were the same for all of the scans. The scan area was defined by determining four corner points in XY coordinates (controlled by a built-in optical microscope with a charge-coupled device camera), the step size was set to 50 μm. The measurement time was 200 s per point.

The data analysis was performed using the QXAS-AXIL software package (27). The elements of interest were included in the fitting model: Mg, P, S, Ca, Mn, Zn, and Y. The elemental maps were created with X-Ray Lab software (X-Ray Lab, Atominstitut, Vienna, Austria). The line scans represent the plotted central line (lengthwise) throughout the scan (data normalized to the maximum value) allowing for easier comprehension of the changes in distributions of elements (prepared using Microsoft Excel 2016). The fluorescence spectrum was plotted using Origin (version 8.6, OriginLab Corporation, Northampton, Massachusetts, USA).

Results and discussion

The following elements were identified as implant constituents: magnesium (Mg), calcium (Ca), manganese (Mn), zinc (Zn), and yttrium (Y). The mineralized areas of the bone can be distinguished by the high content of calcium (Ca) and phosphorus (P), which are two of the main constituents of hydroxyapatite (HA, $Ca_{10}(PO4)_6(OH)_2$). Sulfur (S) is also present in the bone tissue, and less mineralized proteoglycan-containing regions of bone can, therefore, also be identified, as they are rich in sulfur. The Figure 67 demonstrates an exemplary XRF spectrum obtained at the interface implant-bone, with both components of the implant (Mg, Mn, Zn, and Y) and bone constituents (P, S, and Ca) being present.

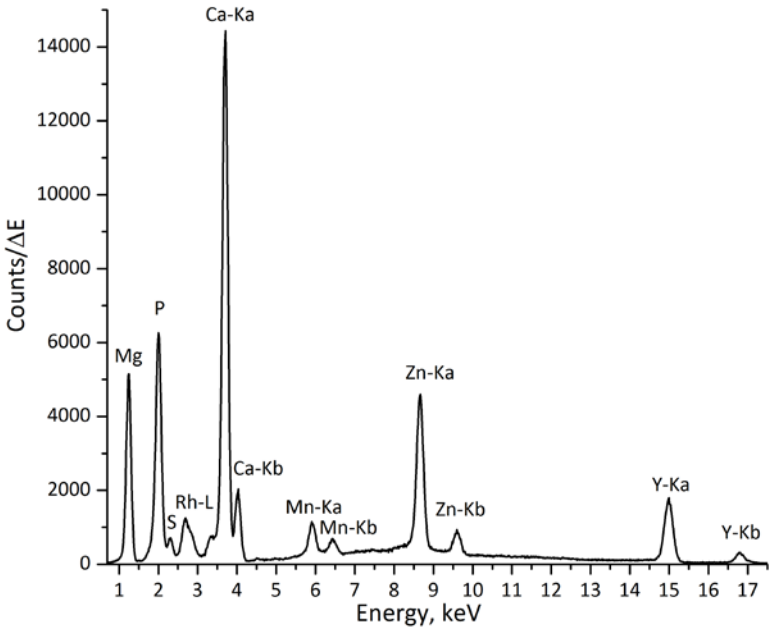

Figure 67. Exemplary spectrum from implant-bone interface (excitation with a Rh-anode X-ray tube), measuring time: 200 s

The implant-bearing thin (about 200 µm) sections of rat bone tissue were scanned in raster mode (x-y coordinates). The area of interest in each sample was chosen individually, depending on the morphology of the bone and the state of the implanted material. In the sections, where large parts of the pin remained (one-, three-, and 12-months dwelling time), scans were performed transverse to the pin. For the samples, where the greatest part of the pin degraded (six-, nine-, and 18-months dwelling time), the measurements were performed on the former position of the pin, where it had already been replaced by newly-formed bone tissue.

The elemental maps were produced for Mg, Mn, Y, P, S, and Ca, based on the data obtained. The maps display the distributions of these elements according to their intensities in the scanned area. Figure 68(a) shows the elemental maps obtained for the one-month-old sample. The area selected for the scan (Fig. 68(b)) starts at the implant and covers a substantial part of the adjacent bone, allowing the observation of the change in the distribution of the elements of interest in the implant- and bone-containing parts of the scan. For easier comprehension of Mg, Y, and Ca variations a single central longitudinal line from the corresponding elemental maps was selected, the values were normalized to the maximum and the line was plotted (Fig. 68(c)). It can, therefore, be seen for the one-month-old sample, that a sharp decrease in Mg, contrasting with a simultaneous elevation of Ca, indicates the implant-bone interface. As expected, Mg and Y were roughly co-localized, but in the case of Y a less abrupt decrease from the implant towards the proximal bone tissue can be observed. Additionally, a horizontal scan was performed, Figure 69.

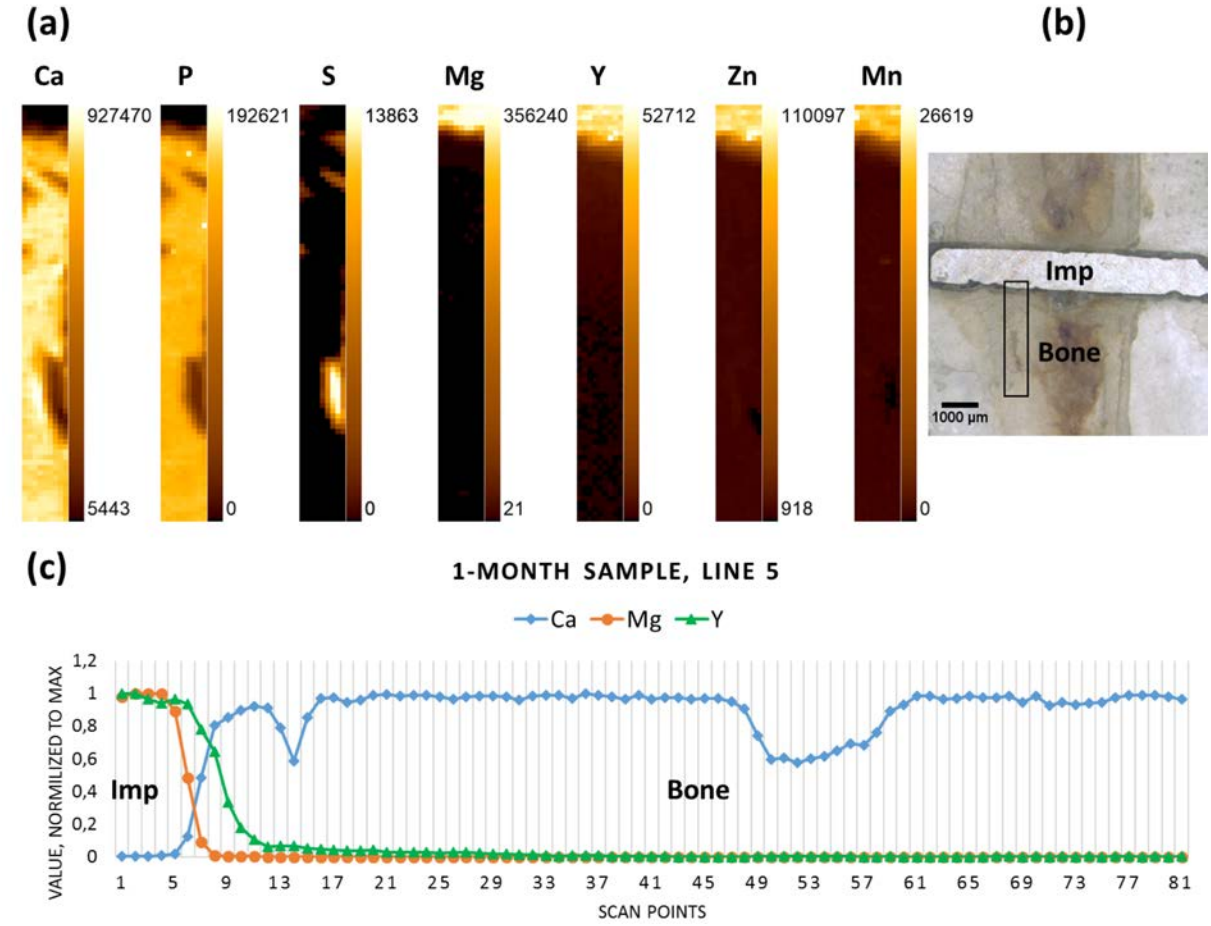

Figure 68. One-month sample (a) elemental maps, 9 × 81 pixels—corresponding to 0.4 mm × 4 mm; (b) micrograph, the black rectangle outlines the area where the scanning was done; and (c) line scan (line 5); "Imp" denotes the position of the implant, "Bone" denotes the adjacent bone tissue

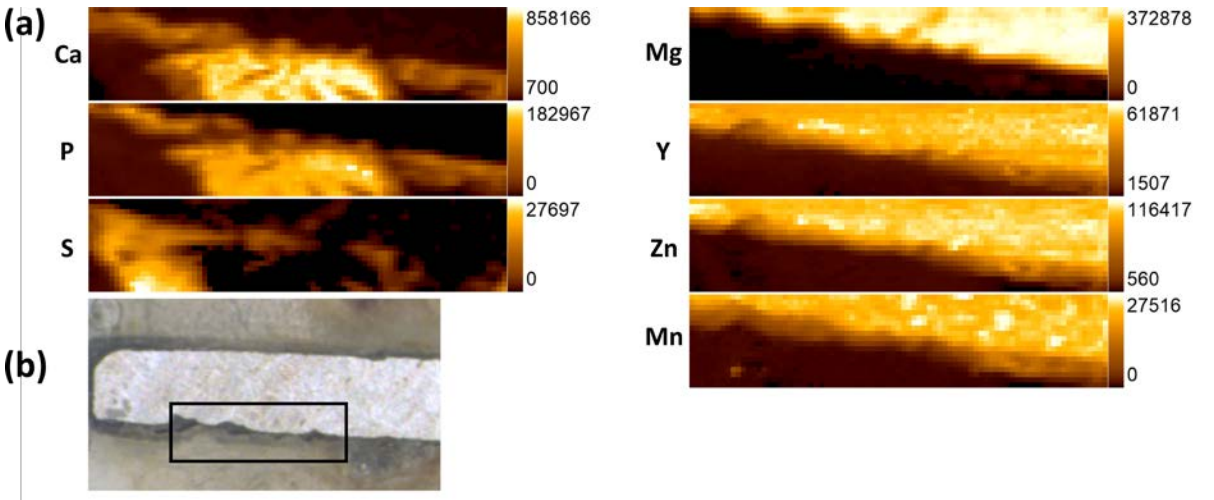

Figure 69. One-month sample scanned horizontally: (a) elemental maps, 81 × 18 pixels—corresponding to 4 mm × 0.85 mm and (b) micrograph with an approximate position of the scan area

The three-months-old sample, where degradation had already progressed, yet a large part of the pin remained in the tissue, exhibits similar behaviour for the elements in question, with a drop in Mg and an increase in Ca designating the interface, while Y gradually decreases over some distance from the interface (Figures 70-71).

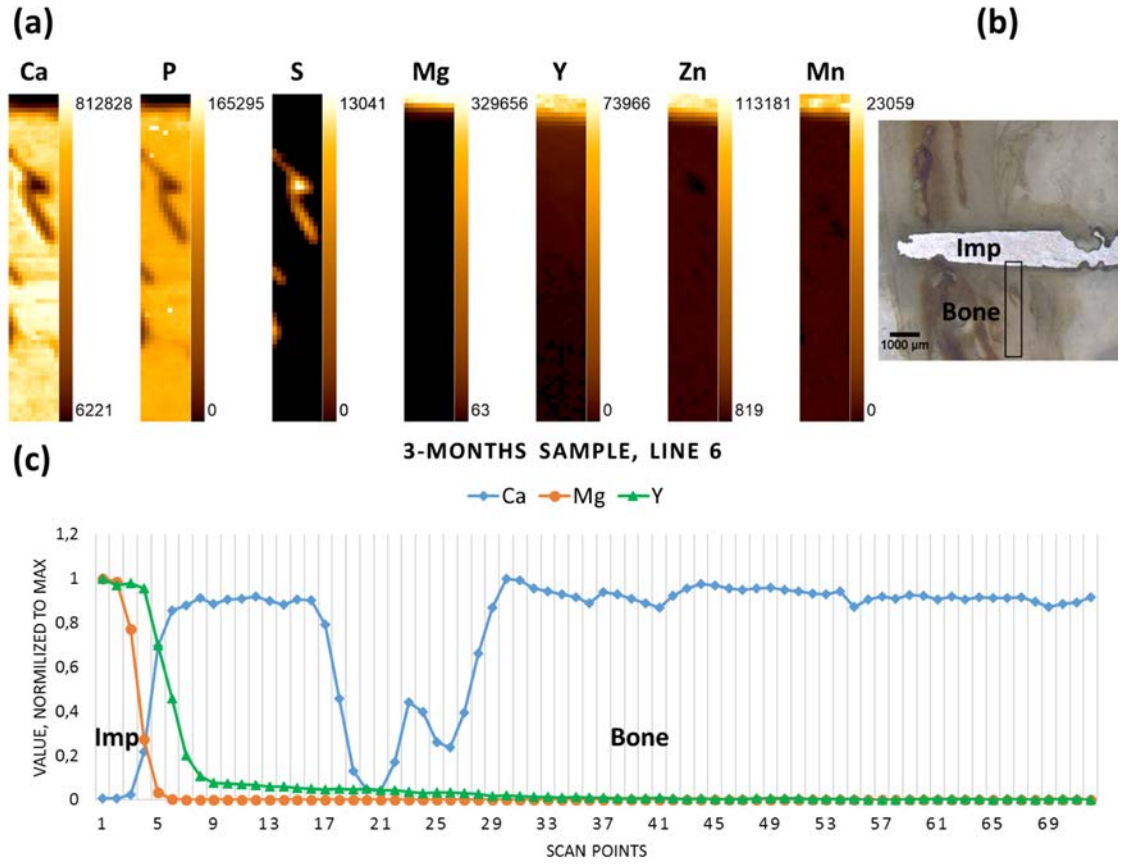

Figure 70. Three-months sample (a) elemental maps, 11 × 72 pixels—corresponding to 0.5 mm × 3.55 mm; (b) micrograph denoting the scanning area; and (c) line scan (line 6)

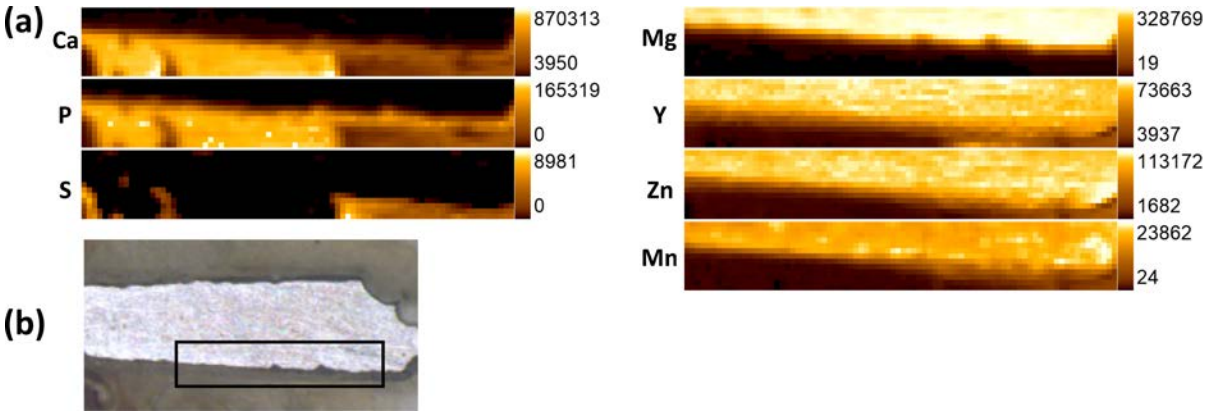

Figure 71. Three-months sample scanned horizontally: (a) elemental maps, 82 × 13 pixels—corresponding to 4.05 mm × 0.6 mm; (b) micrograph with an approximate position of the scan area

The Figure 72(b) shows the micrograph of the six-month-old sample, where only a small part of the implanted pin remained. The horizontal scan performed on the previous position of the pin (including the remaining implant chunk) reveals no specific accumulations of Mg in the newly formed bone tissue, whereas it can be seen that Y has remained on the position of the pin, even in the regions where the implant had already degraded (Figure 72(a, c)). A vertical scan is not included, as it seems to have been covering mostly PMMA.

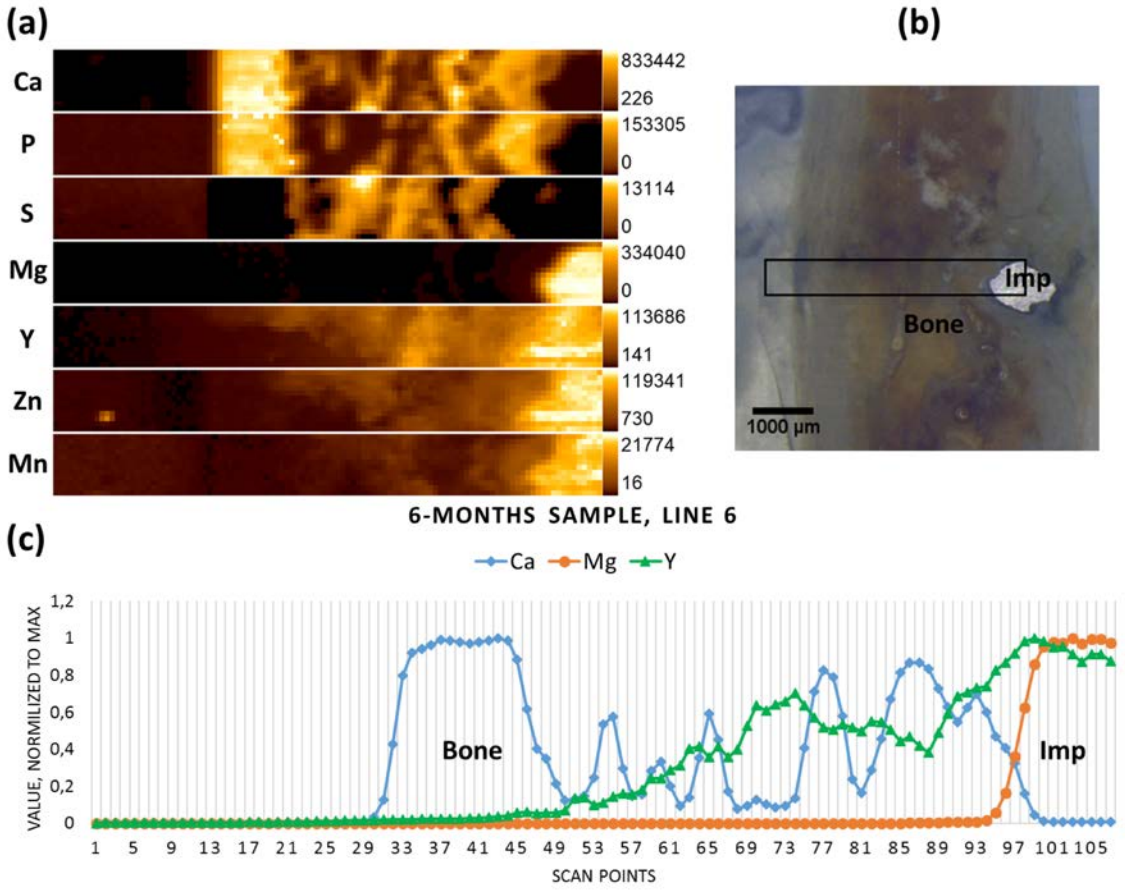

Figure 72. Six-months sample (a) elemental maps, 107 × 12 pixels—corresponding to 5.3 mm × 0.55 mm; (b) micrograph showing the scanning area; and (c) line scan (line 6)

The implanted pin in the nine-month-old sample had mostly degraded, though some metal chunks were still visible; the scanned area lies on the previous position of the implant, already replaced by newly-formed tissue (Fig. 73(b)). No metallic particles could be recognised in this selected area using the microscope, however both the elemental map and the line scan indicate the presence of the minute Mg-containing particles (hot spot on the Mg elemental map), as well as elevated Y (together with the other implant constituents—Mn and Zn) in the right-hand section of the scanned area, which represents less mineralized bone (Figures 73(a,c)). In the newly-formed mineralized bone tissue (high Ca and P, low to no S) low levels of Mg were co-localized with Ca, as usual in healthy bone. The vertical scan (Fig. 74) is also showing presence of Y, but since the interface cannot be defined, we cannot estimate Y spreading.

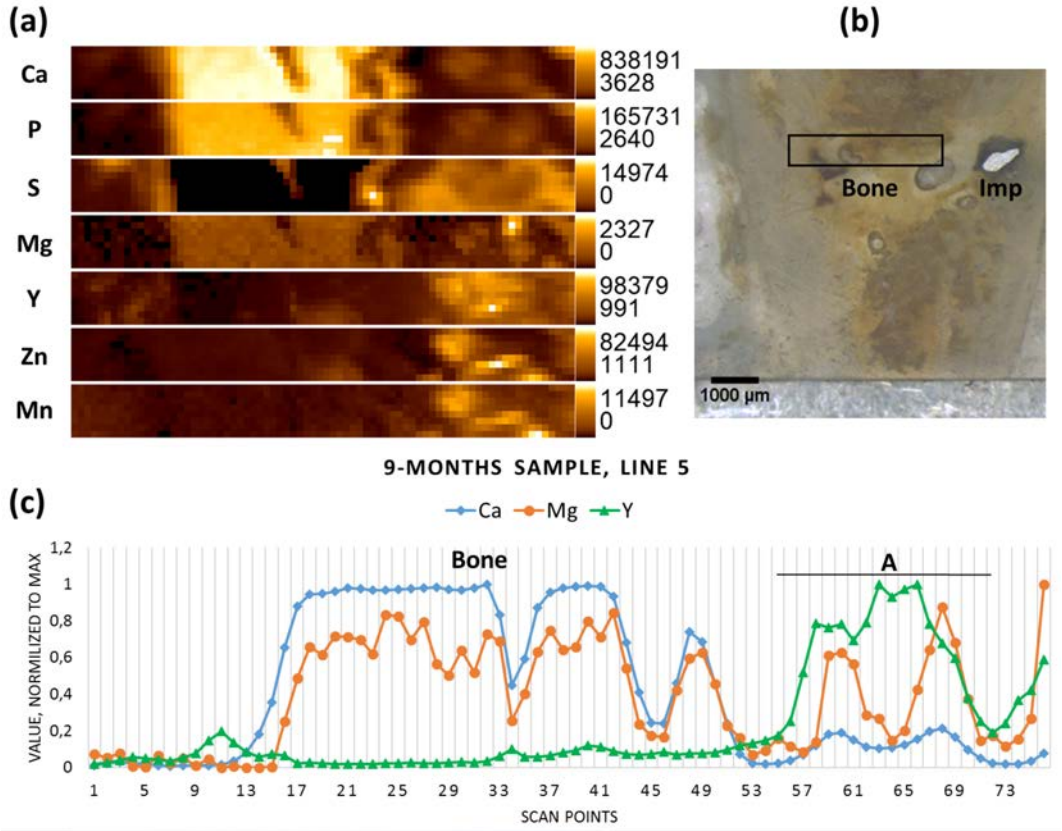

Figure 73. Nine-months sample (a) elemental maps, 76 × 8 pixels—corresponding to 3.75 mm × 0.35 mm; (b) micrograph showing the scanning area; and (c) line scan (line 5), A—accumulation of Y

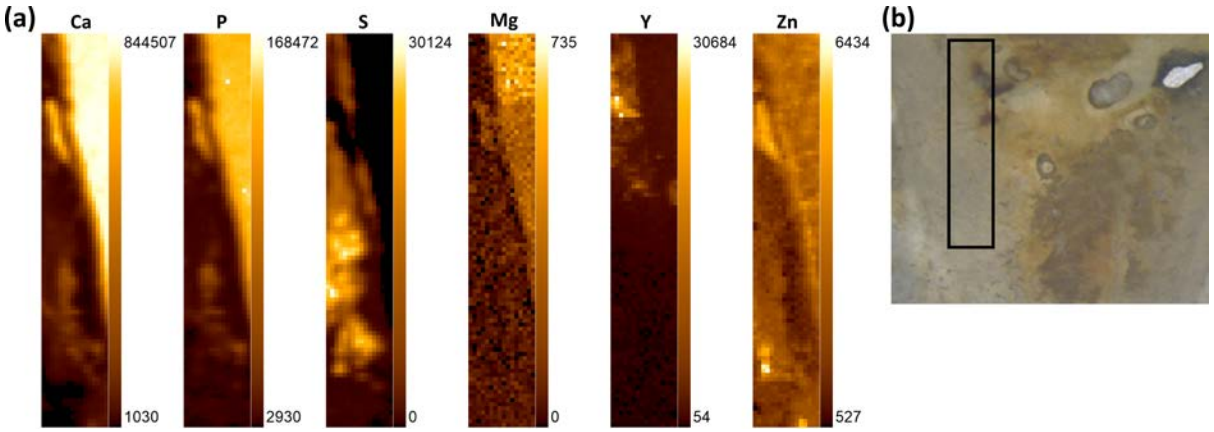

Figure 74. Nine-months sample scanned vertically: (a) elemental maps, 16 × 94 pixels—corresponding to 0.75 mm × 4.65 mm; (b) micrograph with an approximate position of the scan area

In contrast to the six- and nine-month samples, the 12-month-old sample contained rather large non-degraded metal pieces of the implant (probably due to the interindividual differences of the animals used). Therefore, the scan was performed in cortical bone transverse to the pin. The implant-bone interface can be discerned due to inverse correlation between Mg and Ca. Again, in contrast to Mg, Y does not demonstrate a sharp drop in the interface area, and is found further away from the implant, having apparently migrated into the bone tissue (Figures 75-76).

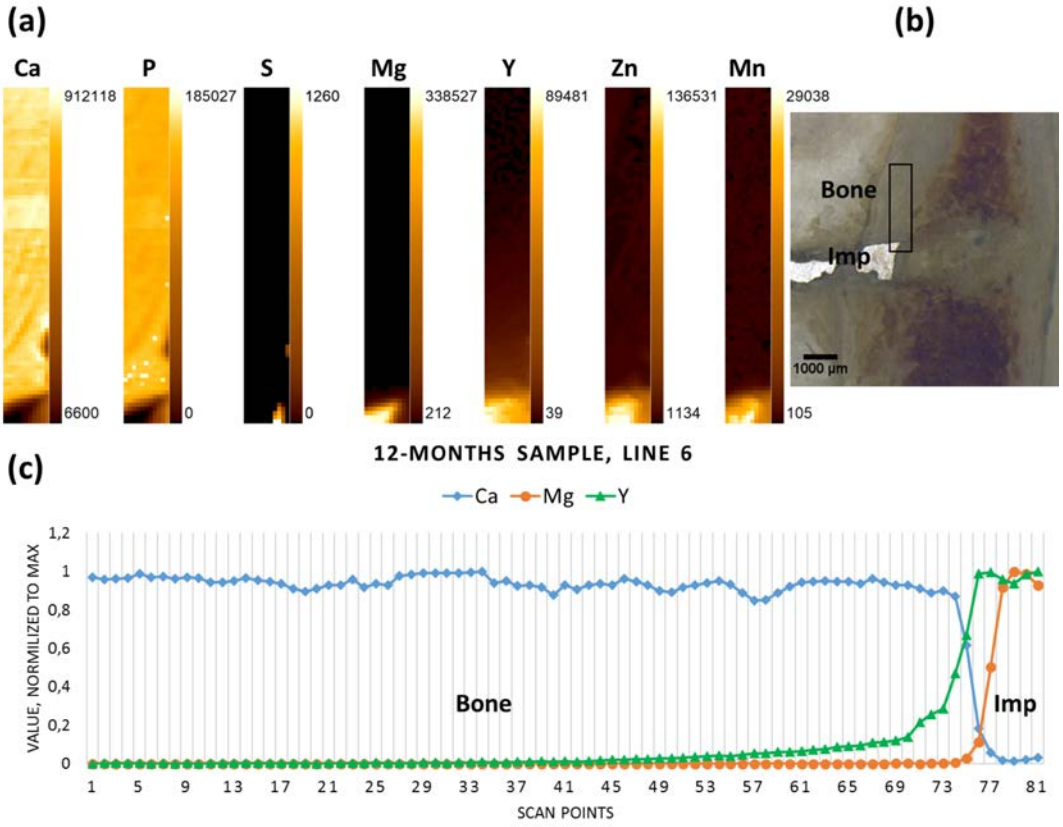

Figure 75. Twelve-months sample (a) elemental maps, 11 × 81 pixels—corresponding to 0.5 × 4 mm; (b) micrograph showing the scanning area; and (c) line scan (line 6)

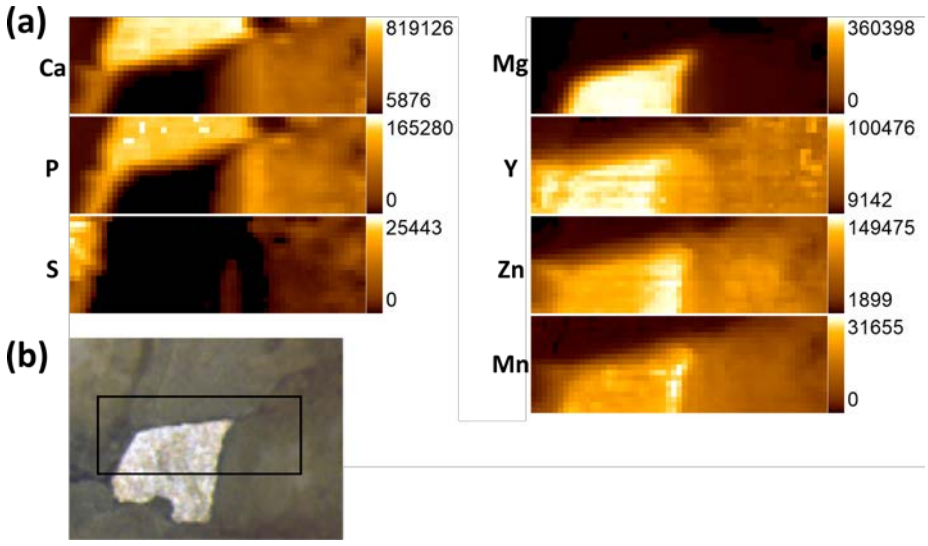

Figure 76. Twelve-months sample scanned horizontally: (a) elemental maps, 55 × 18 pixels—corresponding to 2.7 mm × 0.85 mm; (b) micrograph with an approximate position of the scan area

The degradation process in the 18-months-old sample was on the verge of completion, and no metal pieces could be observed with the microscope. The scan was performed on the previous position of the implant (Fig. 77(b)). As can be seen from the resultant elemental maps, Mg was present at low content in the calcified area of the bone, as usual in healthy bone (Fig. 77(a)). Yttrium, however, was accumulated in the non-mineralized area in the bone marrow and its content decreased towards the corticalis (Fig. 77(c)). No Mn was detected in the sample, and low levels of Zn were mainly found in calcified tissue, which might depict the natural distribution of the element. It should also be

mentioned that, in the case of Zn, the peak count rate of 1000 in the non-calcified region must be considered as the background, in contrast to the calcified zone. The elevated spectral background in the non-calcified zone is due to the high scatter contribution of sulfur and organic components of the non-mineralized matrix. Speckles of Y can be seen also on the vertical scan (Fig. 78).

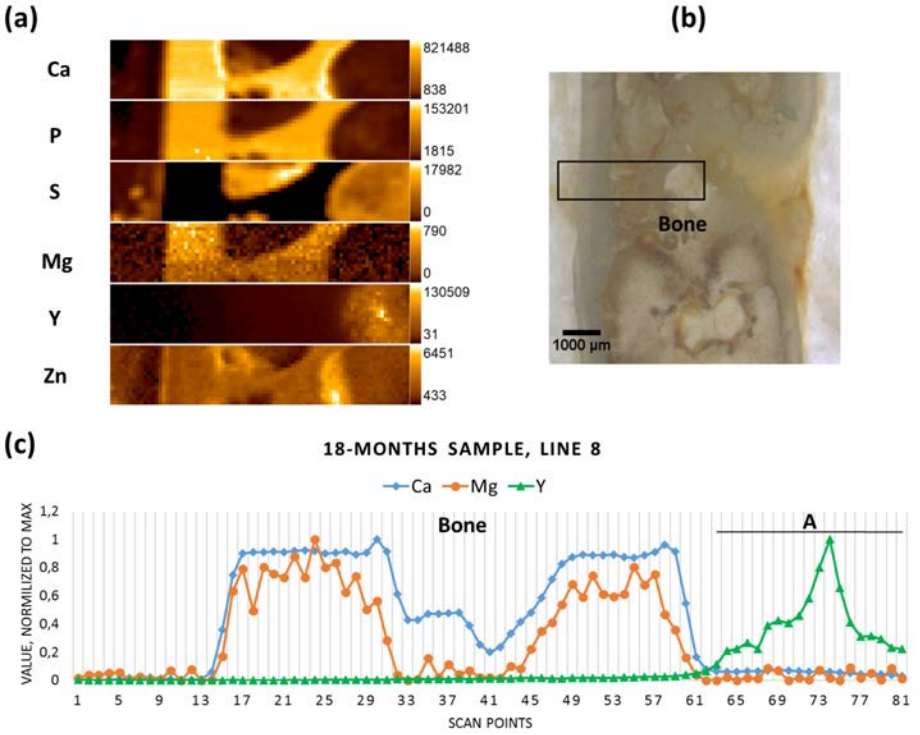

Figure 77. Eighteen-months sample (a) elemental maps, 81 × 16 pixels—corresponding to 4 mm × 0.75 mm; (b) micrograph showing the scanning area; and (c) line scan (line 8)

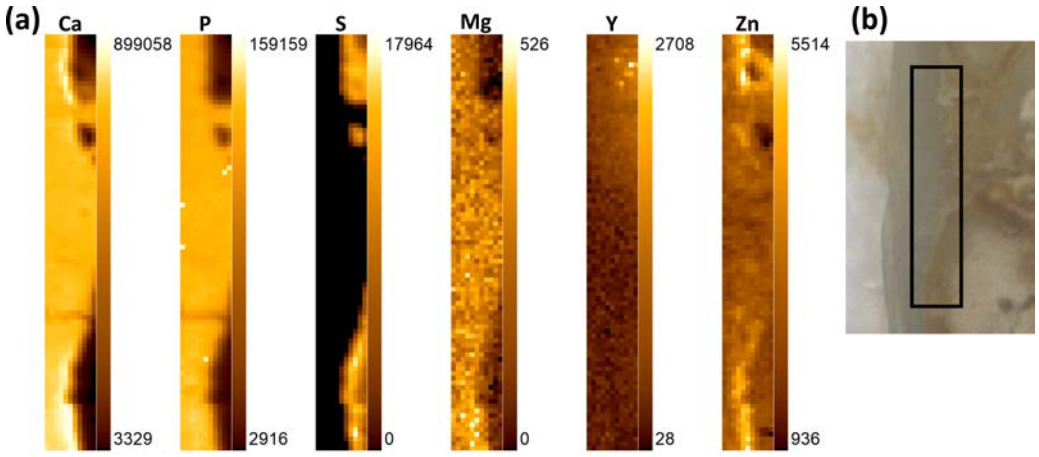

Figure 78. Twelve-months sample scanned vertically: (a) elemental maps, 11 × 89 pixels — corresponding to 0.5 mm × 4.4 mm; (b) micrograph with an approximate position of the scan area

In summary, while Mg content decreased rather sharply at the bone-implant interface (over 99% within ca. 300 µm), and only a very low Mg signal was found in the newly formed bone, Y migrated further into the tissue. The estimation of Y migration is based on the spectral information. In the selected line scan the position in the bone adjacent to the bone-implant interface was defined (the value for Ca is close to 1) and taken as a starting point. The last point on the line scan, for which the Y peak can be observed and distinguished from the spectral background, would mark the migration front

line. The distances over which Y migrated and could be detected are listed in Table 10. It is obvious that the distance increased with the dwelling time.

Table 10. Estimation of Yttrium migration into the bone

Duration of Stay in Bone	Distance from Interface
1 month	950 µm
3 months	1400 µm
12 months	1700 µm

It should be noted, however, that the spatial resolution and information depth differ for each element, and Y can be excited and detected at deeper layers in the sample, in contrast to Ca and Mg (information depth of Mg in bone: 2.3 µm; Ca in bone: 25.7 µm; and of Y in bone: 354 µm (calculated with the X-ray Utilities application)). Therefore, the position of potential Y accumulations (as well as the position of the implant interface) can only be defined approximately.

Conclusions and outlook

By means of µXRF analysis we were able to visualize the distribution of the elements of interest in bone tissue, with a focus on Mg and Y. The degradation process is not gradual, and interindividual variation in response to the implant should also be taken into account. Elemental maps and extracted information in the form of line scans showed a sharp decrease in Mg in the immediate vicinity of the interface and no specific accumulation or aggregation of Mg in the adjacent bone tissue in all of the investigated samples. It can, therefore, be assumed that Mg released during the degradation process is steadily included into the metabolic processes. This agrees with recent investigations where local Mg content was probed by µXRF with even higher resolution at the synchrotron, and no Mg accumulation was found at the interface of the WZ21 implant studied, but only around blood vessels, which are beyond the spatial resolution of the present study (74). The correlation of Mg with Ca might be ascribed to the natural distribution, but there could also be a contribution by secondary excitation of Mg by Ca in highly-mineralized regions of bone. However, it should be admitted, that the analysis of elements with low atomic number is still challenging, and natural concentrations of Mg might lie beyond the detection limits.

In all maps we found a tendency for Y to migrate deeper into the bone tissue than Mg. The distance from the implant rose with the increased dwelling time of the implant in the bone tissue, indicating a progressive distribution and accumulation of Y in bone further away from the implant site. Since Y could also be detected at the former implant position after 18 months, when the implant had already completely degraded, its accumulation has quite a permanent character.

It is known from the literature that Y has a tendency to accumulate in soft tissues, such as liver, spleen, and kidney, and in bone, although the reports about the deposition in bone are conflicting. It was found that small Y particles injected intravenously in rabbits went chiefly to the bone and bone marrow (75). Intravenous injection in rhesus monkeys after four hours resulted in Y accumulation in the epiphyseal plate and periosteum of the femur, but not in bone marrow (76). Appelgren et al. observed high concentration of Y in ossification zones and in periosteal and endosteal layers in mice one hour after injection (77). Herring et al. demonstrated the preferential binding of Y by quiescent and resorbing bone surfaces (78), and it was further shown in vitro that bone sialoprotein might be involved in the mechanism of Y binding (79). It should be noticed, however, that the route of administration (injection) and the short-term exposure to Y in the above-mentioned studies do not allow to fully extend them to the specific case of bioresorbable implanted material, where the mechanism of accumulation (and binding) might be different. With regard to Y-containing alloys it

should be remarked that, in corrosion tests, yttrium migrates to the metal surface of the alloy and is oxidized; therefore, yttrium oxide (Y_2O_3) will accumulate in the degradation layer (80). It could be assumed that the formation of soluble yttrium salts will be taking place at the degradation site, however, further thorough investigations of degradation processes involved are warranted.

Manganese, although it is a minor component of the alloy, should also be mentioned with respect to its physiological and putative toxicological role. Recently, influence of manganese on nervous system and Mn-induced Parkinsonism has attracted much attention (81). It is suggested that bone tissue substantially accumulates Mn, and during the lifetime it could be released slowly, serving as an internal source of Mn exposure (82). In our findings, Mn did not demonstrate any specific accumulations, probably due to its low content in the alloy.

Therefore, further investigations are needed, e.g., using confocal µXRF (also synchrotron radiation-induced µXRF) imaging to identify the distribution of elements in different depth layers; synchrotron XRF tomography to determine the migration of Y in the bone volume, or by X-ray absorption spectroscopy to define the Y compounds in bone tissue.

Micro-X-ray fluorescence analysis (µXRF) with a special spectrometer meeting the requirements for the measurements of low-Z elements was used. It was found that the migration and accumulation behaviour of implant degradation products is element-specific. A sharp decrease in Mg was observed in the immediate vicinity of the interface and no specific accumulation or aggregation of Mg in the adjacent bone tissue was detected. By contrast, Y was found to migrate further into the bone over time and to remain in the tissue even after the complete degradation of the implant. Although the nature of Y accumulations must still be clarified, its potential health impact should be considered.

5. Mn in osteoporosis

Contemporary elemental imaging techniques are greatly contributing into the bone research (83). Synchrotron radiation induced confocal micro-X-ray fluorescence analysis (SR-μXRF) technique was employed for the analysis of trace element distributions in bone tissue. The method allows for scanning the sample surface and obtaining information on distribution of elements with a defined depth resolution. Manganese (Mn), as a potential contributor into the mechanisms of calcium incorporation into bone tissue was in the spotlight of research. The interest in manganese distribution in bone tissue is induced by the findings suggesting its possible influence on fixation (or incorporation) of calcium into bones (84). The experiments performed at ANKA and BESSY-II intend to fathom the importance of manganese in bone metabolism and the interdependence of manganese and bone health, as in the context of osteoporosis.

Human bone samples were analyzed – osteoporotic and healthy controls. Samples were embedded in polymethylmethacrylate (PMMA), producing thick blocks, and the surface polished.

ANKA

To test the assumption about link between osteoporosis and manganese content in bone, human bone samples (transiliac bone biopsy samples) were analyzed (the description of setup is provided in chapter 2.5.2).

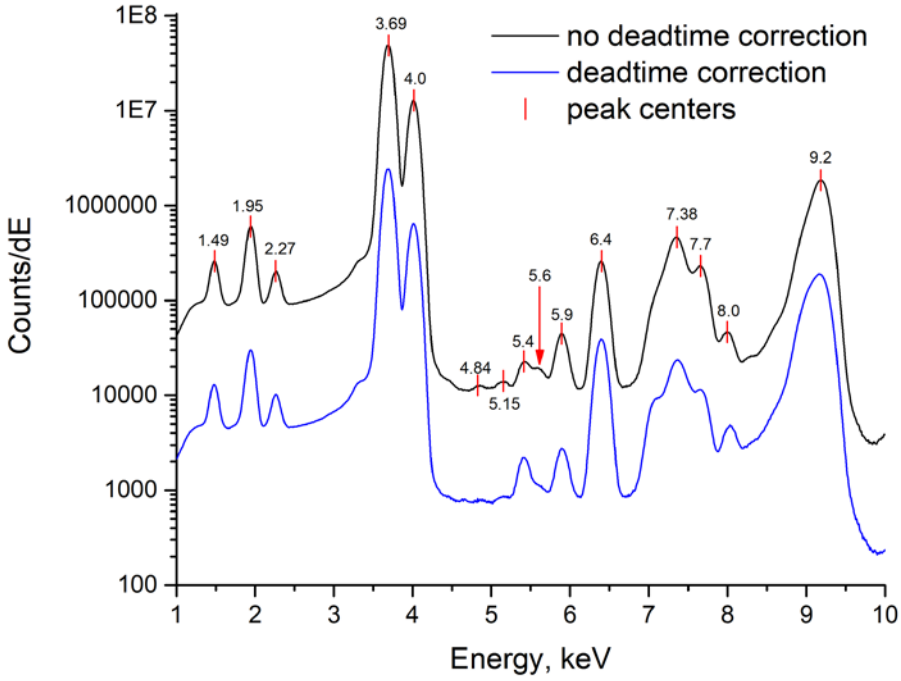

Figure 79. Comparison of sum spectra with and without deadtime correction

The Figure 79 shows the very same exemplary sum spectrum obtained at ANKA synchrotron for one of the samples (control, healthy male individual) – with and without deadtime correction. Apparently, the intense peaks are more pronounced if the deadtime correction is applied. The spectrum was calibrated using PyMCA and plotted with Origin software. The most prominent lines are listed in the table 11 below. Calcium, as a most abundant element is dominating the spectrum, therefore, both escape and sum peaks for Ca lines can be observed. Moreover, the minor peak around 5.6 keV (marked with an arrow) might be interpreted as an escape of an intense Ca-Kα/Ca-Kα sum peak. The minor elements can also be identified in the sum spectrum – e.g. Cr, Fe and Mn. Aluminium peak is

not stemming from the sample composition, but is introduced by the filter installed between the second polycapillary optic and detector (in order to reduce the overpowering Ca signal). As indicated previously in chapter 2.6.2, a sum spectrum gives general overview of the composition, however the interpretation of some minor peaks (e.g. 4.84 keV and 5.15 keV) as well as uncovering the presence of any further minor-/trace elements will have to be confirmed by checking the single spectra.

Table 11. The X-ray lines observed in the sum spectrum shown in Fig. 79

Energy, keV	Element/Line
1.49	Al (from filter material)
1.95	escape of Ca-Kα
2.26	escape of Ca-Kβ
3.69	Ca-Kα
4.0	Ca-Kβ
5.4	Cr-Kα
5.89	Mn-Kα
6.4	Fe-Kα
7.38	Ca-Kα-sum
7.69	Ca-Kβ-sum
8.0	Ca-Kα/Kβ-sum

For the measurements at ANKA synchrotron osteoporotic samples were obtained from male patients with multiple vertebral fractures and low bone mineral density; cause of osteoporosis was unknown. As a reference, healthy bone tissue samples, non-osteoporotic from male patients (middle aged) were measured. Based on Mn to Ca ratio, the histogram (Fig. 80), revealing the distribution of all the pixels, was plotted. The median (black horizontal line) and mean (black square) are shown on the boxplot.

The same procedure was used for the set of samples obtained from female patients (femoral neck biopsies) – osteoporotic femoral neck fracture samples and control samples (forensic autopsies of individuals without metabolic bone diseases), average age of the patients – 81.5 years, ranging from 74 to 92 years (Fig. 81).

In male, healthy and diseased samples can be distinguished with respect to Mn content.

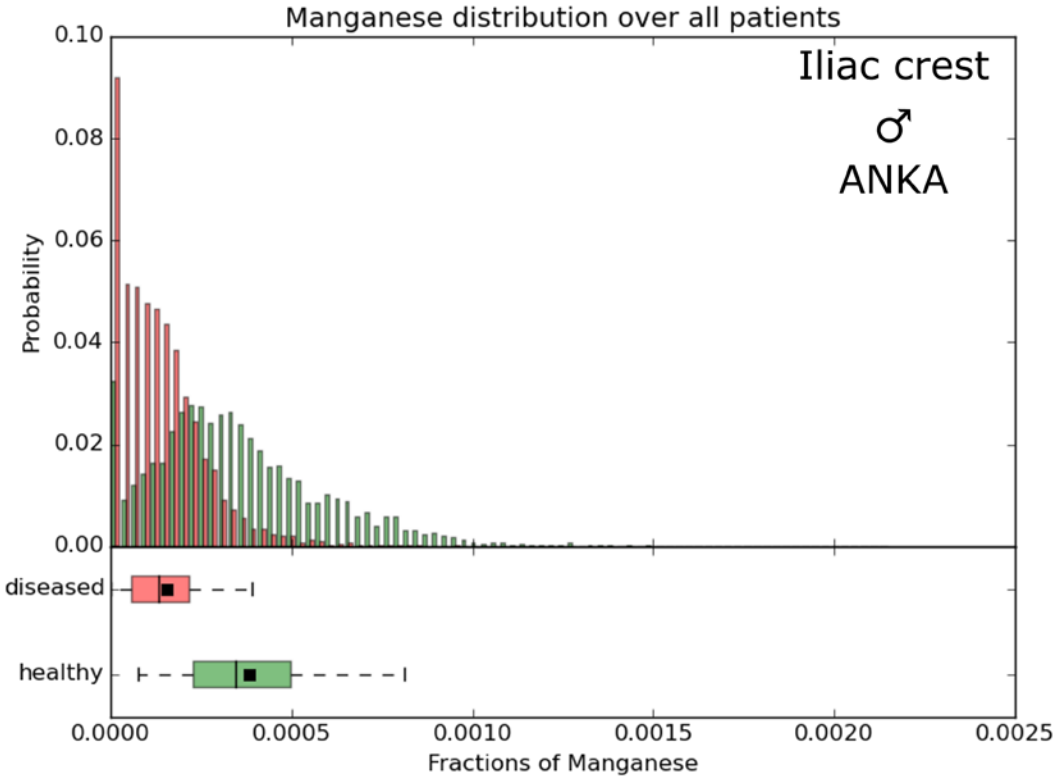

Figure 80. Histogram and boxplots for Mn to Ca ratios over the healthy controls (green) and osteoporotic (red) areas in male samples measured at ANKA

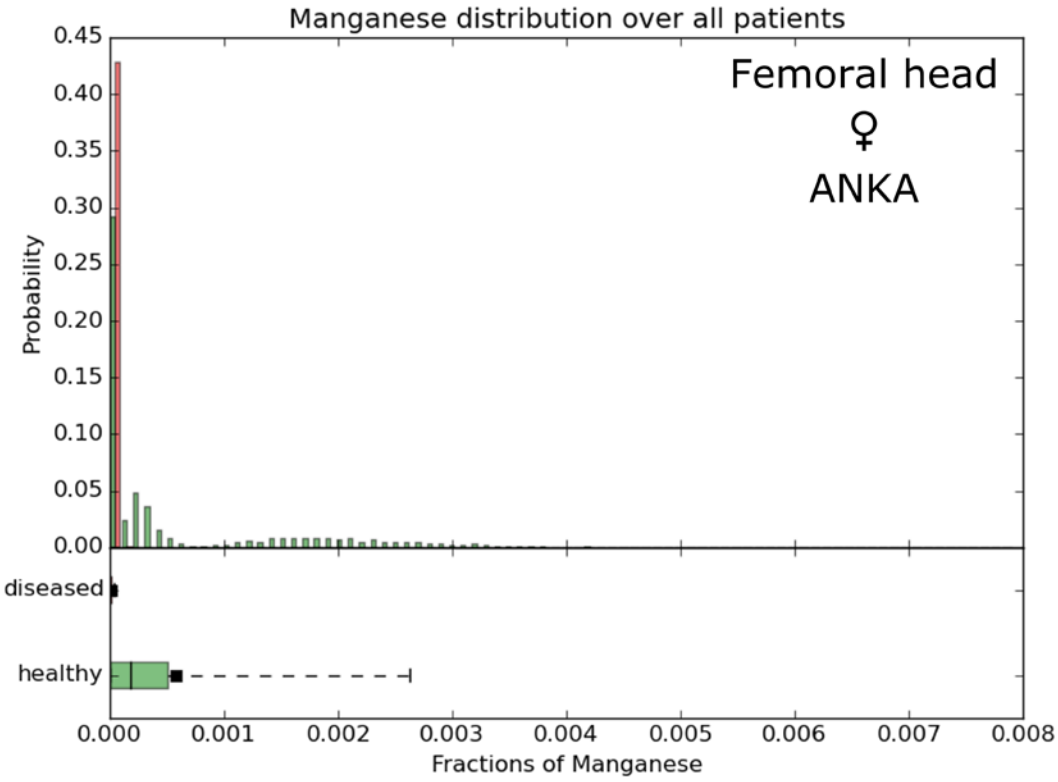

Figure 81. Histogram and boxplots for Mn to Ca ratios over the healthy controls (green) and osteoporotic (red) areas in female samples measured at ANKA

BESSY-II

In order to improve the statistics, we measured new set of osteoporotic and control male samples (5 healthy, 6 osteoporotic) at BESSY-II (see section 2.5.3 for the description of the setup). The same tendency – less Mn in osteoporotic samples still can be observed (Fig. 82).

We also measured set of female samples, the data analysis has to be performed. This set included biopsies taken from iliac crest and also from patients with idiopathic osteoporosis to be comparable to the set of male bone samples (Fig. 83).

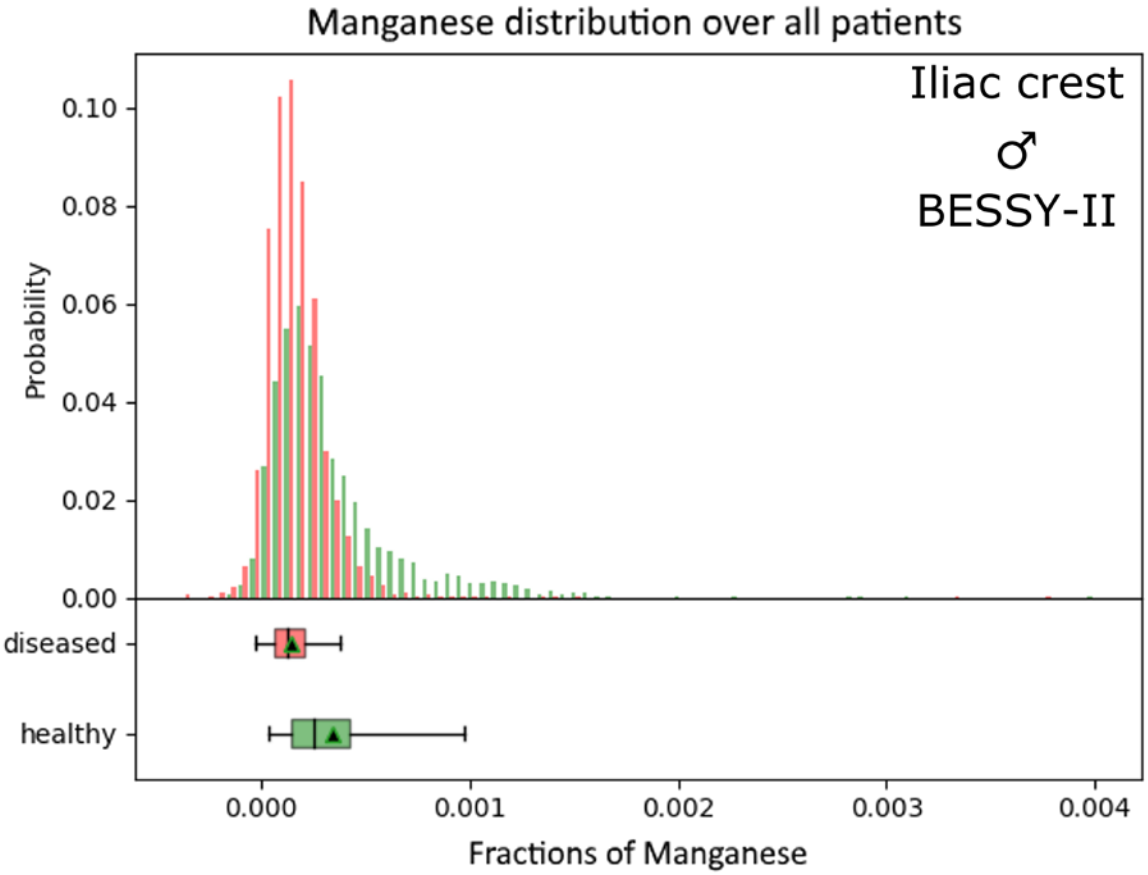

Figure 82. Histogram and boxplots for Mn to Ca ratios over the healthy controls (green) and osteoporotic (red) areas in male samples measured at BESSY-II

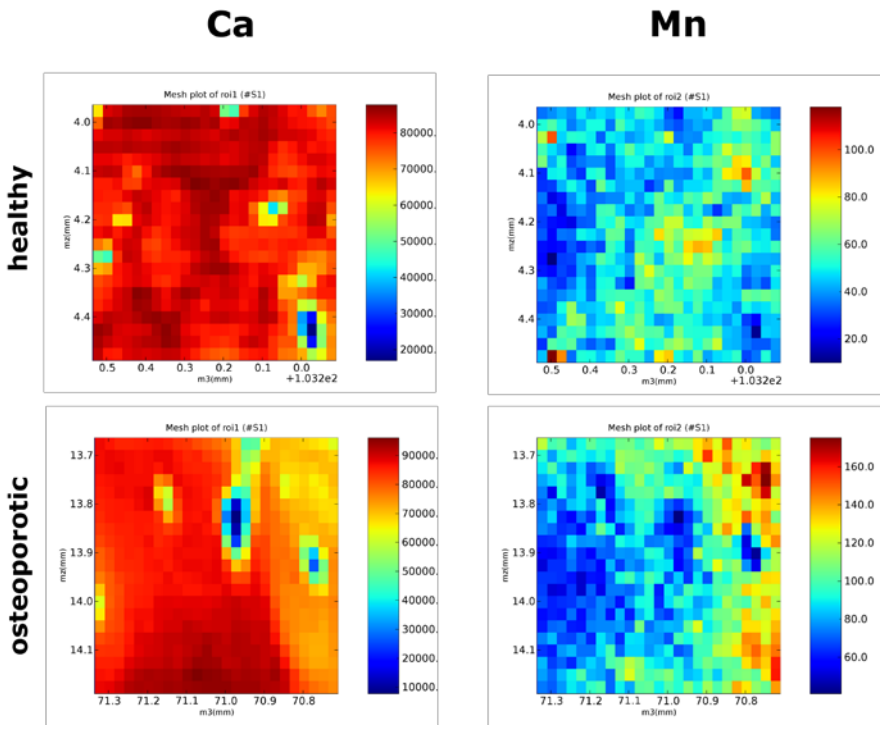

Figure 83. Elemental maps of Ca and Mn from iliac crest biopsies from healthy (top) and osteoporotic (bottom) female individuals measured at BESSY-II

Conclusions and outlook

1. Human bone samples (transiliac bone biopsy samples) from male patients with idiopathic osteoporosis tend to contain less Mn globally in bone tissue as compared to healthy controls
2. For bone samples taken from femoral neck of osteoporotic women such difference in Mn content compared to controls could not be demonstrated
3. Enlarging sample pool of human bone cuts might lead to more firm conclusions regarding the role of Mn in pathogenic pathways in osteoporosis,
4. Due to different measurement conditions, evaluation and data aggregation of the measurements stemming from two (or more) different synchrotrons is not straightforward
5. Novel methods of data analysis and statistical approaches could enable proper data handling and, thus, lead to substantiated statements on the link between manganese content and osteoporosis

6. Gadolinium accumulation in bone tissue

Parts of this chapter were previously published in Scientific Reports (85).

Gadolinium-based contrast agents (GBCAs) are frequently used in patients undergoing magnetic resonance imaging. In GBCAs gadolinium (Gd) is present in a bound chelated form. Gadolinium is a rare-earth element, which is normally not present in human body. Though the blood elimination half-life of contrast agents is about 90 minutes, recent studies demonstrated that some tissues retain gadolinium, which might further pose a health threat due to toxic effects of free gadolinium. It is known that the bone tissue can serve as a gadolinium depot, but so far only bulk measurements were performed.

Here we present a summary of experiments in which for the first time we mapped gadolinium in bone biopsy from a male patient with idiopathic osteoporosis (without indication of renal impairment), who received MRI 8 months prior to biopsy. In our studies performed by means of synchrotron radiation induced micro- and submicro-X-ray fluorescence spectroscopy (SR-XRF), gadolinium was detected in human cortical bone tissue.

The distribution of gadolinium displays a specific accumulation pattern. Correlation of elemental maps obtained at ANKA synchrotron with qBEI images (quantitative backscattered electron imaging) allowed assignment of Gd structures to the histological bone structures. Follow-up beamtimes at ESRF and Diamond Light Source using submicro-SR-XRF allowed resolving thin Gd structures in cortical bone, as well as correlating them with calcium and zinc.

The method of contrast-enhanced MRI (CE-MRI) dates to 1988, when the first gadolinium (Gd)-based contrast agent (GBCA), gadopentetate dimeglumine (Magnevist, Bayer), was approved for clinical use. CE-MRI is a useful imaging tool nowadays, with approximately 30 million procedures done each year worldwide, and more than 300 million procedures already performed to date (86). Estimates show that the GBCAs are administered in 25-35% of all MRI examinations (86,87).

According to the data available, most of the administered dose of GBCAs (regardless of an agent used), should be cleared in less than 2 hours after injections and >95% by 24 hours (88). Recent findings, however, demonstrate that the GBCAs are not fully excreted and the accumulation of Gd in, e.g. neuronal tissues and organs such as brain takes place (89).

The GBCAs are considered to be rather safe, yet there is a number of papers reporting nephrotoxic, hematotoxic, hepatotoxic and neurotoxic effects observed in animals and humans (90). One of the most serious adverse reactions associated with the use of GBCAs is nephrogenic systemic fibrosis (NSF), which had been observed in patients with renal insufficiency (91). NSF is a rare, but serious disease characterized by widespread tissue hardening (primarily skin is affected) with fibrotic nodules and plaques. First described in 1997, it was finally linked to the use of GBCAs in patients with kidney dysfunction in 2006 (91,92). The pathophysiological mechanism involved remains unclear, though the dissociation of Gd from GBCA is usually indicated as the causative factor (88,93). Due to renal insufficiency, the elimination of GBCA will be reduced, more of the dissociated Gd will be available, leading to tissue accumulation and further manifestation of Gd toxicity. The linear GBCAs due to their lower thermodynamic and kinetic stability (compared to macrocyclic GBCAs) are now considered as high-risk agents in patients with severe renal disease (94).

The analysis by secondary ion mass spectrometry (SIMS) and inductively coupled plasma mass spectrometry (ICP-MS) techniques of skin biopsies from patients suffering from NSF after GBCA intake revealed Gd accumulations, which were inhomogeneous and co-localized with calcium (95) and phosphorus (96). In 2010 application of synchrotron radiation induced X-ray fluorescence spectroscopy (SR-XRF) for investigation of skin samples of NSF patients independently by High et al. and George et al. also confirmed depositions of Gd coinciding with other elements (97,98).

Multiorgan Gd depositions in NSF patient, involving skin, liver, lungs, intestinal wall (ileum), kidney, lymph node, skeletal muscle, dura mater and cerebellum, were reported by Sanyal et al. by performing scanning electron microscopy (SEM) with energy-dispersive X-ray spectroscopy (EDS) analysis (99).

There is a growing body of research devoted to the investigation of possible GBCAs adverse effects in patients with normal renal function and, specifically, the retention of Gd. It would not be an overstatement to say, that a main focus lies on the retention of Gd by brain tissues. A recent study by Flood et al. connects increased signal intensity in children with repeated exposure to linear GBCAs (100). Again, the use of less stable linear GBCAs is more likely to result in the deposition, however studies demonstrate, that the macrocyclic agents might be retained as well (89,101). In view of this, the European Medicines Agency (EMA) issued recommendations for the restriction of linear GBCAs in body scans (94).

Recently, accumulation of Gd in bone tissue received deserved attention, especially given the fact that bone tissue retains Gd from GBCAs to a greater degree (23 times higher levels) compared to brain (101). Darrah et al. used ICP-MS to measure Gd content (bulk) in bone tissue in osteoporotic and osteoarthritic (previously exposed to Gd) and osteoarthritic (non-exposed, used as controls) patients, and concluded that Gd can be retained for longer than 8 years after the exposure (102). Series of in vivo experiments by M. Lord et al. contributed substantially to the current knowledge about Gd retention. The group developed an in vivo XRF device and obtained quantitative data on Gd content in the bone tissue of exposed patients in comparison with control subjects (103,104).

However, very little is known about the distribution of Gd in bone on the microscopic level. Our group has already employed the method of synchrotron radiation induced micro-X-ray fluorescence (SR-µXRF) for the characterization of distribution of trace elements, such as lead (Pb), zinc (Zn) and strontium (Sr) in healthy and diseased bone and cartilage samples (83,105,106). Within this project we applied SR-µ-/ and sub-µXRF for the detection and mapping of Gd distribution within bone tissue. To the best of our knowledge these measurements are the first attempt to image Gd accumulations in the bone.

Experimental

Patient and bone samples preparation

The patient – male individual, 54y, diagnosed with male idiopathic osteoporosis, multiple vertebral fractures and low bone mineral density, without indication of renal impairment. A transiliac crest biopsy was harvested from the patient for diagnostic reasons. All study-related procedures were approved and supervised by the local ethical committee of the St. Vincent Hospital Vienna, Austria, an academic teaching hospital of the Medical University of Vienna following the Declaration of Helsinki (DoH). The patient provided written consent for anonymized outcomes to be further used in scientific examinations.

It is known that the patient received MRI eight months prior to biopsy. Unfortunately, up to date we were not able to confirm whether and which contrast agent was used. No other sources of Gd intake are known.

The biopsy was dehydrated and fixed in ethanol and embedded in polymethylmethacrylate (PMMA). In order to avoid contaminations, only fresh and clean solutions of pro analysis quality were used during sample preparation. Typical contamination originating from the polishing procedure and consisting of Cr-Mn-Fe-Ni was identified in only one sample area and routinely excluded in the data analysis (sample demonstrated below, Figure 87). The thick PMMA block was trimmed using a low-speed diamond saw (Buehler Isomet, Lake Pluff, USA), and further sandpapered with decreasing grit size and finally polished by silk cloths loaded with diamond grains (3 µm and 1 µm) using a precision

polishing device (PM5; Logitech Ltd., Glasgow, UK). This ensured the block having a smooth and flat surface, which is necessary for both quantitative backscattered electron imaging (qBEI) and SR-µXRF measurements (ANKA).

A 3 µm-thin cut was prepared out of the PMMA block for the measurements on two high-resolution SR-sub-µXRF beamlines (ESRF and Diamond Light Source synchrotrons), using a microtome (LEICA SM2500; Leica Microsystems GmbH, Wetzlar, Germany). The cutting was performed as close as possible to the original surface – we estimate the offset to less than 15 µm. The resultant cut was sandwiched between two 8 µm Kapton foils and fastened to a plexiglass frame.

Quantitative backscattered electron imaging (qBEI)

qBEI was used to determine the degree of tissue mineralization. Making use of the dependency of the backscatter electron coefficient on the local electron density (average atomic number) of the target material, this method allows to derive the degree of mineralization of bone and further to evaluate the calcium concentration (weight percent, wt% Ca). Hence, bright areas in the grey scale qBEI images refer to higher, and the dark ones to lower mineralized matrix (higher vs. lower Ca content). This method requires flat polished surface in order to derive quantitative information, therefore is only possible for bone samples as PMMA embedded blocks. The measurements were performed using a digital scanning electron microscope equipped with a four quadrant semiconductor backscattered electron detector (DSM 962; Zeiss, Oberkochen, Germany), operated at 20 keV beam energy. Areas were scanned with ×200 nominal magnification (pixel resolution 1 µm). The information depth of qBEI depends on the mineralization and is in the range of 1–1.5 µm. The details on the technique can be found in reference (63).

SR-XRF measurements and data processing

ANKA

The measurements on the PMMA block sample were performed at the confocal FLUO beamline at ANKA (KIT, Karlsruhe, Germany). For the first beamtime (two areas on the surface of the block, Fig. 85) beam size was defined at Ti-Ka (4.51 keV) as 27 µm × 18 µm × 24.5 µm (hor. × vert. × dep.), with the excitation energy of 9.2 keV (the energy optimized for the detection of manganese due to the original purpose of the experiment). The step size was 25 µm × 15 µm. For the second beamtime (another two areas, Fig. 86) the beam size was defined at Ti-Ka as 28 µm × 19.5 µm × 35 µm (hor. × vert. × dep.), the step size was 25 µm × 17µm, same excitation energy 9.2 keV. In both measurement sessions the setup included W-Si multilayer monochromator, 2 polycapillary half-lenses, 20 µm Al detector-filter, Vortex 50 mm^2 silicon-drift detector, and XIA Mercury digital pulse processor. The angle between source and detector was 90º. The acquisition time was 15-17 seconds per spot (pixel) depending on the area. See the exemplary single spectrum in Figure 84 (left). The description of the setup can also be found in chapter 2.5.2, an exemplary sum spectrum from the same dataset is included in chapter 5.

ESRF

Measurements on the thin section with submicrometer resolution were performed at the ID13 microfocus beamline at ESRF (Grenoble, France); beam size 50 nm, defined using Siemens star standard. The excitation energy was set to 12.7 keV (corresponds to highest flux available at the beamline). The beamline was equipped with multilayer Laue lens optics, Vortex-EM silicon drift detector (Hitachi, USA), positioned on the rear side, “behind” the sample (i.e. the angle between source and detector is more than 90º). The step size was 500 nm with 20 s acquisition time per spot.

See the exemplary single spectrum in Figure 84 (right). The description of the setup can also be found in chapter 2.5.4.

Diamond Light Source

Measurements on the same slice as analysed at the ESRF were also conducted at submicro-X-ray fluorescence setup on the B16 beamline at Diamond Light Source (Didcot, UK). The excitation energy was set to 12.7 keV to match that used at ESRF. The beam size (FWHM at 12.7 keV) was determined as about 500 nm × 610 nm (V × H) – taking into account the overlap in 45º geometry – using a 50 µm-diameter Au wire knife edge. The setup included a RuB_4C multilayer monochromator, 150 µm pinhole and a single-element 90 Ex Vortex detector (50 mm^2), positioned at 90° to the beam. The step size was 500 nm with an acquisition time 15 s per spot. Additional information on the setup we used for the experiment can be found in reference (26), see also chapter 2.5.5.

Data processing

For the ANKA dataset, the spectra were processed using AXIL software (27). Spectra recorded at ESRF and Diamond Light Source were processed with PyMCA (28). The quality of fitting was further validated and text images for each element of interest were obtained using in-house software LP-map (42). Finally, ImageJ (44) was used to process the text images and to produce the elemental maps and overlays. Elemental maps are presented in counts per second (cps).

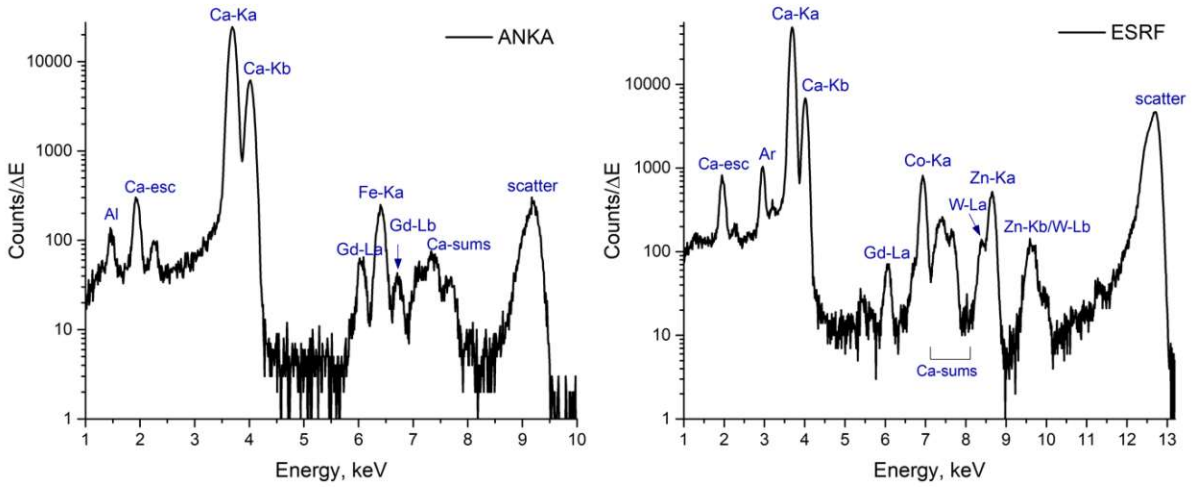

Figure 84. Exemplary spectra featuring gadolinium: ANKA (left) and ESRF (right)

Results and discussion

The SR-µXRF measurements in the cortical region of the human iliac crest biopsy revealed highly localized accumulations of Gd. This observation was done at the ANKA synchrotron during the beamtime dedicated to the detection of manganese. The two scans recorded during this first beamtime are presented in Figure 85. The Figure 85 shows Gd and Ca elemental maps as well as a composite image, where qBEI is superimposed on the Ca map (marked as qBEI/Ca). On the Gd map all the pixels above a certain threshold (in the range of 1-3 counts per second (cps), selected individually for each map) are selected and marked via mask (green lines). The exact same mask is applied to the Ca map and, finally, the Ca map with the mask is superimposed on the qBEI, creating the qBEI/Ca composite image. The resolution of qBEI images is higher than that of the elemental maps and facilitates assignment of the Gd structures. Indeed, it can be seen, that Gd accumulation happens

within the specific restricted compartments: (i) in cement lines separating two bone packets (signified with black arrows), and (ii) at the interface between mineralized matrix and vascular canals, corresponding to the walls of Haversian and Volkmann's canals (marked with red asterisks).

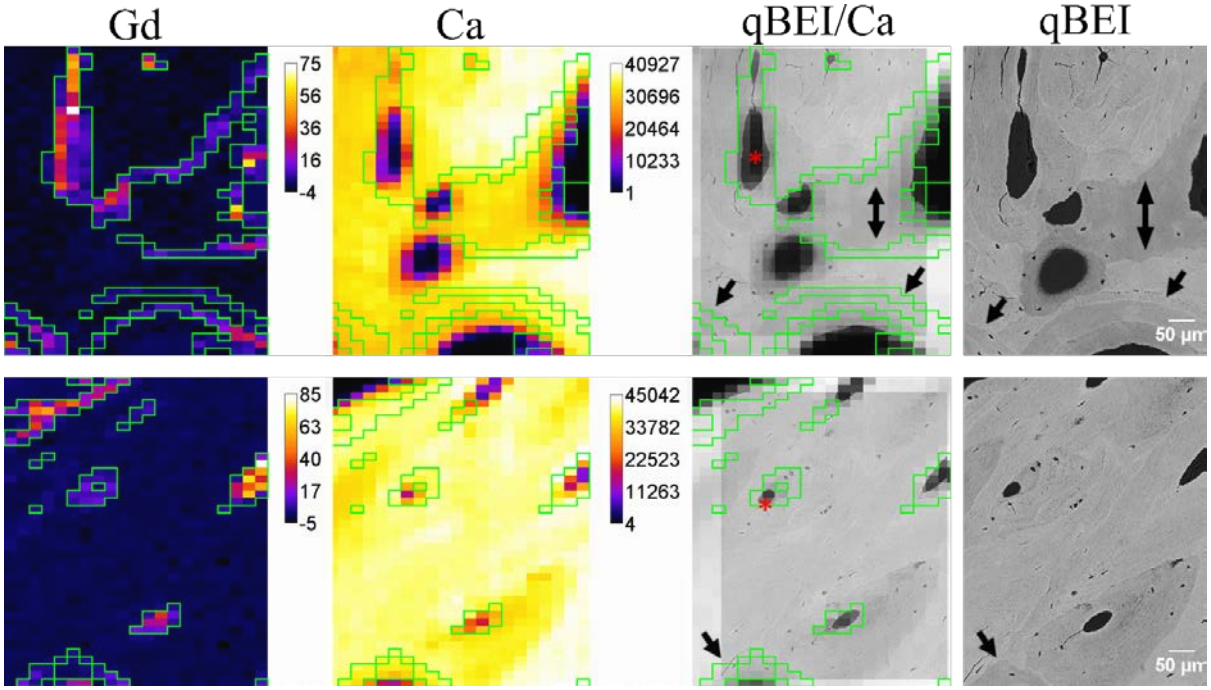

Figure 85. Elemental maps of Gd and Ca (in cps) obtained at ANKA, composite qBEI/Ca overlay and corresponding qBEIs of two areas. The area size for maps of 21 × 41 pixels corresponds to 500 × 600 µm²; for qBEIs 450 × 570 µm². The black arrows (composite image and qBEI) point at cement lines; red asterisk – canals.

During the follow-up beamtime we scanned two additional areas, but as the setup was adjusted differently, it was less sensitive to Gd (Gd signal was lower). For illustrative purposes those two additional areas are demonstrated in Figure 86. Due to specifics of the spectra, the spectral background was fitted with the negative values for Gd. Therefore, in order to improve the contrast, negative values on these Gd maps were set to zero.

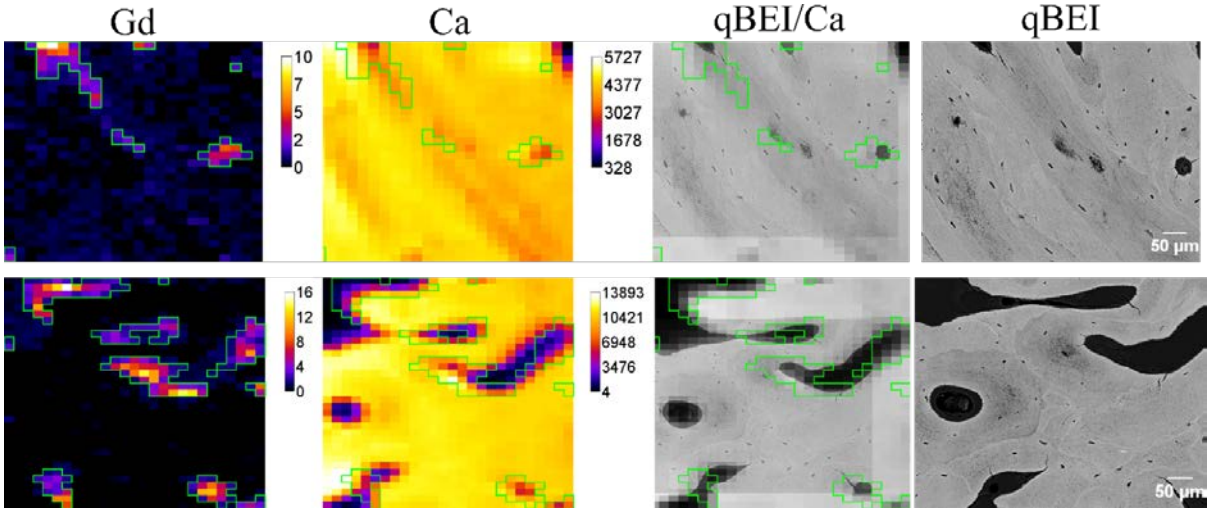

Figure 86. Gd and Ca elemental maps (in cps) obtained at ANKA, composite image and corresponding qBEIs of two areas. Top image: area size for maps 24 × 30 pixels, 575 × 493 µm²;

Bottom image: area size maps 27 × 35 pixels, 650 × 578 µm²; Dimensions for both qBEIs 570 × 450 µm².

In addition, in the Gd map of the region shown in the bottom row of Figure 86, another threshold was introduced – Cr-Mn-Fe-Ni contamination was identified in the hole (the corresponding maps of Cr, Mn, and Fe are shown in Fig. 87, (see also chapter 3.2, section "Supporting SEM-EDX measurements of the instruments and materials used in sample preparation"), and this region was masked, and the values were also set to zero.

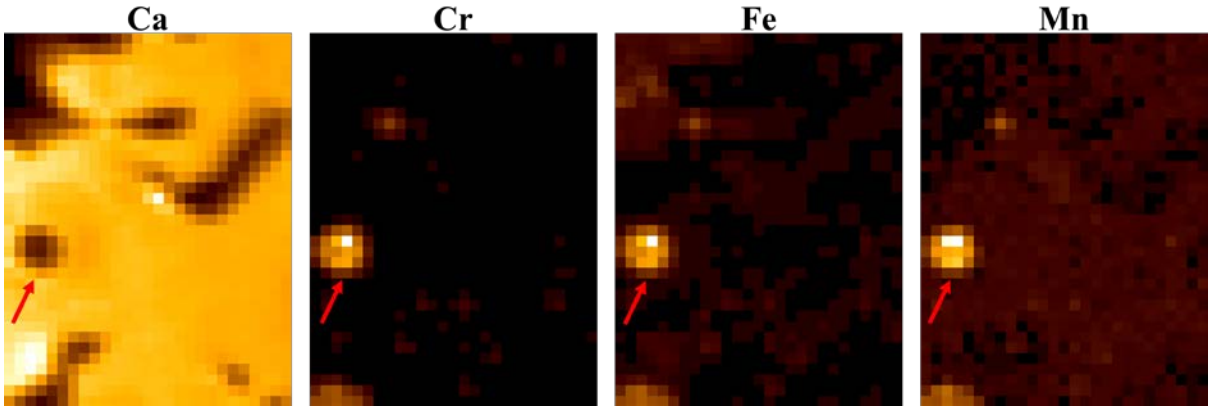

Figure 87. Untreated maps for Ca, Cr, Fe, and Mn; site of contamination indicated by red arrow

The alleged cement line Gd structures are mainly 1-pixel thick (elemental maps), however the correct estimation of their thickness is not possible based on these maps only. As can be seen from the qBEI image, cement lines have a thickness <5 µm. Hence, the confocal system at ANKA with the resolution of ~20 µm can be used for locating the Gd accumulation, but gives an overestimation of the sizes of those structures, while underestimating the relative elemental content.

Therefore, as a next step, we aimed to resolve the thin structures within the mineralized bone tissue in higher resolution. These scans were performed at ESRF and Diamond Light Source synchrotrons at beamlines featuring submicrometer beam sizes. The non-confocal setups on both synchrotrons call for thin samples, therefore a slice of 3 µm thickness was prepared out of the original PMMA block as close as possible to the qBEI-measured surface. As the excitation energy was higher compared to the ANKA synchrotron, we detected a broader range of elements including zinc (Zn), which is also known to accumulate in cement lines (83). Therefore, correlating Gd and Zn distributions provided additional information.

Figure 88 shows the elemental maps of Ca, Gd and Zn obtained at ESRF. The Ca map confirms that the entire field of view was positioned within the mineralized matrix. It can be seen, that Gd is only found in a restricted region, roughly the horizontal width of this structure can be estimated as 10-15 µm. Gd shows a unique distribution, and remarkably, it is exclusively detected in the area, where also Zn is present in high content. As reliable qBEI imaging cannot be performed on thin sections, here the composite image is prepared by overlaying Ca (red) and Gd (green) elemental maps. Due to the high intensity of the beam at ESRF, the area mapped there was subject to radiation damage and can be recognised by darker colour compared to the surrounding tissue – the respective area is marked on the light microscopy.

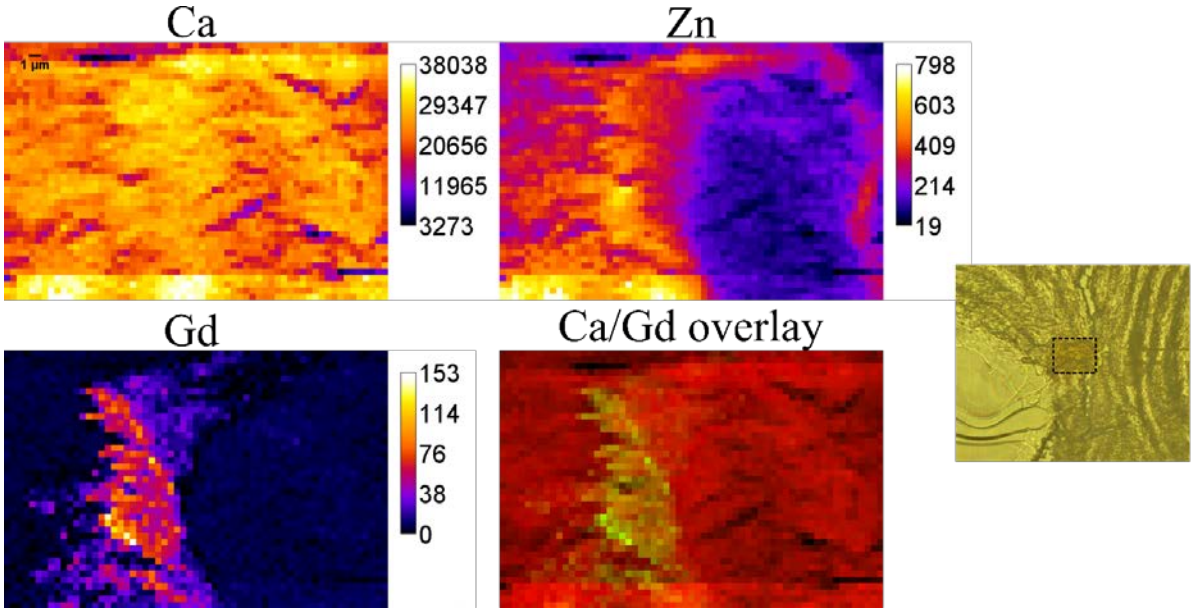

Figure 88. Elemental maps (in cps), composite image obtained at ESRF and light microscopy. Area size is 61 × 41 pixels corresponding to 30 × 20 µm²

The very same sample which we have measured at ESRF, although a different area of it, was later investigated during the beamtime at Diamond Light Source. Figure 89 shows the elemental maps of Ca, Gd and Zn obtained at the Diamond Light Source and the composite image of Ca (red) and Gd (green) overlay. The horizontal width of this Gd structure is around 10 µm. In this experiment Gd found to be located within the calcified area as well – and again Zn and Gd locally correlate, supporting the previous observations based on the ESRF measurements.

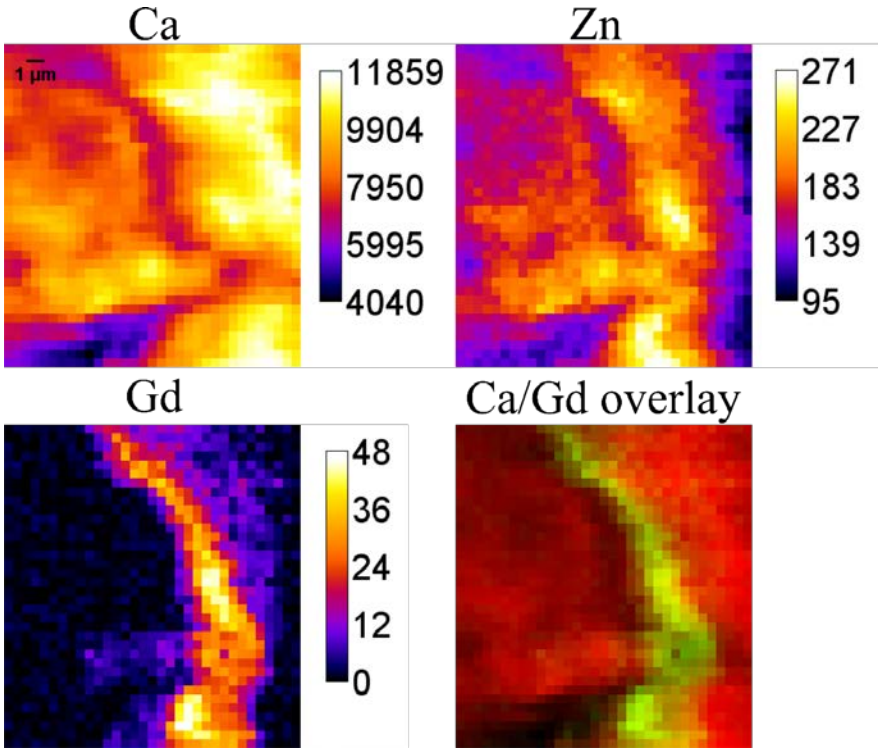

Figure 89. Elemental maps (in cps) and composite image obtained at Diamond Light Source. Area size is 33 × 36 pixels corresponding to 16 × 17.5 µm²

Additional composite images of Zn and Gd overlays (ESRF and Diamond Light Source) are shown below, Figure 90.

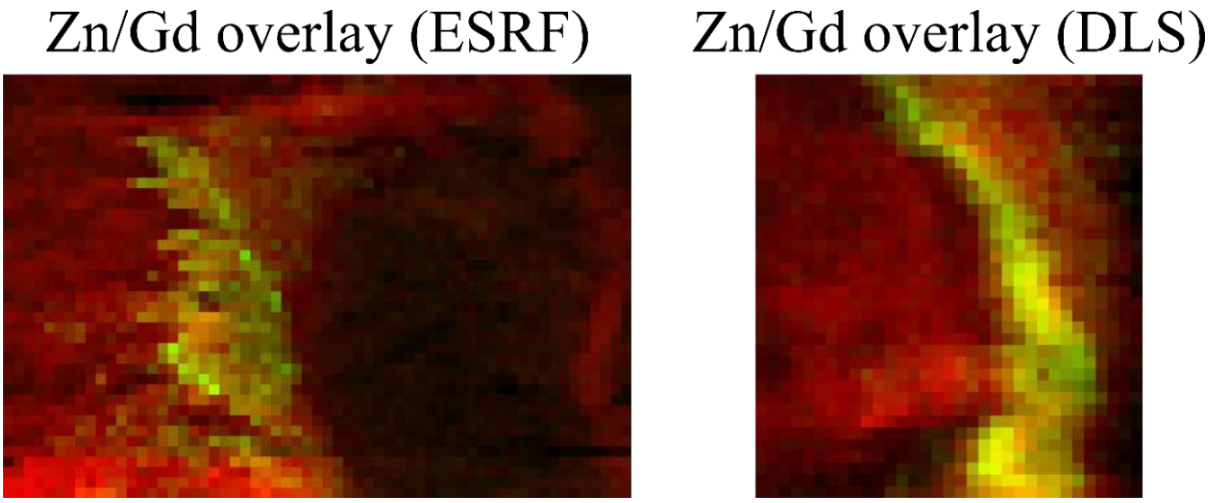

Figure 90. Composite images of Zn (red) and Gd (green) overlays from ESRF (left, corresponds to Fig. 88) and Diamond Light Source (right, corresponds to Fig. 89)

It should be noted that we also detected cobalt (Co) in both regions measured at ESRF and Diamond Light Source – exhibiting a similar local distribution as Ca. Co is one of the essential heavy metal elements normally involved in physiological processes, e.g. as a constituent of Vitamin B_{12} (cobalamin) or certain enzymes. However, we suspect that Co might also be introduced by the sample preparation procedure (see also chapter 3.2, section "Supporting SEM-EDX measurements of the instruments and materials used in sample preparation"). Co maps (ESRF and Diamond Light Source) are shown in Figure 91.

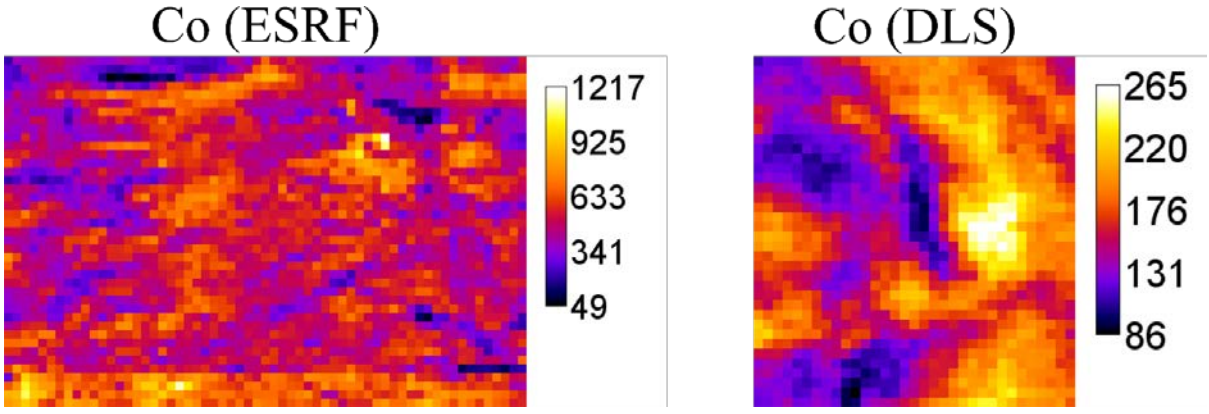

Figure 91. Co maps (in cps): ESRF (left, corresponds to Fig. 88); Diamond Light Source (right, corresponds to Fig. 89)

Quantification attempt

We performed quantification of the maps obtained at DLS with two different methods. We are confining the analysis to these maps due to the following reasons:

1) In thin sample absorption matrix effects can be neglected – and the sample measured at DLS is a thin cut;

2) During the same beamtime at DLS we measured reference material (further details below).

Further, since the section measured at ESRF and DLS was the same one, the obtained concentrations can be safely applied in relation to ESRF maps as well.

While the areas measured at the ESRF and DLS are different – and, therefore the concentrations can differ as well, the ratios, obtained using maximum values of Ca, Zn and Gd are well aligned (see the Table 12 below).

Table 12. Ratios of maximal values for Ca, Zn, Gd – from ESRF and DLS elemental maps (in cps)

Element ratio	ESRF	Diamond Light Source
Ca:Gd	47.7	43.8
Ca:Zn	248.6	247.1
Zn:Gd	5.2	5.6

Quantification approach 1. Fundamental parameters

Application of fundamental parameters method for quantification requires certain information to be known (generally it consists of two steps – calibration, using the sample of known composition and then analysis of unknown sample). In case of our samples, such information is not available. Further limitation is the intrinsic inhomogeneity of the sample. Therefore, we can perform the calculations for one pixel only.

Since bone Ca content is better explored, than other elements, we will use Ca content as a reference. We select one pixel from the DLS map – where all elements of interest are present – and for the calculations assume, that the value of Ca in this point is 100 000 µg/g – which is close to the values reported by (107) for the same kind of material – transiliac bone samples.

The results for calculated concentrations for Gd and Zn are given in Table 13.

Table 13. FP-based content of elements in point 22:17 of DLS map

Element	Concentration, µg/g	Value in cps
Gd	267.5	45
Zn	197.4	238
Ca	100 000 (putative)	10375

The point with coordinates 22:17 (x:y) is marked on the Figure 92 below:

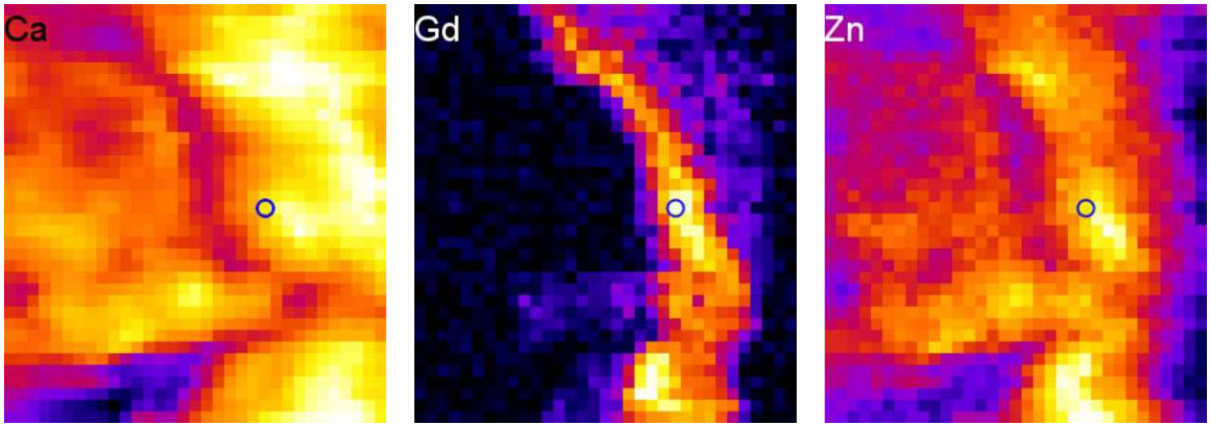

Figure 92. Ca, Gd and Zn maps obtained at DLS with the pixel considered for FP method approach – marked with circle

However high the obtained value for Gd might seem, it will only increase, if we plug a greater number for Ca concentration into the equation – although, one also should bear in mind, that this is only the single-pixel value within the accumulation sight, and therefore cannot be really compared with the averaged bulk values given in literature.

Quantification approach 2. Recalculation with sensitivities estimated from standard reference material

During the same beamtime we also measured standard reference material, NIST SRM 1412 – Multicomponent glass, in order to characterize the setup (see chapter 2.5.5, Figures 31-32). The experiment and procedure are described in (26). The glass is a fitting reference material for our purposes, since it contains the elements, which can be exited with 12.7 keV via L-lines. The sensitivities for Zn and Ca could be taken directly from the standard measurements – and the sensitivity for Gd had to be extrapolated based on the known values for Sr, Cd and Ba; the values are included in Table 14, and the maps recalculated in µg/units are presented below. But the glass standard is not a thin film standard, so the obtained sensitivities are supposed to be lower than for thin film approximation leading to lower concentration values of Ca, Gd and Zn for the bone sample.

Table 14. Sensitivities K/L-lines – SRM NIST 1412

	Element	Sensitivity, cps*g/µg	Comment
K	Ca	0.079	
	Zn	4.7	
L	Gd	0.7	extrapolated value

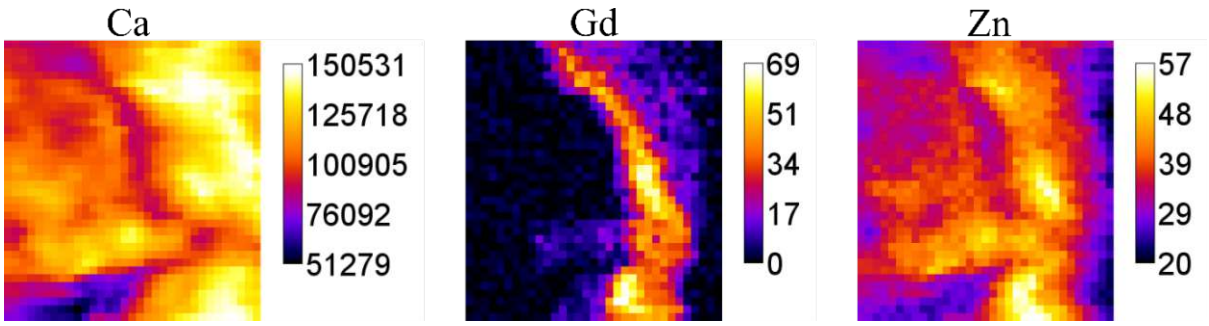

Figure 93. Ca, Gd and Zn elemental maps (in µg/g) from Diamond Light Source

As Ca content is the best "reference" to judge about the obtained result – the range 50 000-150 000 µg/g (seen from the calibration bars of the Fig. 93) seems reasonable according to literature values (107,108). With all the given limitations, the Zn values also do not fall far from the range given by Zioła-Frankowska et al. – ca. 40-110 µg/g.

Sources of exposure

In the present paper we demonstrated the distribution of Gd within cortical bone tissue, and its correlation with the other detected elements. It is known from the patient's history, that MRI was carried out 8 months prior to the biopsy, but it remains unknown whether a contrast agent was used. Hence, we cannot assert that the Gd signal originates from retention from this single exposure event. It is fair to note, that other than CE-MRI sources of exposure to Gd are possible (109,110).

Rare-earth elements (REE) mining and processing can be mentioned in this respect, although the reports on the occupational exposure associated with negative health outcomes other than

pneumoconiosis are sporadic. Li et al. found higher urinary levels of La, Nd, Ce and Gd in exposed workers dealing with Ce and La oxides ultrafine particles and nanoparticles compared to non-exposed (111), however the next paper from the group (presumably on the same subjects), on creatinine adjusted urinary levels of REEs, did not show significant difference in gadolinium levels (112). We were unable to find reports on deposition of gadolinium in occupationally exposed subjects.

In the recent years the anthropogenic Gd pollution, especially in aquatic systems, became a topic of extensive research (113–115). However, we doubt that the low concentrations of Gd in tap water could lead to the found accumulation in bone tissue; and given the likely subject's occupational history, the likelihood of presumable occupational exposure to elevated concentrations of gadolinium is remote.

Our hypothesis is that the observations made in this study could be generally characteristic for the Gd uptake by bone, regardless of the source. Imaging experiments on larger number of biopsies from patients with known history of Gd exposure are required to systematically determine Gd accumulation/retention with respect to the source and are planned to be done after this pioneer study.

Analysis ex vivo, localization within bone

To date the Gd retention in bone was investigated in bulk, and in many cases ICP-based techniques were employed for the analysis (101,102,116,117). Research undertaken by inductively coupled plasma atomic emission spectroscopy (ICP-AES) and ICP-MS compared linear GBCA (Omniscan) to macrocyclic (ProHanse) and revealed higher levels of retention in bone in case of linear contrast agent (116,117). One investigation employing SEM-EDS for the analysis reported that no Gd was detected in the bone. That might be due to the detection limits of the chosen method or due to the preceding sample preparation, as the sample had been decalcified (99). While the detection limits of EDS are typically around 0.5 wt%, SR-XRF spectrometry (as employed in the present study) features a much higher sensitivity down to sub-ppm (26), thus making this method more suitable for the local analysis of trace elements like Gd. Indeed, the anticipated Gd concentrations in bone after exposure to GBCA are within few ppm, which is supported by the bulk measurements (up to 1.77 µg Gd/g bone (117)) and *in vivo* experiments (mean 1.19 µg Gd/g bone (104)).

Since the concentration of gadolinium in the detected structures is of considerable interest, we attempted the quantification of local Gd content – and obtained the maximum values in the range of 70-270 µg/g (locally detected maximum concentration, indicative, not to be confused with bulk values mentioned above!) – the detailed procedure is described in supplementary material. This correlates well with the results obtained in a comparable elemental imaging experiment using skin biopsy, where the hot spot concentrations in Gd maps exceed 100 µg/g (118).

By correlating elemental maps obtained at ANKA synchrotron and qBEI images, we were able to assign the histological structures, which seem to be prone to Gd accumulation, namely (i) cement lines and (ii) vascular pore walls (interface to Haversian/Volkmann's canals). Conceivably, deposition within the walls of canals is due to the direct vicinity to the blood vessels which feature the main delivery pathway of Gd after exposure. The cement lines are marking the osteon boundaries, they are mineral-rich and collagen deficient (compared to the mineralized matrix of the osteon), and also contain non-collagenous proteins, such as osteopontin, glycosaminoglycans, osteocalcin, and bone sialoprotein) (119). The cement lines are laid down at the reversal phase of osteon formation (i.e. before the formation of the new sequential lamellae) (120). Supposing that the transient Gd exposure occurred at this phase of osteon formation, it is plausible, that Gd may be included in the composition of the cement line and adjacent lamellas.

Correlation with other elements, possible mechanisms of retention

The correlation of Gd with other elements can shed light on the chemical environment of Gd within the accumulations and on the mechanism of retention. Data available on Gd depositions in skin suggest a colocalization with such elements as Ca, P and Zn. Abraham et al. observed Gd in association with Ca by SIMS (95). Birka et al. used LA-ICP-MS and concluded, that matching Gd and P distributions suggest the presence of insoluble deposits of $GdPO_4$ in the tissue section; and the Gd and Ca correlation could suggest that Gd causes calcium-containing depositions, which trigger calcification (96). George et al. investigated Gd accumulation in skin affected by NSF using SR-XRF, and found clear correlation between Gd, Ca and P distributions, and the use of extended absorption fine structure spectroscopy (EXAFS) further allowed to assume Gd presence in form of $GdPO_4$-like structures (98). An inhomogeneous Zn distribution was also found throughout the Gd and Ca deposits, though it was concluded that Zn does not show a simple correlation with those elements in skin. At the same time, High et al. also with the use of SR-XRF observed colocalization of Gd, Ca and Zn in skin tissue and hypothesized that Ca and Zn facilitate displacement of Gd from the chelating agent (97). Interesting results were obtained by Clases et al., who investigated not only skin, but also brain depositions, using LA-ICP-MS. In skin elemental distribution of Gd, P, Ca and Zn correlated in location and shape, pointing to the abundance of insoluble phosphate species, while in brain correlations and co-localisation of Gd with P, Ca, Zn, as well as Fe was observed (118).

However, despite of all the ongoing research, the mechanism of the Gd incorporation in bone remains undetermined, and the form, in which it is deposited, is not known. The investigation of spatial distribution of Gd within bone can be instrumental in understanding that, and such studies are called for (121). Although skin deposition mechanism might differ from the accumulation in bone, we also found Gd in calcified regions. Darrah et al. suggested, that ionic Gd^{3+} released from Gd-chelates is subsequently incorporated into the carbonated calcium hydroxyapatite mineral phase of bone (102). Such a process, so-called “transmetallation”, in which the molecule of GBCA supposedly undergoes in *in vivo* environment, refers to the competition between endogenous cations (Fe^{3+}, Zn^{2+}, Mg^{2+}, Ca^{2+}, etc.) and Gd^{3+}, as well as between endogenous anions (carbonate, hydroxide, phosphate, etc.) and the ligand. The Ca-transmetallation is supported by Gd similarity to Ca, the ionic radii of the ions are 107.8 pm for Gd and 114 pm for calcium. In this context, we would like to mention our previous study on Sr incorporation into bone, as Sr is also chemically similar to Ca. In patients who received Sr ranelate for treatment of osteoporosis, Sr was predominantly found in the newly formed bone matrix (formed in the period of increased Sr serum levels) and it was incorporated into the hydroxyapatite crystals changing/increasing the crystal lattice constant (122,123). Therefore, we could hypothesise, that Gd retention is of the same nature, which can be further assessed by speciation analysis.

The other possible transmetallation competitor is Zn, which was already suggested by some of the *ex vivo* measurements of skin depositions discussed above. In 2010, S. Greenberg published a case report on a patient with chronic Zn poisoning, pointing at possible Gd retention due to Gd-Zn transmetallation (124). With our measurements performed at Diamond Light Source and ESRF synchrotrons with submicrometer beams we focused on the Gd structures within mineralized bone. These imaging experiments revealed a local overlapping of Gd and Zn. Although their distribution patterns are not the same, Gd appears to be present only in the areas of high Zn content. The previous investigations by our group demonstrated high content of Zn, Pb and Sr in the cement lines (83). Present findings showing interdependencies between Gd and Zn, might support the Gd-Zn transmetallation as mechanism of Gd retention.

Significance and possible toxicity

Gadolinium belongs to the group of rare-earth elements, it is normally not found in living organisms, and it is highly toxic in its free ionic Gd^{3+} form (88). Bone tissue is metabolically active, and continually undergoes remodelling. Therefore, slow endogenous Gd release into the bloodstream is likely to occur, and the risk is even higher in subjects with increased bone resorption (pregnancy,

lactation, during menopause; in osteoporotic patients) (102,125). Increase in safety concerns regarding the use of GBCAs triggered animal research, investigating Gd retention by various tissues, under single or repeated administration of GBCAs in healthy animals, as well as in induced disease models. Jost et al. compared linear and macrocyclic GBCAs with regard to brain deposition in rats after 2 weeks of repeated administration using LA-ICP-MS (126). Previously unknown site of Gd accumulation was identified by Delfino et al., who observed Gd deposition in the periodontal tissues in murine model with induced renal disease, using SR-XRF and LA-ICP-MS (127). Interesting results showing differential accumulation of Gd by different bone tissues – cortical, trabecular bone and bone marrow in juvenile and adult rats by ICP-MS were published by Fretellier et al (128). An interesting line of research – usage of GBCAs in pregnancy and potential effect of Gd on foetus, were investigated by Prola-Netto et al. in rhesus macaques, and although only extremely low levels of Gd were found in juvenile tissues after in utero exposure, femur was identified as a site of consistent Gd retention in all the animals (129). Until now, however, the studies allowing elucidation of mechanisms of Gd incorporation into bone, as well as its further fate, were not undertaken, therefore, animal models and studies involving human biopsies are called for (130).

The knowledge about deposition of Gd from GBCAs in bone is of importance, especially in the view of recently gained evidence of its accumulation behaviour in brain tissue, and possible risks associated with toxicity of free Gd. To the best of our knowledge these measurements are the first attempt of imaging Gd accumulations in the bone tissue, which is of exceptional value for understanding the mechanisms of Gd retention and, further, for predictions regarding the safety of GBCAs.

Conclusions and outlook

The obtained Gd concentration can only be given as indicative, and, since both used methods of quantification have certain limitations, it might be more correct to provide the range for the maximum content, i.e. 70-270 µg/g. This value obtained from the small bone area and representing localized Gd accumulation by no means can be compared with the literature averaged bulk values.

Summarizing the key questions for the further research we suggest to focus on:

(i) systematic analysis of biopsies from patients with known history of GBCA intake in comparison with controls without clinical Gd exposure,

(ii) animal studies comparing Gd-supplemented and control animals to distinguish accumulation patterns for continuous, as well as short time exposure events,

(iii) quantification of Gd within bone which can be achieved using matrix-matched standards (the other elemental imaging methods, such as LA-ICP-MS and SIMS could be applied as well);

(iv) the speciation of the deposited Gd has to be performed, e.g. by XANES and EXAFS to gain knowledge about the specific chemical form, which is essential in predicting the possible health hazard (toxicity).

7. Concluding remarks and outlook

In this thesis the versatility of µXRF as a stand-alone technique for analysis of biological material, and also in combination with other imaging modalities is demonstrated.

Collaboration on 'marrying' µXRF with other imaging methods such as LA-ICP-MS and MALDI-MSI had been fostered and successfully realized within the frame of doctoral program MEIBio at TU Wien. In both cases thin slices of biological tissues were employed, and each sample was analysed twice: by laboratory µXRF and by other modality.

Sections of chicken phalanges were imaged by tandem MALDI-MSI + µXRF, which allowed collecting both elemental and molecular information – e.g. distribution of a specific lipid and Ca/P (see chapter 3.1). This project allowed testing different kinds of supporting materials and workflows. The techniques have similar lateral resolution and based on our experiments can very well be applied to one and the same sample. Further refining of sample preparation procedure could be recommended for future measurements, yet overall, the described approach can already be employed. Correlated µXRF + MALDI-MSI output has apparent value in biomedical research.

LA-ICP-MS and µXRF are both elemental imaging techniques. In the proof-of-concept project we investigated a complex biological sample – cuts of human femoral head – with laboratory µXRF and LA-ICP-MS (see chapter 3.2). Distribution information in bone and cartilage was provided for following elements: Ca, P, S, Zn, K (with µXRF only in one sample). LA-ICP-MS also supplemented elemental maps of "light metals" – Na and Mg. The comparison of the techniques and correlation of the qualitative and quantitative results was performed.

The third attempted combination of methods included SR-µXRF (ANKA) and ToF-SIMS (chapter 3.3). The measurements were performed on one sample, PMMA-embedded bone block. The applicability of such a combination can be improved through a well-designed sample preparation. Due to higher resolution of ToF-SIMS (which by far exceeded the resolution of the employed synchrotron setup), the methods can be profitably used in the order µXRF → ToF-SIMS to resolve specific tissue/cellular structures (by ToF-SIMS) within broader/coarser context supplied by (SR-)/µXRF.

As a stand-alone technique laboratory µXRF allowed visualizing the distribution of elements in rat bone tissue carrying embedded implant (at different degradation stages), with a focus on Mg and Y (chapter 4). In all the samples a tendency for Y to migrate deeper into the bone tissue was observed. By contrast, Mg content sharply decreased in the immediate vicinity of the implant's interface. For such composition of Mg-based alloys, a potential health impact of Y should be considered.

Two more projects, dealing with investigation of human bone samples were carried out at synchrotron facilities.

A possible connection between osteoporosis and Mn content in osseous tissue was studied (chapter 5). Transiliac bone biopsy samples from male patients with idiopathic osteoporosis tend to contain less Mn globally in bone tissue as compared to healthy controls. For bone samples taken from femoral neck of osteoporotic women such difference in Mn content compared to controls could not be demonstrated.

Gd distribution was investigated in human bone tissue (chapter 6). Gd accumulations were observed within the specific structures: cement lines and at the interface between mineralized bone matrix and vascular canals (so-called Haversian and Volkmann's canals). Furthermore, Gd concentration was assessed in such accumulations, and according to the evaluation it is in the range 70-270 µg/g. The potential sources of Gd include administration of gadolinium-based contrast agent for MRI procedure, but also the environmental exposure is possible – which calls for the further investigations.

7.1 Outlook

A few general remarks can be made:

- Whether µXRF is used individually or in combination, sample preparation procedures require great scrutiny. In our experience, detailed sample preparation protocols are hard to come by. However, even less information is available on potential influence of the sample preparation procedure on a sample (e.g. introduction of unwanted elements, which are otherwise not present in the sample; washing out/smearing of the elements or, vice versa, creation of artificial 'hotspots' and accumulations) as well as on the lack thereof. A shift in the scientific community encouraging systemic investigations of this aspect and publication of the results would be highly desirable.
- The development of the wider array of commercially available certified matrix-matching standards is invaluable for elemental imaging.
- There is a great potential in combining the imaging methods. But before method correlations are proposed for specific topics and projects, they could be thoroughly and intensively investigated on model samples. A PhD programs such as MEIBio offer an ideal academic milieu for this kind of research.
- In many instances within the frame of this thesis, home-made software and manual handling had to be employed. Therefore, automated data management and software solutions (fitting, imaging, correlation, statistical, etc.) available to the broad scientific community, as well as workshops, articles, manuals devoted to exchange of knowledge in this areas deserve universal support.

With regard to the projects described in this thesis, some additional investigations can be proposed.

In case of Mn in osteoporotic samples:

- For part of the dataset (female samples, measured at BESSY synchrotron) the data analysis has to be performed;
- A portion of the sample set, male iliac crest biopsies, was investigated twice – both at ANKA, and BESSY. Upon „extracting" these specific samples, we would expect to see comparable elemental ratios across synchrotrons;
- If the latter assumption is confirmed that would in turn allow aggregating and combining the data from these two synchrotrons.

Due to potential health implications, the Gd project also deserves follow-up investigations, which could include:

- Collection of relevant samples (biopsies from patients with known history of GBCA intake in comparison with controls without clinical Gd exposure) and their systematic analysis of biopsies;
- Animal studies comparing Gd-supplemented and control animals;
- Cross-validation of the qualitative and quantitative results obtained by SR-µXRF is still possible (as the samples are essentially intact). For this analysis preparation of matrix-matched standards with Gd would be necessary, and the measurements can be performed using, for example LA-ICP-MS;
- Finally, the speciation analysis can be performed using the available samples, to gain knowledge about the specific chemical form in which Gd is stored in bone tissue. This can be done e.g. by XANES.

Bibliography

1. Taylor A, Barlow N, Day MP, Hill S, Patriarca M, White M. Atomic spectrometry update: review of advances in the analysis of clinical and biological materials, foods and beverages. J Anal At Spectrom [Internet]. 2017;32(3):432–76. Available from: https://pubs.rsc.org/en/content/articlelanding/2014/JA/c4ja90001d

2. Janssens K, Adams FC, Rindby A. Microscopic X-ray Fluorescence Analysis. Chichester: John Wiley and Sons; 2000.

3. Klockenkämper R, von Bohlen A. Total-Reflection X-Ray Fluorescence Analysis and Related Methods [Internet]. 2nd ed. Klockenkämper R, von Bohlen A, editors. Hoboken, New Jersey: John Wiley & Sons, Inc.; 2014. 552 p. Available from: http://doi.wiley.com/10.1002/9781118985953

4. Haschke M. Micro-X-Ray Fluorescence Spectroscopy - Instrumentation and Applications. Springer-Verlag Berlin Heidelberg GmbH. 2014. 367 p.

5. Jenkins R, Gould RW, Gedcke D. Quantitative X-Ray Spectrometry. Dekker M, editor. X-Ray Spectrometry. New York & Basel: Marcel Dekker Inc.; 1981. 586 p.

6. Janssens K. X-Ray Fluorescence Analysis. In: Handbook of Spectroscopy [Internet]. Weinheim, Germany: Wiley-VCH Verlag GmbH & Co. KGaA; 2014. p. 449–506. Available from: http://hdl.handle.net/10067/429170151162165141

7. Kraihamer M. Optimization of a low power spectrometer for Total Reflection X-ray Fluorescence analysis [Internet]. TU Wien; 2017. Available from: https://doi.org/10.34726/hss.2017.39325

8. Singh S, Versaci R, Laso Garcia A, Morejon L, Ferrari A, Molodtsova M, et al. Compact high energy x-ray spectrometer based on forward Compton scattering for high intensity laser plasma experiments. Rev Sci Instrum [Internet]. 2018 Aug;89(8):085118. Available from: http://aip.scitation.org/doi/10.1063/1.5040979

9. Lawrence Berkeley National Laboratory. X-ray data booklet [Internet]. 3 edition. Lawrence Berkeley National Laboratory; 2009. 176 p. Available from: https://xdb.lbl.gov/xdb-new.pdf

10. Shen G, Wang Y. High-pressure Apparatus Integrated with Synchrotron Radiation. Rev Mineral Geochemistry [Internet]. 2014 Jan 1;78(1):745–77. Available from: https://pubs.geoscienceworld.org/rimg/article/78/1/745-777/141081

11. DESY (Deutsches Elektronen-Synchrotron). How does a synchrotron radiation source work? [Internet]. Available from: https://photon-science.desy.de/research/students__teaching/primers/synchrotron_radiation/index_eng.html

12. Winick H, Brown G, Halbach K, Harris J. Wiggler and undulator magnets. Phys Today [Internet]. 1981 May;34(5):50–63. Available from: http://physicstoday.scitation.org/doi/10.1063/1.2914568

13. Beckhoff B, Kanngießer B, Langhoff N, Wedell R, Wolff H, editors. Handbook of Practical X-Ray Fluorescence Analysis [Internet]. Handbook of Practical X-Ray Fluorescence Analysis. Berlin, Heidelberg: Springer Berlin Heidelberg; 2006. Available from: http://link.springer.com/10.1007/978-3-540-36722-2

14. Mirion Technologies Inc. Si(Li) Detector X-ray | Silicon Lithium Detector for X-ray Spectroscopy Data Sheet [Internet]. 2013. p. 3. Available from: https://www.mirion.com/products/sili-detector-x-ray-silicon-lithium-detector-for-x-ray-spectroscopy

15. Oxford Instruments. Silicon Drift Detectors Explained [Internet]. Oxford Instruments. 2012. p.

28. Available from: http://www.oxford-instruments.com/products/x-ray-microanalysis/Documents/SDD Explained.pdf

16. Rauwolf M. Distribution of Zinc and other trace elements in pathological human bone and in histological transition zones : An approach with micro and nano resolution elemental imaging by synchrotron XRF. Technische Universität Wien; 2018.

17. Yamauchi K, Mimura H, Kimura T, Yumoto H, Handa S, Matsuyama S, et al. Single-nanometer focusing of hard x-rays by Kirkpatrick-Baez mirrors. J Phys Condens Matter. 2011;23(39).

18. Snigireva I, Snigirev A. X-Ray microanalytical techniques based on synchrotron radiation. J Environ Monit [Internet]. 2006;8(1):33–42. Available from: https://doi.org/10.1039/B511446M

19. AXO Dresden GmbH. AXO X-ray Optics [Internet]. 2022. Available from: https://www.axo-dresden.de/en/products/x-ray-optics

20. Wobrauschek P, Frank B, Zöger N, Streli S, Cernohlawek N, Jokubonis C, et al. Micro XRF of light elements using a polycapillary lens and an ultra thin window silicon drift detector inside a vacuum chamber. Adv X-ray Anal. 2005;48:229–35.

21. Smolek S, Streli C, Zoeger N, Wobrauschek P. Improved micro x-ray fluorescence spectrometer for light element analysis. Rev Sci Instrum [Internet]. 2010 May [cited 2014 Jul 24];81(5):053707. Available from: http://www.ncbi.nlm.nih.gov/pubmed/20515145

22. Simon R, Buth G, Hagelstein M. The X-ray-fluorescence facility at ANKA, Karlsruhe: Minimum detection limits and micro probe capabilities. Nucl Instruments Methods Phys Res Sect B Beam Interact with Mater Atoms [Internet]. 2003 Jan;199:554–8. Available from: https://linkinghub.elsevier.com/retrieve/pii/S0168583X02014180

23. Zizak I. The mySpot beamline at BESSY II. J large-scale Res Facil JLSRF [Internet]. 2016 Dec 21;2:A102. Available from: https://jlsrf.org/index.php/lsf/article/view/95

24. ESRF. ID13 - MICROFOCUS BEAMLINE [Internet]. Available from: https://www.esrf.fr/cms/live/live/en/sites/www/home/UsersAndScience/Experiments/XNP/ID13.html

25. Diamond Light Source. B16: Test Beamline [Internet]. Available from: https://www.diamond.ac.uk/Science/Research/Optics/B16.html

26. Rauwolf M, Turyanskaya A, Ingerle D, Szoboszlai N, Pape I, Malandain AW, et al. Characterization of a submicro-X-ray fluorescence setup on the B16 beamline at Diamond Light Source. J Synchrotron Radiat [Internet]. 2018 Jul 1;25(4):1189–95. Available from: https://doi.org/10.1107/S1600577518006203

27. International Atomic Energy Agency (IAEA). Quantitative X Ray Analysis System. User's Manual and Guide to X Ray Fluorescence Technique [Internet]. 2009. Available from: https://www.iaea.org/publications/7884/quantitative-x-ray-analysis-system

28. Solé VA, Papillon E, Cotte M, Walter P, Susini J. A multiplatform code for the analysis of energy-dispersive X-ray fluorescence spectra. Spectrochim Acta Part B At Spectrosc. 2007 Jan;62(1):63–8.

29. Alfeld M, Janssens K. Strategies for processing mega-pixel X-ray fluorescence hyperspectral data: a case study on a version of Caravaggio's painting Supper at Emmaus. J Anal At Spectrom [Internet]. 2015;30(3):777–89. Available from: https://pubs.rsc.org/en/content/articlelanding/2015/JA/C4JA00387J

30. Zlabinger J. Development of a peak deconvolution software for X-ray fluorescence spectra

[Internet]. TU Wien; 2022. Available from: https://doi.org/10.34726/hss.2022.86963

31. Turyanskaya A, Smetaczek S, Pichler V, Rauwolf M, Perneczky L, Roschger A, et al. Correlation of µXRF and LA-ICP-MS in the analysis of a human bone-cartilage sample. J Anal At Spectrom [Internet]. 2021;36(7):1512–23. Available from: https://pubs.rsc.org/en/content/articlelanding/2021/JA/D1JA00007A

32. Euro-BioImaging ERIC [Internet]. Available from: https://www.eurobioimaging.eu/

33. BioImaging Austria - Correlated Multimodal Imaging Node Austria (CMI) [Internet]. Available from: https://www.bioimaging-austria.at/

34. Svirkova A, Turyanskaya A, Perneczky L, Streli C, Marchetti-Deschmann M. Multimodal imaging of undecalcified tissue sections by MALDI MS and µXRF. Analyst [Internet]. 2018;143(11):2587–95. Available from: https://doi.org/10.1039/C8AN00313K

35. Fujimura Y, Miura D. MALDI Mass Spectrometry Imaging for Visualizing In Situ Metabolism of Endogenous Metabolites and Dietary Phytochemicals. Metabolites [Internet]. 2014 May 9;4(2):319–46. Available from: http://www.mdpi.com/2218-1989/4/2/319

36. Ščupáková K, Balluff B, Tressler C, Adelaja T, Heeren RMA, Glunde K, et al. Cellular resolution in clinical MALDI mass spectrometry imaging: the latest advancements and current challenges. Clin Chem Lab Med [Internet]. 2020 Jun 25;58(6):914–29. Available from: https://www.degruyter.com/document/doi/10.1515/cclm-2019-0858/html

37. Tuck M, Grélard F, Blanc L, Desbenoit N. MALDI-MSI Towards Multimodal Imaging: Challenges and Perspectives. Front Chem [Internet]. 2022 May 9;10(May):1–11. Available from: https://www.frontiersin.org/articles/10.3389/fchem.2022.904688/full

38. Good CJ, Neumann EK, Butrico CE, Cassat JE, Caprioli RM, Spraggins JM. High Spatial Resolution MALDI Imaging Mass Spectrometry of Fresh-Frozen Bone. Anal Chem [Internet]. 2022 Feb 22;94(7):3165–72. Available from: https://pubs.acs.org/doi/10.1021/acs.analchem.1c04604

39. Boughton BA, Thinagaran D, Sarabia D, Bacic A, Roessner U. Mass spectrometry imaging for plant biology: a review. Phytochem Rev [Internet]. 2016 Jun 13;15(3):445–88. Available from: http://link.springer.com/10.1007/s11101-015-9440-2

40. Pushie MJ, Pickering IJ, Korbas M, Hackett MJ, George GN. Elemental and Chemically Specific X-ray Fluorescence Imaging of Biological Systems. Chem Rev [Internet]. 2014 Sep 10;114(17):8499–541. Available from: http://pubs.acs.org/doi/abs/10.1021/cr4007297

41. Svirkova A, Turyanskaya A, Allmaier G, Streli C, Marchetti-Deschmann M. Sectioning of undecalcified bone tissue for multimodal MALDI-MS and µ-XRF imaging [Internet]. OurCon III, Pisa, Italy. 2015. Available from: https://repositum.tuwien.at/handle/20.500.12708/99902

42. Perneczky L. Implementation of a confocal synchrotron radiation induced micro X-ray fluorescence system for bone analysis at the X-ray fluorescence beamline of ELETTRA synchrotron [Internet]. TU Wien; 2018. Available from: https://doi.org/10.34726/hss.2018.35502

43. Smolek S. Entwicklung eines energiedispersiven Mikro-Röntgenfluoreszenzspektrometers zur Analyse leichter Elemente [Internet]. TU Wien; 2014. Available from: https://doi.org/10.34726/hss.2014.25309

44. Schneider CA, Rasband WS, Eliceiri KW. NIH Image to ImageJ: 25 years of image analysis. Nat Methods [Internet]. 2012 Jul 1;9(7):671–5. Available from: http://dx.doi.org/10.1038/nmeth.2089

45. Hachmöller O, Buzanich AG, Aichler M, Radtke M, Dietrich D, Schwamborn K, et al.

Elemental bioimaging and speciation analysis for the investigation of Wilson's disease using µXRF and XANES. Metallomics [Internet]. 2016;8(7):648–53. Available from: https://doi.org/10.1039/C6MT00001K

46. Moore KL, Chen Y, van de Meene AML, Hughes L, Liu W, Geraki T, et al. Combined NanoSIMS and synchrotron X-ray fluorescence reveal distinct cellular and subcellular distribution patterns of trace elements in rice tissues. New Phytol [Internet]. 2014 Jan;201(1):104–15. Available from: http://doi.wiley.com/10.1111/nph.12497

47. Lombi E, Smith E, Hansen TH, Paterson D, de Jonge MD, Howard DL, et al. Megapixel imaging of (micro)nutrients in mature barley grains. J Exp Bot [Internet]. 2011 Jan;62(1):273–82. Available from: https://doi.org/10.1093/jxb/erq270

48. Kleeweiss A. Quantifizierungsalgorithmen für Röntgenfluoreszenzanalyse mit Sekundärtargetanregung von verschiedenen Probenarten [Internet]. TU Wien; 2019. Available from: https://doi.org/10.34726/hss.2019.53801

49. Pichler V. Ansätze zur Quantifizierung in der Mikro-XRF-Analyse unter Verwendung eines speziellen Spektrometers für leichte Elemente [Internet]. TU Wien; 2019. Available from: https://doi.org/10.34726/hss.2019.52703

50. Limbeck A, Galler P, Bonta M, Bauer G, Nischkauer W, Vanhaecke F. Recent advances in quantitative LA-ICP-MS analysis: challenges and solutions in the life sciences and environmental chemistry. Anal Bioanal Chem [Internet]. 2015 Sep 14;407(22):6593–617. Available from: https://doi.org/10.1007/s00216-015-8858-0

51. Ghent University. Laser ablation-ICP-MS [Internet]. Available from: https://www.ams.ugent.be/laser-ablation-icp-ms

52. HORIBA. X-ray Fluorescence Analyzers [Internet]. Available from: https://www.horiba.com/ind/scientific/products/x-ray-fluorescence-analyzers-xrf/

53. Bonta M. Quantification strategies for elemental imaging of biological samples using Laser Ablation-Inductively Coupled Plasma-Mass Spectrometry (LA-ICP-MS) [Internet]. TU Wien; 2016. Available from: https://doi.org/10.34726/hss.2016.39590

54. Gholap DS, Izmer A, De Samber B, van Elteren JT, Šelih VS, Evens R, et al. Comparison of laser ablation-inductively coupled plasma-mass spectrometry and micro-X-ray fluorescence spectrometry for elemental imaging in Daphnia magna. Anal Chim Acta [Internet]. 2010 Apr;664(1):19–26. Available from: https://doi.org/10.1016/j.aca.2010.01.052

55. Reifschneider O, Vennemann A, Buzanich G, Radtke M, Reinholz U, Riesemeier H, et al. Revealing Silver Nanoparticle Uptake by Macrophages Using SR-µXRF and LA-ICP-MS. Chem Res Toxicol [Internet]. 2020 May 18;33(5):1250–5. Available from: https://pubs.acs.org/doi/10.1021/acs.chemrestox.9b00507

56. Neves VM, Heidrich GM, Rodrigues ES, Enders MSP, Muller EI, Nicoloso FT, et al. La2O3 Nanoparticles: Study of Uptake and Distribution in Pfaffia glomerata (Spreng.) Pedersen by LA-ICP-MS and µ-XRF. Environ Sci Technol [Internet]. 2019 Sep 17;53(18):10827–34. Available from: https://pubs.acs.org/doi/10.1021/acs.est.9b02868

57. Van Malderen SJM, Laforce B, Van Acker T, Vincze L, Vanhaecke F. Imaging the 3D trace metal and metalloid distribution in mature wheat and rye grains via laser ablation-ICP-mass spectrometry and micro-X-ray fluorescence spectrometry. J Anal At Spectrom [Internet]. 2017;32(2):289–98. Available from: https://doi.org/10.1039/C6JA00357E

58. Kollmer F, Paul W, Krehl M, Niehuis E. Ultra high spatial resolution SIMS with cluster ions - approaching the physical limits. Surf Interface Anal [Internet]. 2013 Jan;45(1):312–4. Available from: https://onlinelibrary.wiley.com/doi/10.1002/sia.5093

59. van der Heide P. Secondary Ion Mass Spectrometry: An Introduction to Principles and Practices [Internet]. Hoboken, NJ, USA: John Wiley & Sons, Inc.; 2014. 384 p. Available from: http://doi.wiley.com/10.1002/9781118916780

60. De Samber B, De Rycke R, De Bruyne M, Kienhuis M, Sandblad L, Bohic S, et al. Effect of sample preparation techniques upon single cell chemical imaging: A practical comparison between synchrotron radiation based X-ray fluorescence (SR-XRF) and Nanoscopic Secondary Ion Mass Spectrometry (nano-SIMS). Anal Chim Acta [Internet]. 2020 Apr;1106(January):22–32. Available from: https://doi.org/10.1016/j.aca.2020.01.054

61. Veith L, Dietrich D, Vennemann A, Breitenstein D, Engelhard C, Karst U, et al. Combination of micro X-ray fluorescence spectroscopy and time-of-flight secondary ion mass spectrometry imaging for the marker-free detection of CeO2 nanoparticles in tissue sections. J Anal At Spectrom [Internet]. 2018;33(3):491–501. Available from: https://doi.org/10.1039/C7JA00325K

62. Mazel V, Richardin P, Debois D, Touboul D, Cotte M, Brunelle A, et al. Identification of Ritual Blood in African Artifacts Using TOF-SIMS and Synchrotron Radiation Microspectroscopies. Anal Chem [Internet]. 2007 Dec 1;79(24):9253–60. Available from: https://pubs.acs.org/doi/10.1021/ac070993k

63. Roschger P, Fratzl P, Eschberger J, Klaushofer K. Validation of quantitative backscattered electron imaging for the measurement of mineral density distribution in human bone biopsies. Bone [Internet]. 1998 Oct [cited 2014 Jul 4];23(4):319–26. Available from: http://www.sciencedirect.com/science/article/pii/S8756328298001124

64. Roschger P, Paschalis EP, Fratzl P, Klaushofer K. Bone mineralization density distribution in health and disease. Bone [Internet]. 2008 Mar [cited 2014 May 27];42(3):456–66. Available from: http://www.sciencedirect.com/science/article/pii/S8756328207008162

65. Brenner F. Advanced applications of time-of-flight secondary ion mass spectrometry for high resolution elemental imaging analysis [Internet]. TU Wien; 2017. Available from: http://hdl.handle.net/20.500.12708/78770

66. Henss A, Hild A, Rohnke M, Wenisch S, Janek J. Time of flight secondary ion mass spectrometry of bone—Impact of sample preparation and measurement conditions. Biointerphases [Internet]. 2016 Jun;11(2):02A302. Available from: http://avs.scitation.org/doi/10.1116/1.4928211

67. Schaepe K, Bhandari DR, Werner J, Henss A, Pirkl A, Kleine-Boymann M, et al. Imaging of Lipids in Native Human Bone Sections Using TOF–Secondary Ion Mass Spectrometry, Atmospheric Pressure Scanning Microprobe Matrix-Assisted Laser Desorption/Ionization Orbitrap Mass Spectrometry, and Orbitrap–Secondary Ion Mass Spectrometry. Anal Chem [Internet]. 2018 Aug 7;90(15):8856–64. Available from: https://pubs.acs.org/doi/10.1021/acs.analchem.8b00892

68. Turyanskaya A, Rauwolf M, Grünewald T, Meischel M, Stanzl-Tschegg S, Löffler J, et al. µXRF Elemental Mapping of Bioresorbable Magnesium-Based Implants in Bone. Materials (Basel) [Internet]. 2016 Sep 30;9(10):811. Available from: http://www.mdpi.com/1996-1944/9/10/811

69. Chen Y, Xu Z, Smith C, Sankar J. Recent advances on the development of magnesium alloys for biodegradable implants. Acta Biomater [Internet]. 2014;10(11):4561–73. Available from: http://dx.doi.org/10.1016/j.actbio.2014.07.005

70. Kraus T, Fischerauer SF, Hänzi AC, Uggowitzer PJ, Löffler JF, Weinberg AM. Magnesium alloys for temporary implants in osteosynthesis: In vivo studies of their degradation and interaction with bone. Acta Biomater [Internet]. 2012 Mar;8(3):1230–8. Available from: http://dx.doi.org/10.1016/j.actbio.2011.11.008

71. Hänzi AC, Gerber I, Schinhammer M, Löffler JF, Uggowitzer PJ. On the in vitro and in vivo degradation performance and biological response of new biodegradable Mg–Y–Zn alloys☆. Acta Biomater [Internet]. 2010 May;6(5):1824–33. Available from: http://dx.doi.org/10.1016/j.actbio.2009.10.008

72. Celarek A, Kraus T, Tschegg EK, Fischerauer SF, Stanzl-Tschegg S, Uggowitzer PJ, et al. PHB, crystalline and amorphous magnesium alloys: Promising candidates for bioresorbable osteosynthesis implants? Mater Sci Eng C [Internet]. 2012;32(6):1503–10. Available from: http://dx.doi.org/10.1016/j.msec.2012.04.032

73. Castellani C, Lindtner RA, Hausbrandt P, Tschegg E, Stanzl-Tschegg SE, Zanoni G, et al. Bone-implant interface strength and osseointegration: Biodegradable magnesium alloy versus standard titanium control. Acta Biomater [Internet]. 2011;7(1):432–40. Available from: http://dx.doi.org/10.1016/j.actbio.2010.08.020

74. Grünewald TA, Rennhofer H, Hesse B, Burghammer M, Stanzl-Tschegg SE, Cotte M, et al. Magnesium from bioresorbable implants: Distribution and impact on the nano- and mineral structure of bone. Biomaterials [Internet]. 2016;76:250–60. Available from: http://www.sciencedirect.com/science/article/pii/S0142961215008649

75. Ramsden EN. A Review of Experimental Work on Radio-yttrium Comprising 1. The Tissue Distribution, 2. The Mechanism of Deposition in Bone, and 3. The State in the Blood. Int J Radiat Biol Relat Stud Physics, Chem Med [Internet]. 1961 Jan 3;3(4):399–410. Available from: http://www.tandfonline.com/doi/full/10.1080/09553006114550461

76. Daigneault EA. The distribution of intravenously administered yttrium chloride (carrier free) in the rhesus monkey. Toxicol Appl Pharmacol [Internet]. 1963 May;5(3):331–43. Available from: http://linkinghub.elsevier.com/retrieve/pii/0041008X63900929

77. Appelgren L-E, Nelson A, Ullberg S. Distribution of Yttrium 91 In Mice Studied by Whole Body Autoradiography. Acta Radiol Ther Phys Biol [Internet]. 1966;4(1):41–8. Available from: http://www.tandfonline.com/doi/full/10.3109/02841866609133130

78. Herring GM, Vaughan J, Williamson M. Preliminary report on the site of localization and possible binding agent for yttrium, americium and plutonium in cortical bone. Health Phys [Internet]. 1962 Dec;8:717–24. Available from: http://www.ncbi.nlm.nih.gov/pubmed/13954076

79. Williams PA, Peacocke AR. The binding of calcium and yttrium ions to a glycoprotein from bovine cortical bone. Biochem J [Internet]. 1967 Dec 1;105(3):1177–85. Available from: http://www.ncbi.nlm.nih.gov/pubmed/16742544

80. Johnson I, Liu H. A Study on Factors Affecting the Degradation of Magnesium and a Magnesium-Yttrium Alloy for Biomedical Applications. Zheng J, editor. PLoS One [Internet]. 2013 Jun 14;8(6):e65603. Available from: https://doi.org/10.1371/journal.pone.0065603

81. Chen P, Chakraborty S, Mukhopadhyay S, Lee E, Paoliello MMB, Bowman AB, et al. Manganese homeostasis in the nervous system. J Neurochem [Internet]. 2015 Aug;134(4):601–10. Available from: https://onlinelibrary.wiley.com/doi/10.1111/jnc.13170

82. O'Neal SL, Zheng W. Manganese Toxicity Upon Overexposure: a Decade in Review. Curr Environ Heal Reports [Internet]. 2015 Sep 1;2(3):315–28. Available from: http://link.springer.com/10.1007/s40572-015-0056-x

83. Pemmer B, Roschger A, Wastl A, Hofstaetter JG, Wobrauschek P, Simon R, et al. Spatial distribution of the trace elements zinc, strontium and lead in human bone tissue. Bone [Internet]. 2013 Nov;57(1):184–93. Available from: https://doi.org/10.1016/j.bone.2013.07.038

84. Landete-Castillejos T. Alternative hypothesis for the origin of osteoporosis The role of Mn. Front Biosci [Internet]. 2012 [cited 2014 Aug 13];E4(4):468. Available from: https://doi.org/10.2741/e468

85. Turyanskaya A, Rauwolf M, Pichler V, Simon R, Burghammer M, Fox OJL, et al. Detection and imaging of gadolinium accumulation in human bone tissue by micro- and submicro-XRF. Sci Rep [Internet]. 2020 Dec 14;10(1):6301. Available from: http://www.nature.com/articles/s41598-020-63325-9

86. Lohrke J, Frenzel T, Endrikat J, Alves FC, Grist TM, Law M, et al. 25 Years of Contrast-Enhanced MRI: Developments, Current Challenges and Future Perspectives. Adv Ther [Internet]. 2016 Jan 25;33(1):1–28. Available from: http://link.springer.com/10.1007/s12325-015-0275-4

87. Fraum TJ, Ludwig DR, Bashir MR, Fowler KJ. Gadolinium-based contrast agents: A comprehensive risk assessment. J Magn Reson Imaging [Internet]. 2017 Aug;46(2):338–53. Available from: https://onlinelibrary.wiley.com/doi/10.1002/jmri.25625

88. Ramalho J, Semelka RC, Ramalho M, Nunes RH, AlObaidy M, Castillo M. Gadolinium-Based Contrast Agent Accumulation and Toxicity: An Update. Am J Neuroradiol [Internet]. 2016 Jul 1;37(7):1192–8. Available from: http://www.ajnr.org/cgi/doi/10.3174/ajnr.A4615

89. Guo BJ, Yang ZL, Zhang LJ. Gadolinium Deposition in Brain: Current Scientific Evidence and Future Perspectives. Front Mol Neurosci [Internet]. 2018;11(September):1–12. Available from: https://www.frontiersin.org/article/10.3389/fnmol.2018.00335/full

90. Rogosnitzky M, Branch S. Gadolinium-based contrast agent toxicity: a review of known and proposed mechanisms. BioMetals [Internet]. 2016 Jun 6;29(3):365–76. Available from: http://link.springer.com/10.1007/s10534-016-9931-7

91. Grobner T. Gadolinium - a specific trigger for the development of nephrogenic fibrosing dermopathy and nephrogenic systemic fibrosis? Nephrol Dial Transplant [Internet]. 2006 Jun 1;21(6):1745–1745. Available from: http://ndt.oxfordjournals.org/cgi/doi/10.1093/ndt/gfl294

92. Marckmann P, Skov L, Rossen K, Dupont A, Damholt MB, Heaf JG, et al. Nephrogenic Systemic Fibrosis: Suspected Causative Role of Gadodiamide Used for Contrast-Enhanced Magnetic Resonance Imaging. J Am Soc Nephrol [Internet]. 2006 Sep;17(9):2359–62. Available from: https://pubmed.ncbi.nlm.nih.gov/16885403/

93. Idée J-M, Fretellier N, Robic C, Corot C. The role of gadolinium chelates in the mechanism of nephrogenic systemic fibrosis: A critical update. Crit Rev Toxicol [Internet]. 2014;44(10):895–913. Available from: http://www.ncbi.nlm.nih.gov/pubmed/25257840

94. EMA. European Medicines Agency - Human medicines - Gadolinium-containing contrast agents. 2017;(July). Available from: https://www.ema.europa.eu/en/medicines/human/referrals/gadolinium-containing-contrast-agents

95. Abraham JL, Chandra S, Thakral C, Abraham JM. SIMS imaging of gadolinium isotopes in tissue from Nephrogenic Systemic Fibrosis patients: Release of free Gd from magnetic resonance imaging (MRI) contrast agents. Appl Surf Sci [Internet]. 2008 Dec;255(4):1181–4. Available from: https://doi.org/10.1016/j.apsusc.2008.05.140

96. Birka M, Wentker KS, Lusmöller E, Arheilger B, Wehe CA, Sperling M, et al. Diagnosis of Nephrogenic Systemic Fibrosis by means of Elemental Bioimaging and Speciation Analysis. Anal Chem [Internet]. 2015 Mar 17;87(6):3321–8. Available from: https://pubs.acs.org/doi/10.1021/ac504488k

97. High WA, Ranville JF, Brown M, Punshon T, Lanzirotti A, Jackson BP. Gadolinium

deposition in nephrogenic systemic fibrosis: An examination of tissue using synchrotron x-ray fluorescence spectroscopy. J Am Acad Dermatol [Internet]. 2010;62(1):38–44. Available from: http://dx.doi.org/10.1016/j.jaad.2009.07.018

98. George SJ, Webb SM, Abraham JL, Cramer SP. Synchrotron X-ray analyses demonstrate phosphate-bound gadolinium in skin in nephrogenic systemic fibrosis. Br J Dermatol [Internet]. 2010 Nov;163(5):1077–81. Available from: http://linkinghub.elsevier.com/retrieve/pii/S0048357511000411

99. Sanyal S, Marckmann P, Scherer S, Abraham JL. Multiorgan gadolinium (Gd) deposition and fibrosis in a patient with nephrogenic systemic fibrosis--an autopsy-based review. Nephrol Dial Transplant [Internet]. 2011 Nov 1;26(11):3616–26. Available from: https://doi.org/10.1093/ndt/gfr085

100. Flood TF, Stence N V, Maloney JA, Mirsky DM. Pediatric Brain: Repeated Exposure to Linear Gadolinium-based Contrast Material Is Associated with Increased Signal Intensity at Unenhanced T1-weighted MR Imaging. Radiology [Internet]. 2017 Jan;282(1):222–8. Available from: https://pubs.rsna.org/doi/10.1148/radiol.2016160356

101. Murata N, Gonzalez-Cuyar LF, Murata K, Fligner C, Dills R, Hippe D, et al. Macrocyclic and Other Non–Group 1 Gadolinium Contrast Agents Deposit Low Levels of Gadolinium in Brain and Bone Tissue. Invest Radiol [Internet]. 2016 Jul;51(7):447–53. Available from: https://journals.lww.com/00004424-201607000-00005

102. Darrah TH, Prutsman-Pfeiffer JJ, Poreda RJ, Ellen Campbell M, Hauschka P V, Hannigan RE. Incorporation of excess gadolinium into human bone from medical contrast agents. Metallomics [Internet]. 2009;1(6):479–88. Available from: http://www.ncbi.nlm.nih.gov/pubmed/21305156

103. Lord ML, McNeill FE, Gräfe JL, Galusha AL, Parsons PJ, Noseworthy MD, et al. Confirming improved detection of gadolinium in bone using in vivo XRF. Appl Radiat Isot [Internet]. 2017;120:111–8. Available from: http://dx.doi.org/10.1016/j.apradiso.2016.12.011

104. Lord ML, Chettle DR, Gräfe JL, Noseworthy MD, McNeill FE. Observed Deposition of Gadolinium in Bone Using a New Noninvasive in Vivo Biomedical Device: Results of a Small Pilot Feasibility Study. Radiology [Internet]. 2017;000(0):171161. Available from: http://pubs.rsna.org/doi/10.1148/radiol.2017171161

105. Roschger A, Hofstaetter JG, Pemmer B, Zoeger N, Wobrauschek P, Falkenberg G, et al. Differential accumulation of lead and zinc in double-tidemarks of articular cartilage. Osteoarthritis Cartilage [Internet]. 2013 Nov [cited 2014 Jul 4];21(11):1707–15. Available from: http://www.sciencedirect.com/science/article/pii/S1063458413008650

106. Rauwolf M, Pemmer B, Roschger A, Turyanskaya A, Smolek S, Maderitsch A, et al. Increased zinc accumulation in mineralized osteosarcoma tissue measured by confocal synchrotron radiation micro X-ray fluorescence analysis. X-Ray Spectrom [Internet]. 2017;46(1):56–62. Available from: http://doi.wiley.com/10.1002/xrs.2727

107. Ščančar J, Milačič R, Benedik M, Bukovec P. Determination of trace elements and calcium in bone of the human iliac crest by atomic absorption spectrometry. Clin Chim Acta [Internet]. 2000 Mar;293(1–2):187–97. Available from: https://linkinghub.elsevier.com/retrieve/pii/S0009898199002399

108. Zioła-Frankowska A, Kubaszewski Ł, Dąbrowski M, Kowalski A, Rogala P, Strzyżewski W, et al. The Content of the 14 Metals in Cancellous and Cortical Bone of the Hip Joint Affected by Osteoarthritis. Biomed Res Int [Internet]. 2015;2015:1–23. Available from: http://www.hindawi.com/journals/bmri/2015/815648/

109. Gwenzi W, Mangori L, Danha C, Chaukura N, Dunjana N, Sanganyado E. Sources, behaviour,

and environmental and human health risks of high-technology rare earth elements as emerging contaminants. Sci Total Environ [Internet]. 2018;636:299–313. Available from: https://doi.org/10.1016/j.scitotenv.2018.04.235

110. Pagano G, Thomas PJ, Di Nunzio A, Trifuoggi M. Human exposures to rare earth elements: Present knowledge and research prospects. Environ Res [Internet]. 2019;171(February):493–500. Available from: https://doi.org/10.1016/j.envres.2019.02.004

111. Li Y, Yu H, Zheng S, Miao Y, Yin S, Li P, et al. Direct Quantification of Rare Earth Elements Concentrations in Urine of Workers Manufacturing Cerium, Lanthanum Oxide Ultrafine and Nanoparticles by a Developed and Validated ICP-MS. Int J Environ Res Public Health [Internet]. 2016 Mar 22;13(3):350. Available from: http://www.mdpi.com/1660-4601/13/3/350

112. Li Y, Yu H, Li P, Bian Y. Assessment the Exposure Level of Rare Earth Elements in Workers Producing Cerium, Lanthanum Oxide Ultrafine and Nanoparticles. Biol Trace Elem Res [Internet]. 2017;175(2):298–305. Available from: http://dx.doi.org/10.1007/s12011-016-0795-z

113. Rogowska J, Olkowska E, Ratajczyk W, Wolska L. Gadolinium as a new emerging contaminant of aquatic environments. Environ Toxicol Chem [Internet]. 2018 Jun 19;37(6):1523–34. Available from: https://onlinelibrary.wiley.com/doi/10.1002/etc.4116

114. Lingott J, Lindner U, Telgmann L, Esteban-Fernández D, Jakubowski N, Panne U. Gadolinium-uptake by aquatic and terrestrial organisms-distribution determined by laser ablation inductively coupled plasma mass spectrometry. Environ Sci Process Impacts [Internet]. 2016;18(2):200–7. Available from: https://doi.org/10.1039/C5EM00533G

115. Lindner U, Lingott J, Richter S, Jiang W, Jakubowski N, Panne U. Analysis of Gadolinium-based contrast agents in tap water with a new hydrophilic interaction chromatography (ZIC-cHILIC) hyphenated with inductively coupled plasma mass spectrometry. Anal Bioanal Chem [Internet]. 2015 Mar 9;407(9):2415–22. Available from: http://link.springer.com/10.1007/s00216-014-8368-5

116. Gibby WA, Gibby KA, Gibby WA. Comparison of Gd DTPA-BMA (Omniscan) versus Gd HP-DO3A (ProHance) retention in human bone tissue by inductively coupled plasma atomic emission spectroscopy. Invest Radiol [Internet]. 2004;39(3):138–42. Available from: http://www.ncbi.nlm.nih.gov/pubmed/15076005

117. White GW, Gibby W a, Tweedle MF. Comparison of Gd(DTPA-BMA) (Omniscan) Versus Gd(HP-DO3A) (ProHance) Relative to Gadolinium Retention in Human Bone Tissue by Inductively Coupled Plasma Mass Spectroscopy. Invest Radiol. 2006;41(3):272–8.

118. Clases D, Fingerhut S, Jeibmann A, Sperling M, Doble P, Karst U. LA-ICP-MS/MS improves limits of detection in elemental bioimaging of gadolinium deposition originating from MRI contrast agents in skin and brain tissues. J Trace Elem Med Biol [Internet]. 2019;51(October 2018):212–8. Available from: https://doi.org/10.1016/j.jtemb.2018.10.021

119. Milovanovic P, vom Scheidt A, Mletzko K, Sarau G, Püschel K, Djuric M, et al. Bone tissue aging affects mineralization of cement lines. Bone [Internet]. 2018;110:187–93. Available from: https://doi.org/10.1016/j.bone.2018.02.004

120. Skedros JG, Clark GC, Sorenson SM, Taylor KW, Qiu S. Analysis of the Effect of Osteon Diameter on the Potential Relationship of Osteocyte Lacuna Density and Osteon Wall Thickness. Anat Rec Adv Integr Anat Evol Biol [Internet]. 2011 Sep;294(9):1472–85. Available from: http://doi.wiley.com/10.1002/ar.21452

121. Gräfe JL, McNeill FE. Measurement of gadolinium retention: current status and review from an applied radiation physics perspective. Physiol Meas [Internet]. 2018 Jun 28;39(6):06TR01. Available from: https://iopscience.iop.org/article/10.1088/1361-6579/aacc16

122. Roschger P, Manjubala I, Zoeger N, Meirer F, Simon R, Li C, et al. Bone Material Quality in Transiliac Bone Biopsies of Postmenopausal Osteoporotic Women After 3 Years Strontium Ranelate Treatment. J Bone Miner Res [Internet]. 2009 Oct 19;25(4):091019190442039–35. Available from: http://doi.wiley.com/10.1359/jbmr.091028

123. Li C, Paris O, Siegel S, Roschger P, Paschalis E, Klaushofer K, et al. Strontium is Incorporated Into Mineral Crystals Only in Newly Formed Bone During Strontium Ranelate Treatment. J Bone Miner Res [Internet]. 2009 Oct 29;25(5):091029141139034–22. Available from: http://doi.wiley.com/10.1359/jbmr.091038

124. Greenberg SA. Zinc Transmetallation and Gadolinium Retention after MR Imaging: Case Report. Radiology [Internet]. 2010 Dec;257(3):670–3. Available from: http://pubs.rsna.org/doi/10.1148/radiol.10100560

125. Swaminathan S. Gadolinium Toxicity: Iron and Ferroportin as Central Targets. Magn Reson Imaging [Internet]. 2016;8–11. Available from: http://linkinghub.elsevier.com/retrieve/pii/S0730725X16301217

126. Jost G, Frenzel T, Boyken J, Lohrke J, Nischwitz V, Pietsch H. Long-term Excretion of Gadolinium-based Contrast Agents: Linear versus Macrocyclic Agents in an Experimental Rat Model. Radiology [Internet]. 2019 Feb;290(2):340–8. Available from: https://doi.org/10.1148/radiol.2018180135

127. Delfino R, Biasotto M, Candido R, Altissimo M, Stebel M, Salomè M, et al. Gadolinium tissue deposition in the periodontal ligament of mice with reduced renal function exposed to Gd-based contrast agents. Toxicol Lett [Internet]. 2019 Feb;301:157–67. Available from: https://linkinghub.elsevier.com/retrieve/pii/S0378427418320575

128. Fretellier N, Granottier A, Rasschaert M, Grindel A-L, Baudimont F, Robert P, et al. Does Age Interfere With Gadolinium Toxicity and Presence in Brain and Bone Tissues? Invest Radiol [Internet]. 2019 Feb;54(2):61–71. Available from: http://journals.lww.com/00004424-201902000-00001

129. Prola-Netto J, Woods M, Roberts VHJ, Sullivan EL, Miller CA, Frias AE, et al. Gadolinium Chelate Safety in Pregnancy: Barely Detectable Gadolinium Levels in the Juvenile Nonhuman Primate after in Utero Exposure. Radiology [Internet]. 2018 Jan;286(1):122–8. Available from: http://pubs.rsna.org/doi/10.1148/radiol.2017162534

130. Kanal E, Tweedle MF. Residual or Retained Gadolinium: Practical Implications for Radiologists and Our Patients. Radiology [Internet]. 2015 Jun;275(3):630–4. Available from: http://pubs.rsna.org/doi/full/10.1148/radiol.2015150805

Curriculum vitae

EMPLOYMENT

since 04/2020	Project assistant in the installation and maintenance of a Heritage Science Node at X-ray center, TU Wien
04/2015 – 11/2018	Project assistant in FWF project "3D and 2D Distribution of Trace Elements in Pathological Human Bone and in Histological Transition Zones - An Approach with Micro and Nano Resolution Elemental Imaging by Synchrotron XRF" in Radiation Physics group, Atominstitut, TU Wien, Vienna, Austria
02/2014 – 02/2017	Research assistant (pre-doc) in Radiation Physics group, Atominstitut, TU Wien, Vienna, Austria
11/2009 – 05/2013	Researcher in Federal State Budgetary Institution "*Scientific Centre* for *Expert* Evaluation of Medicinal *Products*" of Russian Ministry of *Health, Moscow, Russia*

EDUCATION

since 01/2014	Molecular and Elemental Imaging in Bioscience (MEIBio) PhD Program at TU Wien
09/2004 – 07/2009	Pharmacy at Moscow Medical Academy, Department of Pharmacy Qualification: pharmacist (MPharm), Diploma cum laude

ADDITIONAL TRAINING

10/2010 – 06/2012	Translation and Interpreting at Lomonosov Moscow State University, Faculty of Foreign Languages and Area Studies Additional qualification: Translator and Interpreter in the Field of Professional Communications
08/2009 – 07/2010	Postgraduate Program in Pharmaceutical Technology at Moscow Medical Academy (now I.M. Sechenov First Moscow State Medical University) Qualification: certified specialist in pharmaceutical technology and biopharmaceutics

INTERNATIONAL EXPERIENCE

since 2017	Experiments at European Synchrotron Radiation Facility (ESRF), Grenoble, France
since 2016	Experiments at Synchrotron Radiation Facility DIAMOND, Harwell Science and Innovation Campus, Oxfordshire, UK
since 2016	Experiments at Synchrotron Radiation Facility ELETTRA, Basovizza Trieste, Italy
since 2015	Experiments at Synchrotron Radiation Facility BESSY II, Helmholtz-Zentrum Berlin für Materialien und Energie, Berlin, Germany
since 2014	Experiments at Synchrotron Radiation Facilities ANKA, Karlsruhe, Germany
08/2012	University of Bath; Department of Politics, Languages & International Studies – Course in Russian-English Interpreting and Translation, Bath, England

AWARDS

2015, 2017	Best XRF Poster Award at the Annual Denver X-ray Conference
2016	Young investigator award at the 43rd Annual European Calcified Tissue Society Congress, Rome

TEACHING

since 2016	Co-supervision of Master‘s students (L. Perneczky, A. Winkler)
since 2016	Practical Course in X-Ray Analytical Methods
since 2015	Supervision of project works
since 2015	Practical Exercise in Archaeometry

EXTRACURRICULAR ACTIVITIES

since 2018	Reviewer for the journal of Trace Elements in Medicine and Biology (ISSN: 0946-672X)
04/2018	Töchtertag 2018, Atominstitut, TU Wien XRF of bijouterie objects with girls 11-16 year old
09/2016 – 02/2017	Member of the organising team of 26th Seminar Activation Analysis and Gamma Spectroscopy (SAAGAS 26)
01/2016, 02/2017	FIT – Frauen in die Technik, Atominstitut, TU Wien Informationsveranstaltung für Schülerinnen im Alter von 16 bis 19 Jahren

Publications

The list of publications is organized in the chronological order.

Scientific articles in peer-reviewed journals

1. F. Bilo, L. Borgese, J. Prost, M. Rauwolf, A. Turyanskaya, P. Wobrauschek, P. Kregsamer, C. Streli, U. Pazzaglia and L. Depero. Atomic layer deposition to prevent metal transfer from implants: an X-Ray Fluorescence study. Applied Surface Science 359: 215–220, December 2015, doi: 10.1016/j.apsusc.2015.09.248
2. A. Turyanskaya, M. Rauwolf, T.A. Grünewald, M. Meischel, S. Stanzl-Tschegg, J.F. Löffler, P. Wobrauschek, A.M. Weinberg, H.C. Lichtenegger and Christina Streli. µXRF Elemental Mapping of Bioresorbable Magnesium-Based Implants in Bone. Materials 9(10), 811; September 2016, doi:10.3390/ma9100811
3. L. Borgese, F. Bilo, A. Zacco, E. Bontempi, M. Pasquali, S. Federici, J. Prost, M. Rauwolf, A. Turyanskaya, C. Streli, P. Kregsamer, P. Wobrauschek and L.E. Depero. (Invited) ALD to Prevent Metal Transfer from Implants. ECS Transactions 75(6): 167-175, September 2016, doi: 10.1149/07506.0167ecst
4. M. Rauwolf, A. Turyanskaya, A. Roschger, J. Prost, R. Simon, O. Scharf, M. Radtke, T. Schoonjans, A. Guilherme Buzanich, K. Klaushofer, P. Wobrauschek, J. G. Hofstaetter, P. Roschger, and C. Streli. Synchrotron radiation micro X-ray fluorescence spectroscopy of thin structures in bone samples: comparison of confocal and color X-ray camera setups. Journal of Synchrotron Radiation 24: 307-311, January 2017, doi: 10.1107/S1600577516017057
5. M. Rauwolf, B. Pemmer, A. Roschger, A. Turyanskaya, S. Smolek, A. Maderitsch, P. Hischenhuber, M. Foelser, R. Simon, S. Lang, S.E. Puchner, R. Windhager, K. Klaushofer, P. Wobrauschek, J.G. Hofstaetter, P. Roschger and C. Streli. Increased zinc accumulation in mineralized osteosarcoma tissue measured by confocal synchrotron radiation micro X-ray fluorescence analysis: Increased zinc accumulation in mineralized osteosarcoma. X-Ray Spectrometry 46: 56-62, January 2017, doi: 10.1002/xrs.2727
6. A. Svirkova, A. Turyanskaya, L. Perneczky, C. Streli, M. Marchetti-Deschmann. Multimodal imaging of undecalcified tissue sections by MALDI MS and µXRF. Analyst, 143: 2587-2595, April 2018, doi: 10.1039/C8AN00313K
7. L. Perneczky, M. Rauwolf, D. Ingerle, D. Eichert, F. Brigidi, W. Jark, S. Bjeoumikhova, G. Pepponi, P. Wobrauschek, C. Streli, A. Turyanskaya. Temporary implementation and testing of a confocal SR-µXRF system for bone analysis at the X-ray Fluorescence beamline at Elettra. Nuclear Instruments and Methods in Physics Research A, 897: 114–119, July 2018, doi: 10.1016/j.nima.2018.04.012
8. M. Rauwolf, A. Turyanskaya, D. Ingerle, N. Szoboszlai, I. Pape, A. Malandain, O. Fox, L. Hahn, K. Sawhney, C. Streli. Characterization of a submicro-X-ray fluorescence setup on the B16 beamline at Diamond Light Source. Journal of Synchrotron Radiation, Volume 25, Part 4: 1189-1195, July 2018, doi: 10.1107/S1600577518006203
9. C. Streli, M. Rauwolf, A. Turyanskaya, D. Ingerle, P. Wobrauschek. Elemental imaging of trace elements in bone samples using micro and nano- X-ray fluorescence spectrometry. Applied Radiation and Isotopes, 149: 200–205, July 2019, doi: 10.1016/j.apradiso.2019.04.033
10. A. Turyanskaya, M. Rauwolf, V. Pichler, R. Simon, M. Burghammer, O. J. L. Fox, K. Sawhney, J. G. Hofstaetter, A. Roschger, P. Roschger, P. Wobrauschek & C. Streli. Detection and imaging of gadolinium accumulation in human bone tissue by micro- and submicro-XRF. Sci Rep 10, 6301, April 2020, doi: 10.1038/s41598-020-63325-9
11. D. A. Cardenas, A. Turyanskaya, M. Rauwolf, A. Panahifar, D. Cooper, G. R. Wohl, C. Streli, P. Wobrauschek, Ana Pejović-Milić. Determining Elemental Strontium Distribution in Rat Bones Treated with Strontium Ranelate and Strontium Citrate using 2D micro-XRF and 3D Dual Energy

K-Edge Subtraction Synchrotron Imaging. X-Ray Spectrometry, Volume 49, Issue3: 424-433, May/June 2020, doi: 10.1002/xrs.3127
12. A. Winkler, M. Rauwolf, J.H. Sterba, P. Wobrauschek, C. Streli, A. Turyanskaya. Total reflection X -ray fluorescence analysis of elemental composition of herbal infusions and teas. Journal of the Science of Food and Agriculture, Volume100, Issue11: 4226-4236, August 2020, doi: 10.1002/jsfa.10463
13. A. Turyanskaya, S. Smetaczek, V. Pichler, M. Rauwolf, L. Perneczky, A. Roschger, P. Roschger, P. Wobrauschek, A. Limbeck, C. Streli. Correlation of μXRF and LA-ICP-MS in the analysis of a human bone-cartilage sample. Journal of Analytical Atomic Spectrometry, Issue 7, 36: 1512 – 1523, July 2021, doi: 10.1039/D1JA00007A
14. S. Reier, A. Turyanskaya, P. Heimel, N. Frischauf, D. Meusburger, T. Heuser, N. Drexler, A. Janovszky, C. Streli, P. Slezak, B. Plochberger, P. Dungel, A. Szabo, A. Walter. Cross-modality imaging of bisphosphonate-treated murine jawbones. Analyst, Issue 14, 146, 4683-4699, July 2021, doi: 10.1039/D0AN02373F
15. J. Obhođaš, V. Valković, A. Vinković, D. Sudac, I. Čanađija, T. Pensa, Ž. Fiket, A. Turyanskaya, T. Bretschneider, C. Wilhelmer, G. Gunchin, P. Kregsamer, P. Wobrauschek, and C. Streli. X-ray Fluorescence Techniques for Element Abundance Analysis in Wine. ACS Omega, 6, 35: 22643–22654, August 2021, doi: 10.1021/acsomega.1c02731
16. M. Rauwolf, A. Turyanskaya, P. Wobrauschek, K. Sawhney, A. Roschger, P. Roschger, C. Streli, J. Hofstätter. Thickness determination of the tidemark of human articular cartilage using high-resolution micro-XRF imaging of zinc and lead. Osteoarthritis and Cartilage Open, 3, S. 1 – 6, September 2021, doi: 10.1016/j.ocarto.2021.100182

Book contributions

1. K. Keuenhof, A. Turyanskaya, C. Streli et al.: "Multimodality imaging beyond CLEM: Showcases of combined in-vivo preclinical imaging and ex-vivo microscopy to detect murine mural vascular lesions"; in: "Methods in Cell Biology/Correlative Light and Electron Microscopy IV", T. Müller-Reichert, P. Verkade (Hrg.); Elsevier, 2020, ISBN: 978-0-12-822058-0, S. 389 - 415
2. C. Streli, A. Turyanskaya: "Micro-X-ray fluorescence spectroscopy"; in: "Imaging Modalities for Biological and Preclinical Research: A Compendium Volume 1", Institute of Physics Publishing, 2021, ISBN: 9780750330572, S. 1 - 7

Conference contributions

Talks

1. C. Streli, P. Wobrauschek, D. Ingerle, J. Prost, M. Rauwolf, A. Turyanskaya. Synchrotron Radiation Induced X-ray spectrometry - special techniques and applications. IAEA Technical Meeting on Developments in Instrumentation and Novel Techniques for X-Ray Spectrometry Applications, Vienna, Austria (**invited**); 28 September – 02 October 2015

2. A. Turyanskaya, M. Rauwolf, A. Roschger, B. Pemmer, J. Prost, R. Simon, P. Roschger, J. G. Hofstaetter, T. Landete-Castillejos and C. Streli. Synchrotron µXRF analysis of Manganese distribution in antler and human bone. International Conference on Progress in Bone and Mineral Research 2015 and the Annual Autumn Conference of the Austrian Society for Bone and Mineral Research, Vienna, Austria; 3-5 December 2015

3. M. Rauwolf, B. Pemmer, A. Roschger, A. Turyanskaya, R. Simon, R. Windhager, K. Klaushofer, J. G. Hofstaetter, P. Roschger and C. Streli. Distribution of Zinc in human high-grade osteosarcoma and healthy tissue determined with confocal synchrotron radiation micro X-ray Fluorescence analysis. International Conference on Progress in Bone and Mineral Research 2015 and the Annual Autumn Conference of the Austrian Society for Bone and Mineral Research, Vienna, Austria; 3-5 December 2015

4. A. Svirkova, A. Turyanskaya, C. Streli, M. Marchetti-Deschmann. Sample preparation of sections with undecalcified bone for multimodal MALDI-MS and µ-XRF imaging. 12th ASAC-JunganalytikerInnen-Forum, Graz, Austria; 10-11 June 2016

5. A. Turyanskaya, M. Rauwolf, A. Roschger, J. Prost, P. Hischenhuber, T. Landete-Castillejos, R. Simon, P. Wobrauschek, P. Roschger, J.G. Hofstaetter, C. Streli. Manganese distribution in antler and human bone by SR-µXRF analysis. European Conference on X-ray Spectrometry, Gothenburg, Sweden; 19-24 June 2016

6. M. Rauwolf, B. Pemmer, A. Roschger, A. Turyanskaya, S. Smolek, A. Maderitsch, P. Hischenhuber, C. Weixelbaumer, M. Foelser, R. Simon, S. Lang, S. Puchner, R. Windhager, K. Klaushofer, P. Wobrauschek, P. Roschger, J. Hofstaetter and C. Streli. Zinc accumulation in mineralized osteosarcoma tissue determined with confocal SR-µXRF. European Conference on X-ray Spectrometry, Gothenburg, Sweden; 19-24 June 2016

7. P. Wobrauschek, M. Rauwolf, A. Turyanskaya, J. Prost and C. Streli. X-ray spectrometry with Synchrotron radiation. Symposium: Future Possible Use of Neutron and Synchrotron Sources by the Austrian User Community, Graz, Austria; 15-16 September 2016

8. A. Winkler, M. Rauwolf, A. Turyanskaya, J. Sterba, P. Wobrauschek and C. Streli. Spurenelementanalyse mit Totalreflexionsröntgenfluoreszenz. 66th Yearly Meeting of the Austrian Physical Society, Vienna, Austria; 27-29 September 2016

9. M. Rauwolf, B. Pemmer, A. Roschger, A. Turyanskaya, S. Smolek, A. Maderitsch, P. Hischenhuber, R. Simon, S. Lang, S. Puchner, R. Windhager, K. Klaushofer, J. Hofstätter, P. Roschger, C. Streli. Synchrotron radiation micro XRF analysis of zinc in osteosarcoma tissue. 26th Seminar Activation Analysis and Gamma Spectroscopy (SAAGAS 26), Vienna, Austria; 20-22 February 2017

10. C. Streli, M. Rauwolf, A. Turyanskaya, B. Pemmer, D. Ingerle, P. Roschger, A. Roschger, J. Hofstätter, N. Szoboszlai. Hard X-ray Spectroscopy of Biological Material using Synchrotron Radiation. NESY Winterschool (2017), Altaussee, Austria (**invited**); 06-10 March 2017

11. A. Turyanskaya, M. Rauwolf, P. Wobrauschek, C. Streli. Elemental bioimaging in bone by micro-X-ray-fluorescence spectroscopy (µXRF). 16th International Symposium on Trace Elements in Man and Animals (TEMA-16), International Society for Trace Element Research in Humans (ISTERH 2017), St. Petersburg, Russia; 26-29 June 2017

12. A. Turyanskaya, M. Rauwolf, L. Perneczky, A. Svirkova, M. Bonta, A. Limbeck, M. Marchetti-Deschmann, A. Roschger, P. Roschger, P. Wobrauschek, C. Streli. Multimodal Imaging of Biological Samples: Correlation of µXRF with MALDI-MSI and with LA-ICP-MS. Annual Denver X-ray Conference 2017, Big Sky, USA; 31 July – 4 August 2017

13. M. Rauwolf, A. Turyanskaya, A. Roschger, I. Pape, K. Sawhney, P. Wobrauschek, P. Roschger, J. Hofstätter, C. Streli. Zinc (Zn) and Lead (Pb) Accumulation in the Tidemark of Articular Cartilage with High-resolution micro-XRF. Annual Denver X-ray Conference 2017, Big Sky, USA; 31 July – 4 August 2017

14. M. Rauwolf, B. Pemmer, A. Roschger, A. Turyanskaya, S. Smolek, A. Maderitsch, P. Hischenhuber, R. Simon, S. Lang, S. Puchner, R. Windhager, K. Klaushofer, J. Hofstätter, P. Roschger, C. Streli. Synchrotron Radiation Micro XRF Analysis of Zinc in Osteosarcoma Tissue. Jahrestagung FG Nuklearchemie, GDCh Scientific Forum Chemistry 2017, Berlin, Germany (**invited**); 10-14 September 2017

15. C. Streli, P. Wobrauschek, D. Ingerle, M. Rauwolf, A. Turyanskaya, J. Prost, L. Perneczky, G. Pepponi. GIXRF, SR-TXRF-XANES and µ-XRF. IAEA technical meeting: Trends in Analytical Applications and Instrumental Developments of Synchrotron Based X-Ray Spectrometry Techniques (2017), Vienna, Austria; 03 October 2017

16. C. Streli, M. Rauwolf, A. Turyanskaya, D. Ingerle, P. Wobrauschek. X-ray spectrometry of biological material. BOKU Seminar, Vienna, Austria (**invited**); 25 January 2018

17. A. Svirkova, A. Turyanskaya, C. Streli, M. Marchetti-Deschmann. Molecular and Elemental Imaging for comprehensive information - the combination of MALDI MSI and µXRF. Austrian Cluster for Tissue Regeneration - Annual Meeting 2018, Vienna, Austria; 12-13 March 2018

18. M. Marchetti-Deschmann, M. Holzlechner, A. Svirkova, M. Bonta, A. Turyanskaya, J. Lohninger, C. Streli, A. Limbeck. Molecular and Elemental Imaging by Mass Spectrometry and micro X-Ray Fluorescence. 36th Informal Meeting on Mass Spectrometry, Köszeg, Hungary (**invited**); 06-09 May 2018; abstract in: "36th Informal Meeting on Mass Spectrometry Book", (2018), ISBN: 978-963-7067-37-2

19. M. Marchetti-Deschmann, M. Holzlechner, A. Svirkova, M. Bonta, A. Turyanskaya, J. Lohninger, C. Streli, A. Limbeck. Molecular Mass Imaging Combined with Elemental Information - From Multiple Modes to Multiple Sensors. Talk: 66th ASMS Conference on Mass Spectrometry and Allied Topics, San Diego, CA, USA; 03-07 June 2018; abstract in: "ASMS Annual Proceedings", (2018)

20. A. Turyanskaya, M. Rauwolf, L. Perneczky, A. Svirkova, S. Smetaczek, A. Limbeck, M. Marchetti-Deschmann, A. Roschger, P. Roschger, P. Wobrauschek, C. Streli. Multimodal imaging of biological samples: correlation of µXRF with MALDI-MSI and with LA-ICP-MS. EXRS/European Conference on X-Ray Spectrometry, Ljubljana, Slovenia; 24-29 June 2018

21. C. Streli, M. Rauwolf, A. Turyanskaya, D. Ingerle, P. Wobrauschek. Elemental imaging of trace elements in bone samples. Keynote Lecture: XVI Conferencia Latinoamericana de analisis por tecnicas de rayos X, Pucon, Chile (**invited**); 04-07 November 2018

22. C. Streli, M. Rauwolf, A. Turyanskaya, D. Ingerle, P. Wobrauschek. Elemental Imaging of Trace Elements in Bone Samples. Annual Denver X-ray Conference 2019, Lombard, IL, USA (**invited**); 5-9 August 2019

23. A. Turyanskaya, M. Rauwolf, V. Pichler, R. Simon, O. J. L. Fox, K. J. S. Sawhney, M. Burghammer, J. G. Hofstaetter, A. Roschger, P. Roschger, P. Wobrauschek, C. Streli. Gadolinium mapping in bone by XRF spectroscopy.17th International Congress on Photobiology. 18th Congress of the European Society for Photobiology (2019 ESP-IUPB World Congress), Barcelona, Spain (**invited**); 25-30 August 2019

24. M. Marchetti-Deschmann, M. Holzlechner, A. Svirkova, M. Bonta, A. Turyanskaya, M. Großgarten, A. Balbekova, K. Wieland, B. Lendl, A. Limbeck: Correlative Multimodal Imaging in Mass Spectrometry. 30th MassSpec-Forum Vienna, Vienna, Austria; 19-20 February 2019; in: "Book of Abstracts", (2019), 24

25. A. Turyanskaya, M. Rauwolf, V. Pichler, M. Burghammer, J. G. Hofstaetter, A. Roschger, P. Roschger, P. Wobrauschek, C. Streli, K. Sawhney. Gadolinium mapping in bone by micro-/submicro-XRF. EXRS 2022/European Conference on X-Ray Spectrometry, Bruges, Belgium, 26 June-1 July 2022

Poster Presentations

1. A. Turyanskaya, M. Rauwolf, A. Roschger, B. Pemmer, J. Prost, R. Simon, P. Roschger, J.G. Hofstaetter, T. Landete-Castillejos, K. Klaushofer, P. Wobrauschek and C. Streli: Spatially resolved manganese distribution in antler and human bone. 64th Annual Denver X-Ray Conference, Westminster, USA; 3-7 August 2015

2. A. Turyanskaya, T.A. Gruenewald, M. Meischel, M. Rauwolf, J. Prost, H. Lichtenegger, S.E. Stanzl-Tschegg, A.M. Weinberg, P. Wobrauschek and C. Streli: Magnesium diffusion from implant into bone tissue observed by µXRF imaging. 64th Annual Denver X-Ray Conference, Westminster, USA; 3-7 August 2015

3. M. Rauwolf, A. Turyanskaya, A. Roschger, B. Pemmer, J. Prost, R. Simon, M. Radtke, T. Schoonjans, O. Scharf, A. Guilherme, P. Roschger, J.G. Hofstaetter, R. Windhager, K. Klaushofer, P. Wobrauschek and C. Streli: SR-µXRF of bone samples - a comparison of a confocal and a CXC setup 64th Annual Denver X-Ray Conference, Westminster, USA; 3-7 August 2015

4. A. Svirkova, A. Turyanskaya, G. Allmaier, C. Streli and M. Marchetti-Deschmann: Sectioning of undecalcified bone tissue for multimodal MALDI-MS and µ-XRF imaging. Ourcon III, Pisa, Italy; 27-29 October 2015

5. A. Svirkova, A. Turyanskaya, T. Bretschneider, C. Streli, M. Marchetti-Deschmann. Sample preparation of tissue containing undecalcified bone for multimodal MALDI-MS and µ-XRF imaging. 27th MassSpec Forum Vienna, Vienna; 23-24 February 2016

6. A. Turyanskaya, M. Rauwolf, A. Roschger, J. Prost, B. Pemmer, R. Simon, P. Roschger, J.G. Hofstaetter, T. Landete-Castillejos, P. Wobrauschek, C. Streli. Manganese distribution in bone tissue by SR-µXRF. 43rd Annual European Calcified Tissue Society Congress, Rome, Italy; 14–17 May 2016

7. M. Rauwolf, B. Pemmer, A. Roschger, A. Turyanskaya, R. Simon, S. Lang, S. E. Puchner, R. Windhager, K. Klaushofer, P. Wobrauschek, J. G. Hofstaetter, P. Roschger and C. Streli.

Increased zinc accumulation in mineralized osteosarcoma tissue. 43rd Annual European Calcified Tissue Society Congress, Rome, Italy; 14–17 May 2016

8. A. Turyanskaya, T.A. Gruenewald, M. Rauwolf, M. Meischel, J. Prost, L. Perneczky, H. Lichtenegger, S.E. Stanzl-Tschegg, A. Weinberg, P. Wobrauschek, C. Streli. Magnesium-based biodegradable orthopedic implants by µXRF. European Conference on X-ray Spectrometry, Gothenburg, Sweden; 19-24 June 2016

9. M. Rauwolf, A. Turyanskaya, A. Roschger, J. Prost, R. Simon, I. Pape, K. Sawhney, P. Wobrauschek, P. Roschger, J. Hofstaetter and C. Streli. SR-µXRF analysis of the zinc distribution in healing osteoporotic fractures. European Conference on X-ray Spectrometry, Gothenburg, Sweden; 19-24 June 2016

10. A. Winkler, M. Rauwolf, A. Turyanskaya, C. Streli and J. Sterba. Total X-ray reflection spectrometry analysis of trace elements in tea and herbal infusions. European Conference on X-ray Spectrometry, Gothenburg, Sweden; 19-24 June 2016

11. P. Wobrauschek, P. Allinger, A. Turyanskaya, A. Utz, S. Smolek, D. Ingerle and C. Streli. MAXI 2D-spectrometer: compact scanning device with variable spot size in the mm range for large area macro-scans. European Conference on X-ray Spectrometry, Gothenburg, Sweden; 19-24 June 2016

12. A. Turyanskaya, M. Rauwolf, A. Roschger, J. Prost, P. Hischenhuber, R. Simon, P. Roschger, J.G. Hofstaetter, K. Klaushofer, P. Wobrauschek, C. Streli. Manganese distribution in healthy and osteoporotic human bone. 65th Annual Denver X-Ray Conference, Rosemont, USA; 1-5 August 2016

13. A. Turyanskaya, T.A. Gruenewald, M. Meischel, M. Rauwolf, J. Prost, L. Perneczky, H. Lichtenegger, S.E. Stanzl-Tschegg, A.M. Weinberg, P. Wobrauschek, C. Streli. Elemental imaging on biodegradable orthopedic implants by µXRF. 65th Annual Denver X-Ray Conference, Rosemont, USA; 1-5 August 2016

14. M. Rauwolf, B. Pemmer, A. Roschger, A. Turyanskaya, S. Smolek, A. Maderitsch, P. Hischenhuber, C. Weixelbaumer, M. Foelser, R. Simon, S. Lang, S. E. Puchner, R. Windhager, K. Klaushofer, P. Wobrauschek, P. Roschger, J.G. Hofstaetter, C. Streli. Increased zinc accumulation in mineralized osteosarcoma tissue measured by SR-µXRF analysis. 65th Annual Denver X-Ray Conference, Rosemont, USA; 1-5 August 2016

15. M. Rauwolf, A. Turyanskaya, A. Roschger, B. Pemmer, J. Prost, R. Simon, I. Pape, K. Klaushofer, P. Wobrauschek, P. Roschger, J.G. Hofstaetter, C. Streli. Zn distribution in healing osteoporotic fractures measured by SR-µXRF analysis. 65th Annual Denver X-Ray Conference, Rosemont, USA; 1-5 August 2016

16. A. Turyanskaya, M. Rauwolf, L. Perneczky, T.A. Gruenewald, M. Meischel, H. Lichtenegger, S.E. Stanzl-Tschegg, A.M. Weinberg, P. Wobrauschek and C. Streli. Exploitation of µXRF spectrometer for Bio-Imaging. X-Ray Microscopy Conference (XRM2016), Oxford, UK; 15-19 August 2016

17. M. Rauwolf, A. Turyanskaya, A. Roschger, J. Prost, R. Simon, I. Pape, M. Radtke, O. Scharf, T. Schoonjans, A. Guilherme Buzanich, K. Sawhney, P. Wobrauschek, P. Roschger, J.G. Hofstaetter and C. Streli. Zinc distribution in human bone: SR-micro X-ray fluorescence imaging of osteoporotic samples. X-Ray Microscopy Conference (XRM2016), Oxford, UK; 15-19 August 2016

18. D. Ingerle, N. Szoboszlai, I. Pape, K. Sawhney, A. Turyanskaya, M. Rauwolf, and C. Streli. High resolution imaging of metal localization in cancer cells at the B16 beamline at Diamond. X-Ray Microscopy Conference (XRM2016), Oxford, UK; 15-19 August 2016

19. L. Perneczky, A. Turyanskaya, S. Smolek, M. Rauwolf, P. Wobrauschek and C. Streli. Confocal µXRF spectrometer for analysis of 3-dimensional spatial distribution of low to high Z elements. 66th Yearly Meeting of the Austrian Physical Society, Vienna, Austria; 27-29 September 2016

20. A. Winkler, M. Rauwolf, A. Turyanskaya, J. Sterba, P. Wobrauschek and C. Streli. Total X-ray reflection fluorescence spectrometry analysis of trace elements in tea and herbal infusions. 66th Yearly Meeting of the Austrian Physical Society, Vienna, Austria; 27-29 September 2016

21. M. Rauwolf, B. Pemmer, A. Roschger, A. Turyanskaya, S. Smolek, A. Maderitsch, P. Hischenhuber, M. Foelser, R. Simon, S. Lang, S. E. Puchner, R. Windhager, K. Klaushofer, J. G. Hofstaetter, P. Roschger and C. Streli. Confocal SR-µXRF measurements of increased Zinc accumulation in mineralized osteosarcoma. 66th Yearly Meeting of the Austrian Physical Society, Vienna, Austria; 27-29 September 2016

22. A. Svirkova, A. Turyanskaya, C. Streli, M. Marchetti-Deschmann. Method development for sample preparation of sections with undecalcified bone for multimodal MALDI MS and µ-XRF imaging. Ourcon IV, Ustron, Poland; 17-21 October 2016

23. A. Turyanskaya, M. Rauwolf, L. Perneczky, T. Gruenewald, M. Meischel, H. Lichtenegger, S.E. Stanzl-Tschegg, A. Weinberg, P. Wobrauschek, C. Streli. µXRF spectrometer at Atominstitut for bio-imaging applications. 26th Seminar Activation Analysis and Gamma Spectroscopy (SAAGAS 26), Vienna, Austria; 20-22 February 2017

24. G. Gamauf, L. Perneczky, A. Turyanskaya, J.H. Sterba, C. Streli. Non-destructive depth analysis of Sueki ceramics using confocal µXRF spectrometry combined with NAA data. 26th Seminar Activation Analysis and Gamma Spectroscopy (SAAGAS 26), Vienna, Austria; 20-22 February 2017

25. L. Perneczky, A. Turyanskaya, S. Smolek, M. Rauwolf, P. Wobrauschek, C. Streli. Confocal µXRF spectrometer for low to high Z element analysis. 26th Seminar Activation Analysis and Gamma Spectroscopy (SAAGAS 26), Vienna, Austria; 20-22 February 2017

26. A. Winkler, M. Rauwolf, A. Turyanskaya, J.H. Sterba, C. Streli. Total X-ray reflection fluorescence spectrometry of black tea and herbal infusions. 26th Seminar Activation Analysis and Gamma Spectroscopy (SAAGAS 26), Vienna, Austria; 20-22 February 2017

27. A. Pejovic-Milic, D. Cardenas, A. Turyanskaya, M. Rauwolf, G. Wohl, C. Streli, P. Wobrauschek. Elemental mapping in rat bones treated with strontium ranelate and strontium citrate using µXRF. 16th International Symposium on Trace Elements in Man and Animals (TEMA-16), International Society for Trace Element Research in Humans (ISTERH 2017), St. Petersburg, Russia; 26-29 June 2017

28. A. Turyanskaya, M. Rauwolf, T. Bretschneider, P. Wobrauschek, C. Streli, A. Roschger, J. Hofstätter, P. Roschger, I. Zizak. Investigation of the Local Manganese Distribution in Bone in Female and Male Osteoporosis Compared to Healthy Controls. Annual Denver X-ray Conference 2017, Big Sky, USA; 31 July – 04 August 2017

29. A. Turyanskaya, L. Perneczky, M. Rauwolf, P. Wobrauschek, C. Streli, D. Eichert, F. Brigidi, W. Jark, S. Bjeoumikhova, G. Pepponi, P. Roschger. Implementation of a Confocal SR-

microXRF System for Bone Analysis at the X-ray Fluorescence Beam Line at Elettra. Annual Denver X-ray Conference 2017, Big Sky, USA; 31 July – 04 August 2017

30. M. Rauwolf, A. Turyanskaya, A. Roschger, P. Wobrauschek, P. Roschger, J. Hofstätter, C. Streli. Novel Clustering Approach for the Segmentation of Elemental Distributions in Human Bone. Annual Denver X-ray Conference 2017, Big Sky, USA; 31 July – 4 August 2017

31. A. Winkler, M. Rauwolf, A. Turyanskaya, J.H. Sterba, C. Streli. Trace elements analysis in tea and herbal infusions by means of TXRF. 17th International Conference on Total Reflection X-Ray Fluorescence Analysis and Related Methods (TXRF2017), Brescia, Italy; 19-22 September 2017

32. D. Meusburger, K. Keuenhof, P. Slezak, P. Heimel, N. Frischauf, B. Plochberger, C. Streli, A. Turyanskaya, T. Heuser, N. Fellner, K. Macfelda, T. Wanek, C. Schöfer, M. Glösmann, A. Walter. BioImaging Austria – Correlated Multimodal Imaging. MIC Festival – Medical Imaging in Personalized Medicine, Medical University Vienna, Vienna, Austria; 14 June 2018

33. A. Turyanskaya, M. Rauwolf, O. Fox, I. Pape, K. Sawhney, T. Grünewald, M. Burghammer, J. Hofstätter, A. Roschger, P. Roschger, P. Wobrauschek, C. Streli. Detection of Gadolinium accumulation in bone by XRF. EXRS 2018/European Conference on X-Ray Spectrometry, Ljubljana, Slovenia; 24-29 June 2018

34. M. Rauwolf, A. Turyanskaya, A. Roschger, I. Pape, K. Sawhney, P. Wobrauschek, P. Roschger, C. Hofstätter, C. Streli. Micro-XRF analysis of zinc and lead accumulation in the tidemark of articular cartilage. EXRS 2018/European Conference on X-Ray Spectrometry, Ljubljana, Slovenia; 24-29 June 2018

35. A. Turyanskaya, M. Rauwolf, V. Pichler, P. Wobrauschek, C. Streli, T. Grünewald, M. Burghammer, O. Fox, I. Pape, K. Sawhney, J. Hofstätter, A. Roschger, P. Roschger. Detection on of Gadolinium Accumulation in Bone by XRF. Denver X-ray conference (2018), Westminster, USA; 06-10 August 2018

36. M. Rauwolf, A. Turyanskaya, D. Ingerle, C. Streli, N. Szoboszlai, I. Pape, A. Malandain, O. Fox, K. Sawhney, L. Hahn. The Submicro-X-ray Fluorescence Setup on the B16 Beamline at Diamond Light Source. Denver X-ray conference (2018), Westminster, USA; 06-10 August 2018

37. A. Svirkova, A. Turyanskaya, L. Perneczky, C. Streli, M. Marchetti-Deschmann. Multimodal imaging of undecalcified tissue sections by MALDI MS and µXRF. XXII International Mass Spectrometry Conference, Florence, Italy; 26-31 August 2018; abstract in: "Conference Program of the XXII International Mass Spectrometry Conference", (2018), ISBN: 9788890738852; 913 - 914

38. A. Turyanskaya, A. Svirkova, L. Perneczky, C. Streli, M. Marchetti-Deschmann: Correlative multimodal imaging of chicken phalanx sections by µXRF and MALDI MSI. CMI Imaging in the Life Sciences Meeting 2018, Vienna, Austria; 20-21 September 2018

39. A. Turyanskaya, M. Rauwolf, V. Pichler, T. Grünewald, M. Burghammer, O. Fox, I. Pape, K. Sawhney, J. Hofstätter, A. Roschger, P. Roschger, P. Wobrauschek, C. Streli. Imaging of Gadolinium accumulation in bone by XRF. CMI Imaging in the Life Science Meeting 2018, Vienna, Austria; 20-21 September 2018

40. K. Keuenhof, D. Meusburger, C. Streli, A. Turyanskaya, T. Heuser, N. Fellner, M. Brandstetter, H. Kotisch, T. Wanek, C. Schöfer, M. Glösmann, K. Macfelda, A. Walter. Imaging across modalities, scales and species. CMI Imaging in the Life Science Meeting 2018, Vienna, Austria; 20-21 September 2018

41. D. Meusburger, B. Plochberger, N. Frischauf, C. Streli, P. Wobrauschek, A. Turyanskaya, P. Dungel, P. Heimel, P. Slezak, A. Walter. Multimodal Imaging to assess regenerative processes in BIS-related osteonecrosis. CMI Imaging in the Life Science Meeting 2018, Vienna, Austria; 20-21 September 2018

42. M. Rauwolf, R. Wanzenböck, A. Turyanskaya, D. Ingerle, A. Guilherme Buzanich, S. Lang, R. Windhager, M. Radtke, J. G. Hofstaetter, A. Roschger, P. Roschger, S. Sprio, L. Preti, A. Tampieri, C. Streli. Determination of the Oxidation State of Zinc and Strontium in Mineralized Osteosarcoma Tissue by Micro X-ray Fluorescence XANES. Annual Denver X-ray Conference 2019, Lombard, IL, USA; 5-9 August 2019

43. M. Rauwolf, A. Turyanskaya, B. Pemmer, A. Roschger, S. Smolek, A. Maderitsch, P. Hischenhuber, R. Simon, S. Lang, S. E. Puchner, K. Klaushofer, P. Wobrauschek, P. Roschger, J. G. Hofstaetter, C. Streli. Analysis of zinc in osteosarcoma tissue by synchrotron radiation micro XRF. 17th International Congress on Photobiology. 18th Congress of the European Society for Photobiology (2019 ESP-IUPB World Congress), Barcelona, Spain; 25-30 August 2019

44. A. Turyanskaya, M. Rauwolf, V. Pichler, R. Simon, M. Burghammer, O. Fox, K. Sawhney, J. Hofstaetter, A. Roschger, P. Roschger, P. Wobrauschek, C. Streli. Imaging of Gadolinium accumulation in bone by XRF. Biennial Meeting ViCEM – Vienna Center for Engineering in Medicine, Vienna, Austria, 14-15 November 2019

45. M. Rauwolf, A. Turyanskaya, B. Pemmer, A. Roschger, S. Smolek, A. Maderitsch, P. Hischenhuber, R. Simon, S. Lang, S. E. Puchner, K. Klaushofer, P. Wobrauschek, P. Roschger, J. G. Hofstaetter, C. Streli. Analysis of zinc in osteosarcoma tissue by synchrotron radiation micro XRF. Conference on Multimodality Imaging in Life Sciences 2019, COMULIS & BioImaging Austria – CMI, Vienna, Austria, 21-22 November 2019

46. A. Turyanskaya, S. Smetaczek, V. Pichler, M. Rauwolf, A. Roschger, P. Roschger, A. Limbeck, C. Streli. Correlation of µXRF and LA-ICP-MS in analysis of human bone-cartilage sample. Conference on Multimodality Imaging in Life Sciences 2019, COMULIS & BioImaging Austria – CMI, Vienna, Austria, 21-22 November 2019

47. A. Turyanskaya, M. Rauwolf, V. Pichler, M. Burghammer, O. Fox, K. Sawhney, J. Hofstätter, A. Roschger, P. Roschger, P. Wobrauschek, C. Streli. Imaging of Gadolinium accumulation in human bone by XRF. Online Conference: 2020 Virtual SSRL/LCLS Users' Meeting, Stanford, USA; 28 September – 10 October 2020

48. A. Turyanskaya, St. Smetaczek, V. Pichler, M. Rauwolf, L. Perneczky, A. Roschger, P. Roschger, A. Limbeck, C. Streli. Correlation of µXRF and LA-ICP-MS in analysis of human bone-cartilage sample. 31st MassSpec Forum Vienna (2020), Vienna, Austria; 25-26 February 2020